UNIVERSITÀ DEGLI STUDI DI TRIESTE

XXX CICLO DEL DOTTORATO DI RICERCA IN

INGEGNERIA E ARCHITETTURA

Evacuation dynamics in the maritime field: modelling, simulation and real-time human participation

Settore scientifico-disciplinare: ING-IND/01 ARCHITETTURA NAVALE

Ph.D. Candidate
Gabriele Montecchiari

DOCTORATE COORDINATOR
Diego Micheli
University of Trieste

SUPERVISOR
Gabriele Bulian
University of Trieste

CO-SUPERVISOR
Paolo Gallina
University of Trieste

ACADEMIC YEAR 2016/2017

UNIVERSITÀ DEGLI STUDI DI TRIESTE

XXX CICLO DEL DOTTORATO DI RICERCA IN

INGEGNERIA E ARCHITETTURA

Evacuation dynamics in the maritime field: modelling, simulation and real-time human participation

Settore scientifico-disciplinare: ING-IND/01 ARCHITETTURA NAVALE

Ph.D. Candidate
Gabriele Montecchiari

DOCTORATE COORDINATOR
Diego Micheli
University of Trieste

SUPERVISOR
Gabriele Bulian
University of Trieste

CO-SUPERVISOR
Paolo Gallina
University of Trieste

ACADEMIC YEAR 2016/2017

ABSTRACT

The topic of evacuation analysis is becoming increasingly important in the maritime field, especially after the recent approval of relevant amendments to SOLAS. These amendments make evacuation analysis in early design stage mandatory not only for ro-ro passenger ships, as in the past, but also for other passenger ships, constructed on or after 1st January 2020, carrying more than 36 passengers. Tools used to perform evacuation simulations are generally run in a non-interactive batch mode. However, the introduction of the possibility for humans to interactively participate in a simulated evacuation process together with computer controlled agents in an immersive virtual environment, can open a series of interesting possibilities for design, research and development.

Therefore, with particular reference to the maritime field, the research described in this dissertation is focused on the development and implementation of a mathematical model for simulating the dynamics of evacuation processes, which also allows real time human interaction through the use of virtual reality.

The developed mathematical model, which is capable of naturally embedding human interaction, was verified and validated through a series of tests and through comparisons with other models and experimental data, as well as by referring to the relevant guidelines proposed by the International Maritime Organization (IMO). Particular attention was given to the calibration and validation of the counterflow model, developed during the research activity, and to the analysis of flow-density relation. The possibility of real time user participation, consisting in the user taking control over an agent inside the simulation, was introduced along with a vibrotactile haptic interface which was created to enhance the user perception of the surrounding virtual environment. The developed tool and user interfaces were adopted in an experiment where the subject was immersed in a virtual environment and interacted with simulated agents. The analysis of experiments provided results on the effects of the developed haptic interface on the subjects' behaviour. Moreover, the obtained data allowed comparing the behaviour of subjects with that of simulated agents.

The mathematical model was subsequently extended with the introduction of ship motion effects on agents behaviour, considering that, in the maritime field, the platform is usually moving. Fictitious forces, in the developed model, are directly applied to the agents and might therefore modify their trajectories. This represents an added value of the proposed model, because, usually, the effects of ship motions are embedded in simulation models only through a speed reduction. The model was used to assess ship motion effects in some IMO test cases. Finally, the tool was tested on a specifically developed case targeting the maritime field whose geometry was ideated as a simplification of the general plan of a real cruise vessel. The evacuation simulations were run firstly without ship motions, then with some representative situations combining heel, trim and periodic motions and, finally, with motions due to irregular waves. Ship motions, in this latter case, have been generated considering a notational cruise vessel whose dimensions were in line with the cruise vessel the test geometry was inspired to. A model introducing ship motion effects on the control of the avatar was finally developed, together with an approach to provide perception of ship motions through the developed vibrotactile interface.

Models and results presented in this dissertation provide new insight to the field of ship evacuation analysis and to the application of virtual reality in this field.

SOMMARIO

L'analisi delle performance dal punto di vista dell'evacuazione sta acquisendo sempre più importanza in campo navale, specialmente in seguito alla recente approvazione degli emendamenti alla SOLAS che rendono obbligatoria l'analisi di evacuazione durante lo stadio iniziale di progettazione non solo per le navi passeggeri Ro-Ro, come in passato, ma anche per le altre navi passeggeri con più di 36 passeggeri, costruite dal 1 Gennaio 2020. Gli strumenti utilizzati per le simulazioni di evacuazione funzionano solitamente in modalità batch non interattiva. Tuttavia l'introduzione della possibilità di una partecipazione interattiva da parte dell'utente nel processo di evacuazione insieme agli agenti simulati, in un ambiente virtuale immersivo, potrebbe aprire nuove possibilità di ricerca e sviluppo.

Quindi, con particolare attenzione al campo navale, la ricerca descritta in questa tesi si è concentrata sullo sviluppo ed implementazione di un modello per la simulazione dei processi di evacuazione, che permette anche un'interazione umana in tempo reale attraverso l'utilizzo della realtà virtuale.

Il modello sviluppato, che permette di introdurre in modo naturale l'interazione umana, è stato verificato e validato attraverso una serie di test, tramite confronti con altri modelli e con dati sperimentali, e riferendosi alle pertinenti linee guida della International Maritime Organization (IMO). Si è prestata particolare attenzione al processo di calibrazione e validazione del modello di counterflow, sviluppato durante l'attività di ricerca, e all'analisi della relazione flusso-densità. Si è inoltre introdotta la possibilità, per un utente, di partecipare in tempo reale al processo di evacuazione controllando un agente. Parallelamente è stata sviluppata un'interfaccia vibro-tattile con lo scopo di migliorare la percezione dell'ambiente virtuale circostante. La strumentazione sviluppata è stata utilizzata in un esperimento in cui ciascun soggetto partecipante è stato immerso in un ambiente virtuale dove ha potuto interagire con gli agenti controllati dal computer. L'analisi dei dati sperimentali ha fornito risultati riguardo agli effetti dell'interfaccia vibro-tattile sul comportamento degli utenti. Inoltre, i dati ottenuti hanno permesso un confronto fra il comportamento degli utenti e quello degli agenti controllati dal computer.

Poiché, in campo navale, la piattaforma è tipicamente mobile, il modello matematico è stato esteso introducendo l'effetti dei moti nave sul comportamento degli agenti. Nel modello sviluppato le forze apparenti dovute ai moti sono direttamente applicate agli agenti e ne possono modificare le traiettorie. Questo aspetto costituisce un valore aggiunto del modello proposto poiché, generalmente, l'effetto dei moti nave viene introdotto nei modelli di simulazione solo con una riduzione della velocità. Il modello è stato utilizzato per studiare gli effetti dei moti nave in alcuni casi test proposti dall'IMO. Infine, il modello è stato testato su di un caso test prettamente navale specificatamente sviluppato. La geometria del caso test sviluppato è stata ideata come semplificazione dei piani generali di una reale nave da crociera. Le simulazioni di evacuazione sono state condotte senza moti nave, con combinazioni di angoli di rollio e assetto, con moti periodici e con moti dovuti a mare irregolare al traverso. In quest'ultimo caso i moti sono stati generati considerando una carena di una nave da crociera non esistente, ma realistica e in linea con la nave da cui la geometria del caso test è stata ispirata. Infine, è stato ideato un modello per introdurre gli effetti dei moti nave sul controllo dell'avatar, insieme ad un approccio per fornire la percezione dei moti nave attraverso l'interfaccia vibro-tattile sviluppata.

I modelli e i risultati presentati in questa tesi forniscono nuove idee e informazioni riguardo l'analisi dei processi di evacuazione in campo navale e l'applicazione della realtà virtuale in tale campo.

ACNOWLEDGMENTS

This work was carried out thanks to the financial support from the Ph.D. scholarship G/3-Cycle XXX financed by MIUR “Progetto Giovani Ricercatori” through University of Trieste.

This page is intentionally left blank

TABLE OF CONTENTS

LIST OF FIGURES

This page is intentionally left blank

LIST OF TABLES

1 INTRODUCTION

One of the key rules of ship design is that a ship should be her own best lifeboat. However, in the operational life of a vessel there might be unfortunate cases of emergencies, such as flooding and fire, which could require the abandonment of the ship. In the maritime sector the assessment of the ship layout from the point of view of evacuation is particularly important in case of vessels carrying a large number of people on-board. The analysis of evacuation performance represents, therefore, an important topic in the field of ship safety, and it is then not a surprise that ship evacuation analysis is addressed by present international regulations. Moreover, evacuation analysis in the maritime sector is nowadays gaining increasing attention and this is driving evolutions of relevant regulations. At the same time, a detailed assessment of evacuation performance requires complex mathematical models, which are typically based, to a large extent, on semi-empirical models tuned on experimental data. A specific aspect of evacuation from ships, which has no counterpart in the civil sector, is the possible presence of motions. Evacuees may therefore need to abandon the vessel under the effects of a moving platform. It is therefore necessary, in general, that mathematical models for ship evacuation are able to represent also the effects of ship motions. Given the mentioned high level of underlying semi-empiricism, the process for the development, tuning and validation of evacuation mathematical model is, therefore, an essential step to provide confidence in their performance. In this respect, the difficulties associated with the carrying out of experiments represent a limitation for the development of mathematical models. Experimental difficulties call for the exploration of alternative approaches, such as the use of virtual reality and real-time human participation in the simulated evacuation process, which could provide some support in the collection of surrogate data with respect to the true experimental ones. Moreover, virtual reality could also be of help in the design process, in order to provide the designer a first-person point of view and an immersive perception of the ship layout and of possible evacuation control strategies.

The above considerations represented the starting point for the research activity leading to the present thesis. In the following, firstly, some of the mentioned aspects are briefly

addressed, leaving details to the other relevant chapters of the thesis. At the end of this chapter, the main objectives of the research activity are summarised and the structure of the thesis is described.

1.1 International regulations addressing ship evacuation analysis

Currently, minimum requirements in terms of ship evacuation performance are specified, at an international level, within the framework of SOLAS (International Convention for the Safety of Life at Sea [87]). SOLAS was firstly adopted in 1914, as a response to the accident of Titanic. The main objective of SOLAS is to specify minimum standards for the construction, equipment and operation of the ships, in order to guarantee a sufficient level of safety. SOLAS was subsequently modified and emended many times and the current version of SOLAS Convention is referred to as SOLAS 1974, as emended, ([87]) and it is continuously undergoing evolutions through the amendment process.

The organization specifically appointed to develop international regulations in the maritime field is the International Maritime Organization (IMO), which is a specialized agency of the United Nations, and which was established in 1948, originally with the name of IMCO (Inter-Governmental Maritime Consultative Organization). Among the tasks of IMO, the development and implementation of minimum standard requirements aimed at enhancing ship safety for ships engaged in international trades is fundamental ([88]).

The importance of assessing the ship layout from the point of view of evacuation, early in the design stage, in order to improve the safety of the passengers was already recognized by IMO in the past. Evacuation analysis was initially mandatory only for ro-ro passenger vessels constructed on or after 1 July 1999. Originally, such analysis was mandatory, early in the design process, under SOLAS ([87]) Ch.II-2 requirements, in accordance to the interim guidelines contained in MSC/Circ.909 [152], issued in 1999. Afterwards, MSC/Circ.909 was firstly replaced by MSC/Circ.1033 [150] in 2002. Guidelines in MSC/Circ.1033 were no longer specific for ro-ro passenger ships, but were intended to address passenger ships in general (in case of voluntary application). In the meantime, simplified evacuation analysis for high speed passenger craft, as required by the International Code of Safety for High-Speed Craft, 2000 (2000 HSC Code [86]), was initially addressed through the guidelines MSC/Circ.1001 [149] in 2001, which was then superseded by MSC/Circ.1166 [151] in 2005. The guidelines for passenger ships in MSC/Circ.1033 were then replaced by MSC.1/Circ.1238 [146] in 2007. As a further step, in 2016, a set of amendments to SOLAS Ch.II-2 (SOLAS, [87]) were adopted through MSC.404(96) [148]. Part of such amendments have made mandatory the evacuation analysis for the evaluation of escape routes, early in the design process, also for all passenger ships constructed on or after 1 January 2020 carrying more than 36 passengers (in addition to ro-ro passenger ships constructed on or after 1 July 1999, for which the analysis was already mandatory). In parallel, the IMO Maritime Safety Committee (MSC) also approved the revised guidelines on evacuation analysis for new and existing passenger ships, MSC.1/Circ.1533 [147] in 2016, which superseded the previous guidelines from MSC.1/Circ.1238 [146].

According to MSC.1/Circ.1533 [147] evacuation analysis should be adopted for:

- Assessing the evacuation process through benchmark scenarios provided in the guidelines. The assessment is mostly performed by analysing the overall duration of the evacuation process.
- Identify congestion points and/or critical areas (e.g. areas of intense cross or counter flows).

MSC.1/Circ.1533 [147] indicates that the analyses are to be carried out, as a minimum, by referring to four different benchmark scenarios (cases 1 to 4). In the two primary cases, a night case (case 1) and a day case (case 2), all escape routes are considered available. Then, a night case (case 3) and a day case (case 4) are to be considered, either with one complete run of stairways having largest capacity unavailable, or with an increased number of people in the considered main vertical zone coming from an adjacent main vertical zone. Two additional cases may also be considered, namely an "open deck" scenario (case 5) and an "embarkation" scenario (case 6), but are not mandatory.

Evacuation analysis is based on models capable of simulating, to some extent, the evacuation process in time domain by taking the geometry of the ship as input. The aforementioned four evacuation scenarios can be simulated through two different approaches indicated in MSC.1/Circ.1533 [147]. The first type of approach, called "simplified evacuation analysis", is based on evacuation models modelling the crowd as a whole, and it is based on the representation of the evacuation process borrowing concepts from the fluid dynamics ([78], [83]). The second type of approach allowed by MSC.1/Circ.1533 [147], called "advanced evacuation analysis", is based on mathematical models capable of reproducing each evacuee singularly with its own properties. This last method is considered more accurate since it is closer to reality.

Nowadays, many different evacuation models exist which are capable of performing advanced evacuation analysis (e.g. [12], [56], [106], [113], [129], [214], [219]). Clearly, the determination of the level of accuracy to which models are able to reproduce the reality is a crucial issue when the final target is the application of such models for advanced evacuation analysis, particularly in case of large and complex vessels. The relevance of the evacuation analysis, in fact, depends on the capability of the simulation tool to correctly reproduce the real behaviour of the people involved in the evacuation process. However, one of the biggest difficulties for carrying out an objective evaluation of the performance and capabilities of different available evacuation models is the lack of experimental data to compare them with.

In order to provide minimum standard requirements for an evacuation tool to be adopted for evacuation analysis, MSC.1/Circ.1533 [147] proposes a series of tests, referred to as "IMO tests", which are based on very simplified, actually archetypal, geometries and test conditions. Such tests are intended for being used for the verification of the evacuation models. It was however observed by Ronchi [179], that the IMO test cases can be considered as "verification tests", but they do not represent a set of "validation" test cases for an evacuation tool.

1.2 Difficulties associated with the development, tuning and validation of models for ship evacuation analysis

An exhaustive quantitative validation is fundamental to assess the effectiveness of the calibration of the parameters of an evacuation tool. However, the lack of experimental data, mostly due to the difficulty of performing evacuation experiments involving many subjects, prevents evacuation tools from undergoing a deep and extensive validation process. This situation represents an important problem for evacuation analysis.

Another specific difficulty in modelling the evacuation process in the maritime field is associated with the possibility that the evacuation process occurs on a moving/inclined platform due to ship motions induced by waves, or due to (quasi-)static heel and/or trim induced by, e.g., flooding, wind, etc. The effects of the forces perceived by the evacuees (induced by gravity due to inclinations, or due to motion-induced accelerations), may not be negligible, as already acknowledged by IMO (MSC 78/INF.8 [145], SDC 2/INF.9 [192]). Motion effects should, thus, be embedded in evacuation models intended for being used in the maritime field.

It is however to be underlined that MSC.1/Circ.1533 [147] does not consider a scenario with ship motion. Nevertheless, some evacuation tools specifically targeting the maritime field (e.g., [113], [135], [169]) embed approaches aimed at considering, to some extent, the effects of ship motion on the behaviour of the evacuees. However, also the process of developing reliable models addressing the effects of ship motions on evacuation is significantly affected by the lack of detailed experimental data to compare with.

One important problem concerning the development, tuning and validation of evacuation tools is, hence, represented by the combined great necessity of, and, at the same time, the significant difficulty of, gathering experimental data, due the difficulties in performing experiments. Recent developments of virtual reality hardware and software may, however, provide an additional tool to gather data on human behaviour by performing virtual experiments instead of, or to complement real experiments.

1.3 Use of virtual reality for ship evacuation simulations

Evacuation tools are generally used in batch mode for the purpose of safety assessment of a design. In such an approach, the user does not participate in the on-going simulation. However, introducing the possibility for users to interactively participate in the evacuation process, together with the agents, can open a series of interesting possibilities for design, research and development, which seem to have not yet been deeply explored, particularly in the maritime field.

Immersive virtual reality is an emergent technique in the field of pedestrian dynamics and evacuation simulation. The recent availability in the market of low cost hardware for immersive virtual reality such as head mounted displays (Oculus VR [161]) and, in parallel, the flourishing of development environments supporting this kind of hardware, have given a boost to the research in this field. Virtual reality has been shown to

represent a promising tool to gather information about human behaviour (e.g. [143], [163]). However, the use of virtual reality, while showing significant potentials, presents also some limitations. Pérez Arias et al. [170] highlight, in particular, the lack of contact perception which prevents users from behaving realistically in the virtual world in conditions of very high density.

Also in case of use of virtual reality, a further complication specific to the maritime field is the possible presence of ship motions during an evacuation scenario, which cause passengers to perceive external forces due to platform inclinations and/or dynamic motions, and which eventually may affect the behaviour of evacuees. Reproducing such effects in a virtual reality environment intended for evacuation simulations is, however, a complex task. Motions could be (partially) reproduced by means of large and costly hardware installations such as those used for ship handling/bridge simulators (e.g. [14], [37], [110], [131]). However, such facilities are not suitable, due to costs, if the intention is to envision a broader use of virtual reality in the maritime evacuation field.

1.4 Objectives of the research activity and structure of the thesis

The aforementioned background inspired a multidisciplinary research activity aimed at the development, implementation and application of an agent based evacuation mathematical model specifically targeting the maritime field, with some distinctive characteristics.

One of the objectives was that the developed model could be verified and validated and could be suitable for the advanced evacuation analysis as suggested by MSC.1/Circ.1533 [147]. To this end, the process of verification and validation was expected to be carried out through comparison with experimental outcomes and with outcomes from other simulation tools, and by performing the IMO tests suggested by the MSC.1/Circ.1533 [147].

A second objective, concerning human participation, was that the mathematical model could potentially allow a seamless integration, within the simulation, of agents controlled by humans (“avatars”) and of computer controlled agents (or simply “agents”).

In addition, one of the objectives was that the developed model could take into account the effects of ship motions on evacuees, by direct application of perceived forces to each agent and by modification of the evacuees behaviour.

In the course of the research activity, therefore, a mathematical model fulfilling the aforementioned objectives was developed and embedded in a specifically developed simulation tool allowing real-time human participation within the on-going simulation. This thesis presents a description of the model and reports the results obtained with the developed simulation tool, both with and without user interaction.

The thesis is structured in ten chapters. Each chapter is provided with an introduction, describing the content of the chapter, and with a conclusion, summarising the main outcomes.

The agent based mathematical model is thoroughly described and discussed in Chapter 2, where a review of the state of the art regarding evacuation models and tools is also provided. The material was partially presented in [138], [139] and [140].

In Chapter 3 particular attention is given to the process of development and tuning of a new counterflow sub-model, which was developed in the course of this research.

Chapter 4 focuses on the process of verification and validation of the model. Firstly, simulation results for the standard IMO test cases are presented, together with comparison with results from, mainly, the software FDS+Evac. Then, comparisons between simulations and experimental data from literature are reported and discussed, for a series of different conditions. In the processing of simulation data, particular attention is given to the proper analysis and reporting of the statistical properties of the considered quantities: The material was partially presented in [139].

Chapter 5 provides the description of the implementation of the user interfaces allowing the user to join the simulation in real time. Particular attention is given to a newly developed haptic interface which allows the user to perceive contacts and proximity of agents during a simulation. The material was partially presented in [140] , [141] and [142].

Chapter 6 describes a test case where real users interact inside the simulation through virtual reality in a counterflow condition. The chapter reports the comparisons between the results obtained by real users and those obtained by simulated agents. Scope of the comparison is the assessment of the degree to which simulated agents can reproduce the real human behaviour. Moreover, a series of results concerning the assessment of effectiveness of the haptic interface are also presented. The material was partially presented in [141] and [142].

Chapter 7 presents in detail the model which was developed in order to consider ship motion effects on the dynamics of agents. The chapter reports a review of evacuation models available in literature which consider the effects of ship motion. The differences between the developed model and those existing in literature are highlighted and discussed.

Chapter 8 is devoted to the description of a developed test condition, specific to the maritime field. The condition is a realistic one but it is still sufficiently simple to be quite easily reproduced. The proposed test case consists of two cabin decks and a deck leading to an assembly station, which are connected by a staircase. The test case is run with and without ship motion. The effects of ship motion are studied in case of static heel and trim angles, in case of periodic roll motions, and in case of irregular motions. The calculation of motions in the latter condition is carried out in irregular beam waves, considering a notational, but realistic, cruise vessel. The considered vessel and the ship motions calculation procedure are thoroughly described in the chapter.

In Chapter 9 a model is then proposed and discussed, which allows the possibility of adding ship motion to the experience of the user when using virtual reality. Ship motions are introduced both from the point of view of the avatar control, as well as from the point of view of the perception of the forces, which is introduced by means of the haptic interface developed in Chapter 5.

The final chapter summarizes the conclusion from the research and discusses possible future developments.

This page is intentionally left blank

2 EVACUATION MODEL

As previously observed in Chapter 1, nowadays a wide range of different evacuation models exist, and each of them has its peculiarity and its range of applications. Moreover the outcomes of evacuation models might be also quite different when some parameters are modified. It is, therefore, very important that an evacuation model is presented in a detailed way with all its parameters in order to provide the possibility of comparison with other evacuation models.

Moved by those motivations this chapter presents an overview focused on contextualizing the developed model in the framework of other evacuation models and tools. The second section will be, instead, dedicated to the detailed description of the model and finally the implementation in the chosen development environment will be discussed.

2.1 Existing modelling techniques and simulation tools: an overview

Due to the multitude of evacuation modelling techniques it is necessary to perform a classification to better understand the base concepts and peculiarities of each of them.

The only identifiable common properties of all evacuation models are the dimension of the considered space, which is usually bi-dimensional, and the fact that each simulation is performed in the time domain. Other properties such as the continuity of the space representation or the modelling of the crowd are, instead, different in different models.

Considering, in particular, the modelling of the crowd, according to MSC.1/Circ.1533 [147], two distinct methods can be used for the evacuation analysis: a "simplified" one and an "advanced" one. The simplified evacuation analysis is based, fundamentally, on a so-called "macroscopic" type of modelling for the crowd behaviour, which considers the crowd as a whole. The advanced evacuation analysis is,

instead, expected to make use of models based on "microscopic" or "mesoscopic" which allow considering each individual separately.

Although many other different way of classifying crowd evacuation models have been proposed in literature, for example by Duives et al. [41], Kendik [103] Vermuyten et al. [220] and Zheng et al. [239], in the following overview of evacuation models, the classification concerning the scale is adopted, following the MSC.1/Circ.1533 [147].

Further classifications between the models will be introduced only to differentiate between models having the same scale.

2.1.1 Macroscopic models

Macroscopic models are based on the evidences that crowd can be approximately modelled by approaches borrowed from fluid-dynamics. The fundaments of this theory are represented by the observation of analogies between the motion of the crowd and of fluids. One of the first to observe this analogy was Henderson [78] who modelled the speed/velocity distributions functions of different crowd flows using the Maxwell-Boltzmann distribution. In macroscopic models the crowd is considered as a continuum and its state, depending on time and space, is described by means of local quantities such as density, linear momentum or energy.

The most basic macroscopic model, presented by Huges [82], [83] models the crowd considering two main assumptions:

- Conservation of the number of pedestrian. This assumption expresses with the following equation:

$$\frac{\partial \rho}{\partial t} + \frac{\partial}{\partial x}(\rho \cdot u)\frac{\partial}{\partial y}(\rho \cdot v) = 0 \tag{2.1}$$

  where ρ $[m^{-2}]$ is the density: the expected number of people per unity of area at a given time t and at a location (x, y) and (u, v) $[m/s]$ is the expected 2-dimensional vector expressing the velocity of individuals at a given time t and at a location (x, y) .
  The model assumes that the variations with respect to the expected values are negligible and thus density and velocity are taken as their local mean values.

- The normalized flow it is assumed to depend on the density following a relation which is also known as fundamental diagram (cfr. [223] and Chapter 4) in accordance to the equation:

$$u = f(\rho)\phi_x, v = f(\rho)\phi_y \tag{2.2}$$

  where (ϕ_x, ϕ_y) determines the direction of the flow and $f(\rho)$ is the aforementioned flow density relation.

A modelling based on the very same concepts in proposed in MSC.1/Circ1533 ([147]) for the simplified evacuation analysis. The model presented in in MSC.1/Circ1533, allows also to simulate the reduction of flow in one direction due to a counterflow condition. This possibility is obtained by the introduction of a counterflow correction factor. Moreover, MSC.1/Circ.1533 [147] proposes a differentiation of the flow density relation considering the different facilities.

The initial simple first order model was enhanced and modified to allow the description of more complex phenomena.
Jiang et al. [94], [95] presented a second-order macroscopic model capable of reproducing typical crowd phenomena, such as stop-and-go waves, which could not be reproduced by first order models. Colombo et al. [26] describe a macroscopic model capable of considering the raise of panic condition and the consequent decrease of the flow in case of high density. A macroscopic model capable of reproducing the lane formations is, instead, presented by Colombo et al.[27].

The main positive aspect about macroscopic models is the reduced computational time with respect to microscopic models. However, they are characterized by substantial limitations. Helbing et al. [72] observe that while fluid dynamics seems o describe well crowd motion in “normal” situations, instead, the granular aspect of the crowd emerges in panic conditions. Moreover situations with very low densities where there is the need of providing the exact position of each evacuee can be described with difficulties by macroscopic models. Finally it is impossible to take into account individual properties and behaviour of single pedestrians.

Macroscopic models could not be adopted in the present study, as in an application with virtual reality where the user controls a single evacuee all evacuees should be modelled as separated entities. Their description will, therefore, not be addressed in detail any further.

2.1.2 Agent based modelling: microscopic and mesoscopic models

The agent-based modelling technique is a way to model the interactions between multitudes of entities which is considered more accurate than the “equation-based” macroscopic approach (e.g., [69], [93]) because it is capable of modelling each entity separately.

The agent-based computing is used in many different fields such as economics and politics and in accordance to the context the “agents” represent the acting entities of the model (e.g. companies in the case of an economic model or states in the case of a political model). A bibliometrics analysis of the use of the term “agent” in different fields was presented by Niazi [157]. They prove the wide spread of this concept in last decades providing also a very detailed list of references of its use in different fields.

The difficulty of properly defining the term “agent” derives, indeed, from this widespread use in fields often not directly connected one with the other. An analysis of the concept of agent-based computing and modelling is carried out in

Wooldridge and Jennings [227] and subsequently by Jennings [93]. Summarizing, the main features characterising agents are:

- **Being identifiable**: the entities should be clearly identifiable in the model. They therefore should have precise boundaries (spatial boundaries are usually present only if the modelled entities have a volume/area) and interfaces to communicate with the rest of the simulated environment.

- **Being autonomous**: each entity should have control over its internal status and its actions.

- **Have a precise goal**: each entity is designed to fulfil a precise target.

- **Being pro/re-active**: each entity should acquire data from the surrounding environment and develop a proper reaction which is finalized to pursue the goal.

In the context of pedestrian models, the "agent", in most cases, models a real pedestrian with its attitudes and behaviours. The two terms are, therefore, considered interchangeable in this context ([7]). Hoogendoorn and Bovy [81] propose a similar definition, which is more oriented towards the actual implementation of the model, describing agents as "encapsulation of code and data". In the model presented herein the term "agent" will identify a single modelled pedestrian and will be thus used in a way similar to the one described by Batty [7] to indicate each entity modelling a single pedestrian in the simulation.

The "agent-based" pedestrian models, differently from macroscopic models, allow to consider the heterogeneity of the population and to obtain information concerning the state of each single pedestrian at each time instant during the simulation. The discretization of the space might be considered to further classify agent based modelling.

As observed by Deere [34] the space might be represented in three possible modes: coarse meshes, fine meshes and continuous meshes. Among these modes only the fine meshes and continuous meshes allow a microscopic modelling. Models based on coarse meshes, consider the space of the simulation as constituted by areas and corridors (nodes of the mesh) updating the number of people present in each node at each time step. As people are not modelled singularly, this kind of space representation does not allow a microscopic modelling. Only the fine mesh and the continuous mesh space representation will be hence adopted for further classifying microscopic models.

In models using fine meshes, the space is, instead, divided into small nodes (in general triangular or square) connected one to the other via arcs. Each node can be occupied by a single pedestrian. Models using this kind of meshes are agent based. Examples of these types of models are provided by EXODUS ([53], [56]) or by Ha et al. [65].

Models using continuous meshes are the most computational demanding agent-based evacuation models as in this case agents can occupy every position in the space. For each agent, thus, the status vector is a vector $(x_1, x_2, x_3, v_1, v_2, v_3)$ where the first three components represent the components of the position vector and the last three are the

components of the speed. The status vector is defined in a connected domain of $\mathbb{R}^6$. Examples of models based on continuous meshes are provided by Vassalos et al. [219], Guarinet al. [63] and by Korhonen [112].

The aforementioned classification through space discretisation represents only one of the possible way of classifying agent based models. Another possible classification might be performed considering again the scale of the model and distinguishing between Mesoscopic and Microscopic models.

2.1.2.1 Mesoscopic models

In agent-based mesoscopic models, agents' behaviour depends on global quantities (aggregate flow characteristics) such as the density or mean crowd speed around the considered agent. Example of agent-based models showing some mesoscopic characteristic is presented by Hoogendoorn and Bovy [81] and by Vassalos et al. [219].

The dependence of agent behaviour from density, as an example, is justified by the introduction of the "perceived density" concept. Human are considered capable of estimating the local density which is often estimated by the number of people inside an area around the agent divided by the extent of the considered interaction area. The agents are then assumed to adapt their speed in accordance to the perceived local density, following the flow density relations measured experimentally ([219]).

As a results, the experimentally measured flow density relation often adopted as validation for microscopic model ([236]), in this case is implemented in the model itself.

This kind of models, however, does not simulate in detail the one-on-one interactions occurring between each couple of people.

2.1.2.2 Microscopic models

Microscopic modelling is considered by Bellomo et al. [8] "the best scale to build crowd models as it is focused on one-on-one interactions". In microscopic models the agent behaviour is emerging from the modelling of the interactions with other agents and with the environment and each interaction is considered and modelled separately and depends on the specific properties of the agent.

Microscopic models adopting a fine mesh discretization of the space are, for example, the cellular automata models. The behaviour of each agent, in these models, depends on the situation of the surrounding cells and on specific agents properties. Example of these models were reported by Schadschneider et al. [190], Ha et al. [65] and by Feliciani and Nishinari [46].

Phenomena such as the lane formation and the jamming transition were reproduced with cellular automata models for example by Tajima et al. [208] and by Weifeng et al. [224]. Cellular automata, although being microscopic models, still allow a computation much faster than the continuous microscopic models as observed by Duives et al. [41]. However Duives et al. [41] also observes that they have some limitations as they cannot, for instance, reproduce the widening of the wedge at the exit

from a bottle neck. Moreover in cellular automata models the density is bounded to a maximum which depends on the underlying degree of space discretization. As a result, cellular automata models have difficulties in modelling high density situations.

The microscopic models considering, instead, a continuous space, might be classified by differentiating them between force based models and no force based models. While in the latter models the instantaneous velocity vector is set directly at each time step of the simulation (examples are provided by Degond et al. [35], Moussaid et al. [144], Robin et al. [177]), in force based models agents are modelled as rigid bodies which move under the action of forces and the time history of each agent status vector is calculated by integrating the Newtonian equations of motion for each agent in the simulation.

In particular, in social force models the global force applied to each agent is the result of the sum of different force contributions. The model implemented in the tool developed during this study is social force based, hence the overview of this topic will be more detailed with respect to the other models and will be treated in the next section.

2.1.2.3 Social force models

The social force models were firstly introduced by Helbing and Molnar [71].The feature characterizing these models is the possibility of determining the motion of an agent, and thus its instantaneous status, through the following dynamics equation:

$$m_i \cdot \frac{d\mathbf{v}_i(t)}{dt} = \sum_{\mathbf{F}_i^k \in F_i^{soc}} \mathbf{F}_i^k \tag{2.3}$$

were the index i refers to the agent, m_i [kg] represents the mass of the agent, $\mathbf{v}_i(t)$ is the agent instantaneous two dimensional velocity vector on the deck/floor plane, F_i^{soc} is the set of all social forces related to the agent i and $\mathbf{F}_i^j$ is a specific social force modelling a single specific behaviour of the agent.

The main modelled behaviours, which are common to all social force models and which are present also in Helbing and Molnar [71], are:

1. Each person tries to direct himself towards the target (exit) at an almost constant speed which is considered the more comfortable speed.

2. Each person tries to avoid contacts with other agents.

3. Each person tries to avoid contacts with walls.

The first behaviour is often described by a motive force. One of the most used formulations of the motive force is as follows:

$$\mathbf{F}_i^{\text{mot}} = \frac{m_i}{\tau_i}\left(\mathbf{v}_i^0(t) - \mathbf{v}_\mathbf{i}(t)\right) \tag{2.4}$$

were τ_i is a constant and $\mathbf{v}_i^0(t)$ is the desired velocity vector. The motive force is thus the result of the sum of two forces: a propulsive force (the term $\frac{m_i}{\tau_i}\mathbf{v}_i^0(t)$) allowing the agent to reach the desired speed, and a viscous friction (term $-\mathbf{v}_i(t)\cdot\frac{m_i}{\tau_i}$) which tends to slow down the agent. The combination of the two terms tend to bring the agent to the desired speed.

The forces modelling the avoidance behaviours described by the points 2 and 3 in the previous list are essentially repulsive forces which decrease as the distance between the interacting agents increases. The decrease is exponential in the model described by Helbing and Molnar [71], of the type reported in the following equation:

$$\mathbf{F}_i^{repulsive} = \sum_j A e^{f(dist(i,j))} \tag{2.5}$$

where j is an agent different from i and A is a scaling factor governing the magnitude of the force. Another formulation of the repulsive force is proposed by Löhner [127]. In this case the force dependence on distance is a rational function of the normalized distance between the agents, as it is reported in the equation below:

$$\mathbf{F}_i^{repulsive} = \sum_j A\left(\frac{1}{1-\left(dist(i,j)/r_i\right)^2}\right) \tag{2.6}$$

where $dist(i,j)$ is the distance between agents, r_i is agent i radius (used to normalize the distance) j is an agent different from i and A is a scaling factor governing the magnitude of the force.

Helbing and Johansson [70] observe that anisotropy is inherent in the interaction between people and this is due to the fact that, generally, the contact avoidance attitude is stronger if the obstacle is placed in front of the subject and weaker when the obstacle is behind. This feature is present in the most sophisticated social force models such as those described by Helbing and Johansson [70], Korhonen [112]. In these cases the repulsive interaction force exerted by an agent j on another agent i depends not only on the distance between agents, but also on the angle formed by the distance vector connecting the interacting agents and the instantaneous velocity vector of agent i .

Other different human behaviours were subsequently described either by direct modification of the motive force equation, modification of the social forces, or by the addition of other social forces, starting from the pre-existing model by Helbing and Molnar [71]. Some examples of these behaviours are reported in the table below, with associated references.

Table 2.1: Crowd behaviours modelled through social force based models and corresponding references.

Behaviour	References
Nervousness	[73], [121]
Counterflow	[76], [64], [168]
Behaviour on stairs	[174]
Waiting	[97]
Herding	[73], [31]
Grouping	[228]
Overtaking	[231]
Mutual information	[229]

Finally, another difference between social force models is provided by the different models of human shape. In some cases ([73], [121]) the human body in two dimensions is modelled as a circle, whereas in some others ([76], [174]) the human body is represented by three circles in order to take into account also human asymmetry.

The human asymmetry concerns not only the contacts but, in some cases, also the interaction between agents. In the models described by Helbing and Molnar [71] and by Helbing and Johansson [70] the repulsive interaction force is modelled elliptically. It is observed that this non-circular formulation has the effect of leading to "smother sliding evading manoeuvres" when agents are interacting.

Models considering human asymmetry often need to introduce, in addition to translations, also the rotation of the body. This eventually requires the addition of a torque, because in this case agents need to be oriented towards their target and they modify their orientation in accordance to interaction with other agents.

2.1.3 Evacuation models and tools

Starting from the previously described modelling categories, a big variety of evacuation simulation models were developed. Some models have been sufficiently developed to be implemented in (sometime commercially available) simulation tools for practical engineering applications. In other cases, presented models remained at a prototype status. However, only few of them have been specifically developed to target the maritime field and have the possibility to use ship-motion data in order to reproduce the effects of ship motions on human behaviour.

In Table 2.2 a list is presented of some evacuation tools, highlighting those specifically developed in the maritime field and those designed to take into account the effects of ship motions in the simulation. Although the presented list is updated and reports also the most recently developed tools, it can't be considered exhaustive as in the present period many new evacuation tools are being developed while the existing ones are being enhanced. The list, which might be considered an updated version of the table reported by Deere [34], can however offer a wide view on the existing simulation tools and more specifically on those targeting the maritime field.

In Table 2.2, up-to-date references of publications adopting or describing the relevant tool are reported, when available. It was, however, impossible to find available

references for eight of the tools presented by Deere [34]: these tools are reported only by name in the table. Other, not exhaustive and less updated lists of simulation tools are proposed by Kuligowski et al. [119] and by Schadschneider et al. [190]. Finally, Mohamed et al. [137] who also reports a brief description for each model.

Table 2.2: List of evacuation tools with references. The tools directly aiming to an application in the maritime field are highlighted by (*).

Tool/Model name	References	Tool/Model name	References
AENEAS/PedGo*	[135], [214]	FDS+Evac	[75] ,[111], [112]
ALLSAFE	[80]	Helios*	[129]
ASERI	-	IMEX*	[106]
BFIRES-II	[206]	Legion	[9]
BGRAF	-	MA&D	-
BuildGEM	[221]	Magnetic Model	[162]
BUMPEE	[130]	MASCM	[128]
Cube Avenue	[201], [202]	MASSEgress	[1]
CRISP	[51]	MASSIVE Software	[132]
DBES	[48]	MASSMotion	[176]
EARM	-	Muss & Thalmann	[155]
ESM	[198]	Myriad II	-
Evacnet4	[2],[136]	Nomad	[21]
EvacSim	[154], [172]	PathFinder	[212]
EvacuationNZ	-	PedFlow	[118], [235]
EVI*	[63], [219]	PedGo	[109]
Exit89	[43], [180]	Pedroute/Paxport	[19]
EXITT	[122]	PedSim	[210]
(Maritime)EXODUS*	[53], [55], [56]	S-Cape*	[12]
F.A.S.T.	[114],[115]	SimPed	[32]
EPT	[67]	Simulex	[211]
E-Scape	[175]	SimWalk	[232]
EESCAPE	[102], [103]	SMART Move	[198]
EGRESS	[104]	SpaceSensor	[137]
Egress Complexity Model	-	STEPS	[205], [222]
EgressPro	-	Takahashi's flud model	. [209]
ENTROPY	[38]	TIMTEX	[28]
FireScap	[45]	VELOS*	[57], [58], [113]
FlowTech	[99]	VISSIM/Viswalk	[79], [173]
FPETool	[156]	WayOut	[200]
GridFlow	[25]	Zet	[39]

Table 2.2 shows that a limited number of tools were directly developed to be applied in the maritime field and, of these tools, only few are capable of simulating the effects of ship motions on agents. Integrating these effects might however be crucial to correctly simulate conditions of large static inclination/trim angles or large dynamic motions where it is reasonable to imagine that people egress might be slowed by the forces, induced by motions, and perceived by the agents.

The mathematical model adopted in the present work was created starting from the FDS+Evac implementation ([112]) of the social force model. A social force model was preferred due to its consistency with real physics laws and to its capability of modelling most of the crowd observed phenomena Duives et al. [41]. Moreover, as agents are considered in the model as rigid bodies, fictitious forces due to ship motions can be directly applied, instantaneously, to the agents leading to consequent possible influence on their trajectory allowing a more direct and physically consistent extension of the model to consider ship motion effects.The three circle representation as implemented in FDS+Evac was chosen because it sufficiently represents the asymmetry of human volume, while still allowing a reasonably fast computation. Finally, a continuous mesh was chosen as agents are required to be represented with continuity to allow real time interaction with virtual reality. In the course of development, it was necessary to introduce a series of modelling modifications to the model adopted as a starting point. Such modifications will be detailed and justified in the following, where the model is thoroughly analysed.

2.2 Evacuation simulation model: full description of evacuation model

The simulation approach presented herein is based on a social force model. In particular, the social force-based model was implemented starting from the model proposed by Helbing and Molnar [71] and the model embedded in the software FDS+Evac (Korhonen [112]). However, as already anticipated, a series of modifications to such models have been introduced. While more details will be given in the subsequent sections, the main modifications can be summarised as to have addressed the following aspects:

- Motive force;
- Counter-flow;
- Stairs model;
- Model of random forces;
- Psychological forces;
- Effect of vertical direction in psychological forces;
- Limitation of forces;
- Interaction with walls and obstacles;
- Random forces;
- Route finding.

In the developed model, agents move in a 2-dimensional manifold. Agents and obstacles are modelled in 2-dimensions (considering the projection on the XY-plane), while the third component is treated separately and derives from geometric constrains.

Each agent is thus considered as a rigid body having three degrees of freedom: the translation along x-axis and y-axis, and the rotation around the vertical axis. The 2-dimensional movement (translation and rotation) of each agent is described by rigid body dynamics laws. For translation, the equation of motion is

$$m_i \cdot \ddot{\mathbf{x}}_i(t) = \mathbf{F}_i^g(t) \tag{2.7}$$

where m_i [kg] is the mass of the i-th agent, $\mathbf{x}_i(t)$ [m] is its instantaneous position vector, $\mathbf{F}_i^g(t)$ (N) is the global instantaneous force vector acting on the i-th agent, and dots indicate differentiation with respect to time. The rotation around the agent's vertical axis is described by the following equation:

$$I_{z,i} \cdot \ddot{\phi}_i(t) = T_i^g(t) \tag{2.8}$$

where $I_{z,i}$ [$\mathrm{kg \cdot m^2}$] is the agent inertia, $\phi_i(t)$ [rad] is the orientation angle, $T_i^g(t)$ [$\mathrm{N \cdot m}$] is the instantaneous torque acting on the agent.

The agent's translational movements are caused by the global force $\mathbf{F}_i^g(t)$, which is applied at each time step of the simulation and is the sum of different contributions, each modelling a specific human behaviour or attitude. The summary of the forces contributions is presented in Table 2.3.

As social forces are all applied to the agents' centre of mass they do not generate torque. The change of body orientation is, instead, modelled separately through social torques. In this way social torques are complementary to social forces in modelling each specific behaviour/condition. A more detailed description of the modelled forces and torques is given in the relevant subsequent sections.

As it can be noted from Table 2.3, a random force and a random torque are also applied during the simulation, and their role is twofold. On the one hand, they mimic a certain level of inherent natural randomness in the agents' behaviour. On the other hand, the addition of a random noise prevents unnatural impasse situations (equilibria of the dynamical system) from occurring.

Table 2.3: List of forces/torques and associated behaviours.

Type of action/interaction	Symbol	Behaviour
Motive force and torque	$\mathbf{F}_i^{\mathrm{mot}}$, T_i^{mot}	Agents are oriented and move towards their target.
Agent-agent interaction	$\mathbf{F}_i^{\mathrm{a}}$, T_i^{a}	Agents avoid collisions with other agents.
Wall-agent interaction	$\mathbf{F}_i^{\mathrm{w}}$, T_i^{w}	Agents avoid collisions with walls.
Counter-flow	$\mathbf{F}_i^{\mathrm{cf}}$, T_i^{cf}	Agents modify direction and orientation if in counter-flow.
Random force and torque	$\mathbf{F}_i^{\mathrm{rand}}$, T_i^{rand}	Random fluctuation.

In principle, the global force $\mathbf{F}_i^{\mathrm{g}}$ acting on the agent is, hence, the sum of the different force contributions, as mentioned in Table 2. However, while motive force values are typically associated with corresponding accelerations (forces per unit mass) close to real measured acceleration values, the models for the repulsive and counter-flow forces can

lead to very high forces per unit mass. As a result, a direct summing of the single contributions can lead to unrealistic accelerations of the agents. This phenomenon was observed also by Lakoba et al. [121]. To address this situation, the raw global force, in the model presented herein, is subject to a two-step clamping procedure, as follows:

$$\begin{cases} \mathbf{F}_i^{\mathrm{p},*}(t) = \mathbf{F}_i^{\mathrm{cf}}(t) + \mathbf{F}_i^{\mathrm{a}}(t) + \mathbf{F}_i^{\mathrm{w}}(t) \\ \mathbf{F}_i^{p}(t) = \min\left(\left\|\mathbf{F}_i^{\mathrm{p},*}(t)\right\|, m_i \cdot b_f\right) \cdot \dfrac{\mathbf{F}_i^{\mathrm{p},*}(t)}{\left\|\mathbf{F}_i^{\mathrm{p},*}(t)\right\|} \\ \mathbf{F}_i^{\mathrm{g},*}(t) = \mathbf{F}_i^{\mathrm{p}}(t) + \mathbf{F}_i^{\mathrm{rand}}(t) + \mathbf{F}_i^{\mathrm{mot}}(t) \\ \mathbf{F}_i^{\mathrm{g}}(t) = \min\left(\left\|\mathbf{F}_i^{\mathrm{g},*}(t)\right\|, m_i \cdot b_f\right) \cdot \dfrac{\mathbf{F}_i^{\mathrm{g},*}(t)}{\left\|\mathbf{F}_i^{\mathrm{g},*}(t)\right\|} \end{cases} \tag{2.9}$$

where b_f [$\mathrm{m/s^2}$] is the limit determining the maximum acceptable acceleration and m_i [kg] is the agent mass. The typical maximum acceleration of human during normal movements is indeed limited, and this limitation is reproduced in the model by the parameter b_f, which needs to be calibrated. In this respect, Weidmann [223] reports that acceleration during normal walking does not typically exceed 1.96 $\mathrm{m/s^2}$ ($0.2g$). In the social force model, however, social forces also play the role of braking forces, as they act to slow down agents when they need to avoid contacts with obstacles on their trajectory. Those kinds of situation, where a strong brake force is needed, cannot be considered as normal walking situations. For this reason it was consider more appropriate to use a value higher than $0.2g$, and the parameter b_f was set to 3 $\mathrm{m/s^2}$. This value is also in line with the experimental data presented by Tirosh and Sparrow [213], where the situation of abrupt gait interruption is analysed. In addition to its relevance from the point of view of the underlying physics, the introduction of a bound on the force $\mathbf{F}_i^{\mathrm{g}}$ has also a positive numerical effect, because it facilitates keeping accuracy in the integration of the equations of motion in case of increased the time steps. This is extremely useful in case real time updating is required, and real-time application is one of the final scopes of the research activity reported herein.

The social torque is clamped in a similar way using a limiting value of angular acceleration (or torque per unit inertia), b_t [$\mathrm{rad/s^2}$]. Due the lack of data, b_t has been calibrated considering the maximum possible angular acceleration that can be generated by the motive torque (as reported later in (2.13)), which occurs when the agent is rotated backwards with respect to its preferred direction. The obtained value is $b_t = 62.83$ $\mathrm{rad/s^2}$.

The motion of the agents is governed by the mentioned 2-dimensional rigid body dynamics laws in open space, with the exception of contact situations. Usually, social force models use a spring-damper approach to model contacts ([71], [112], [127]). Instead, in the presented model, contacts are managed directly by the physics engine embedded in the development environment (see section 2.2.10).

In the following subsections a detailed description is provided of a series of characteristics of the simulation model.

2.2.1 Characteristics of the agents

Each agent is associated with a set of characteristic properties which change from agent to agent. These properties can be grouped into geometrical, mechanical and behavioural properties.

Geometrical properties concern the way each agent is represented in the simulation. Each agent, corresponding to an evacuee in the simulation, has a defined shape and occupies a precise area that determines agents' interactions and collisions with obstacles and other agents. This shape must resemble human shape as closely as possible. A straightforward method of modelling human geometry is by approximating human projected shape to a circle. However, this kind of simplification does not consider human asymmetry. To cope with this limitation, Helbing and Molnar [71] propose to model the human body with an ellipse. Unfortunately, using ellipses, which at a first glance seems to be a simple shape, is actually computationally very onerous. Korhonen [112]and Qu et al. [174], therefore, proposed to represent each evacuee with three circles (arms and chest). This kind of geometrical representation is still capable of considering human asymmetry and is also much less computationally expensive than the ellipse representation. As a result, this type of 3-circle representation is the one which has been selected for representing the area occupied by each agent in the present model.

Following Korhonen [112], each agent is represented by 3-circles having centre on the same line. The central circle models the chest while the lateral ones model the arms (Figure 2.1), and the geometry of the agent is globally determined by the maximum radius r_{max}, the arm radius r_a and the chest radius r_c (Figure 2.1). Moreover, each agent is associated also with a total height h in the vertical direction.

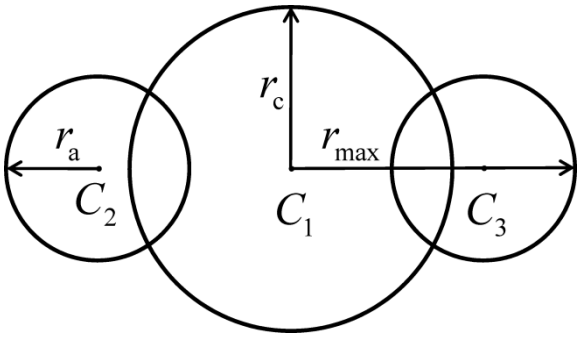

Figure 2.1: Agent geometry.

The mass and the moment of inertia are the mechanical properties of each agent, and, following the idea by Korhonen [112], they are obtained by a scaling based on the agent's dimensions. In particular, starting from to the reference case specified in

FDS+Evac where an agent of mass $m = 80$ kg is assumed to have inertia $I_Z = 4\ \mathrm{kg \cdot m^2}$, $r_{\max} = 0.27$ m, $r_c = 0.16$ m and $h = 1.8m$ ([112]), the scaling is carried out as follows:

$$\begin{cases} h = k_h \cdot r_{\max} \\ m = k_m \cdot r_{\max}^2 \\ I_z = k_I \cdot m \cdot \left(r_c^{\,2} + r_{\max}^{\,2} \right) \\ \text{with} \\ k_h = \dfrac{1.8}{0.27} = 6.67 \quad ; \quad k_m = \dfrac{80}{0.27^2} = 1097 \dfrac{kg}{m^2} \\ k_I = \dfrac{4}{80 \cdot \left(0.16^2 + 0.27^2 \right)} = 0.508 \end{cases} \tag{2.10}$$

The way each agent interacts with the environment to reach its target is governed by the agent's properties and parameters. Most of those parameters are fixed and equal for all agents. Other parameters, are, instead, specified as random variables with associated distributions. In this latter category of parameters there are the unimpeded walking speeds (on flat terrain, while ascending and while descending stairs), the relaxation coefficient τ (for the motive force model) and the response time. The values of these parameters, which are typically modified in each random realization of the simulation, differ from one agent to another in such a way to reproduce the heterogeneity of the population. All random parameters contribute to the aleatory uncertainty inherent in the model.

For simulations in the maritime field, IMO MSC.1/Circ.1533 [147] provides information regarding the distribution of agents among different age/gender categories, of unimpeded speeds distributions on flat terrain and on stairs and of response time. However, no information is provided regarding the other agents' parameters which are required in the present model. Therefore, for parameters not addressed by IMO MSC.1/Circ.1533 [147], reference is made to the distributions specified by FDS+Evac ([112]), as reported in Table 2.4. In the table the notation $U(a,b)$ indicates a uniform distribution in the interval $[a,b]$, and it can be noted that r_c and r_a are deterministically associated with $r_{\max}$ (for which the distribution is explicitly provided).

Table 2.4: Agent's dimensions.

Agent type	$r_{\max}$ (m)	$r_c / r_{\max}$
Adult	$U(0.22, 0.29)$	0.5882
Male	$U(0.25, 0.29)$	0.5926
Female	$U(0.22, 0.26)$	0.5833

2.2.2 Motive force

The original motive force model by Helbing and Molnar [71] is based on the combined action of a propulsive force, which aims at reaching the desired speed in the desired direction, and a viscous friction component, which acts as a damper, as follows:

$$\mathbf{F}_i^{\text{mot}} = \frac{m_i}{\tau_i^f}\left(\mathbf{v}_i^0(t) - \mathbf{v}_i(t)\right) \tag{2.11}$$

where $\mathbf{v}_i^0(t)$ [m/s] is the instantaneous desired speed, $\mathbf{v}_i(t)$ [m/s] is the instantaneous speed, m_i (kg) is the mass of the agent and τ_i^f [s] is a relaxation coefficient determining the strength of the force. The instantaneous desired speed is associated with the routing algorithm, as described later in the relevant section 2.2.9.

It has been observed, both in literature ([121]) as well as from the initial simulations carried out with the original implementation of the present model, that social repulsive forces may cause excessive acceleration that eventually induce unrealistic high speeds. In parallel, Tirosh and Sparrow [213] observed that, in human gait, peaks of breaking (decelerating) forces can be larger than peaks of accelerating forces. Starting from these evidences, the original motive force model has therefore been modified by introducing an additional term which is aimed at generating larger friction in case of large instantaneous velocities. Such modification has been devised in such a way not to modify the original motive force in case of more standard conditions, characterised by acceleration from rest or low speed, or in case of small deviations from the desired speed.

The modified model takes the following form:

$$\begin{cases} \text{if } \left\|\delta\mathbf{v}_i(t)\right\| = 0: \quad \mathbf{F}_i^{\text{mot}}(t) = \mathbf{0} \\ \text{if } 0 < \left\|\delta\mathbf{v}_i(t)\right\| \le s: \quad \mathbf{F}_i^{\text{mot}}(t) = \dfrac{m_i}{\tau_i^f} \cdot \left\|\delta\mathbf{v}_i(t)\right\| \cdot \delta\hat{\mathbf{v}}_i(t) \\ \text{if } \left\|\delta\mathbf{v}_i(t)\right\| > s: \\ \mathbf{F}_i^{\text{mot}}(t) = \dfrac{m_i}{\tau_i^f} \cdot \left(\left\|\delta\mathbf{v}_i(t)\right\| + q_{\text{mot}} \cdot \left(\left\|\delta\mathbf{v}_i(t)\right\| - k_{\text{mot}} \cdot v_i^0(t)\right)\right) \cdot \delta\hat{\mathbf{v}}_i(t) \\ \text{where} \\ \delta\mathbf{v}_i(t) = \mathbf{v}_i^0(t) - \mathbf{v}_i(t) \quad ; \quad \delta\hat{\mathbf{v}}_i(t) = \dfrac{\delta\mathbf{v}_i(t)}{\left\|\delta\mathbf{v}_i(t)\right\|} \quad ; \\ s = k_{mot} \cdot \mathbf{v}_i^0(t) \quad ; \quad q_{\text{mot}} > 0 \quad ; \quad k_{\text{mot}} > 1 \end{cases} \tag{2.12}$$

The dimensionless parameter q_{mot} controls the magnitude of the additional motive force when the module of the instantaneous speed difference $\delta\mathbf{v}_i(t)$ exceeds the specified

threshold governed by the dimensionless parameter k_{mot}. Herein, the two parameters have been tentatively set to $k_{\text{mot}} = 1.25$ and $q_{\text{mot}} = 3$.

The parameter τ_i^f is often set to a value of 0.5 s ([74]; [73]; [121]). However, a series of simulation tests carried out on the IMO test case 4 of MSC.1/Circ.1533 [147] showed that $\tau_i^f = 0.5$ s leads to excessive flow rate compared to the maximum one prescribed by MSC.1/Circ.1533. For this reason the parameter τ_i^f was chosen to be uniformly distributed in the interval $[0.8,1.2]$ s, in accordance to the values proposed by Korhonen [112]. While this is the reference model for the parameter τ_i^f to be associated to each agent as an agent's property, the instantaneous value of τ_i^f during a simulation can be modified, depending on the situation, by the nervousness model, as described later in the relevant section 2.2.7.

A representative plot of the behaviour of the nonlinear motive force with the considered model parameters is shown in Figure 2.2.

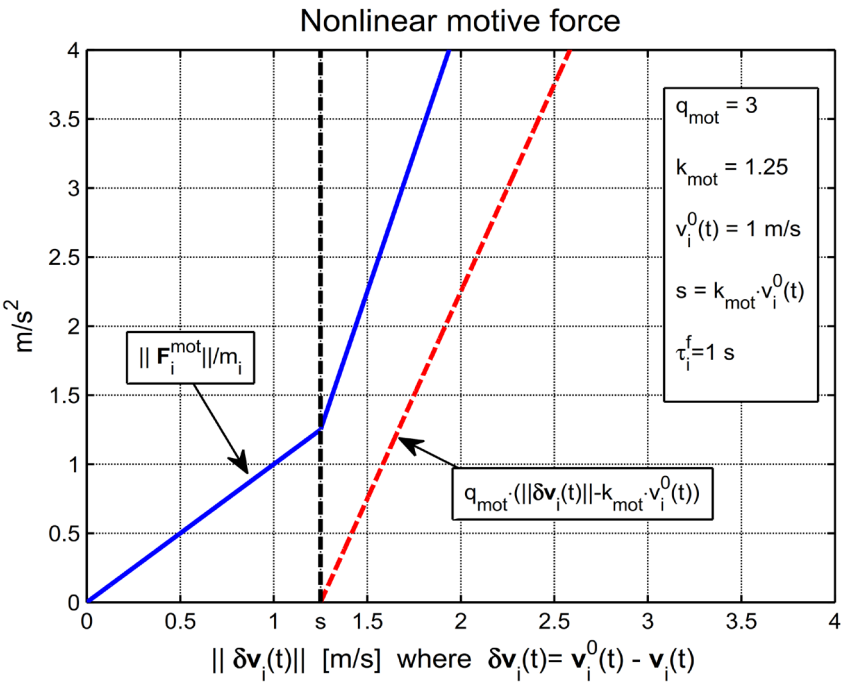

Figure 2.2: Example representative plot of nonlinear motive force behaviour.

The motive torque describes the attitude of each agent to rotate towards its desired direction and it is described using the following model from Korhonen [112]:

$$T_i^{\text{mot}}(t) = \frac{I_i}{\tau_i^t} \cdot \left(\frac{\left(\phi_i^0(t) - \phi_i(t)\right)}{\pi} \cdot \omega^0 - \omega_i(t) \right) \tag{2.13}$$

where $\phi_i^0(t)$ [rad] is the instantaneous desired orientation angle, $\phi_i(t)$ [rad] is the instantaneous orientation angle (defined in $[-\pi,\pi]$), $\omega_i(t)$ [rad/s] is the instantaneous angular speed, τ_i^t (s) is the relaxation parameter of the motive torque, and ω^0 [rad/s] is a scaling parameter. While τ_i^t controls directly the viscous dissipation of the model, the parameter ω^0, combined with τ_i^t, controls the restoring term of the motive force. According to the approach used in FDS+Evac ([112]), the relaxation parameter τ_i^t is herein assumed to scale with τ_i^f so that $\tau_i^t = k_\tau \cdot \tau_i^f$ where k_τ is a fixed parameter. In line with Korhonen [112], k_τ was set to 0.2 s and ω^0 was set to 4π rad/s.

Finally, the parameters associated with the motive force and motive torque model are summarized in Table 2.5.

Table 2.5: Parameters of the motive force and torque model, and corresponding values.

τ_i^f	q_{mot}	k_{mot}	τ_i^t	k_τ	ω^0
$U(0.8\,s, 1.20\,s)$	3	1.25	$k_\tau \cdot \tau_i^f$	0.2	4π rad/s

2.2.3 Agent-agent interaction

The repulsive interaction force between agents models the way people try to avoid contacts and keep distance between each other. This force was firstly introduced by Helbing and Molnar [71]. However, herein, the FDS+Evac model by Korhonen [112] is implemented, as this latter is based on the three circle representation of human body. Herein, such starting point model is also slightly modified in order to better address the case of zero agent speed.

With reference to the geometrical scheme reported in Figure 2.3, the force exerted on agent i by agent j is described as follows:

$$\mathbf{F}_{ij}^{\,\mathrm{a}}(t) = A_i^{\mathrm{a}}(t) \cdot e^{-\left(\frac{d_{ij}-r_{ij}}{B_{\mathrm{a}}}\right)} \cdot \left(\lambda_{\mathrm{a}}\left(v_i(t)\right) + \left(1-\lambda_{\mathrm{a}}\left(v_i(t)\right)\right) \cdot \left(\frac{1+\cos(\theta_{ij}^{\mathrm{a}})}{2} \right) \right) \cdot \widehat{\mathbf{d}}_{ij} \qquad (2.14)$$

where $d_{ij} - r_{ij}$ is the effective (skin-to-skin) distance between the closest agents' circles, $\widehat{\mathbf{d}}_{ij}$ is the versor of the vector $\mathbf{d}_{ij}$ connecting the centres of closest circles (oriented from agent j to agent i), θ_{ij}^{a} is the angle between the instantaneous speed $\mathbf{v}_i(t)$ of agent i and the vector $\mathbf{D}_{ij}$ connecting the two agents' centres (from agent i to agent j).

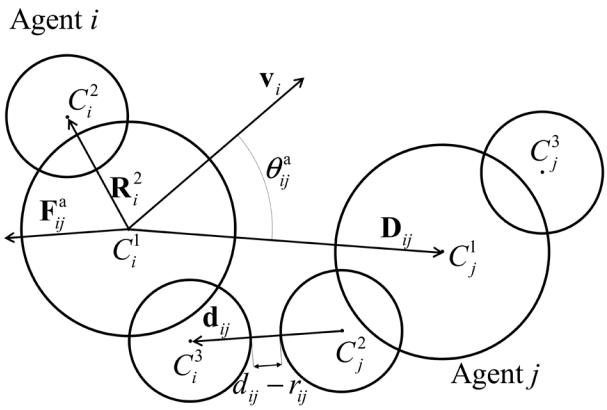

Figure 2.3: Agent-agent interaction

The coefficient $A_i^{\mathrm{a}}(t)$ (N), is, in general, time dependent, because, according to the FDS+Evac model ([112]), it is described as follows:

$$A_i^{\mathrm{a}}(t) = A_{\mathrm{a}} \cdot \max\left(0.5, \frac{v_i(t)}{v_i^0(t)}\right) \tag{2.15}$$

where A_{a} [N] is a fixed constant, and $v_i(t)$ and $v_i^0(t)$ are, respectively, the modules of the instantaneous and of the desired speed. The parameter A_{a} determines the strength of the force. In order to set the value for this parameter, reference was made to the value used by Helbing et al. [73], i.e. $A_{\mathrm{a}} = 2 \cdot 10^3$ N . As Lakoba et al. [121] correctly observes, using this value for the A_{a} parameter might lead to forces far from being realistic. In the model presented herein, however, this issue is indirectly addressed by the clamping procedure described in equation (2.9), as it is understood that the agent-agent interaction force, when considered in isolation, is to be intended more as an indication of an intention from the agent rather than, strictly, a physical force.

The parameter B_{a} controls the decay of the force as a function of the relative agent's distance, and, according to Helbing et al. [73], it is set to $B_{\mathrm{a}} = 0.08$ m . Considering the exponential decay associated to B_{a} , this clarifies that the agent-agent interaction is a close-distance type of interaction, and it can be neglected when agents are sufficiently far each other (as a note, this is an extremely important factor in a model that targets a real-time application, as in this case).

The second part of equation (2.14) concerns the anisotropy of agent-agent interaction, and it is controlled by the parameter λ_a . In general, it is assumed that the agent-agent interaction force is larger if the agent j is placed in front of the instantaneous direction of agent i and, conversely, it is smaller when agent j is placed behind the instantaneous direction of agent i . This corresponds, in general, to an anisotropy parameter $0 \le \lambda_a < 1$, with the model anisotropy increasing for smaller values of λ_a . However, in case $v_i(t) = 0$ (idle agent) the angle θ_{ij}^{a} is not defined. Korhonen [112] assumed in their

model that idle agents have an increased perception of the other agents around them, and therefore no anisotropy is applied to them ($\lambda_a = 1$). While this observation can be considered reasonable, this choice makes the interaction force discontinuous with respect to the angle θ_{ij}^{a} whenever any anisotropy is assumed in presence of an agent speed ($\lambda_a \neq 1$). In order to address this, actually minor, issue, the model presented herein considers a weak dependence of the anisotropy parameter on the module of the instantaneous agent's speed $v_i(t)$. In particular, λ_a is taken equal to 1.0 when $v_i(t) = 0$, it is taken equal to the nominal value (discussed later) when $v_i(t) \geq 0.01 m/s$, and it is linearly interpolated for intermediate values of $v_i(t)$. Eventually, this modification leads to a force which is defined with continuity and avoid oscillation near $v(t) = 0$, while not drastically modifying agents' behaviour with respect to the original modelling by Korhonen [112].

Regarding the actual value of the anisotropy parameter λ_a, different alternatives have been proposed in literature. Johansson et al. [96] suggested $\lambda_a \approx 0.1$ following a parameter identification technique, using evolutionary optimization, based on video recorded data. In FDS+Evac ([112]) a standard value $\lambda_a = 0.3$ is used, with an indication that this value can be increased to 0.5 in case a faster egress is required. Liao et al. [124] performed a calibration study regarding the anisotropy parameter λ_a in the FDS+Evac model, observing that the increase of the parameter λ_a up to 0.5 allows obtaining a flow rate which is closer to experimental results. With reference to the application to the maritime field, which is the target of this study, simulations with the presented model indicated that considering $\lambda_a = 0.5$ led to an instantaneous flow rate in the IMO test case 4 in MSC.1/Circ.1533 [147], which, is not always below the imposed IMO limit of 1.33 p/s, as reported in Figure 2.4. A further analysis was carried on using the same experimental data proposed by Liao et al. [124] discussed in (Chapter 4).

Therefore, eventually, a value $\lambda_a = 0.3$ has been chosen as default parameter for the model presented herein, since it seemed more appropriate for the purpose of studying a situation of ordered evacuation in line with the requirements of IMO. More experimental results are however needed to properly determine this coefficient and its possible dependencies on the detailed characteristics of the evacuation condition.

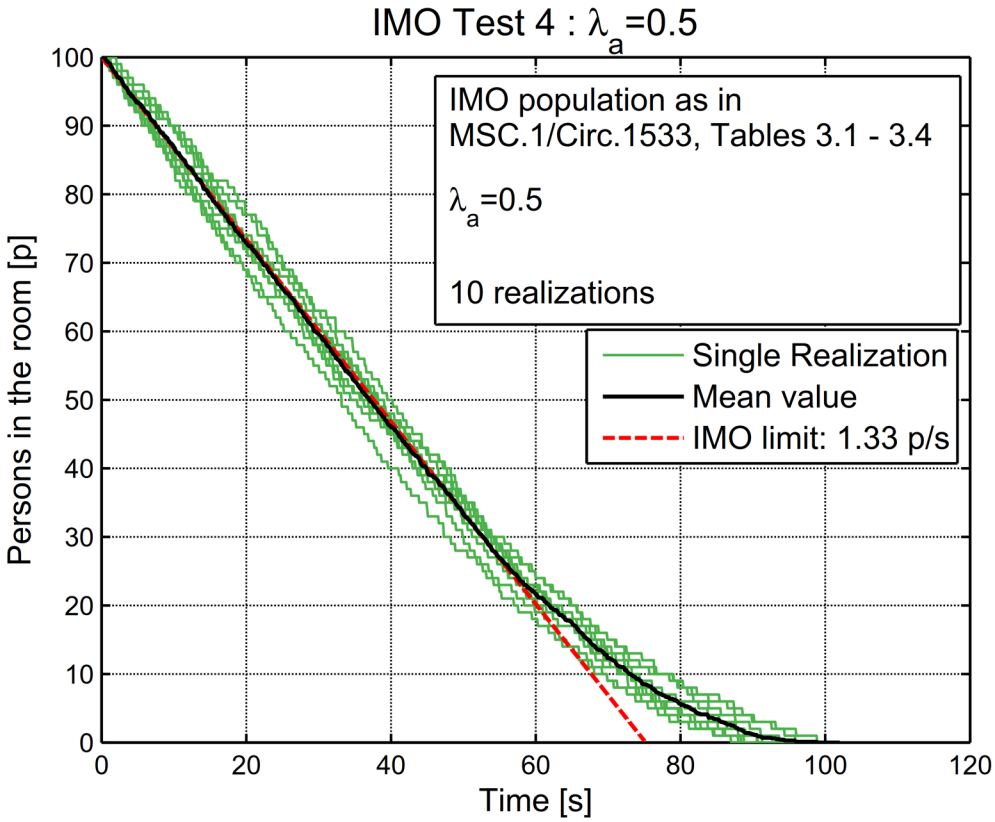

Figure 2.4: IMO Test 4 performed with $\lambda_a = 0.5$.

In parallel to the agent-agent interaction force, the agent-agent interaction model considers also the effect of a torque. In particular, the torque models the way people rotate their body in order to avoid contacts. The agent-agent interaction torque is not directly generated by the interaction force, which is, instead, considered to be applied in the centre of mass of the agent.

The torque exerted by agent j on agent i is expressed as follows:

$$\mathbf{T}_{ij}^{\mathrm{a}}(t) = \max_{h\in\{1,2,3\}}\left(\mathbf{R}_i^2 \times \mathbf{F}_{ij}^{2h}\right) + \max_{h\in\{1,2,3\}}\left(\mathbf{R}_i^3 \times \mathbf{F}_{ij}^{3h}\right) \tag{2.16}$$

where, with reference to Figure 2.3 Figure 3, $\mathbf{R}_i^k$ is the vector connecting the agent centre $\mathbf{C}_i^1$ to the arm centre $\mathbf{C}_i^k$. $\mathbf{F}_{ij}^{kh}$ is the virtual force calculated from equation (2.14) by considering, however, the circle centres $\mathbf{C}_i^k$ and $\mathbf{C}_j^h$, instead of the closest circle centres. The force $\mathbf{F}_{ij}^{kh}$ is, thus, directed as the vector $\mathbf{d}_{ij}^{kh}$ connecting the two centres.

Finally, the resulting agent-agent interaction force and torque exerted on agent i are given by the summation of the contribution from all interacting agents j, i.e.

$$\begin{cases} \mathbf{F}_i^{\,\mathrm{a}}(t) = \sum_{j \text{ interacting}} \mathbf{F}_{ij}^{\,\mathrm{a}}(t) \\ \mathbf{T}_i^{\,a}(t) = \sum_{j \text{ interacting}} \mathbf{T}_{ij}^{\,a}(t) \end{cases} \tag{2.17}$$

Agents do not interact when a wall is placed between them, i.e. when they are not visible each other. A visibility check between agent i and j is therefore carried during the simulation: if the segment connecting the centres of agents intersects the mesh representing the environment (walls, floors, stairs, …), the two agents are considered to be not visible each other.

Moreover, considering the exponential spatial decay in the interaction effects (see (2.14)), agents are considered to be non-interacting when their skin-to-skin distance exceeds $10 \cdot B_a$. This last check allows to significantly reduce the computational time in case of simulations with a large number of agents, by reducing the number of agents to be taken into account in the calculation of the agent-agent interaction force at each time step. A summary of parameters associated with the agent-agent interaction model is reported in Table 2.6.

Table 2.6: Parameters of agent-agent interaction model, and corresponding values.

A_{a}	λ_{a}	B_{a}
$2 \cdot 10^3$ N	$\begin{cases} 1.0 & \text{for } v_i(t) = 0\ m/s \\ 1 - 70 \cdot v_i(t) & \text{for } 0\ m/s < v_i(t) < 0.01\ m/s \\ 0.3 & \text{for } v_i(t) \geq 0.01\ m/s \end{cases}$	0.08 m

2.2.4 Agent wall interaction

The repulsive interaction force between agents and walls (obstacles in general) models the way people try to avoid contacts with, and keep distance from, obstacles and walls. In the present model walls and obstacles are considered as three dimensional objects modelled by appropriate triangular meshes. The agent-wall interaction force is determined on the basis of the distance between the agent and the closest point on the geometrical mesh. Moreover, the model can deal with generic shapes of the walls and obstacles, making it very flexible also in case of complex walls/obstacles geometries which, therefore, do not need strong modelling simplifications.

Starting from, and modifying, the background from the model proposed by Helbing and Molnar [71] and by Korhonen [112], the model for the agent-wall interaction force is very similar to the single agent-agent interaction force model (2.14), and, with reference to Figure 2.5, it is described as follows:

$$\mathbf{F}_i^{\,\mathrm{w}} = A_i^{\mathrm{w}}(t) \cdot e^{-\left(\frac{d_i - r_i}{B_{\mathrm{w}}}\right)} \cdot \left(\lambda_{\mathrm{w}}\left(v_i(t)\right) + \left(1 - \lambda_{\mathrm{w}}\left(v_i(t)\right)\right) \cdot \left(\frac{1 + \cos(\theta_i^{\mathrm{w}})}{2} \right) \right) \cdot \hat{\mathbf{d}}_i \tag{2.18}$$

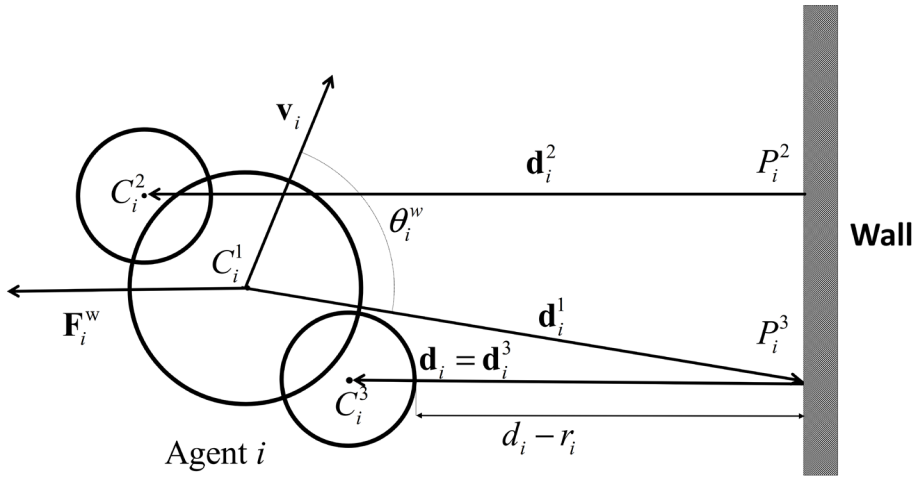

Figure 2.5: Agent-wall interaction.

The agent-wall interaction torque is modelled as the sum of two contributions, which can be considered as the torques associated with each agent arm, as follows:

$$\mathbf{T}_i^{\mathrm{w}} = \left(\mathbf{R}_i^2 \times \mathbf{F}_i^2\right) + \left(\mathbf{R}_i^3 \times \mathbf{F}_i^3\right) \tag{2.19}$$

where, with reference to Figure 2.5 and for $h \in \{2,3\}$ (left and right arm, respectively), $\mathbf{R}_i^h$ is the vector connecting the agent centre to the centre $\mathbf{C}_i^h$ and $\mathbf{F}_i^h$ is a force calculated according to (2.18) but using different variables which are associated with the considered agent arm. The direction of the force $\mathbf{F}_i^h$ is the direction of vector $\mathbf{d}_i^h$ connecting the point $\mathbf{P}_i^h$ (the wall closest point from the centre $\mathbf{C}_i^h$) to the centre $\mathbf{C}_i^h$ (note that $\mathbf{d}_i^1$ is oriented opposely with respect to $\mathbf{d}_i^2, \mathbf{d}_i^3$). The considered effective distance is the one between the wall and the circle centred $\mathbf{C}_i^h$. The anisotropic component is calculated using an angle θ_i^h between the instantaneous agent and velocity $\mathbf{v}_i(t)$ and the vector $-\mathbf{d}_i^h$.

A summary of parameters associated with the agent-wall interaction model is reported in Table 2.7.

Table 2.7: Parameters of agent-wall interaction model, and corresponding values.

A_{w}	λ_{w}	B_{w}
$2 \cdot 10^3$ N	$\begin{cases} 1.0 & \text{for } v_i(t) = 0 \ m/s \\ 1 - 80 \cdot v_i(t) & \text{for } 0 \ m/s < v_i(t) < 0.01 \ m/s \\ 0.2 & \text{for } v_i(t) \geq 0.01 \ m/s \end{cases}$	0.04 m

2.2.5 Counter-flow

Agent-agent repulsive force/torque alone cannot properly model the behaviour of pedestrians in situations of counter-flow, i.e. in those situations where agents have opposite (or different) directions. In such cases, a model is required which is specifically suited to model the lateral shift which is typically performed by pedestrians in order to avoid incoming people.

Different studies have been carried out in relation to the counter-flow situation (e.g. Isobe et al. [89]; Zhang et al. [236]), which highlighted recurring patterns in experiments. The most observed pattern is the lane formation: people tend to form separated lanes, and this configuration tends to maximize the flow rate, as it is reported by Zhang et al. [236].

Two main approaches can be identified from the existing literature on how to integrate counter-flow models in the social force modelling. One approach is based on the modelling of the counter-flow as an additional force component, as suggested by Guo [64] and by Pelechano et al [168]. In the alternative approach, instead, the response to a counter-flow situation is modelled through a modification of the agent's instantaneous desired speed, as described by Heliövaara et al. [76].

Herein, a new model is presented, which has been developed in the course of the present study. The tuning of some of the model parameters will be treated separately in Chapter 3.

The model is a short-range one, describing the pedestrian reaction to a counter-flow situation through an additional force, i.e. in line with the former of the two approaches described above. Conceptually in line with the agent-agent interaction model, for a considered agent, the interactions with each incoming agent in a counter-flow condition are considered separately, and single contributions are then summed up

In the presented model, for the considered agent, the classification of whether any other incoming agent is in counter-flow is based only on instantaneous physically observable variables, such as the instantaneous speed, the body orientation and the position of the incoming pedestrian

First, with reference to Figure 2.6 and Figure 2.7, the following quantities p_1, p_2 and p_3 are defined:

$$p_1 = \left\langle \hat{\mathbf{v}}_i^0, \widehat{\mathbf{D}}_{ij} \right\rangle = \cos\left(\theta_{ij}\right) \tag{2.20}$$

$$p_2 = -\left\langle \hat{\mathbf{v}}_i^0, \hat{\mathbf{n}}_j \right\rangle = -\cos\left(\eta_{ij}\right) = \cos\left(\pi - \eta_{ij}\right) \tag{2.21}$$

$$p_3 = f(v_{ij}^{r0}) \tag{2.22}$$

where the $\langle .,. \rangle$ operator indicates the dot product, $\hat{\mathbf{v}}_i^0$ is the versor of agent i desired speed vector $\mathbf{v}_i^0$, $\widehat{\mathbf{D}}_{ij}$ is the versor of the vector $\mathbf{D}_{ij}$ connecting agents centres, $\hat{\mathbf{n}}_j$ is the

orientation vector of agent j (pointing towards the front direction of the agent). The function $f(v_{ij}^{r0})$ depends on the component, along the direction $\hat{\mathbf{v}}_i^0$, of the relative speed of agent j with respect to agent i, as follows:

$$\begin{cases} v_{ij}^{r0} = \left\langle \hat{\mathbf{v}}_i^0, (\mathbf{v}_j - \mathbf{v}_i) \right\rangle \\ f(v_{ij}^{r0}) = \begin{cases} 1 & \text{for } v_{ij}^{r0} < 0 \\ 1 - \dfrac{v_{ij}^{r0}}{V_{\mathrm{i}}^{\mathrm{cf}}} & \text{for } 0 \le v_{ij}^{r0} \le V_{\mathrm{i}}^{\mathrm{cf}} \\ 0 & \text{for } v_{ij}^{r0} > V_{\mathrm{i}}^{\mathrm{cf}} \end{cases} \end{cases} \tag{2.23}$$

The reference speed $V_{\mathrm{i}}^{\mathrm{cf}}$ (m/s) is defined as a function of the unimpeded walking speed v_i^{u}, which is a specific characteristic of each agent, i.e.

$$V_{\mathrm{i}}^{\mathrm{cf}} = k_{\mathrm{cf}} \cdot v_i^u \tag{2.24}$$

An agent j is defined to be in counter-flow with respect to the considered agent i, when the following conditions are all fulfilled:

$$p_1 \ge \cos(\theta_{\mathrm{cf}}) \tag{2.25}$$
$$d_{ij} - r_{ij} < D_{\mathrm{cf}} \tag{2.26}$$
$$p_2 > 0 \tag{2.27}$$
$$p_3 > 0 \tag{2.28}$$

Conditions (2.25) and (2.26) refer to the relative position of agent j with respect to agent i, taking into account this latter's desired velocity. A counter-flow condition is potentially identified only if agent j is positioned within an angular sector of amplitude θ_{cf} around the direction identified by $\hat{\mathbf{v}}_i^0$ (see (2.25)), and, in addition (see (2.26)), agent j is also closer to agent i than a cut-off distance D_{cf}, considering the effective skin-to-skin distance $d_{ij} - r_{ij}$ between the closest circles among agents. A graphical representation is shown in Figure 2.6.

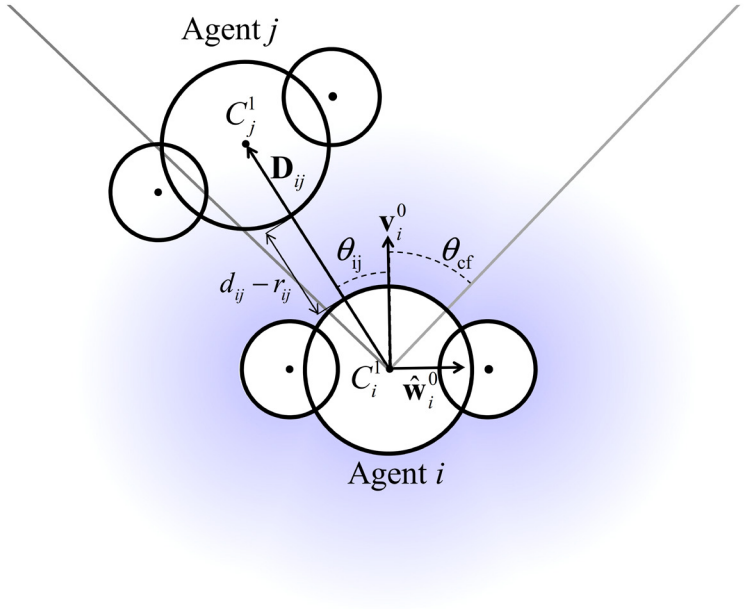

Figure 2.6: Example of counter-flow situation when considering only conditions (2.25) and (2.26).

The condition (2.27) identifies a potential counter-flow situation on the basis of the angle between the desired speed of agent i and the orientation of agent j, and this condition prevents from considering, for instance, agents in a queue as being in a counter-flow situation. Finally, condition (2.28) identifies potential counter-flow situation using the component of the relative velocity of agent j with respect to agent i along the direction of the desired speed of agent i. In particular, through (2.22) and (2.28), agent j is identified as being potentially in counter-flow whenever such component is strictly negative or, alternatively, positive, but smaller than the threshold $V_{\mathrm{i}}^{\mathrm{cf}}$ (see (2.23)). This latter case allows to properly identify counter-flow situations also in those conditions, typically of low speed, when the agents are facing each other and the agent j is moving backward. Allowing the counter-flow to be triggered also when the relative speed is slightly positive is necessary in order to apply the counter-flow force with continuity in situations of high crowd density. Indeed, in these situations, due to interaction forces, it was observed that agents might sometimes have velocities with opposite direction with respect to their desired ones. In such conditions the counter-flow model would randomly be triggered on and off without the introduction of the threshold $V_{\mathrm{i}}^{\mathrm{cf}}\left(>0\right)$ in (2.22) - (2.28). Conditions (2.27) and (2.28) are exemplified in Figure 2.7.

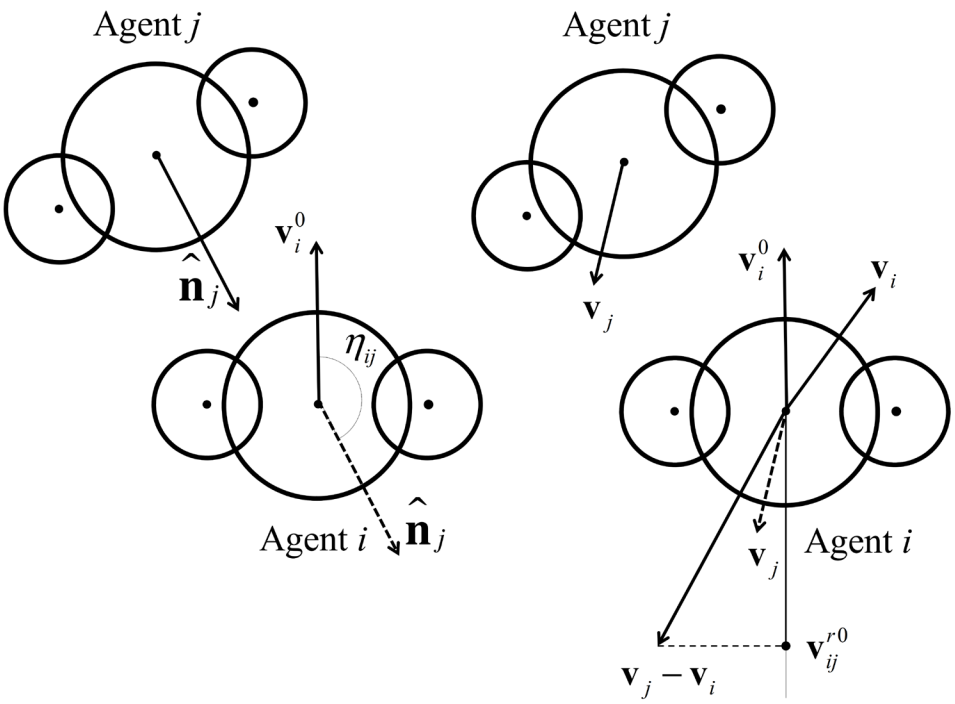

Figure 2.7: Example of counter-flow situation when considering only conditions and (2.27) and (2.28).

When the agent j is identified to be in counter-flow with respect to agent i, the module of its contribution to the counter-flow force on agent i is modelled as follows:

$$\left\|\mathbf{F}_{ij}^{\mathrm{cf}}\right\| = A_{\mathrm{cf}} \cdot \left(1 - \frac{d_{ij} - r_{ij}}{D_{\mathrm{cf}}}\right) \cdot \left(\left(\frac{p_1 - \cos(\theta_{\mathrm{cf}})}{1 - \cos(\theta_{\mathrm{cf}})}\right) \cdot p_2\right)^{\alpha_{\mathrm{cf}}} \cdot p_3 \tag{2.29}$$

Whenever a counter-flow condition is identified, the model for $\left\|\mathbf{F}_{ij}^{\mathrm{cf}}\right\|$ is continuous with respect to all the dependent variables, and $\left\|\mathbf{F}_{ij}^{\mathrm{cf}}\right\|$ decreases to 0 as any of the counter-flow conditions (2.25)-(2.28) is not satisfied. The numerical values selected for the various parameters for the determination of $\left\|\mathbf{F}_{ij}^{\mathrm{cf}}\right\|$ are described in the following.

The threshold speed V_{cf} in (2.22) has tentatively been fixed to 10% of unimpeded agent speed v_i^{U}, i.e. $k_{\mathrm{cf}} = 0.10$ in (2.24)(2.23), since, from simulations, this value provides realistic outcomes in case of counter-flow situations characterised by high density.

The numerical specification of θ_{cf} and D_{cf} corresponds, basically, to the specification of the region of positioning of agent j with respect to agent i within which the counter-flow model can be triggered (shortly, the "counter-flow region"), and this is fundamental to identify a potential counter-flow condition. The counter-flow region defined by Heliövaara et al. [76] is roughly elliptical, extending 3 m ahead of agent i and up to 1.5 m on its sides. The same maximum extents have been used by Pelechano et al [168], but with a counter-flow region having a rectangular shape. The

implicit counter-flow region considered for the model presented herein is defined considering the skin-to-skin distance $d_{ij} - r_{ij}$, and takes into account, therefore, the actual agents' dimensions. The threshold distance D_{cf} at which the model is triggered has been tentatively fixed to $2\ \text{m}$. This value appeared reasonable for the short-range nature of the model and in line with the indications available in literature. Regarding the parameter θ_{cf}, which, in the present model, characterises the half width of the angular sector within which agent j needs to be in order for being considered in a potential counter-flow condition, its value was tentatively set to $45°$. This value was set taking into account that, in the model by Heliövaara et al. [76], an agent tends to proceed undisturbed when there are no agents in counter-flow in a frontal sector with a width of around $\pm 40° \div \pm 45°$.

The strength of the counter-flow force depends on the parameter A_{cf} [N] which requires a calibration. A first calibration of this parameter has been made using IMO test case 8 reported in MSC.1/Circ.1533 [147] and experimental data provided by Isobe et al. [89]. The calibration also addressed the exponent α_{cf} which is another characteristic parameter of the proposed model. The parameter α_{cf} controls the level of interaction with lateral agents and with agents not fully oriented towards $\hat{\mathbf{v}}_i^0$. Reducing the value of α_{cf} increases the force originated by interaction with agents placed laterally or agents not in front of the desired direction of agent i. A good agreement with experimental data by Isobe et al. [89] was obtained with $A_{\text{cf}} = 225\ \text{N}$ and $\alpha_{\text{cf}} = \frac{1}{3}$. The calibration of those parameters will be treated separately in Chapter 3.

Equation (2.29) provides the module of the counter-flow force exerted by agent j on agent i. Regarding its direction, the force is, as a basis, perpendicular to the direction of the desired speed $\hat{\mathbf{v}}_i^0$, since it is intended to model a lateral shift. However, its orientation (right or left with respect to $\hat{\mathbf{v}}_i^0$), depends on the relative position of the agent j in counter-flow with respect to the agent i. In general, agents tend to move in the direction opposite to that where the counter-flow agent is coming from. It has been observed that, in most cultures, there exists a preferred direction for pedestrian traffic which, usually, improves the organization of opposite flows in counter-flow conditions (e.g. [76]; [230]). In order to reproduce this behaviour, in the presented model this preference is expressed by the introduction of an offset angle parameter η_{cf}. In particular, the versor of the counter-flow force is defined as follows:

$$\hat{\mathbf{F}}_{ij}^{\text{cf}} = -1 \cdot \text{sign}\left(\left\langle \hat{\mathbf{w}}_i^0, \hat{\mathbf{D}}_{ij} \right\rangle - \sin\left(\eta_{\text{cf}}\right) \right) \cdot \hat{\mathbf{w}}_i^0 \tag{2.30}$$

where $\hat{\mathbf{w}}_i^0$ is the unit vector oriented from the centre to the right arm of agent i. In case $\eta_{cf} = 0$ there is no preferred direction and the model is symmetrical. According to (2.30), and with reference to Figure 2.6, the counter-flow force will have the same direction as $\hat{\mathbf{w}}_i^0$ if $\vartheta_{ij} \le \eta_{\text{cf}}$ and will have opposite direction otherwise. It is also worth

underlining that the preferred direction is on the right with respect to the desired speed of agent i if η_{cf} is positive, whereas it is on the left if η_{cf} is specified to be negative. Herein, the preferred direction parameter has been tentatively set to $\eta_{\text{cf}} = 12°$, and this value was set in order to obtain a reasonable reproduction of experimental data from Isobe et al. [89] without introducing a too strong right preference.

Eventually, the contribution to the counter-flow force vector due to agent j is determined by combining (2.29) and (2.30).

$$\mathbf{F}_{ij}^{\text{cf}} = \left\| \mathbf{F}_{ij}^{\text{cf}} \right\| \cdot \hat{\mathbf{F}}_{ij}^{\text{cf}} \tag{2.31}$$

In addition to a translational shifting, which is induced by the counter-flow force, also a counter-flow-induced rotation needs to be modelled. In fact, Heliövaara et al. [76] observed that in counter-flow conditions people change their body orientation in order to better fit in narrow spaces, moving shoulder first. This behaviour is fundamental for models, as the present one, representing the human body with its asymmetry, particularly in high-density counter-flow conditions. In the model presented herein, the described behaviour is modelled with a counter-flow torque contribution induced by agent j on agent i, having module as follows:

$$\left\| \mathbf{T}_{ij}^{\text{cf}} \right\| = A_{\text{cft}} \cdot \left(1 - \frac{d_{ij} - r_{ij}}{D_{\text{cft}}} \right) \cdot \left(\left(\frac{p_1 - \cos(\theta_{\text{cf}})}{1 - \cos(\theta_{\text{cf}})} \right) \cdot p_2 \right)^{\alpha_{\text{cf}}} \cdot p_3 \tag{2.32}$$

The previous expression differ from that used for the module of the counter-flow force (2.29) only in the characteristic parameters A_{cft} ($N \cdot m$) and D_{cft} (m).

The counter-flow torque model needs to be activated at a closer distance compared to the counter-flow force model, as the change of orientation of pedestrians typically happens only if people are very close each other. As a result, the spatial scale parameters D_{cft} was tentatively set to $1\ \text{m}$, i.e. half of D_{cf}. Moreover, from calibration simulations a value $A_{\text{cft}} = 30\ \text{N} \cdot \text{m}$ was set, since it was observed that higher values of A_{cft} caused unnaturally fast rotations.

The direction of the torque, which eventually governs the direction of agent i rotational acceleration, is determined by the direction of the force as follows:

$$\hat{\mathbf{T}}_{ij}^{cf} = \text{sign}\left(\left\langle \hat{\mathbf{w}}_i^0, \hat{\mathbf{F}}_{ij}^{\text{cf}} \right\rangle \right) \cdot \hat{\mathbf{z}} \tag{2.33}$$

where $\hat{\mathbf{z}}$ is the versor of the vertical axis. Eventually, the torque contribution due to agent j is determined by combining (2.32) and (2.33).

$$\mathbf{T}_{ij}^{\text{cf}} = \left\| \mathbf{T}_{ij}^{\text{cf}} \right\| \cdot \hat{\mathbf{T}}_{ij}^{\text{cf}} \tag{2.34}$$

The total counter-flow force and torque vectors are determined by summing up the contributions from all agents identified to be in counter-flow:

$$\begin{cases} \mathbf{F}_i^{\mathrm{cf}}(t) = \sum_{j \text{ in counter-flow}} \mathbf{F}_{ij}^{\mathrm{cf}}(t) \\ \mathbf{T}_i^{\mathrm{cf}}(t) = \sum_{j \text{ in counter-flow}} \mathbf{T}_{ij}^{\mathrm{cf}}(t) \end{cases} \tag{2.35}$$

From a series of calibrations, it was observed that this model may generate impasse situations, particularly in the case of bottle necks. In order to avoid such situations, a random variation of direction of the force $\mathbf{F}_i^{\mathrm{cf}}(t)$ is implemented, in such a way that the force does not remain exactly parallel to $\hat{\mathbf{w}}_i^0$. To this end, therefore, the force $\mathbf{F}_i^{\mathrm{cf}}(t)$, while keeping the same module as in (2.29), is oriented by an angle $\delta\psi(t)$ with respect to the nominal direction obtained by (2.30). The time history of angle $\delta\psi(t)$ is generated according to the same procedure described hereinafter for the random forces (see section 2.2.6), within a range $[-\delta\psi_{\mathrm{cf}}, \delta\psi_{\mathrm{cf}}]$. Following calibrations a value $\delta\psi_{\mathrm{cf}} = 15°$ was tentatively set (see Chapter 3).

It is also noted that, similarly to the case of agent-agent interaction, the possible counter-flow interaction is considered only if agent j is visible to agent i, and the same visibility check used for agent-agent interaction forces (see section 2.2.3) is also applied in the case of counter-flow interact.

Finally, a summary of the parameters associated with the counter-flow model is reported in Table 2.8.

Table 2.8: Parameters of counter-flow model, and corresponding values.

D_{cf}	D_{cft}	A_{cf}	A_{cft}	θ_{cf}	η_{cf}	$V_{\mathrm{i}}^{\mathrm{cf}}$	k_{cf}	α_{cf}	$\delta\psi_{\mathrm{cf}}$
2 m	1 m	225 N	30 N·m	45°	12°	$k_{\mathrm{cf}} \cdot v_i^{\mathrm{u}}$	0.1	$\frac{1}{3}$	15°

2.2.6 Random fluctuation

As anticipated in the description of the various force contributions, some random fluctuation is added to several terms. In particular, random forces and random torque are directly applied to each agent. Moreover, random fluctuations are also applied to the angle governing the orientation of the counter-flow force with respect to the agent. The role of the random noise is twofold. On the one hand it mimics a certain level of inherent natural randomness in the agents' behaviour. On the other hand, the addition of a random noise also prevents the occurrence of unnatural impasse situations (equilibria of the dynamical system), which, in real cases, are typically resolved by interactions between pedestrians. However, large magnitudes of random forces can have the opposite effect, by creating impasse situations through so-called "freezing by heating effect" (Helbing and Johansson [70]).

Random fluctuations in the developed mathematical model are all generated using the same type of algorithm. The idea underlying the algorithm is based on the FDS+Evac code implementation ([112]).

The time history of a generic stochastic process $X(t)$, for which a distribution is specified, is generated starting from an initial randomly generated value $x_0 = x(t = 0s)$. Then, given a first time step Δt_1, the random variable X at $t = \Delta t_1$, i.e. x_1, is kept the same as x_0 with probability $P_S(\Delta t_1)$, which means that, equivalently, it is updated with a new independent value sampled from the same distribution with probability $1 - P_S(\Delta t_1)$. The same process is repeated for all the subsequent time steps Δt_i ($i = 2,3,...$), independently from the previous ones, and it allows to generate, in real-time, the discrete time history x_i ($i = 0,1,2,...$). It is also noted that the time step can be, in general, a variable time step. In order to guarantee that the procedure is independent, from a statistical perspective, from the chosen time step, the probability $P_S(\Delta t)$ is taken as follows:

$$P_S(\Delta t) = e^{-\alpha \cdot \Delta t} \tag{2.36}$$

where α [s^{-1}] is a specified time constant. By determining the autocorrelation function of the process, and taking its Fourier transform, it can be proved that the stochastic process $X(t)$ resulting from the described procedure, after removing its mean, has a single-side power spectral density as follows

$$S(\omega) = \frac{\sigma^2}{\pi} \cdot \frac{2 \cdot \alpha}{\omega^2 + \alpha^2} \tag{2.37}$$

where σ^2 is the variance of the process and ω [rad/s] is the circular frequency. The obtained result is independent on the distribution specified for X, and the power spectral density $S(\omega)$ is directly proportional to the variance of the process. The expression (2.36) allows to select the time constant α having a clear view of its effect on the energy distribution of the resulting process in frequency domain. In addition, the knowledge of the theoretical spectrum (2.37) of the process, allows to select α in order to reduce aliasing effects which inevitably occur in simulations with discrete time steps. Figure 2.8 shows the spectral density (2.37) for different value of the parameter α considering a unitary variance

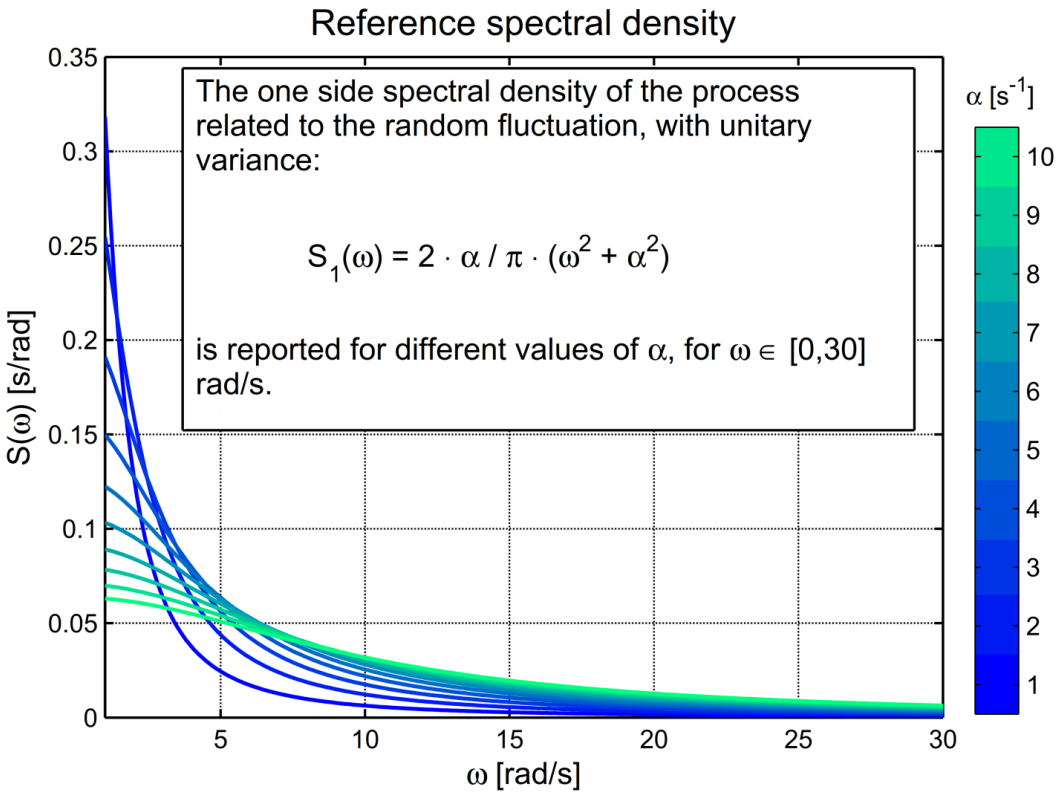

Figure 2.8: Reference spectral density of the process associated to the random fluctuation.

Random forces are conventionally generated, for each agent, by separately generating the force module R_F and the orientation ϑ_F of the force in the simulation reference system. While the distributions for the two variables are different, the update of the variables according to the random procedure specified above is done at the same time for both variables, i.e. the two variables are either both updated or not updated at a generic time instant during the simulation. As a result, the update of the two variables is based on a common parameter α_F. The components of the force are then determined as:

$$\begin{cases} F_x^{\text{rand}} = \cos(\theta_F) \cdot R_F \\ F_y^{\text{rand}} = \sin(\theta_F) \cdot R_F \end{cases} \tag{2.38}$$

The distribution selected for R_F is a truncated Rayleigh, while a uniform distribution in $[0, 2\pi[$ is selected for ϑ_F, and the two variables are statistically independent. As a result, the components F_x^{rand} and F_y^{rand} are approximately (due to the truncation of the Rayleigh distribution) Gaussian and independent. The expression for the distribution of R_F is:

$$\begin{cases} pdf\left(R_F\right) = \dfrac{R_F}{C_F \cdot b_F^2} \cdot \exp\left(-\dfrac{R_F^2}{2 \cdot b_F^2}\right) \\ C_F = 1 - \exp\left(-\dfrac{R_{F,\max}^2}{2 \cdot b_F^2}\right) \\ R_{F,\max} = k_{rf} \cdot b_F \\ R_F \in \left[0, R_{F,\max}\right] \end{cases} \tag{2.39}$$

In order to avoid the possibility of too large random forces due to the tails of the Rayleigh distribution, the truncation is taken at $k_{rf} = 4$. The parameter b_F in (2.39) is indirectly determined by specifying the desired standard deviation σ_{rf} of each force component in (2.38) and noting that, from (2.38) and considering the selected distribution for ϑ_F, the variables F_x^{rand} and F_y^{rand} are both zero mean and independent. It then follows that

$$E\left\{\left(F_x^{\text{rand}}\right)^2 + \left(F_y^{\text{rand}}\right)^2\right\} = 2 \cdot \sigma_{rf}^2 = E\left\{R_F^2\right\} \Rightarrow b_F = \sigma_{rf} \cdot \sqrt{\frac{1 - \exp\left(-\dfrac{k_{rf}^2}{2}\right)}{1 - \exp\left(-\dfrac{k_{rf}^2}{2}\right) \cdot \left(1 + \dfrac{k_{rf}^2}{2}\right)}} \tag{2.40}$$

The standard deviation σ_{rf} is set proportionally to the mass m_i of each agent and it is assumed to scale with the agent unimpeded speed v_i^u, as follows:

$$\begin{cases} \sigma_{rf,i} = m_i \cdot \sigma_{ra} \cdot \dfrac{v_i^u}{v_n} \\ \sigma_{ra} = 0.05\, m/s^2 \quad ; \quad v_n = 1\, m/s \end{cases} \tag{2.41}$$

The parameter α_F which is used for the random update of R_F and ϑ_F is selected as being dependent on the relaxation parameter τ_i^f of the motive force of each agent, as follows:

$$\begin{cases} \alpha_{F,i} = \dfrac{1}{\tau_i^f \cdot k_{\alpha,rf}} \\ k_{\alpha,rf} = 0.2 \end{cases} \tag{2.42}$$

It is worth noting that the selected value of $\alpha_{F,i}$ allows also to keep the aliasing effect due to the discrete time stepping to a negligible level with typical time steps used in the simulations, which are of the order of 0.01 s. Herein the aliasing is considered negligible when at least the 99% of the total variance of the process is contained in the region determined by frequencies lower than the Nyquist one (which is $\pi / \Delta t$).

Analytically integrating the spectral density reported in equation (2.37) and imposing this requirement, the parameter α can be easily determined as a function of the time step. The function identifies all the couples α and Δt for which the 99% of the variance is within the region of frequencies lower than the Nyquist. This dependence is reported in Figure 2.9 where the adopted value for $\alpha_{F,i}$ is highlighted.

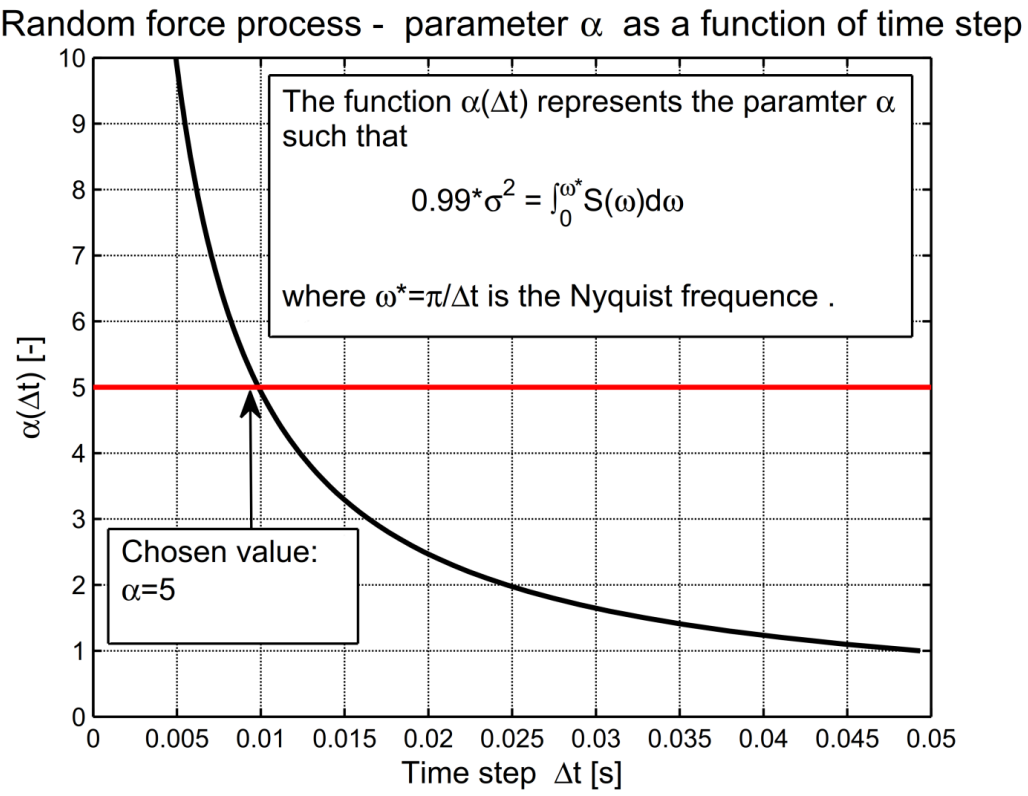

Figure 2.9: Parameter α as a function of the time step to guarantee that that 99% of the total energy of the process is contained in the region of frequencies up to the Nyquist one.

The random torque is generated conceptually in the same way as the components of the random force (32), but retaining only one term as follows:

$$T^{\text{rand}} = \cos(\theta_T) \cdot R_T \tag{2.43}$$

with characteristic parameters, parallel to the ones described in detail for the force, as follows:

$$\begin{cases} \sigma_{rt,i} = I_{z,i} \cdot \sigma_{raa} \quad ; \quad \alpha_{F,i} = \dfrac{1}{\tau_i^t \cdot k_{\alpha,rt}} \\ \sigma_{raa} = 0.5\, rad/s^2 \quad ; \quad k_{\alpha,rt} = 1 \end{cases} \tag{2.44}$$

The random effects for the counter-flow model are all embedded in the random angle $\delta\psi(t)$ used for changing the orientation of the counter-flow force with respect to its nominal direction, as described before in section 1.2.5. The angle $\delta\psi(t)$ is directly

generated according to the procedure described in this section using a uniform distribution in $\left[-\delta\psi_{\mathrm{cf}},\delta\psi_{\mathrm{cf}}\right]$ (see Table 2.8). The parameter α (see (2.36)) used for the random update of $\delta\psi\left(t\right)$ is taken the same as that used for the generation of the random forces (see (2.42)).

2.2.7 Nervousness model

A nervousness model has been implemented in the developed tool to model those situations where people tend to get impatient because they cannot achieve the desired target state. The implementation of a nervousness effect can also typically help in overcoming local impasse situations, which could otherwise appear in the simulations, and which cannot be resolved by the effect of random forces alone. It is however underlined that the nervousness model presented herein is intended to address situation where people, while getting impatient, still follow, however, an orderly evacuation process. The model is not intended to be used for representing situations characterised by extreme levels of nervousness leading to panic phenomena, such as those described by Helbing et al. [73].

The general idea to model nervousness is that some parameters of the social forces are instantaneously modified on the basis of the state of the agent in the past. This idea reproduces the fact that people behaviour is affected not only by instantaneous factors, but also by the short-time memory. In particular, the parameters which are affected by nervousness are the relaxation coefficient τ_i^f of the motive force (see (2.10)), the standard deviation $\sigma_{rf,i}$ of the random force (see (2.41)), and the standard deviation $\sigma_{rt,i}$ of the random torque (see (2.44)). While $\tau_i^f\left(t\right)$ decreases with respect to the nominal value τ_i^f in case of a situation characterised by nervousness, $\sigma_{rf,i}\left(t\right)$ and $\sigma_{rt,i}\left(t\right)$, instead, increase with respect to the nominal values $\sigma_{rf,i}$ and $\sigma_{rt,i}$, respectively. To control such variation of parameters, use is made of an instantaneous nervousness parameter $\xi_{inst}\left(t\right)$, which is defined as follows

$$\xi_{inst}\left(v_{i,//}\left(t\right),\mathbf{v}_i^0\left(t\right)\right)=\begin{cases}\xi_{\max} & \text{for } v_{i,//}\left(t\right)<0\\ 1.0 & \text{for } v_{i,//}\left(t\right)\geq v^*\left(t\right)\\ \dfrac{v_{i,//}(t)}{v_i^*(t)}\cdot\left(1-\xi_{\max}\right)+\xi_{\max} & \text{otherwise}\end{cases} \tag{2.45}$$

where $v_{//}(t)=\langle\mathbf{v}_i\left(t\right),\hat{\mathbf{v}}_i^0\left(t\right)\rangle$ is the component of the instantaneous speed $\mathbf{v}_i\left(t\right)$ along the desired speed direction (in this model it is assumed that $\left\|\mathbf{v}_i^0\right\|=v_i^0\neq 0$, i.e. it is assumed that agents always have a non-zero desired speed), and $\xi_{\max}$ is the parameter controlling the level of nervousness effects. This parameter depends on whether the model is eventually used to define $\tau_i^f\left(t\right)$, $\sigma_{rf,i}\left(t\right)$ or $\sigma_{rt,i}\left(t\right)$. Following some

calculations in case of IMO test case 4 in MSC.1/Circ.1533 [147], the value of $\xi_{\max}$ has been tentatively set, for the different cases, as follows:

$$\begin{cases} \text{For} \quad \tau_i^f(t): \ \xi_{\max} = 1.25 \\ \text{For } \sigma_{rf,i}(t): \ \xi_{\max} = 8.00 \\ \text{For } \sigma_{rt,i}(t): \ \xi_{\max} = 8.00 \end{cases} \tag{2.46}$$

The variable $v_i^*(t)$ is calculated as follows:

$$v_i^*(t) = \begin{cases} k_{nerv} \cdot \dfrac{t}{\tau_i^f} \cdot v_i^0 \ \text{ for } \ 0 < t < \tau_i^f \\ k_{nerv} \cdot v_i^0 \ \text{ for } \quad t \geq \tau_i^f \end{cases} \tag{2.47}$$

with $k_{nerv} = 0.5$. This value of k_{nerv} guarantees that an agent moving from rest in a free field, and having thus speed $v_i(t) = v_i^0 \cdot \left(1 - \exp\left(-t/\tau_i^f\right)\right)$, is not affected by nervousness effects.

In the model presented by Helbing et al. [73], nervousness effects depend only on the instantaneous state. However, in case of evacuation, usually people get nervous when they are forced to maintain a speed which is much lower than their desired one for a relatively long time. This observation indicates that nervousness effects should be linked with the concept of memory. For this reason a memory model was integrated within the nervousness model. In particular, the nervousness parameter at time t is defined as the average of the instantaneous nervousness parameter ξ_{inst} in a specified past time window, i.e:

$$\begin{cases} \xi_{\text{nerv}}(t) = \dfrac{1}{t - t_{\min}} \int_{t_{\min}}^{t} \xi_{inst}(s) ds \\ t_{\min} = \max\left(0, t - T_{\text{mem}}\right) \end{cases} \tag{2.48}$$

where T_{mem} is the (maximum) length of the temporal window considered for the memory of one agent. Herein T_{mem} has been tentatively set to 30 s. Using $\xi_{\text{nerv}}(t)$, eventually, the instantaneous values $\tau_i^f(t)$, $\sigma_{rf,i}(t)$ and $\sigma_{rt,i}(t)$ are determined as follows:

$$\begin{cases} \tau_i^f(t) = \tau_i^f \Big/ \xi_{\text{nerv},\tau_i^f}(t) \\ \sigma_{rf,i}(t) = \sigma_{rf,i} \cdot \xi_{\text{nerv},\sigma_{rf,i}}(t) \\ \sigma_{rt,i}(t) = \sigma_{rt,i} \cdot \xi_{\text{nerv},\sigma_{rt,i}}(t) \end{cases} \tag{2.49}$$

where the subscripts added to ξ_{nerv} indicate that a different nervousness factor is in principle determined for each variable, although in the present modelling $\xi_{\text{nerv},\sigma_{rf},i}(t) = \xi_{\text{nerv},\sigma_{rt},i}(t)$.

2.2.8 Behaviour on stairs

Stairs are a fundamental aspect of ship evacuation, as congestions typically appear at the entrances of stairways. An extension of the model is thus required in order to simulate evacuation on stairs. The fundamental characteristic of evacuation on stairs is the reduction of average pedestrian speed, compared to flat terrain, both in ascending and descending direction. With reference to the maritime field, MSC.1/Circ.1533 [147] provides values for the unimpeded speeds to be taken into account for people ascending and descending stairs when carrying out advanced evacuation analysis. An overview of the state of the art regarding modelling of human behaviour on stairs has been reported by Qu et al. [174], who also described a very detailed mathematical model, taking into account also stairs steps, to be used in the social force framework.

The model used herein for embedding pedestrian behaviours on stairs is more simplified compared to the one presented by Qu et al. [174], in order to reduce the computational time (in view of real-time applications) and to reduce the need for a too detailed geometrical modelling of the stairs. The present model takes into account the fact that the employed social force modelling is inherently based on a 2-D dynamical description of the agents' motion, while the change in vertical coordinate is taken into account as a purely geometrical constraint. Stairs, in particular, are modelled as inclined planes, i.e. without accounting for the detail of steps. Moreover, the geometrical constraint allows to uniquely link the speed parallel to the stairs plane with the projected speed on the planar 2-D domain.

In order to simulate the projected 2-D dynamics of the i-th agent, it is necessary to know the projected desired speed vector $\mathbf{v}_i^0$. However, the information which is available during the simulation when an agent is on a stair are the module $v_i^{03\text{d}}$ of the desired speed, parallel to the stair, and the projected 2-D unit vector $\hat{\mathbf{v}}_i^0$ of the desired direction. In order to determine $\mathbf{v}_i^0$, given the unit vector $\hat{\mathbf{n}}$ normal to the stairs plane, the vector $\mathbf{v}_i^{03\text{d}}$ can be firstly obtained as follows (see also Figure 2.10):

$$\begin{cases} \hat{\mathbf{v}}_i^{03\text{d}} = \dfrac{\hat{\mathbf{v}}_i^0 - \langle \hat{\mathbf{n}}, \hat{\mathbf{v}}_i^0 \rangle \cdot \hat{\mathbf{n}}}{\left\| \hat{\mathbf{v}}_i^0 - \langle \hat{\mathbf{n}}, \hat{\mathbf{v}}_i^0 \rangle \cdot \hat{\mathbf{n}} \right\|} \\ \mathbf{v}_i^{03\text{d}} = \hat{\mathbf{v}}_i^{03\text{d}} \cdot v_i^{03\text{d}} \end{cases} \tag{2.50}$$

afterwards, the 2-D desired speed vector $\mathbf{v}_i^0$ can be obtained by projecting $\mathbf{v}_i^{03\text{d}}$ onto the $xy-$plane, i.e.

$$\mathbf{v}_i^0 = \left(v_{ix}^{03\text{d}}, v_{iy}^{03\text{d}}, 0 \right) \tag{2.51}$$

Of course, the module of the two vectors are such that $\left\|\mathbf{v}_i^0\right\| \le \left\|\mathbf{v}_i^{03d}\right\|$ and this model assures that an agent having a 2-D desired speed v_i^0 reaches a speed v_i^{03d} along the stair.

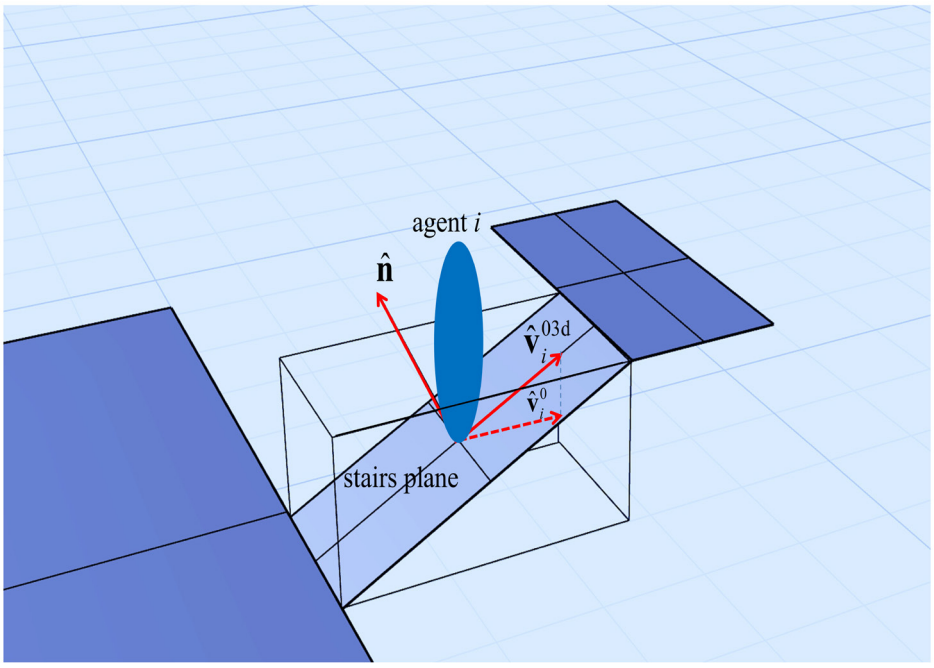

Figure 2.10: Representation of an agent on stairs, with indication of versors $\hat{\mathbf{n}}$, $\hat{\mathbf{v}}_i^0$ and $\hat{\mathbf{v}}_i^{03d}$.

The speed module v_i^{03d} is instantaneously determined on the basis of the angle γ which is formed by the unit vector $\hat{\mathbf{v}}_i^{03d}$ with respect to the horizontal plane. Letting the versor of the vertical axis be $\hat{\mathbf{z}}$, it is:

$$\sin(\gamma) = \left\langle \hat{\mathbf{v}}_i^{03d}, \hat{\mathbf{z}} \right\rangle \tag{2.52}$$

This model allows to define a continuous variation in time of the reference inclination angle γ when the agent moves, possibly in different directions, on the stairs. The function used for representing the dependence $v_i^{03d}(\gamma)$ is reported in Figure 7, together with an indication of the parameters characterising it. A positive value of γ indicates that the agent is moving upwards, conversely, a negative value of γ indicates a movement downwards. The model assumes that an unimpeded agent moves at a speed v_i^u equal to that on flat terrain whenever the inclination is sufficiently small, in the range $\gamma \in [-b_s, b_s]$. Similarly, the unimpeded agent speed is independent on the inclination angle, with reduced values $v_i^{u,\text{down}}$ and $v_i^{u,\text{up}}$ with respect to v_i^u, in the descending range $\gamma \in [-\theta_s - b_s, -\theta_s + b_s]$ and in the ascending range $\gamma \in [\theta_s - b_s, \theta_s + b_s]$, respectively. The speed is assumed to drop to zero when the inclination reaches $\theta_{s\max}$.

Intermediate values are obtained by linear interpolation based on $\sin(\gamma)$. The numerical values for the characterising parameters θ_s, b_s and $\theta_{s\max}$ are reported in Figure 2.11.

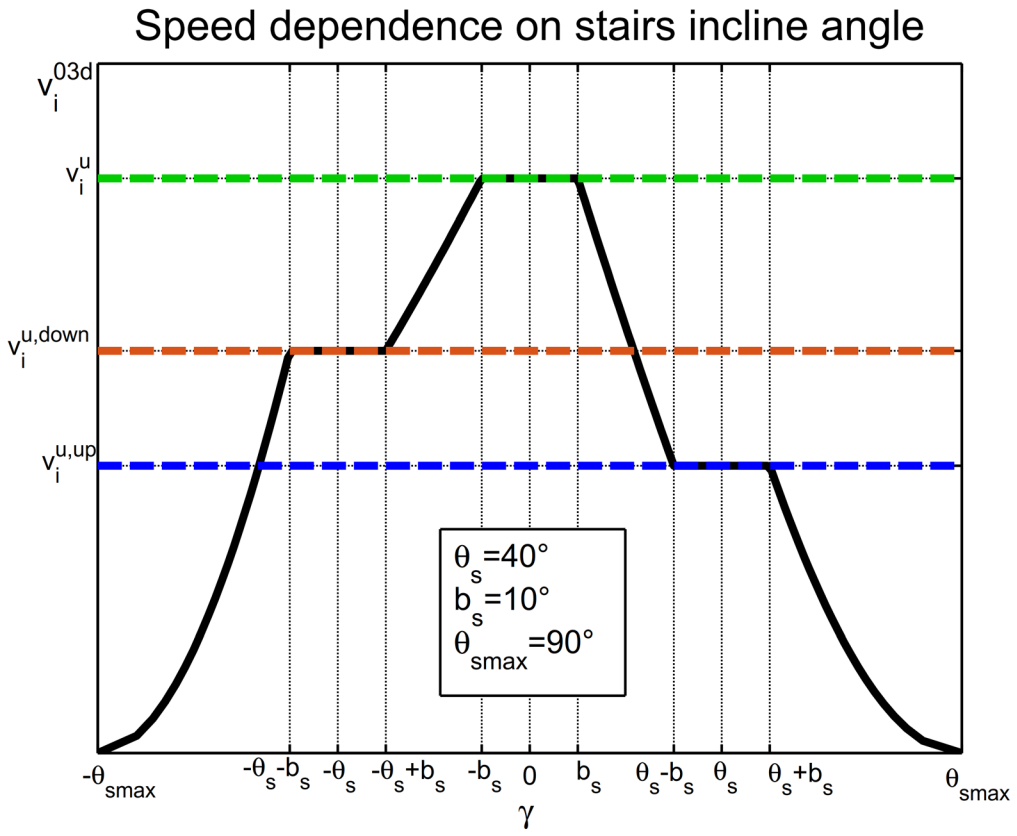

Figure 2.11: Model for the dependence of unimpeded speed v_i^{03d} on the stairs inclination angle γ.

The rationale for the choice of the model and of the parameters is as follows. The desired speed v_i^{03d} is set to the constant value corresponding to the unimpeded speed on flat terrain in the interval $\gamma \in [-10°, 10°]$ as it is reasonable that inclines lower than 10° do not affect the unimpeded speed. Then, specification regarding the speed to be achieved in ascending and descending direction is given in MSC.1/Circ.1533 [147]. In accordance to the International Code for Fire Safety System (FSS CODE, [52]) stairways should not have an incline angle greater than 45° and often the angle ranges from 30° to 45° (see, e.g., the validation data set from SAFEGUARD project ([186]). The parameters $\theta_s = 40°$ and $b_s = 10°$ have therefore been chosen considering these observations, leading to ranges $\gamma \in [-50°, -30°]$ (descending) and $\gamma \in [30°, 50°]$ (ascending). The unimpeded speed associated with these ranges of inclination values have therefore been chosen to correspond to the specifications from MSC.1/Circ.1533 [147], in order to guarantee consistency of simulations in typical layouts. Finally, the parameter $\theta_{s\max}$ was set to a maximum possible incline corresponding to 90°, although this was done only for robustness of the model.

The 3-dimensional extension of the model introduces also the problem of the interaction between agents placed at different vertical coordinates. While all the interaction forces are based on the projected 2-D geometry, the effect of the vertical distance d_{vert} between agents is introduced through a separate multiplicative factor $c_{\text{vert}}(d_{\text{vert}})$, which corrects agent-agent, counter-flow and wall-agent interaction forces and torques. The corrective multiplicative factor $c_{\text{vert}}(d_{\text{vert}})$ is described as follows:

$$c_{\text{vert}}\left(d_{\text{vert}}\right)=\begin{cases} 1 & \text{if } d_{\text{vert}} < d_{\min} \\ 0 & \text{if } d_{\text{vert}} > d_{\max} \\ \dfrac{d_{\max}-d_{\text{vert}}}{d_{\max}-d_{\min}} & \text{otherwise} \end{cases} \tag{2.53}$$

where $d_{\min}$ (m) determines the interval $[0, d_{\min}]$ which does not lead to any correction of the forces/torques, whereas $d_{\max}$ (m) determines the maximum vertical distance above which it is assumed there are no longer interactions. The vertical distance d_{vert} between agents is calculated considering the relative position of agents feet. The value of the characteristics parameters of the model were tentatively set to $d_{\min}=0.5\,m$ and $d_{\max}=1.5\,m$.

2.2.9 Routing

The whole model presented herein is based on the assumption that, at each time step, each agent has a preferred direction $\hat{\mathbf{v}}_i^0$ that ideally directs the agent to its desired target. The routing problem has herein been addressed by using waypoints and areas, with a logic which is conceptually similar to the one adopted in the tool Viswalk ([79], [173]).

The simulation space is considered to be divided into different areas. A specific facility, connecting two areas, is considered as a waypoint. Waypoints are used to model facilities like doors or intersections between corridors, while areas are used to model rooms and corridors. The whole map of possible paths can be therefore considered as a graph, where waypoints and areas are nodes and they are considered connected if they are adjacent. A path is therefore described as a list of areas and waypoints. Although in principle such path could be dynamically modified during the simulation, in the present implementation the agent's path is assigned at the beginning of the evacuation simulation.

The representation of waypoints as single target points, however, is not sufficient to correctly simulate the flow of people through a facility (for example in a bottleneck situation). Therefore waypoints are represented as convex polygonal regions having some of their sides marked as entrance/exit. An example illustration is depicted in Figure 2.12 (left), where an agent i is positioned in an area A and directed to a waypoint W. Since the left side l of the way point W is contained in the area A, we say that the area A is connected to W through l. When the side of the way point is

intended to represent the width of an exit/entrance, its length is set to the effective width, i.e. the clear width reduced by the need for sufficient clearance during the passage of people. Usually people make an estimation of the effective width of a facility when choosing their direction, taking into account the space occupied by their body. Therefore an estimation for the clearance can be based on a reasonable global upper bound for the agents radius $R_{\max}$, and the exit/entrance widths are set to the difference between the width of the facility and $2 \cdot R_{\max}$ (Figure 2.12). Moreover, it reasonable to consider that agents target a point that is not exactly on the facility, but it is instead placed inside the region they occupy and in front of the facility. For these reason hexagonal waypoints regions, as shown in Figure 2.12, have been adopted to represents doors/entrance/exits, while more general shapes can be used in more complex situations. In the typical case of a door, as reported in Figure 2.12, the target point of agent i will be the closest point on the segment l_{in}. The segment l_{in} is obtained by translating l, along its perpendicular, by a distance ε towards the inside of W. Conversely, the segment l_{out} is similarly obtained, but by a translation in the opposite direction, and it is used as target when an agent is inside the waypoint region W and is exiting from it.

The model presented so far does not contain an obstacle avoidance algorithm, since it is assumed that in each situation agents can proceed directly towards the next waypoint. However, in cases of complex geometries with obstacles, this might not be the case. To cope with such situations, a shortest path approach is used. To this end, a triangular mesh of the available area (with holes in correspondence to obstacles) is necessary in addition to the specification of the agent path. The perception of obstacles by the agents is based on three rays, with finite length L (which represent the assumed exploration region of the agent), that are cast starting from agents' arms, at half of the height of the agent, parallel to their desired direction $\hat{\mathbf{v}}_i^0$ (see Figure 2.13). Three rays are used in the algorithm in order to balance the computational effort and the capability of identifying obstacles which are small or which may have complex shapes. In case any of these rays encounters an obstacle, a shortest path algorithm, based on an implementation of the A* algorithm Hart et al. [68], is triggered. The approximate shortest path obtained by connecting the centres of the mesh triangles is subsequently processed with the funnel algorithm, according to the A* Pathfinding Project (Granberg [62]).

Numerical values of the parameters used for the routing model are reported in Table 2.9.

Table 2.9: Parameters of routing model, and corresponding values.

$R_{\max}$	L	ε
0.3 m	3.0 m	0.1 m

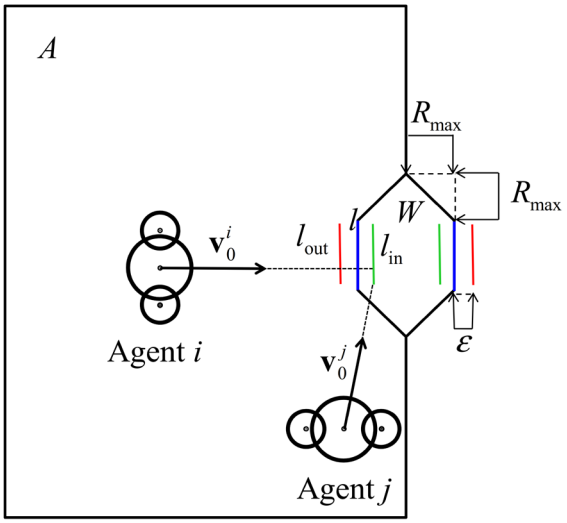

Figure 2.12: Example of routing by means of a waypoint.

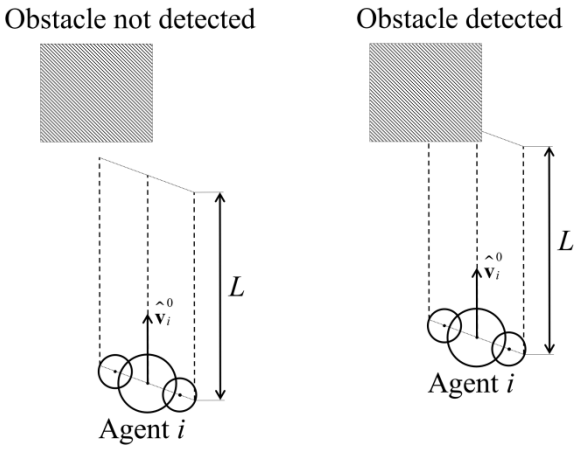

Figure 2.13: Obstacle detection by finite length ray-casting as used for triggering the path-finding algorithm based on shortest path.

It should be highlighted that at the present stage of development, the software does not implement a complex internal logic for the dynamic choice of waypoints by the agents. The choice of waypoint is not influenced by behaviours such as herding as, for example, in case of the model presented by Helbing et al. [73], by grouping or by communication between agents ([229]) and it is not the solution resulting from an optimization problem as in the model presented by Khalid and Yusof [105].

Each agent chooses the waypoint in accordance to its known pre-defined path. There is also the possibility to set a default waypoint for a region. When the agent is in a region for which it has not a specified next waypoint, if the default waypoint of the region the agent is inside has been specified the agent will be directed towards the default waypoint. Instead, if the default waypoint was not specified, the closest waypoint among all waypoints connected to that region is chosen, at the condition that the closest waypoint is not the last one visited before entering the current area, if so the agent choses the second closest waypoint and so on. The present logic, although quite simple,

allows considering also situations were agents are pushed inside regions for which they do not have specified waypoints.

2.2.10 Contacts and collisions

Helbing and Molnar [71] and Korhonen [112] model agent-agent and agent-wall collisions through a force-based spring-damper approach. However, this approach can create numerical integration problems, leading to the need for very small integration time steps, which is problematic in case the target is a real-time simulation. In the model presented herein, collisions are instead resolved by the physics engine integrated in the chosen development environment (PhysX [160]). The physics engine addresses collisions by a direct modification of rigid bodies velocities, and the approach is quite robust also when using relatively large simulation steps. The collision model requires two parameters: the elastic restitution coefficient, that determines the speed after the collision from the speed before the collision, and the friction coefficient for the underlying Coulomb friction model.
Performed simple experiment with the physics engine showed that the modelling of collisions is described by the following equations

$$\begin{aligned} & m_1 \cdot \mathbf{v}_1^i + m_2 \cdot \mathbf{v}_2^i = m_1 \cdot \mathbf{v}_1^j + m_2 \cdot \mathbf{v}_2^f \\ & \left(\frac{1}{2} m_1 \cdot \left(\left\| \mathbf{v}_1^i \right\| \right)^2 + \frac{1}{2} m_1 \cdot \left(\left\| \mathbf{v}_2^i \right\| \right)^2 \right) \cdot k_r{}^2 = \frac{1}{2} m_1 \cdot \left(\left\| \mathbf{v}_1^f \right\| \right)^2 + \frac{1}{2} m_2 \cdot \left(\left\| \mathbf{v}_2^f \right\| \right)^2 \end{aligned} \tag{2.54}$$

where m_1 and m_2 are two masses moving one against the other with speeds $\mathbf{v}_i^2$ and $\mathbf{v}_i^2$, k is the elastic restitution coefficient and $\mathbf{v}_1^f$ and $\mathbf{v}_2^f$ are the speeds of the two masses after the collision.
The elastic restitution coefficient κ_r was calculated in order to tune results from present simulation to those which can be obtained from the spring-damper model of FDS+Evac ([112]) considering the archetypal situation of an agent before and after colliding with a wall.

In FDS+Evac model the collisions are modelled through a force-based spring-damper approachwhere a force is hence applied to each colliding mass. The collision force f_{ij}^c is described by the following equation:

$$\begin{aligned} & f_{ij}^c = \left(k_{ij} \cdot \left(d_{ij} - r_{ij} \right) + c_d \cdot \Delta v_{ij}^n \right) \cdot \mathbf{n}_{ij} + \kappa_{ij} \cdot \left(d_{ij} - r_{ij} \right) \cdot \Delta v_{ij}^t \cdot \mathbf{t}_{ij} \\ & f_{ij}^c = 0 \text{ if } d_{ij} - r_{ij} > 0 \end{aligned} \tag{2.55}$$

where $\mathbf{n}_{ij}$ and $\mathbf{t}_{ij}$ are, respectively, the direction from agent i to agent j and the versor perpendicular to this direction. The term d_{ij} is the distance between the two agents centres and r_{ij} is the sum of the two agents radii: when $d_{ij} - r_{ij} < 0$ the two agents volumes intersect and a contact is detected. The first term of f_{ij}^c models the normal force during the collision whereas the second term models the friction. The parameters

of the FDS+Evac model are $k_{ij} = 12 \cdot 10^4$ kg s^{-2} , $\kappa_{ij} = 4 \cdot 10^4$ kg s^{-1} m^{-1} and $c_d = 500$ kg s^{-1}.

The condition of a single agent of mass m_i [kg] colliding with a wall while having a speed v_i is then described by the following Cauchy problem (see also Figure 2.13):

$$\begin{cases} \ddot{x}(t) \cdot m_i + C_d \cdot \dot{x}(t) + k_i \cdot x(t) = 0; \\ x(0) = 0; \\ \dot{x}(0) = v_i \end{cases} \tag{2.56}$$

were $x(t)$ is the position of the agent at the instant t [s] and $t = 0$ [s] is the instant the agent enters in contact with the wall.

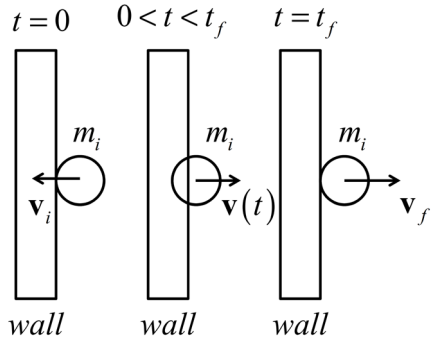

Figure 2.14: Representation of the situation described in equation (2.56).

The solution of the Cauchy problem is given by the following equation:

$$\begin{aligned} x(t) &= e^{-A \cdot t} \cdot \left(\frac{v_i}{\omega} \cdot \sin(\omega \cdot t) \right) \\ \dot{x}(t) &= -A \cdot e^{-A \cdot t} \cdot \left(\frac{v_i}{\omega} \cdot \sin(\omega \cdot t) \right) - e^{-A \cdot t} \cdot \left(v_i \cdot \cos(\omega \cdot t) \right) \\ A &= C_d / (2 \cdot m_i) \\ \omega &= \sqrt{\frac{k_i}{m_i} - A^2} \end{aligned} \tag{2.57}$$

Thus $x(t) = 0$ only if $t = 0$ (initial condition) or $t = \pi / \omega = t_f$ .The coefficient of restitution can thus be calculated as:

$$k = v_f / v_i = e^{A \cdot \pi / \omega} \tag{2.58}$$

Considering the equation (2.58) a value $\kappa_r = 0.8$ was eventually set by considering an agent of mass 75 kg which correspond to the typical human mass used in ship stability calculations, and approximating to the first decimal.

The difference between the adopted model and the model implemented in FDS+Evac made impossible to tune the friction coefficient parameter with FDS+Evac. However, the friction coefficient was set to 0.2 as this parameter is used by Löhner [127] where a Coulomb friction model is implemented.

The collision detection and resolution model is a useful functionality already embedded in the chosen development environment that was adopted in the implementation of the model. Other functionalities embedded in the chosen environment and adopted for the implementation will be presented in the Chapter 5 that will follow.

2.3 Implementation of the model in the chosen development environment

The model was implemented using the game engine Unity3D ([217]) as the reference framework development environment. The choice was mainly influenced by the need of a straight and easy introduction of first person view and human interaction, which are features that will be presented in detail in the next chapters describing the implementation of the user interaction.

In addition, the development environment offered some useful functionalities also concerning the implementation and the calibration of the mathematical model:

- The integration of the rigid-body equations of motions as well as the addressing of contacts can leverage on the integrated physics engine PhysX (PhysX [160]). Moreover the physics engine offers an optimized ray-casting algorithm that has been used to prevent agents from interacting when separated by walls, decks, landings, stairs etc.
- The environment allows a direct importing and straightforward rendering of geometries described by generic 3D meshes.
- Within the development environment, the on-going simulation can be visualized in real-time, with the possibility to visualize and modify the simulation parameter on the fly.
- The deployed application can be run in batch-mode. Batch mode can be much faster than real-time, with the increase of speed depending on hardware, complexity of geometry and number of agents. This feature is relevant for typical design purposes, when, usually, human participation is not required.

However, during the development, some limitations associated with the choice of using a game engine environment have also been encountered, which can be summarised as follows:

- The physics engine uses single precision arithmetic to enhance performance. Due to single precision even deterministic simulation loose determinism when ran on different platforms. Although results are qualitatively the same, cross-platform determinism is not guaranteed. However, simulation outputs are inherently stochastic (due to the aleatory uncertainty of the problem) and simulation results must be analysed in the ensemble domain. For this reason, even if two platforms provide different results for the same simulation input (for a fixed random seed value associated to the generation of random effects), the outputs deriving from Monte Carlo simulations and analysed in the ensemble domain are statistically equivalent.

- The collision model implemented in PhysX ([160]) is not really suited for treating very high density situations, where many collisions occur at the same time and agents are almost constantly in contact with each other. The force-based spring-damper approach used by Helbing et al. [73] could be more indicated for these situations, but it would require a significant decrease of the integration time step, and this may become problematic when the target are real-time simulations, as in the case of the present research. Such situations of high density are also difficult to be reproduced through virtual reality, due to the lack of contacts perceptions ([171]). However, the contact model in the chosen development environment was considered to be appropriate for the purpose of the study reported herein, which addresses simulated and experimental conditions characterised by sufficiently calm egress where contacts are occasional and not continuous. Moreover, such an orderly evacuation condition is also the typical situation addressed from a design perspective.

It is finally important to underline that the reported limitations, although worth to be highlighted, have not prevented an effective and fully functional implementation of the model within the Unity3D ([217]) environment, as it will be described in the following chapters.

2.4 Final remarks

The present chapter in its first section offered a review on evacuation modelling techniques and on evacuation tools available for the evacuation analysis.

An evacuation model developed with the specific target of introducing the possibility of real time human participation in the evacuation process is presented in a very detailed way specifying all the model parameters in the second section.

Finally the implementation of the developed model in the adopted development environment was discussed highlighting benefits and limitations.

This page is intentionally left blank

3 TUNING OF COUNTERFLOW MODEL

The condition of counterflow occurs when two people having opposite direction use the same facility (e.g. corridor). Experiments performed to analyse human behaviour in counterflow showed that human in the counterflow condition modify their behaviour in order to increase the flow rate.

The present chapter will address this topic in detail with a review of several counterflow models. Subsequently, the counterflow model developed specifically for the target of the present study will be described. Finally the calibration and sensitivity analysis of some of the parameters of the model will be reported.

3.1 Introduction

In evacuation simulations, evacuees are usually directed towards the same exit(s). It is, thus, typical that close agents move in the same direction towards the same target. Situations where agents have different or opposite targets are more complex and, often, not considered. However, these situations might occur during the evacuation process. In the maritime field this might be due to the fact that the crew needs to reach some specific area during the evacuation, as highlighted in MSC.1/Circ.1533 [147], while passengers move in the opposite direction. In order to obtain reliable data from evacuation simulations, it is, thus, of utmost importance to correctly model human behaviour in this type of situations.

A situation where two groups of people are directed towards opposite targets and need to use the same facility (corridor/exit), can be defined as a counterflow situation. Agent-based models can simulate counterflow situations quite easily, by simply setting different targets for each group of agents. However, human behaviour is modified in counterflow condition compared to conditions where people move in the same, or in

similar, directions. Zhang et al. [236], as an example, observe that humans tend to modify their trajectory and to assume organized patterns when they are in counterflow conditions. The increase of organization has the effect improving the flow rate.

For these reasons many agent-based models need a counterflow sub-model in order to correctly simulate counterflow situations. The problem of modelling human behaviour in counterflow has been addressed in different ways in literature, depending on the specific underlying evacuation model, as it will be described hereinafter in the sections 3.1.1 3.1.2 of this chapter.

The definition of a counterflow model can be divided in the two following fundamental steps:

1. **Definition of the counterflow condition related to the considered model**. Although the concept of counterflow seems very intuitive and thus it seems not to require a specific definition, it is observed that, especially in models allowing an infinite set of possible directions for agents, the introduction of a proper definition for the identification of a condition as a counterflow situation is fundamental.

   The counterflow condition, in agent-based models, is always defined referring to one single agent. Considering an agent i and another agent j, the counterflow condition is a statement $P_i\left(f_j^1,...,f_j^n\right)$ "agent j is in counterflow with respect to agent i" where $f_j^k\ (k=1,...,n)$ is a property of agent j. The agent j is considered to be in counterflow with respect to the agent i if and only if $P_i\left(f_j^1,...,f_j^n\right)$ is true. Typical quantities considered to determine the counterflow condition are:

   - The position of agent j.
   - The distance between the two agents.
   - The direction of velocity for agent j (instantaneous velocity and/or desired velocity).

   A representative example of counterflow condition is provided by the following statement:

   $$j \text{ is in counterflow with } i \Leftrightarrow \left\langle \mathbf{v}_i, \mathbf{v}_j \right\rangle < 0 \tag{3.1}$$

   were $\mathbf{v}_i$ and $\mathbf{v}_j$ are, respectively, the speeds of agent i and agent j and $\langle \cdot,\cdot \rangle$ indicates the scalar product.

2. **Modifications in the behaviour of the agent**. After the counterflow is formally defined, the modification in the behaviour of the agent i in case of detection of one or more counterflow agents should also be defined. The modifications in the behaviour of an agent in presence of one or more agents in counterflow

condition might be modelled by considering each counterflow agent singularly, or, alternatively, by globally considering the whole set of counterflow interactions.

The reported two-step definition will be adopted, in the following sections, to describe and compare several counterflow models available in literature.

3.1.1 Counterflow in discrete models

The complexity of the counterflow condition is reduced in discrete models, due to the fact that only a finite set of possible directions is possible. However, the literature concerning the simulation of counterflow cellular automata models (CA), a particular branch of discrete models, is very rich. Indeed, in spite of their simplicity, Cellular Automata (CA) models are capable of reproducing the main characteristic of the counterflow phenomena. Moreover, many of the approaches adopted for cellular automata have their counterpart in continuous counterflow models.

There are different CA models which, although not directly implementing a counterflow model, they still manage to reproduce, to some extent, counterflow phenomena.
This is the case of the cellular automata model presented by Weng [225]. This model behaves well in low density conditions (density lower than $0.94\ p/m^2$), showing the capability to reproduce correctly the lane formation. In conditions of higher density (density higher than $2.5\ p/m^2$), however, the agents stop in a situation of impasse. The impasse condition occurring in crowd dynamics when the density reaches values so high that the movement of each pedestrian is blocked is called jamming transition. The jamming transition phenomenon is a studied and known phenomenon in high density counterflow condition ([153]; [208]). The occurrence of jamming at a specific high density condition is considered, therefore, a normal behavior of a counterflow model. However, Isobe et al. [89], report experimental outcomes showing that jamming transition does not occur for density values even higher than $2.5\ p/m^2$, differently from the outcomes of the simulations reported by Weng [225]. The model presented by Weng [225], therefore, allows to effectively reproduce low density condition but fails in reproducing correctly conditions with density close to $2.5\ p/m^2$.

An important limitation of CA models is indeed the impossibility of reproducing situations of arbitrary high density, due to the fact that the maximum possible density is set *a priori* and depends on the discretization of the mesh space.

Feliciani and Nishinari [46] propose an interesting CA model where the aforementioned problem concerning density is resolved by the introduction of two important novelties with respect to the CA model presented by Weng [225]:

- Agents are allowed to access to a sub-grid (finer than the standard one) in case all the avaliable directions are occupied. This has the effect of reducing the occurrence of impasse situations by allowing more than one agent to occupy the same cell. The side effect of this modification is the increase of the local density.
- When two agents with opposite directions are in adjacent cells and facing each other they have some probability of exchanging position. This rule also reduces

the occurrence of impasse situations. Moreover it prevents the density from increasing to unnatural values due to the previous rule.

Although no results have been presented by Feliciani and Nishinari [46] concerning the formation of lanes, the model is shown to correctly reproduce some experimental data concerning the flow in counterflow conditions. In the model presented by Feliciani and Nishinari [46], however, only adjacent agents enter in counterflow. This behaviour might seem unnatural as, usually, people adopt a relatively long range counterflow strategy to avoid incoming obstacles as observed both by Montecchiari et al. [141]and by Kretz et al. [116].

A long range strategy is developed by Isobe et al. [89] who add a specific counterflow model to a pre-existing lattice gas CA model. The model is developed with the target of reproducing an experiment concerning a simple counterflow condition in a corridor condition. The population of the experiment was divided in two groups: one starting from the left half of the corridor and moving towards the right end of the corridor, and the other, starting from the right half and moving towards the left end of the corridor.
Although the aforementioned counterflow situation, reported by Isobe et al. [89] is a very simple one, it represents an archetypal situation of counterflow which allows to analyze the main characterics of this phenomenon. Moreover the model described by Isobe et al. [89] shows many features which are present also in continuous models and it is, thus, worth to be presented more in some detail in the following.

The assignment of the initial position and of the desired direction divides the population in two classes: “right walkers” (agents moving from left to right) and “left walkers” (agents moving from right to left). The counterflow condition is hence defined by simply considering these two classes: the agent j is considered in counterflow with respect to agent i if agent j is positioned in the front region of agent i, as shown in Figure 3.1, and the classes of agents i and j are different.

In this CA model the agents move at each time step to the adjacent cell. The next cell is determined by the assignment of a probability to each of the four possible directions (forwards, backwards, left and right). The attitude of each agent to follow agents going in the same direction and to avoid counterflow agents is expressed with a modification of the probability associated to each possible agent direction. The area in front of the agent is divided in three partially overlapping sectors: a central sector ($S_{i,0}$), a left sector ($S_{i,1}$) and a right sector ($S_{i,2}$), as shown in Figure 3.1. Each sector corresponds to the three possible direction the agent might take $\mathbf{u}_{i,0}$ (forward), $\mathbf{u}_{i,1}$ (left), $\mathbf{u}_{i,2}$ (right). The function associating the probability to each direction at each time step is modified with respect to the model without counterflow so that the probability of choosing the direction $\mathbf{u}_{i,k}$ grows proportionally in accordance with the number of non-counterflow agents contained in the corresponding sector $S_{i,k}$.

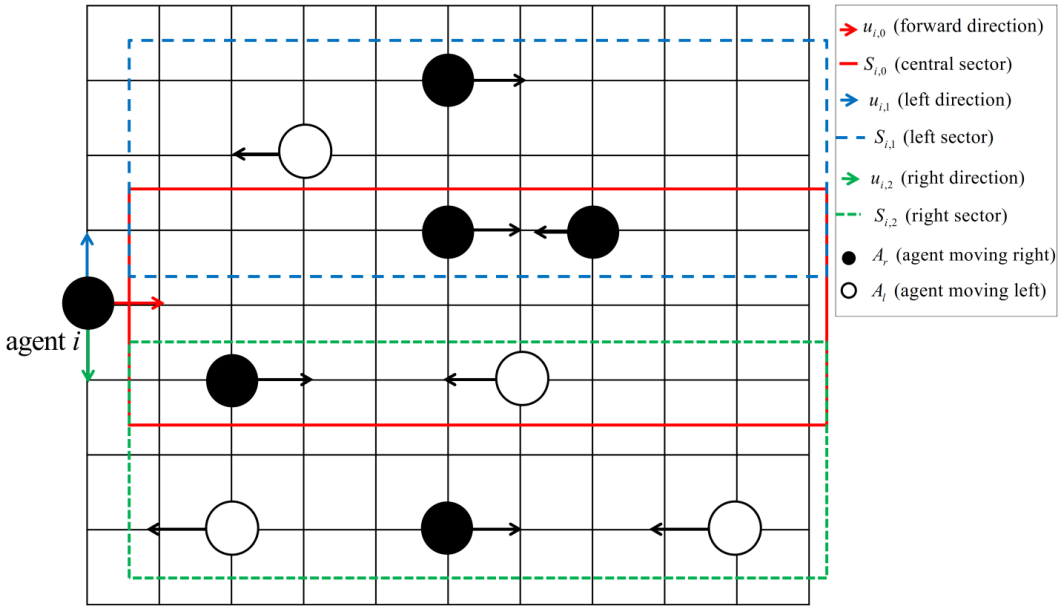

Figure 3.1: Scheme for the description of the counterflow model by Isobe et al. [89].

The distance between the agents is not considered for the determination of the counterflow condition, hence all agents with opposite direction placed in front of agent i are considered to be in counterflow. However, it is reasonable to think that in high density conditions, people would try to avoid only close and visible subjects coming in opposite direction while not considering subjects which are too far away to be not visible. Nevertheless the model by Isobe et al. [89], however, is shown to obtain a reasonable agreement (qualitative and quantitative) with the simple experimental case described in their paper.

The models is perfectly symmetrical, namely *a priori* the agent has the same probability of choosing the right or the left direction. However, as observed by Yang et al. [230] in many cultures the attitude of keeping one precise direction (right or left) is very eradicated and might affect the crowd behaviour in the counterflow condition.

The model presented by Yang et al. [230] depicts the aforementioned attitude of maintaining a preferred direction. Yang et al. [230] observes that in many cultures there is a preferred direction in counterflow conditions.
The study by Yang et al. [230] shows that the introduction of right preference in the model allows obtaining a better agreement with experimental outcomes by slightly increasing the flow rate in simulations compared to a model without direction preference. This result suggests that the right preference is an important feature and thus needs to be reproduced to obtain reliable counterflow models.

The model proposed by Ha et al. [65] adopts the approach based on the three sectors already used by Isobe et al. [89], while introducing also the concept of the interaction radius. In this case, to define the counterflow condition, the distance between agents is also considered. In particular, the agent i can be considered in counterflow with agent j only if their distance is less than the interaction radius. The model developed by Ha et al. [65] might be considered the most complete among the presented CA

counterflow models and indeed it was adopted to model evacuation from complex ship geometries ([167]).

When a complex geometry and wide geometry is implemented, as it is in the case reported by Ha et al. [65], it is fundamental that agents interact only with other visible and relatively close agents. Indeed, as an example, a situation where the behaviour of agents towards the stem of the vessel is affected by agents towards the stern of the vessel would be very unrealistic. Due to this reason a maximum radius determining the region of interactions surrounding each agent is surely necessary. The function of the interaction radius is to reduce the interaction to only close agents and to allow the model to produce reasonably realistic results also in case of wide geometries such as the ones concerning cruise vessels.

3.1.2 Counterflow in continuous models

The determination of the counterflow condition is more complex in models where the space is continuous due to the fact that a continuous set of possible direction for each agent is available in these models.

However not all continuous models have a dedicated counterflow sub-model and provide explicitly the definition of counterflow. The counterflow behaviour, in some continuous models, emerges from sub-models modelling more generic behaviours such as obstacle avoidance or steering.

This is the case of continuous non-force based models, where the counterflow behaviour is often associated to the steering behaviour and to the obstacle avoidance. As a result, these kinds of models rarely have a specific counterflow sub-model. This is the case of, e.g., Ginnis et al. [57], which addresses counterflow through the obstacle avoidance and steering behaviour. The presence of a dedicated counterflow model has however a great impact over simulation outcomes. Considering for example the condition with highest number of counterflow agents in of the IMO test 8 (counterflow in a corridor connecting two rooms), the exit time resulting from Ginnis et al. [57], and the model of Ha et al. [65] are very different: 426 s are obtained by VELOS ([57]) while 216 s are obtained by the cellular automata model presented by Ha et al. [65]. It is particularly evident that the exit time is often larger in models not implementing a specific counterflow model. This is further proven by the results presented in the following, showing that FDS+Evac and the model developed in this study, which are both implementing dedicated counterflow models, lead to results which are closer to the model developed by Ha et al. [65] than to those obtained by Ginnis et al. [57].

The presence of a dedicated counterflow sub-model is, instead, very common in social force models. This is due to the characteristic of obstacle avoidance sub-model which is based usually on repulsive forces. As a result when two counterflow agents meet, they seem to bounce one onto the other instead of avoiding each other as it would seem natural, as observed by Smith et al. [204]. An additional sub-model is, thus, often required to obtain natural behaviours also in counterflow conditions. Several counterflow models have thus been proposed as enhancement of force-based models. In case of force-based models, the definition of counterflow is more complex than for CA models. This is due to the fact that agents move in a continuous domain.

Two possible different approaches can be identified when describing the modification of the agent behaviour in counterflow condition:

- The desired speed of the agent is modified.
- An additional counterflow-force is applied to the agent.

With the intention of providing examples of different approaches, some representative counterflow models are summarized and compared in the following, highlighting, for each of them, the definition of the counterflow condition and the modification of the behaviour of agents in counterflow.

Pelechano et al [168] defines the counterflow condition considering the instantaneous speed direction: the counterflow is detected when the instantaneous speed are one the opposite of the other, namely $\langle v_i, v_j \rangle < 0$. In analogy with the model developed by Ha et al. [65], also in this case, an interaction area for the counterflow is defined. However, in the model by Pelechano et al [168] the interaction area has the shape of a rectangle placed in front of the agent. The length of the sides of the rectangle parallel to the agent direction vector vary from 1.5 m to 3 m in relation to the number of agents inside the interaction region (perceived density) while the perpendicular sides to the direction vector are 1 m long. The counterflow model by Pelechano et al [168] is embedded in the collision avoidance model and modelled as an additional force. In particular, a lateral force component is added when agent i is placed in front of agent j. When a counterflow is detected, the lateral force is increased, otherwise a weak lateral force is applied anyways to model the overcoming behaviour. This model considers interactions with each agent separately, with a final summing up of all contributions. The right preference is also embedded in the model and the parameter responsible for the right preference is modified in accordance to the local density. The model presented by Pelechano et al [168] aims to qualitatively reproduce crowd behaviours for application in computer graphics. For this reason, no detailed quantitative validation with real experimental data was carried out for this model.

Another model which considers counterflow interaction by separately accounting for each agent in counterflow is presented by Smith et al. [204]. This model however does not apply additional forces to the agents. Instead, it directly modifies the desired velocity vector: an additional speed component, depending on the relative agents position and relative agents speed is added to the original desired velocity. In this case the counterflow condition is defined by referring to the instantaneous speed and considering as maximum interaction distance the same distance adopted for the repulsive forces which is shorter than 1 m. However, it is proven that the counterflow interaction is often long range as observed before, therefore this modelling choice allows to obtain reliable results only in conditions or relatively high density where the visibility radius is very reduced.

In order to allow the model to reproduce realistic behaviours also in low density conditions where counterflow agents at some meters of distance are visible, the interaction radius needs to be augmented.
The interaction radius is surely longer (a maximum of 3 m) in the model proposed by Heliövaara et al. [76] with respect to the one adopted by Smith et al. [204]. The model

by Heliövaara et al. [76] still modifies the desired velocity of the agent as in case of the model by Smith et al. [204]. However, in the model by Heliövaara et al. [76] the modification of the desired velocity does not results from the sum of the contributions originated by the agent-agent interactions considered one by one. Moreover, differently from Smith et al. [204], for the identification of a conterflow condition, the model by Heliövaara et al. [76] considers the desired velocity instead of the instantaneous velocity. Finally compared to Smith et al. [204], the model by Heliövaara et al. [76] is definitely characterised by an increased complexity and by larger number of parameters.

Figure 3.2 show a main reference scheme for the description of the counterflow model presented by Heliövaara et al. [76]. The same notation already used for the model developed by Isobe et al. [89] is adopted in Figure 3.2 and in the following description, in order to highlight the analogies between those two models. According to the model developed by Heliövaara et al. [76], the agent j is in counterflow with agent i if the desired velocity v_i^0 of agent i is opposed with respect to the desired velocity v_j^0 of agent j (i.e. $\langle v_i^0, v_j^0 \rangle < 0$) and agent j is contained in a counterflow area defined in front of agent i (see Figure 3.2). This model, therefore, defines a counterflow condition by explicitly analysing the velocity vectors of agents, as well as the distance between agents.

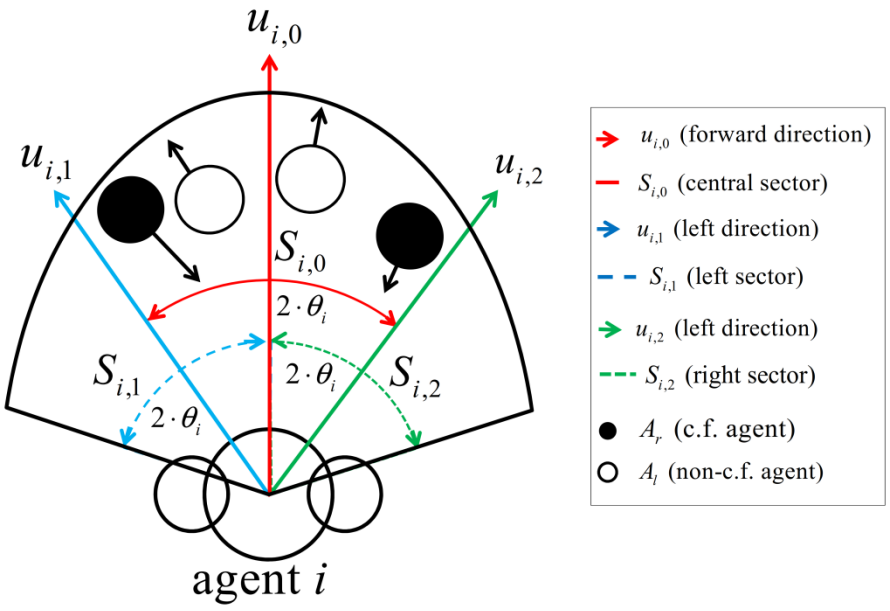

Figure 3.2: Scheme for the description of the counterflow model by Heliövaara et al. [76].

With reference to Figure 3.2, the agents in the area in front of agent i are thus divided in two classes: agents in counterflow with respect to agent i (class $A_{i,\mathrm{cf}}$), and agents going in the same direction as agent i (class $A_{i,\mathrm{ncf}}$). The area considered for the counterflow has approximately the shape of an ellipse with maximum axis of length 3 m and shorter axis of length 1.5 m. As indicated in Figure 3.2, the angular extent of the counterflow region depends on an angle θ_i which varies from 40° to 45° accordingly to

the agent speed. The same angle parameter also controls the extents of the sectors $S_{i,0}$, $S_{i,1}, S_{i,2}$ (central, left and right).
The desired speed of the agent i is then modified considering all the agents in the counterflow area by choosing between three directions: one central corresponding to the desired velocity when no counterflow was applied ($\mathbf{u}_{i,0}$ - forward), one rotated clock-wise ($\mathbf{u}_{i,1}$ - left) by the angle θ_i, and the other rotated counter-clockwise ($\mathbf{u}_{i,2}$ - right) by the angle θ_i (see Figure 3.2).

The three possible directions correspond to the three overlapping sectors $S_{i,0}, S_{i,1}, S_{i,2}$ (central, left and right) in which the area in front of the agent is divided. This counterflow sub-model, hence, somehow resembles, in a continuous framework, the model proposed by Isobe et al. [89], preserving the finiteness of the set of possible desired directions, despite the space continuity used for the main (containing) model.

The desired direction, in case of the model by Heliövaara et al. [76], is chosen between the three possible directions $\mathbf{u}_{i,k}\ (k=0,1,2)$ by maximing an objective function $f_i^{\mathrm{cf}}(k)$ which depends on the index of the sector:

$$\mathbf{v}_i^0 = \mathbf{u}_{i,\bar{k}} : f_i^{\mathrm{cf}}(\bar{k}) = \max_{k\in\{1,2,3\}} f_i^{\mathrm{cf}}(k) \tag{3.2}$$

The value of $f_i^{\mathrm{cf}}(k)$ depends only on the agents contained in the sector $S_{i,k}$: it increases with the number of agents going in the same direction and it decreases with the number of agents in counterflow. The function to be maximized is reported below:

$$\begin{aligned} f_i^{\mathrm{cf}}(k) = & \sum_{\{j:\text{agent } j \text{ is inside } S_{i,k}\}\cap A_{i,\mathrm{cf}}} \frac{c_{df} + d_{df}\cdot\langle \mathbf{v}_j - \mathbf{v}_i, \mathbf{u}_{i,k}\rangle}{\max(0.2, D_{ij})} + \\ & - \sum_{\{j:\text{agent } j \text{ is inside } S_{i,k}\}\cap A_{i,\mathrm{ncf}}} \frac{c_{df} + d_{df}\cdot\langle \mathbf{v}_j, \mathbf{u}_{i,k}\rangle}{\max(0.2, D_{ij})} + \\ & + c_{v_0}(\delta_{k\neq 0} - \delta_{k\neq 0}) + |c_{v_0}|\cdot v_i\cdot\delta_{k=0} + N_0(c_{ncf} + d_{v_0} v_i)\delta_{k=0}\delta_{N_0^{cf}=0} \end{aligned} \tag{3.3}$$

k is the index identifying the sector $S_{i,k}$ ($k\in\{0,1,2\}$) and the correspondent direction $\mathbf{u}_{i,k}$, D_{ij} is the skin-to-skin distance between the agents, $\mathbf{v}_j$ and $\mathbf{v}_i$ are the instantaneous velocity vectors of the agents, $N_0^{\mathrm{cf}} = |\{j : j \text{ is inside } S_{i,0}\}|$ is the number of agent inside the central sector and $N_0^{\mathrm{cf}} = |\{j : j \text{ is inside } S_{i,0}\}\cap A_{i,\mathrm{cf}}|$ is the number of agents in counterflow in the central sector. The function δ_p, where p is a statement, is 1 if p is true and 0 otherwise. The parameter of the function are c_{df}, d_{df}, c_{v_0}, c_{ncf}. The parameter c_{v_0}, in particular, is used to model the preference with respect to one direction following Yang et al. [230] observations. In particular, the right direction is

preferred if $c_{v_0} > 0$. The parameter c_{ncf} is, instead, used to model the attitude of the agent to maintain its initial desired direction in case no counterflow agents are detected. The parameter assures that if no agent is contained in the central region $S_{i,0}$ then the agent does not modify its direction.

A series of modifications of the basic model parameters are also defined by Heliövaara et al. [76] in condition of strong counterflow:

- The repulsive interaction force between agents is reduced.
- The repulsive interaction force between agents and walls is reduced.
- The motive force is increased.

Although these modifications will not be described in detail herein, it can be observed that the counterflow sub-model developed by Heliövaara et al. [76] affects nearly all the other sub-models (agent-agent interaction, wall-agent interaction, motive force).

The model presented by Heliövaara et al. [76] has been validated through different comparisons with experimental data, comprising those provided by Isobe et al. [89], and implemented in the software FDS+Evac (see Korhonen [112]). The counterflow model by Heliövaara et al. [76] represents the most extensively validated counterflow model among those presented herein.

However, in the model by Heliövaara et al. [76], the determination of the counterflow condition is based on a property that is in principle not measurable in a true physical situation: the desired direction of the interacting agents. The definition of counterflow condition based on the desired direction is more robust with respect to one based on the instantaneous velocity, as instantaneous velocity might fluctuate around zero in situations of high density, triggering the counterflow on and off. However it might be argued that while agent i is allowed to know its desired speed (each agent has full access to its own status and properties), it is not allowed, in principle, to know agent j desired speed. The counterflow condition of one agent j with respect to another agent i, should, instead, be estimated from observable quantities related to agent j such as its velocity, orientation and position.

As previousely observed in Chapter 2, the counterflow model proposed herein, differently from Heliövaara et al. [76], considers only observable quantities to provide the definition of the counterflow condition, decision which allows a more consistent implementation of human interaction.

3.1.3 Calibration and validation of counterflow models

Due to its complexity a counterflow model needs to be carefully calibrated and validated through experimental results. The comparison with experimental data might be carried out in qualitative manner, by observing that the model is able to reproduce the main feature characterizing the behaviour in counterflow condition, or qualitatively.

However very few results concerning controlled experiments specifically depicting counterflow conditions are available in literature ([236], [116], Isobe et al. [89]).

Although, as observed by Feliciani and Nishinari [46], experimental results with large number of people would in principle be necessary to properly validate an evacuation simulation tool, it is yet reasonable to assume that the behaviours observed in experiments with a reduced number of people can be considered to be representative and/or driving also behaviours observed at larger scale. As a result, it is possible to consider that, in general, also small scale experiments can still be useful to validate and/or tune simulation models which will eventually be used for simulations at larger scales.
The experiments performed on counterflow described in literature allow the identification of some features which seem to be common to all counterflow conditions. Those features might be adopted, for this reason, for a qualitative validation of counterflow models and are summarized below:

- The presence of people going in counterflow reduces the flow and increases the exit time.
- The exit time increases with the number of counterflow people.
- Lane formation. In counterflow condition people have the tendency to organize in lanes to maximize the flow.
- Right/Left preference. A preferred direction is often present in counterflow condition and this might be due to a cultural factor.

A quantitative comparison with experimental data is more difficult than the qualitative comparison, as experimental data are affected by experimental conditions and population properties which cannot be entirely documented and represented in the simulator.

The difference in the quantitative outcomes from tools present in literature might be significant, as it is exemplified by the comparison proposed by Ha et al. [65] related to the outcomes of simulations of the IMO test 8 (MSC.1/Circ.1533 [147]) (considering the condition with highest number of counterflow agents) obtained with different evacuation model. The exit times obtained by the software EVI ([220]) are approximately 60% larger than those obtained by the cellular automata model proposed by Ha et al. [65]. Moreover, it is observed that the exit times related to same test condition, obtained by the software VELOS ([57]) and reported by Ginnis et al. [57] are again approximately doubled with respect to those obtained with EVI reported by Ha et al. [65].

3.2 Counterflow model and parameters

The counterflow model presented herein, as previously highlighted, is characterized by the fact that the counterflow condition is determined considering only instantaneous and physically measurable properties of the agents (instantaneous speed, orientation, position).

The model applies a counterflow force perpendicular (with a slight random fluctuation on the orientation) with respect to the desired velocity of the agent for each agent in counterflow. The force is proportional to the same quantities adopted to determine the counterflow condition.

3.2.1 Counterflow condition

Considering an agent i and an agent j, with reference to Figure 2.6, the following quantities p_1 p_2 and p_3 are defined:

$$p_1 = \left\langle \hat{\mathbf{v}}_i^0, \hat{\mathbf{D}}_{ij} \right\rangle = \cos\left(\theta_{ij}\right) \tag{3.4}$$

$$p_2 = -\left\langle \hat{\mathbf{v}}_i^0, \hat{\mathbf{n}}_j \right\rangle = -\cos\left(\eta_{ij}\right) = \cos\left(\pi - \eta_{ij}\right) \tag{3.5}$$

$$p_3 = f\left(v_{ij}^{r0}\right) \tag{3.6}$$

where the $\langle .,. \rangle$ operator indicates the dot product, $\hat{\mathbf{v}}_i^0$ is the versor of agent i desired speed vector $\mathbf{v}_i^0$, $\hat{\mathbf{D}}_{ij}$ is the versor of the vector $\mathbf{D}_{ij}$ connecting agents centres and $\hat{\mathbf{n}}_j$ is the orientation vector of agent j (pointing towards the front direction of the agent). The function $f\left(v_{ij}^{r0}\right)$ depends on the component, along the direction $\hat{\mathbf{v}}_i^0$, of the relative speed of agent j with respect to agent i, as follows:

$$\begin{cases} v_{ij}^{r0} = \left\langle \hat{\mathbf{v}}_i^0, (\mathbf{v}_j - \mathbf{v}_i) \right\rangle \\ f(v_{ij}^{r0}) = \begin{cases} 1 & \text{for } v_{ij}^{r0} < 0 \\ 1 - \dfrac{v_{ij}^{r0}}{V_{\mathrm{i}}^{\mathrm{cf}}} & \text{for } 0 \le v_{ij}^{r0} \le V_{\mathrm{i}}^{\mathrm{cf}} \\ 0 & \text{for } v_{ij}^{r0} > V_{\mathrm{i}}^{\mathrm{cf}} \end{cases} \end{cases} \tag{3.7}$$

The reference speed $V_{\mathrm{i}}^{\mathrm{cf}}$ (m/s) is defined as a function of the unimpeded walking speed v_i^{u}, which is a specific characteristic of each agent, i.e.

$$V_{\mathrm{i}}^{\mathrm{cf}} = k_{\mathrm{cf}} \cdot v_i^u \tag{3.8}$$

An agent j is defined to be in counterflow with respect to the considered agent i, when the following conditions are all fulfilled:

$$p_1 \ge \cos\left(\theta_{\mathrm{cf}}\right) \tag{3.9}$$

$$d_{ij} - r_{ij} < D_{\mathrm{cf}} \tag{3.10}$$

$$p_2 > 0 \tag{3.11}$$

$$p_3 > 0 \tag{3.12}$$

Conditions (2.25) and (2.26) refer to the relative position of agent j with respect to agent i, taking into account this latter's desired velocity. A counterflow condition is potentially identified only if agent j is positioned within an angular sector of amplitude

θ_{cf} around the direction identified by $\hat{\mathbf{v}}_i^0$ (see (2.25)), and, in addition (see (2.26)), agent j is also closer to agent i than a cut-off distance D_{cf}, considering the effective skin-to-skin distance $d_{ij} - r_{ij}$ between the closest circles among agents. A graphical representation is shown in Figure 2.6 (left).

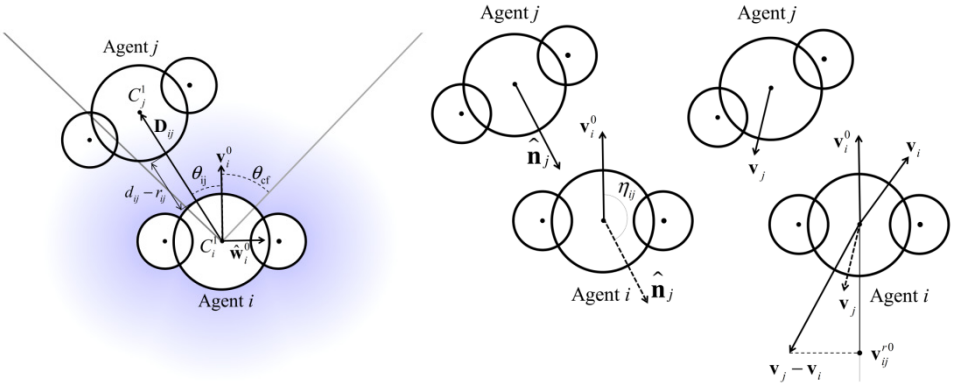

Figure 3.3: Example of counterflow situation when considering conditions (2.25)-(2.26) (left), (2.27) (centre) and (2.28) (right).

The condition (2.27) identifies a potential counterflow situation on the basis of the angle between the desired speed of agent i and the orientation of agent j, and this condition prevents from considering, for instance, agents in a queue as being in a counterflow situation (for a graphical representation of this condition see Figure 2.6). Finally, condition (2.28) identifies potential counterflow situations using the component of the relative velocity of agent j with respect to agent i along the direction of the desired speed of agent i (also for this condition, see the graphical representation in Figure 2.6). In particular, through(3.7), agent j is identified as being potentially in counterflow whenever such component is strictly negative or, alternatively, positive, but smaller than the threshold V_{i}^{cf} (see (2.23)). This latter case allows to properly identify counterflow situations also in those conditions, typically of low speed, when the agents are facing each other and the agent j is moving backward. Allowing the counterflow to be triggered also when the relative speed is slightly positive is necessary in order to apply the counterflow force with continuity in situations of high crowd density. Indeed, in these situations, due to interaction forces, it was observed that agents might sometimes have velocities with opposite direction with respect to their desired ones. In such conditions without the introduction of the threshold $V_{\text{i}}^{\text{cf}}\left(>0\right)$ in (2.25)/ (2.28), the counterflow model would intermittently be triggered on and off.

3.2.2 Counterflow force

When the agent j is identified to be in counterflow with respect to agent i, the module of its contribution to the counterflow force on agent i is modelled as follows:

$$\left\|\mathbf{F}_{ij}^{\text{cf}}\right\| = A_{\text{cf}} \cdot \left(1 - \frac{d_{ij} - r_{ij}}{D_{\text{cf}}}\right) \cdot \left(\left(\frac{p_1 - \cos\left(\theta_{\text{cf}}\right)}{1 - \cos\left(\theta_{\text{cf}}\right)}\right) \cdot p_2\right)^{\alpha_{\text{cf}}} \cdot p_3 \tag{3.13}$$

Whenever a counterflow condition is identified, the model for $\left\|\mathbf{F}_{ij}^{\mathrm{cf}}\right\|$ is continuous with respect to all the dependent variables, and $\left\|\mathbf{F}_{ij}^{\mathrm{cf}}\right\|$ decreases to 0 as any of the counterflow conditions (2.25)-(2.28) is not satisfied. The parameter A_{cf} (N) specifies the force intensity whereas the parameters θ_{cf} and D_{cf} specify the region of positioning of agent j with respect to agent i within which the counterflow model can be triggered, namely the "counterflow region". The parameter α_{cf} controls the level of interaction with lateral agents and with agents not fully oriented towards $\hat{\mathbf{v}}_i^0$.

Equation (2.29) provides the module of the counterflow force exerted by agent j on agent i. Regarding its direction, the force is, as a basis, perpendicular to the direction of the desired speed $\hat{\mathbf{v}}_i^0$, since it is intended to model a lateral shift. However, its orientation (right or left with respect to agent i), depends on the position of the agent in counterflow. In general, agents tend to move in the direction opposite to that where the counterflow agent is coming from. It has been observed that, in most cultures, there exists a preferred direction for pedestrian traffic which, usually, improves the organization of opposite flows in counterflow conditions (e.g [76]; [230]). In order to reproduce this behaviour, in the present model this preference is expressed by the introduction of an offset angle parameter η_{cf}. In particular, the versor of the counterflow force is defined as follows:

$$\hat{\mathbf{F}}_{ij}^{\mathrm{cf}} = -1 \cdot \mathrm{sign}\left(\left\langle \hat{\mathbf{w}}_i^0, \hat{\mathbf{D}}_{ij} \right\rangle - \sin\left(\eta_{\mathrm{cf}}\right)\right) \cdot \hat{\mathbf{w}}_i^0 \tag{3.14}$$

where $\hat{\mathbf{w}}_i^0$ is the unit vector oriented from the centre to the right arm of agent i. In case $\eta_{cf} = 0$ there is no preferred direction and the model is symmetrical. According to (2.30), and with reference to Figure 2.6, the counterflow force will have the same direction as $\hat{\mathbf{w}}_i^0$ if $\vartheta_{ij} \le \eta_{\mathrm{cf}}$ and will have opposite direction otherwise. It is also worth underlining that the preferred direction is on the right with respect to the desired speed of agent i if η_{cf} is positive, whereas it is on the left if η_{cf} is specified to be negative. Eventually, the contribution to the counterflow force vector due to agent j is determined by combining (2.29) and (2.30).

$$\mathbf{F}_{ij}^{\mathrm{cf}} = \left\|\mathbf{F}_{ij}^{\mathrm{cf}}\right\| \cdot \hat{\mathbf{F}}_{ij}^{\mathrm{cf}} \tag{3.15}$$

The direction of the counterflow force is, so far, deterministically defined as being always perpendicular to the desired speed of the agent.

From a series of preliminary calibrations, it was observed that this model may generate impasse situations, particularly in the case of bottlenecks. In order to avoid such situations, a random variation of direction of the force $\mathbf{F}_i^{\mathrm{cf}}(t)$ is implemented, in such a way that the force does not remain exactly parallel to $\hat{\mathbf{w}}_i^0$.

To this end, therefore, the force $\mathbf{F}_i^{\mathrm{cf}}(t)$, while keeping the same module as in (3.15), is oriented by an angle $\delta\psi(t)$ with respect to the nominal direction obtained by (3.15). The time history of angle $\delta\psi(t)$ is generated according to the same procedure described for the random forces (Chapter 2, section 2.2.6), within a range $[-\delta\psi_{\mathrm{cf}}, \delta\psi_{\mathrm{cf}}]$ where $\delta\psi_{\mathrm{cf}}$ is a fixed angle which is discussed in the next section.

This additional feature of the model where the counterflow force has a small random fluctuation with respect to its nominal direction, finds a correspondence with the real condition of two subjects competing for passing through a door. In such condition, each subject needs to decide whether to give way to the other by reducing its speed, or to increase its speed in order to pass before the other.

3.2.3 Counterflow parameters

The parameters in this model are numerous and thus a calibration for each parameter, although in principle possible, practically cannot be performed resorting to experimental data. Some model parameters have thus been set preliminary, whereas some others were set tentatively (Chapter 2).

A specific calibration was performed to set the value of the force intensity A_{cf} and of the parameter α_{cf} controlling the level of interaction with agents not fully oriented towards $\hat{\mathbf{v}}_i^0$.

Figure 3.4 might be considered to the purpose of a more detailed understanding of the influence of these two parameters on the counterflow-force module. The figure shows the intensity of the counterflow force applied to agent i for each position of agent j, varying the two parameters. For simplicity, only the condition where agent j is always oriented opposite with respect to agent i (thus $p_2 = 1$ for each position) is considered.

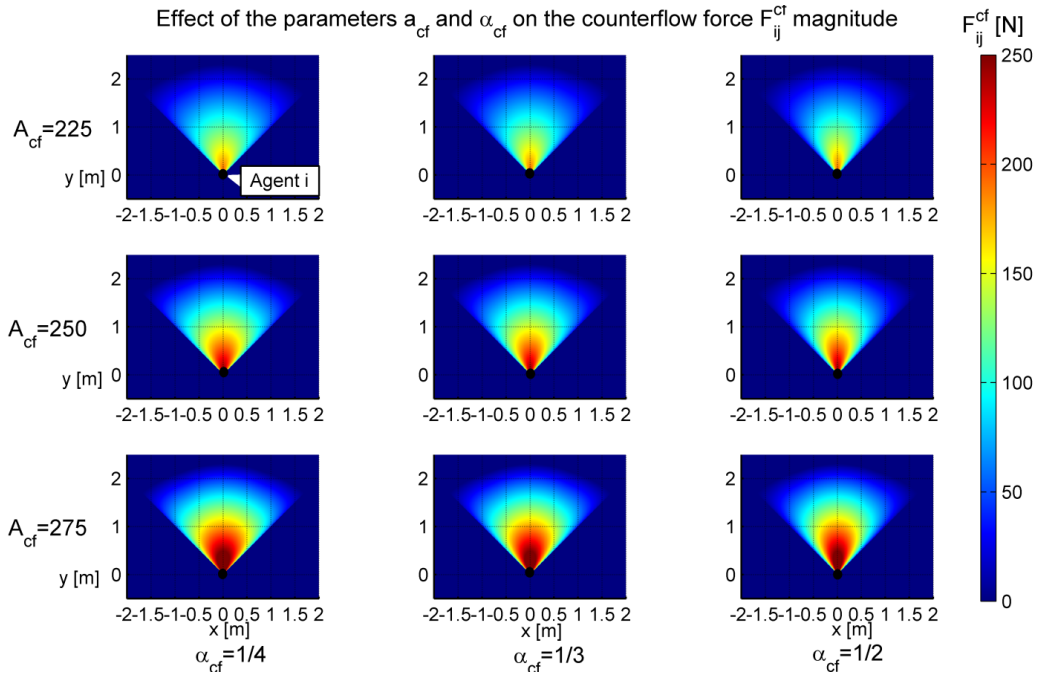

Figure 3.4: Influence of parameters A_{cf} and α_{cf} on the counterflow force.

It is observed from Figure 3.4 that the intensity of the force increases with the parameter A_{cf}. The parameter α_{cf}, instead, modifies the shape of curves along which the intensity of the force is constant: for high values of α_{cf} the agent interacts less with agents not exactly in front of it.

Due to the importance of parameters A_{cf} and α_{cf} on the performance of the counterflow force model, a calibration and a subsequent sensitivity analysis was performed considering data provided by Isobe et al. [89] and the IMO test 8 (MSC.1/Circ.1533 [147]). Results are reported in the next section. A good match with data provided by Isobe et al. [89] was obtained for $A_{cf} = 250$ N and $\alpha_{cf} = 1/3$.

Concerning, instead, the parameter $\delta\psi_{cf}$ ruling the randomness of the counterflow force direction, preliminary simulation showed reasonable behaviours are obtained for $\delta\psi_{cf} < 30°$. Fore higher values the behaviour of agents is modified in unrealistic ways. It was observed that impasse situations often occurred in bottle neck cases, when two agents arrive at the same exit from opposite directions. For this reason a further calibration of the parameter $\delta\psi_{cf}$ was carried out considering the IMO test 4 where a bottleneck condition is represented. The parameter $\delta\psi_{cf} = 15°$ was found reasonable to resolve the impasse situation and obtain results in line with the IMO test 4 requirements.

The calibration of the counterflow parameters will be thoroughly described in the following section.

3.3 Calibration of counterflow model parameters and sensitivity analysis

In the present section the calibration of the two parameter A_{cf} and α_{cf} is carried out through comparison with experimental data from Isobe et al. [89] and a sensitivity analysis is reported using the IMO test 8. Finally, the counterflow angle $\delta\psi_{cf}$ is calibrated relying on IMO test 4.

3.3.1 Calibration using experimental data

The experiment reported in Isobe et al. [89] is an archetypal counterflow condition. The Figure 3.5 shows the setup of the experiment. The initial density is controlled by fixing the initial number of people in the corridor.

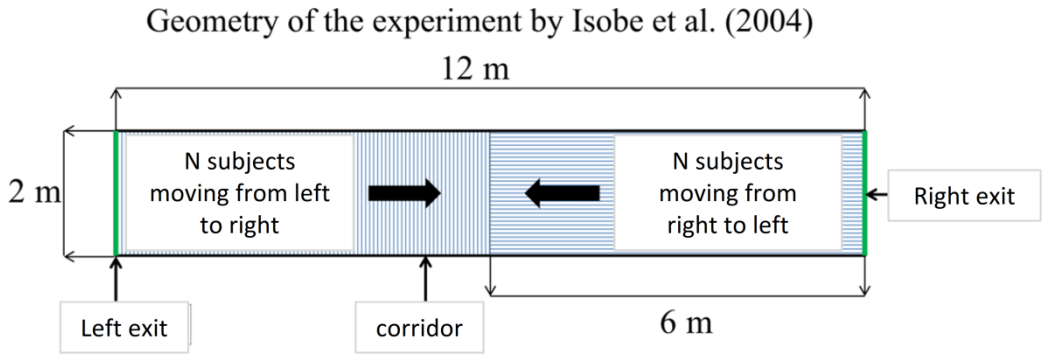

Figure 3.5: Geometry of the experiment performed by Isobe et al. [89].

A set of people was placed on the left side of the corridor, whereas another set was placed on the right side. Each subject was invited to travel the corridor from his/her initial position to the opposite end. The number of people going from left to right is equal to the number of people going from right to left was left in each test session and it is indicated as N. A total of 30 realizations were run for N=10, 15, 20, 25, 30, 35. Subsequently, the average exit time obtained considering all the exit times for each realization and averaging over the realizations of each test condition was reported as a function of N by Isobe et al. [89].

The simulations were run in a similar manner, considering agents randomly positioned in the two halves of the corridor. It was decided to maintain the difference between males and females by using the respective dimensions as reported in Table 4.2.

The unimpeded speed was calculated to be in line with experimental data. Isobe et al. [89] report that the average speed at density 0 (corresponding to one agent) is 1.125 m/s. Considering one of the subjects starting moving from the left half of the corridor towards the right exit and assuming that the starting position is placed exactly in the middle of the left half of the corridor, the agent travels 9 m in a total of 8 seconds. Using the equation for the motive force it is possible to calculate the unimpeded speed so that the average speed is 1.125 m/s. The obtained value for the unimpeded speed v_i^u is 1.2857 m/s.
The speed for males and females were attributed by rescaling the values in IMO MSC.1/Circ.1533 related to “Males younger than 30” and “Females younger than 30” in

order to obtain an average unimpeded speed of 1.2857 m/s which is in line with the experiments. The properties of the agents are reported in the table below.

Table 3.1: Agents properties in the test case presented by Isobe et al. [89].

	$r_{\max}$ (m)	$r_c / r_{\max}$	v_i^u	τ_i^f
Male	$U(0.25\text{ m}, 0.29\text{ m})$	0.5926	$U(1.05\text{ m/s}, 1.75\text{ m/s})$	$U(0.8\text{ s}, 1.20\text{ s})$
Female	$U(0.22\text{ m}, 0.26\text{ m})$	0.5833	$U(0.88\text{ m/s}, 1.47\text{ m/s})$	$U(0.8\text{ s}, 1.20\text{ s})$

Some preliminary simulations were run in order to reduce the range of possible values for the calibration of the parameters A_{cf} and α_{cf}. Reasonable outcomes were found for the parameter A_{cf} ranging in the interval [200 N, 300 N] and for the parameter α_{cf} ranging in the interval [1/2, 1/4]. The performed calibration aims to find the most reliable combination of parameters related to these intervals. To this purpose Figure 3.6 shows the comparison between the experimental outcomes and the simulation outcomes indicated as "UNITS", concerning the average exit time.

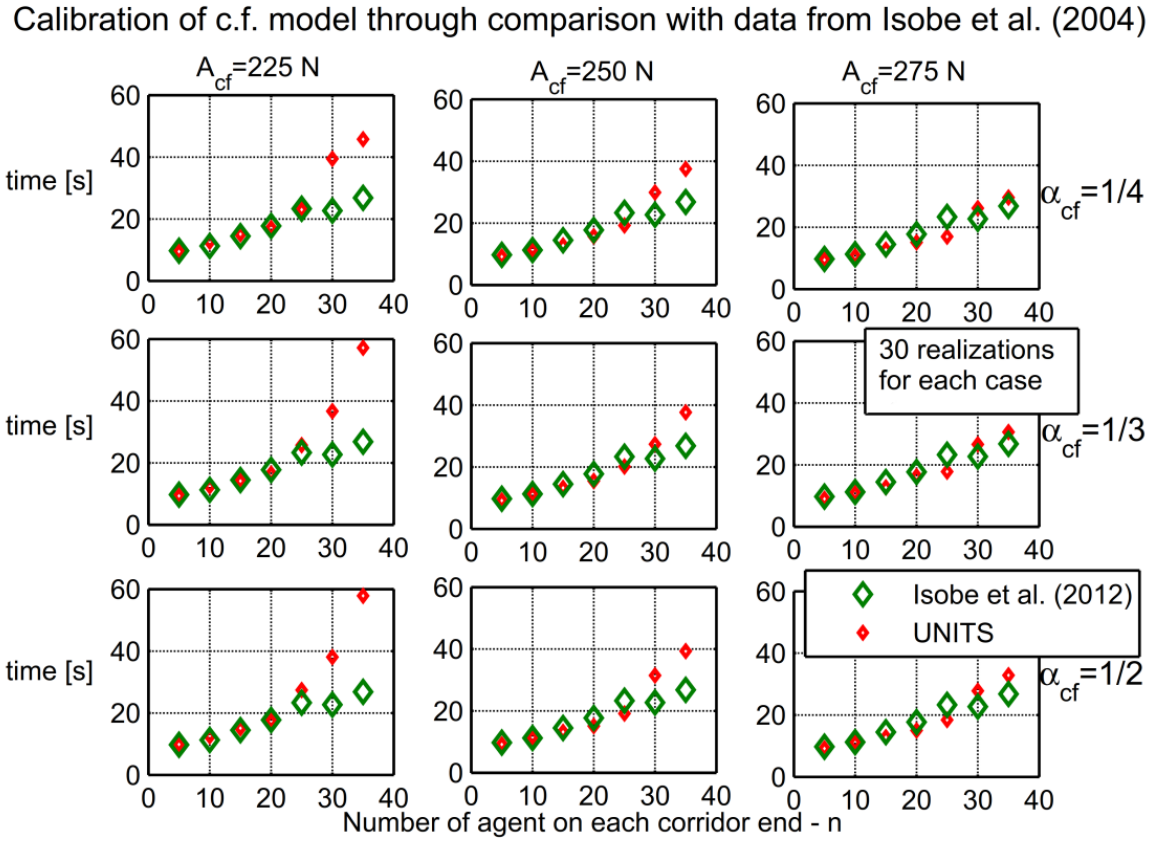

Figure 3.6: Comparison of mean exit times between UNITS simulation outcomes and experimental outcomes for different values of parameters A_{cf} and α_{cf}. A total of 30 realizations were performed for each case.

It is clearly observable from Figure 3.6 that the exit time decreases as the parameter A_{cf} increases. At the same time, the analysis of the mean exit time in Figure 3.6 shows that the modification of the parameter α_{cf} affects only the conditions of higher density (n>25) in the case where the coefficient $A_{cf} = 225\,N$, with a reduction of exit time when the coefficient α_{cf} reduces.
The effect of the parameter α_{cf} is, instead, not marked when $A_{cf} = 250\,N$ and $A_{cf} = 275\,N$, although a slight effect is detectable in the conditions of higher density. The effect is more visible comparing the results where $\alpha_{cf} = 1/2$ to the other two cases: the mean exit time for $\alpha_{cf} = 1/2$ appear to be always higher with respect to the ones obtained for $\alpha_{cf} = 1/3, 1/4$.

A more extensive analysis can be performed considering not only the average exit time, but also the dispersion of data from multiple realizations (i.e. the aleatory uncertainty), as reported in Figure 3.7. Data in Figure 3.7 are reported are reported as scatter plots together with the mean exit time and its corresponding 95% confidence interval considering the 30 realizations for each test condition.

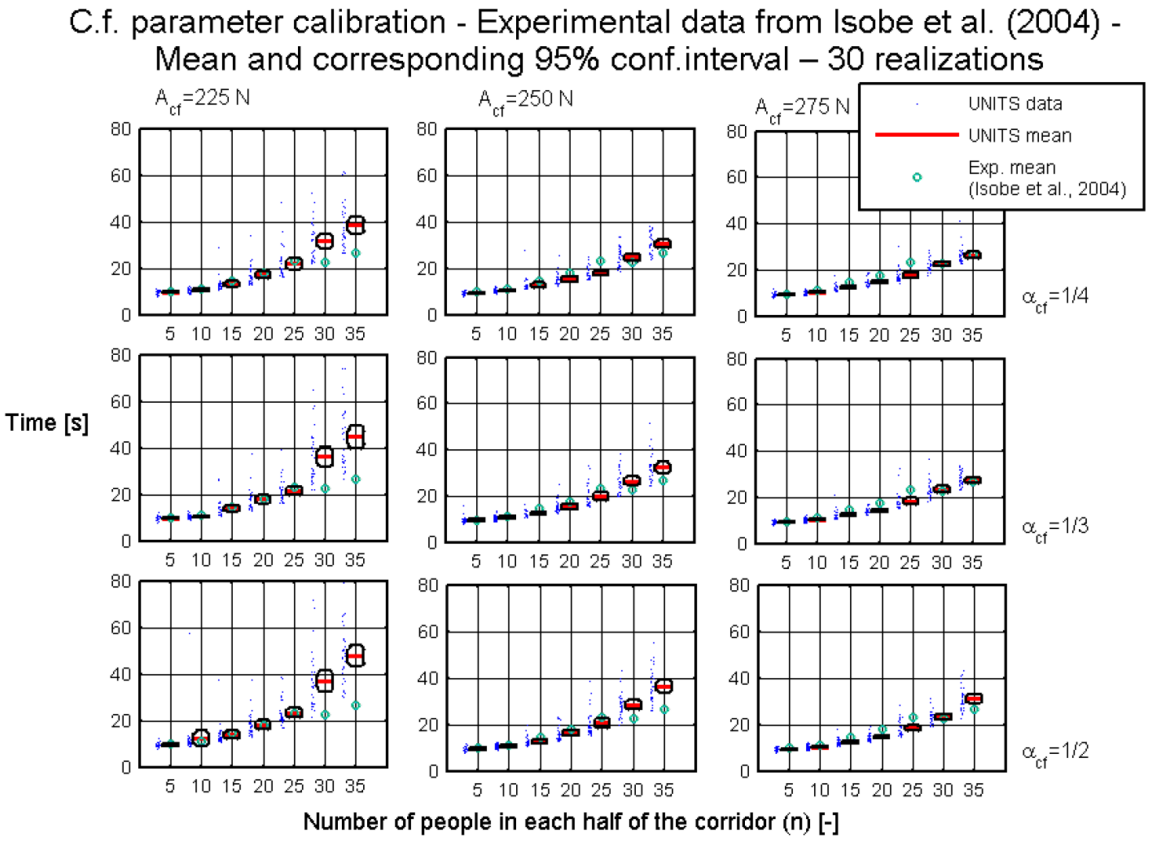

Figure 3.7: Mean exit time with corresponding 95% confidence interval, together with scatter plot of simulation data , for different values of parameters A_{cf} and α_{cf}. A total of 30 realizations were performed for each case. Experimental data from Isobe et al. 2004 are reported for comparison.

Figure 3.7 shows that the absolute dispersion of data in simulations is wider in high density conditions (n=30, 35), while it is smaller in low density conditions (n=10, 20,

25). The increase of data dispersion when the density increases is observed also in some experiments such as Zhang et al. [236] and it might, thus, have affected also the experiment reported by Isobe et al. [89]), although the uncertainty related to the outcomes of this last experiment is not reported in the paper. Some other observation about the results obtained by Isobe et al. [89] seems, however, to support the hypothesis of a reduced reliability of values related to the conditions of highest density. The experimental value obtained in the condition n=30 seems, indeed, not to be in line with the trend of the other values because it is lower than the one obtained for n=25. Moreover, as observed by Isobe et al. [89], the number of subjects couldn't be increased in the experiments more than n=35 as for higher densities subjects couldn't move any more.

Probably in the cases n=30 and n=35 some subjects were uncertain about continuing with the experiment or stopping because of the perceived high density. This might have resulted in a sharp change in their behaviour and in wider dispersion and a reduced reliability of the acquired data. Surely the subjects involved in the experiment would have higher motivation to move in case of a real evacuation condition. It is however impossible to state if this increased motivation would result in a reduction of the exit time (due to an increase of the motive force) ore to an increase of the exit time (due to the faster-is-slower effect).

Although setting $A_{cf} = 275$ N allows a better match with experimental data in high density conditions (n>50), it worsens the match with the experiment in low density (20<n<50). The same issue, although less marked, is observed considering the possibility of setting $\alpha_{cf} = 1/4$.

By considering the aforementioned observations concerning the reliability of the data in high density conditions and observing that the study aims to reproduce an organized egress during orderly evacuation where densities rarely raise higher than 4 p/m^2, it is reasonable to consider of primary importance the fitting to data related to conditions with lower density. The combination $A_{cf} = 250$ N and $\alpha_{cf} = 1/3$ seems, therefore, to be the preferable combination of parameters. Such combination allows, in any case, to obtain a reasonable match with experimental data also in relatively high density conditions while not penalizing the model prediction capabilities at low density conditions.

A further analysis of the effect of the parameters α_{cf} and A_{cf} was performed considering the IMO test 8 and it is reported in the next section.

3.3.2 Sensitivity analysis for counterflow model parameters A_{cf} and α_{cf} considering IMO test 8

The IMO test 8 reported in MSC.Circ1/1533 specifically addresses counterflow condition in an archetypal geometrical configuration. As a result, the test is an appropriate condition for analysing the sensitivity of simulation results to parameters of the developed counterflow model.

As shown in Figure 3.8, the geometry of the test consists of two rooms connected by a corridor. A total of 100 agents move from the end of the left room towards the end of the right room. Four different cases are defined by varying the number of agents which, are instead moving from the end of the right room towards the end of the left room, namely: 0 agents (no counterflow), 10 agents, 50 agents and 100 agents.

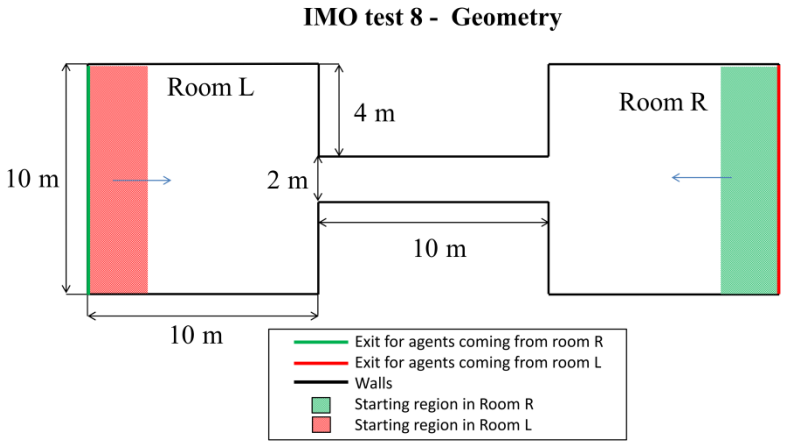

Figure 3.8: Geometry of IMO test 8.

The situation of IMO test 8 is different from the one reported by Isobe et al. [89]. In the condition reported by Isobe et al. [89], people/agents started the evacuation being already inside the corridor, with the two groups in counterflow facing one another. Instead, in the IMO test 8 condition, agents start far apart, and they have therefore the time and space to begin the avoidance lateral shift before coming too close to the other incoming agents.

Figure 3.9 reports the exit time of the latest agent moving from left to right for different combinations of counterflow model parameters A_{cf} and α_{CF}. From the ensemble statistical analysis of 30 independent realization for each condition (number of agents in counterflow), the figure reports curves for median exit time as well as 5%, 25%, 75% and 95% percentiles. Curves of percentiles are reported in order to provide indication of the distribution of data.
Looking at the results in Figure 3.9 it can be noticed that the dependence from the parameter A_{cf} is very marked. Generally, an increase of A_{cf} tends to reduce the dispersion of the data and tends to slightly reduce the median exit time. However, the effect is more marked when moving from $A_{\mathrm{cf}} = 225$ N to $A_{\mathrm{cf}} = 250$ N, and it is less evident when A_{cf} is further increases to 275 N. In this test case the effect of the variation of parameter α_{cf} is very limited, and the variation of α_{cf} mostly affects the upper tail of the distribution of the exit time.

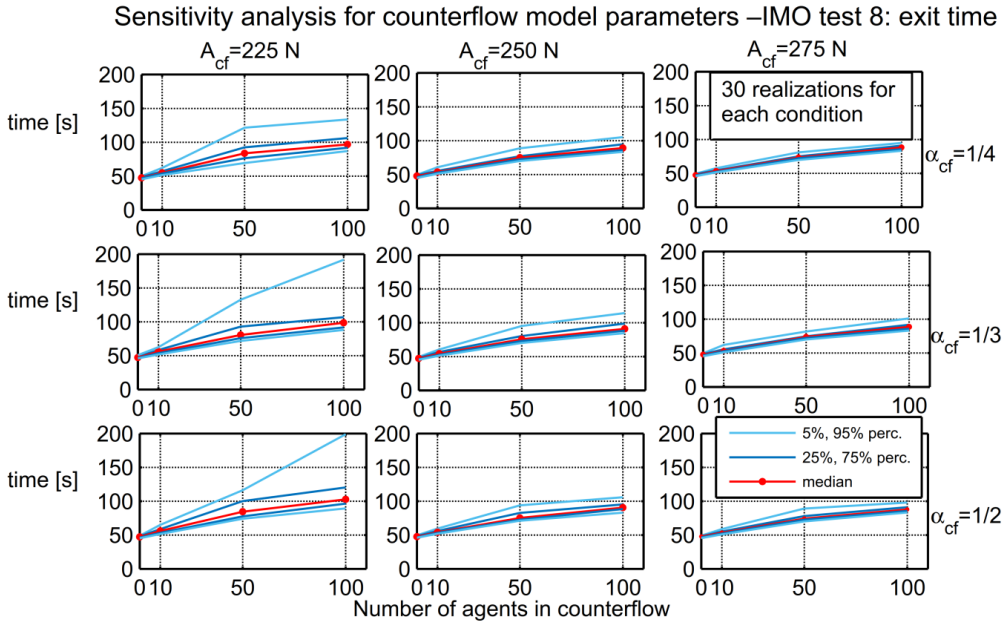

Figure 3.9: Sensitivity analysis for counterflow model parameters A_{cf} and α_{cf} - IMO test 8. A total of 30 realization were performed for each condition (number of agents in counterflow).

The reported analysis shows that the median exit time is not very sensitive to parameters A_{cf} and α_{cf} of the counterflow model. The reduced influence of the intensity of the counterflow force (which is governed by A_{cf}) in this test condition might be due to the fact that agents have enough time to organize in lanes before getting close to incoming counterflow agents. As a result, in most cases, the agents are already organized in lanes when the counterflow force reaches its maximum.

Some visible effects of A_{cf} are, however, present when analysing the upper tails of the distribution, which are represented by 95% percentiles curves. It was observed that the occasional abrupt increase, with respect to the median, of the exit time in one single simulation is due to the occurrence of transitoriy clogging conditions. Increasing the value of the parameter A_{cf} has the effect of reducing the probability of occurrence and also the duration of the clogging condition, thus reducing also the dispersion of the exit time.

3.3.3 Calibration of random orientation $\delta\psi_{cf}$ of counterflow force using IMO test 4

During the testing of the developed counterflow model, it was observed that the present counterflow model may generate unrealistically long impasse situations in those cases where two agents try to access to the same exit but coming from opposite directions. Although this situation is not a standard counterflow condition, the counterflow model is nevertheless triggered because the agents have opposite directions at the entrance of a bottle neck. The triggering of the deterministic version of the counterflow model can create situations of (almost) equilibrium, which eventually prevent the agents from exiting in a realistic time. In order to cope with such situation, as already described (see §3.2.2), a random effect was introduced which randomly orient the counterflow force

around the nominal (deterministic) direction. The counterflow angle $\delta\psi_{cf}$ determines the angular range in which the counterflow force direction might fluctuate with respect to its mean value (which is always perpendicular to the agent desired direction). It was observed that, eventually, the random change of the direction of the counterflow force effectively reduces the duration of impasse situations.

A calibration of the parameter $\delta\psi_{cf}$ was carried considering the IMO test 4 from MSC.1/Circ.1533, which considers a simple bottle neck condition as it is reported in Figure 3.10

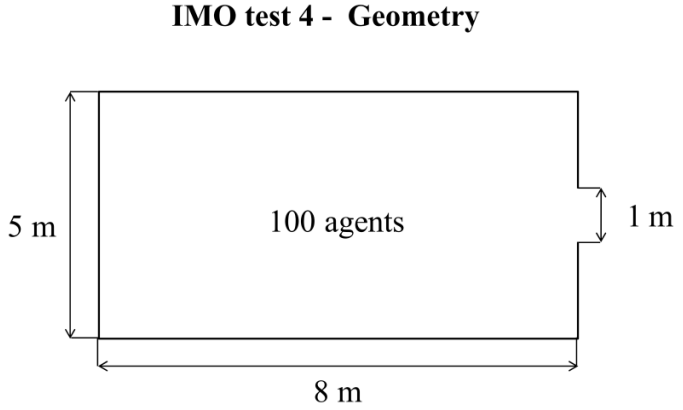

Figure 3.10: IMO test 4 geometry

Figure 3.11 reports the exceedance probability (1-cdf), as estimated from data, for the time intervals elapsed between the exit of one agent and the exit of the next one (i.e. the interarrival time of agents at the exit).For the sake of easier comparison among outcomes with different values of $\delta\psi_{cf}$, the graph shows only data for interarrival time above approximately 1.5 s.

From results in Figure 3.11 it can be observed that increasing the angle $\delta\psi_{cf}$ effectively reduces the probability of long interarrival times, which typically correspond to the occurrence of impasse situations. This effect is particularly visible in the zone around 2-4 s. The difference among the curves is present also for interarrival times longer than 4 second, but it is difficult to clearly detect it due to the reduced number of samples used for the analysis of this case. However it is observed that, in the random simulations carried out (50 in total), the maximum obtained interarrival time is around 6 s for $\delta\psi_{cf} = 30°$, 9 s for $\delta\psi_{cf} = 15°$ and 15 s for $\delta\psi_{cf} = 0$.

Correspondingly, the increase of parameter $\delta\psi_{cf}$ was also observed to lead to an increase of the flow rate. This effect needs to be controlled, because the introduction of the random angle $\delta\psi_{cf}$ in the model is intended for resolving occasional long impasse situations, but it should not significantly affect the global flow rate which should be mostly governed by the motive force and by the agent-agent interaction force. Figure 3.12 reports an analysis of the ensemble domain distribution of the number of agents in the room, as a function of time. Results in Figure 3.12 show that setting $\delta\psi_{cf} = 30°$ has a relatively large impact on the flow rate (consider the average trend of the curve). The

value $\delta\psi_{cf} = 15°$ was therefore preferred as it allows effectively reducing the occasional impasse situations, while having a more limited impact on the flow rate.

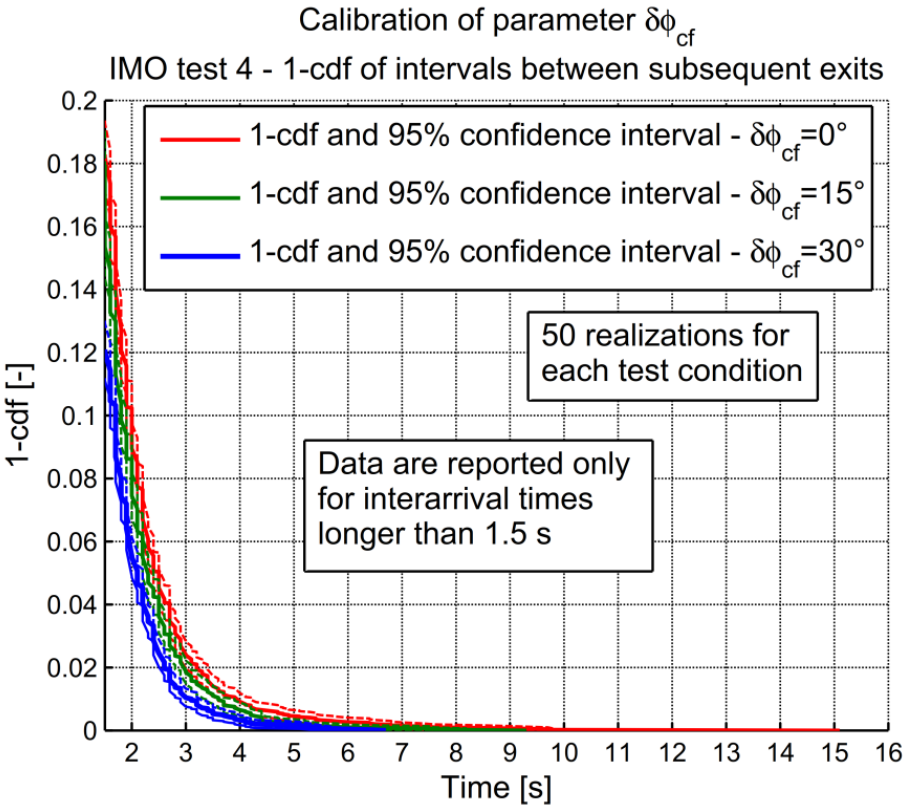

Figure 3.11: Calibration of counterflow model parameter $\delta\psi_{cf}$ - IMO test 4. Probability of exceedence (1-cdf) of time elapsed between the instant one agent reaches the exit and the instant the next agent reaches the same exit (interarrival time at the exit). A total of 50 realizations were performed for each case.

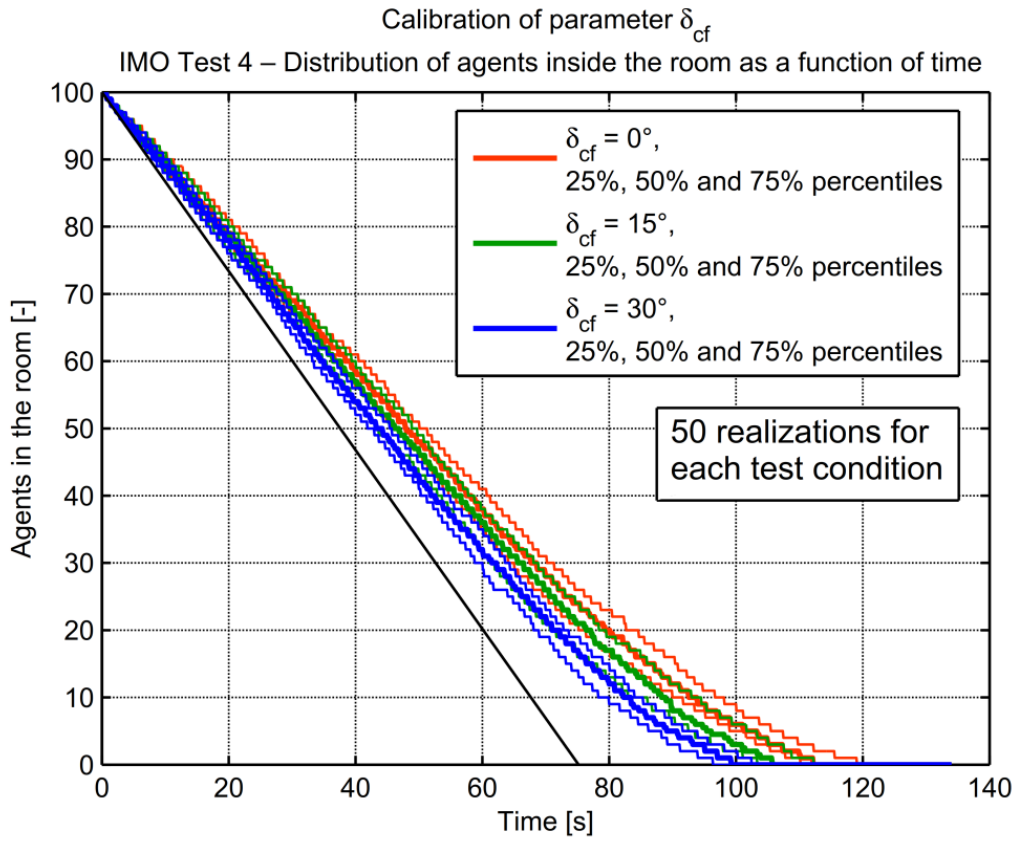

Figure 3.12: Calibration of counterflow model parameter $\delta\psi_{cf}$ - IMO test 4. Time dependent median, and 25% and 75% percentiles of agents inside the room, from ensemble domain analysis. A total of 50 realizations were performed for each case.

3.4 Final remarks

The chapter addressed in detail the model of counterflow and the calibration of the model parameter whose finally selected values are summarized in Table 2.8. The first section of the chapter proposed a survey of different counterflow models highlighting, in each of them, the main recurring patterns of counterflow.

A brief recall of the model of counterflow developed specifically for the present study was proposed specifically focusing on the model parameters.

The calibration performed to set the value of the parameters governing the force intensity of the counterflow and the level of interaction with agents not fully oriented towards the desired direction was described. The calibration was performed by comparison with experimental data. The simulations performed to calibrate the two parameters showed a marked effect of the parameter governing the force intensity on the average exit time. It is observed that the exit time grows as the counterflow force intensity decreases. The effect of the second parameter considered for the calibration is, instead, less marked. The comparison with the experimental data allowed setting a value for the two parameters.

A sensitivity analysis was carried out for the calibrated parameters, considered the IMO test case 8. The analysis confirmed the marked effect of the parameter governing the force intensity on the average exit time observed in the calibration process. The effect of the second parameter was, instead, limited to the dispersion of the distribution of exit times: the dispersion seems to increase when the parameter is lower. This is conjectured to be due to the fact that clogging has a higher probability to occur when the second parameter is lower.

Finally the calibration performed considering IMO test 4 of the parameter governing the amplitude of the random fluctuation of the counterflow force was presented. The calibration showed that the random fluctuation effectively reduces the occurrence of impasse condition at the exit of bottleneck, however if the amplitude of the fluctuation is too large it has also a marked effect on the flow of the agents. A parameter allowing to effectively reducing the occasional impasse situations, while having a limited impact on the flow rate was thus chosen.

The following chapter will be focused on the process of verification and validation of the tool and will report the outcomes from all IMO test cases and comparison with experimental data considering different test conditions.

This page is intentionally left blank

4 VERIFICATION AND VALIDATION

This chapter presents the process of verification and validation of the developed evacuation model. Firstly, the problem of verification and validation of evacuation models is discussed. Afterwards, results are reported based on simulation of tests indicated by the IMO guidelines for validation/verification of evacuation simulation tools in MSC.1/Circ.1533. The subsequent section presents comparisons between simulations and experimental results concerning the flow-density relation (fundamental diagrams). Finally, the last three sections report comparisons between simulations and experimental data for three different cases: the case of a bottleneck condition, the case of an evacuation starting behind aligned objects, and a counterflow condition. Obtained results are finally summarised.

4.1 Introduction

Each evacuation tool, before being applied for evacuation performance assessment, needs to be verified (i.e. proven to correctly implement the mathematical model) and validated (i.e. shown to sufficiently match experimental data).

The process of verification is conceptually relatively simple, as it does not require experimental data and it is, in general, customized accordingly to the implemented evacuation model. In the maritime field the IMO suggests a series of very simple test cases for the verification of an evacuation tool which are reported in Appendix 2 of MSC.1/Circ.1533 [147], i.e. what are typically referred to, briefly, as “IMO test cases” or “IMO tests”. Strictly speaking, only the first three IMO tests should be considered as verification of the model, whereas the other cases are essentially based on the capability of the model to qualitative reproduce human behaviours observed in experiments and might thus be interpreted as a sort of qualitative validation.

Validation is definitely a more complex step in the development of a mathematical evacuation model, as it is based on the comparison between simulation outcomes and data collected through experiments. The comparison between simulation results and experimental results can be made qualitatively or quantitatively. A qualitative validation aims at proving that the simulation tool is capable of reproducing collective phenomena observed in real situations, such as congestion and lane formation, as it is described by Schadschneider et al. [190]. The IMO test cases in MSC.1/Circ.1533 [147], in particular, provide benchmarks, which, as anticipated, are mostly intended for qualitative validations.

Experimental measurements of evacuation and pedestrian behaviours are abundant in literature (e.g. [44], [90], [159], [238],). However, in a many cases, experimental measurements are available in conditions for which the experimenters have limited control (e.g. measurements in real environment) or experimental results are reported without sufficient information for setting up a comparative evacuation simulation (e.g. pedestrian main characteristics, such as unimpeded speeds, gender distribution, mass, dimension are not sufficiently provided). For detailed validation studies, it is necessary to have at disposal experiments carried out under controllable conditions, with all data for setting up simulations appropriately collected and reported. Unfortunately, the availability of highly controlled quantitative validation data sets in literature is very limited (e.g., [89]; [124]). This is due to the complexity of performing human evacuation experiments. Moreover, evacuation experiments are difficult to be repeated for a sufficient number of times, especially when they involve a large number of subjects. These experimental problems limit the possibility of controlling experimental sampling uncertainty and of quantifying the experimental aleatory uncertainty.

Stochastic evacuation models, like the one developed herein are capable of mimicking experimental aleatory uncertainty, potentially allowing, therefore, a comparison with the variability observed in the experimental data, when this is quantified and reported. The outcomes of models embedding stochastic components must be analysed in the ensemble domain, and Monte-Carlo simulations are often implemented for this purpose. It is, thus, fundamental that simulation results are analysed by properly addressing, quantifying and reporting the aleatory uncertainty of the model (e.g. [36], [77]), especially when simulation outcomes are compared to experimental data for validation.

On the basis of the above considerations, a process of verification and validation was performed on the developed mathematical model, and it is presented in the following. The first section of the chapter is dedicated to a verification and to some extent qualitative validation based on the use of the IMO test cases specified by MSC.1/Circ1533 ([147]). The subsequent sections address, instead, validation through direct comparisons with experimental data in different conditions, namely: the case of evacuation through a corridor and a T-junction, the case of a bottleneck condition when exiting from a room, the case of an evacuation starting behind aligned objects to exit a room, and a counterflow condition.

Some results obtained by FDS+Evac [112] and other simulation tools are also reported for comparison purposes. The performed comparisons highlighted the variability of simulation outcomes depending on the adopted simulation tool.

Considering the stochastic nature of the problem, particular attention will be paid to the analysis and reporting of data dispersion and distribution for the considered quantities.

4.2 IMO test cases

Outcomes obtained performing the IMO test cases as suggested in MSC.1/Circ1533 ([147]) are reported in the following. Quantitative analysis and comparisons with the software FDS+Evac ([5], [112]) are presented, in parallel to the qualitative analysis requested by MSC.1/Circ1533. The quantitative comparison with FDS+Evac ([112]) is proposed in order to provide more exhaustive information about the software behaviour in some interesting cases, such as the bottleneck condition (test case 4), the counterflow condition (test case 8) and the condition where a congestion occurs at the bottom of a staircase (test case 11), since this are cases very much related to the maritime field. Moreover the tests are commented referring to information available in literature.

In the simulations, the distribution of agents follows the age/gender population groups distribution reported in Table 4.1, which correspond to Table 3.1 in MSC.1/Circ.1533 [147]. For each agent, the unimpeded speed on stairs was defined to be proportional to the unimpeded speed on flat terrain, in accordance with factors $k^{\mathrm{S,up}}_{\mathrm{group(i)}}$ and $k^{\mathrm{S,down}}_{\mathrm{group(i)}}$ reported in Table 4.1. The coefficients of proportionality were set by noting that the bounds of the intervals of unimpeded speed on stairs in Table 3.5 of the MSC.1/Circ.1533 [147] scale with an approximately constant coefficient with respect the bounds of the intervals of unimpeded speed on flat terrain in Table 3.4 of the MSC.1/Circ.1533 [147].

Table 4.1: Percentage of population for IMO agent classes (passengers), together with corresponding unimpeded speeds on flat terrain and on stairs.

	Population group - passengers									
	G1	**G2**	**G3**	**G4**	**G5**	**G6**	**G7**	**G8**	**G9**	**G10**
Percentage of population	7%	7%	16%	10%	10%	7%	7%	16%	16%	10%
Minimum unimpeded speed [m/s]	0.930	0.710	0.560	0.430	0.370	1.110	0.970	0.840	0.640	0.550
Minimum unimpeded speed [m/s]	1.550	1.190	0.940	0.710	0.610	1.850	1.620	1.400	1.060	0.910
$k_{group(i)}^{S,up}$ [-]	0.51	0.62	0.65	0.65	0.63	0.45	0.49	0.45	0.46	0.45
$k_{group(i)}^{S,down}$ [-]	0.60	0.69	0.80	0.79	0.79	0.68	0.66	0.60	0.60	0.60

G1: Females younger than 30 years; **G2:** Females 30-50 years old; **G3:** Females older than 50 years; **G4:** Females older than 50, mobility impaired (1); **G5:** Females older than 50, mobility impaired (2); **G6:** Males younger than 30 years; **G7:** Males 30-50 years old; **G8:** Males older than 50 years; **G9:** Males older than 50, mobility impaired (1); **G10:** Males older than 50, mobility impaired (2).

$k_{group(i)}^{S,up}$, $k_{group(i)}^{S,down}$: ratio between unimpeded speed on stairs (up and down direction, respectively) and unimpeded speed on flat terrain.

Unfortunately, no information is provided by MSC.1/Circ.1533 regarding the other agents parameters which are required in the present model. Therefore, for parameters not addressed by IMO MSC.1/Circ.1533 [147], reference is made to the distributions specified by FDS+Evac ([112]), as reported in Table 4.2. In the table the notation $U(a,b)$ indicates a uniform distribution in the interval $[a,b]$, and it can be noted that r_c (chest radius) and r_a (arm radius) are deterministically associated with the maximum radius $r_{\max}$ (for which the distribution is explicitly provided).

Table 4.2: Agent dimensions in relation to agent type.

Agent type	Maximum radius $r_{\max}$ (m)	Chest radius ratio $r_c / r_{\max}$	Arm radius ratio $r_a / r_{\max}$
Adult	$U(0.22, 0.29)$	0.5882	0.3725
Male	$U(0.25, 0.29)$	0.5926	0.3704
Female	$U(0.22, 0.26)$	0.5833	0.3750

4.2.1 IMO test 1 (Maintaining set walking speed in corridor)

The description of the test, according to MSC.1/Circ.1533, is as follows:

"One person in a corridor 2 m wide and 40 m long with a walking speed of 1 m/s should be demonstrated to cover this distance in 40 s."

The geometry adopted to run this test case is reported in Figure 4.1 where the area considered for the test is highlighted. Figure 4.2 reports the longitudinal coordinate (x-coordinate) of the agent along the corridor as a function of time as obtained from the simulations. It can be observed that, after the initial time required by the agents to achieve the target speed (the agent starts with speed equal to zero), the speed remains constant and equal to the unimpeded one. It is thus demonstrated that the agent travels a distance of 40 m in 40 s in the analysed region.

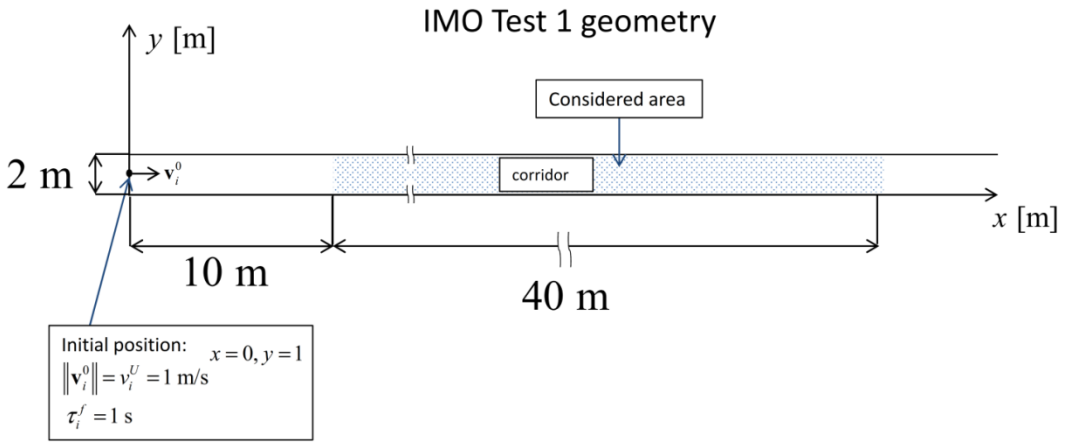

Figure 4.1: Geometry and parameters adopted for the IMO test 1.

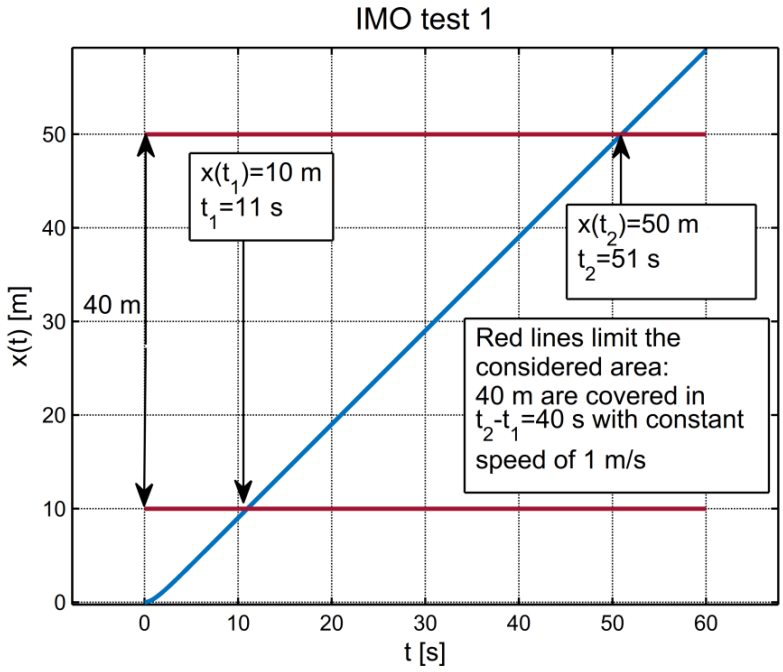

Figure 4.2: IMO test case 1. Longitudinal coordinate of agent along the corridor as a function of time. Red lines limit the 40 m long segment of the entire corridor which was considered for the analysis.

4.2.2 IMO test 2 and 3 (Maintaining set walking speed on staircase – up and down)

The description of both test 2 (up staircase) and test 3 (down staircase), according to MSC.1/Circ.1533, is as follows:

"One person, on a stair 2 m wide and having a length of 10 m measured along the incline, with a walking speed of 1 m/s, should be demonstrated to cover this distance in 10 s".

The geometry adopted to run this test case is reported in Figure 4.3 where the section of stair considered for the test is highlighted. Two situations are considered, i.e. the ascending condition (test 2) and descending condition (test 3).

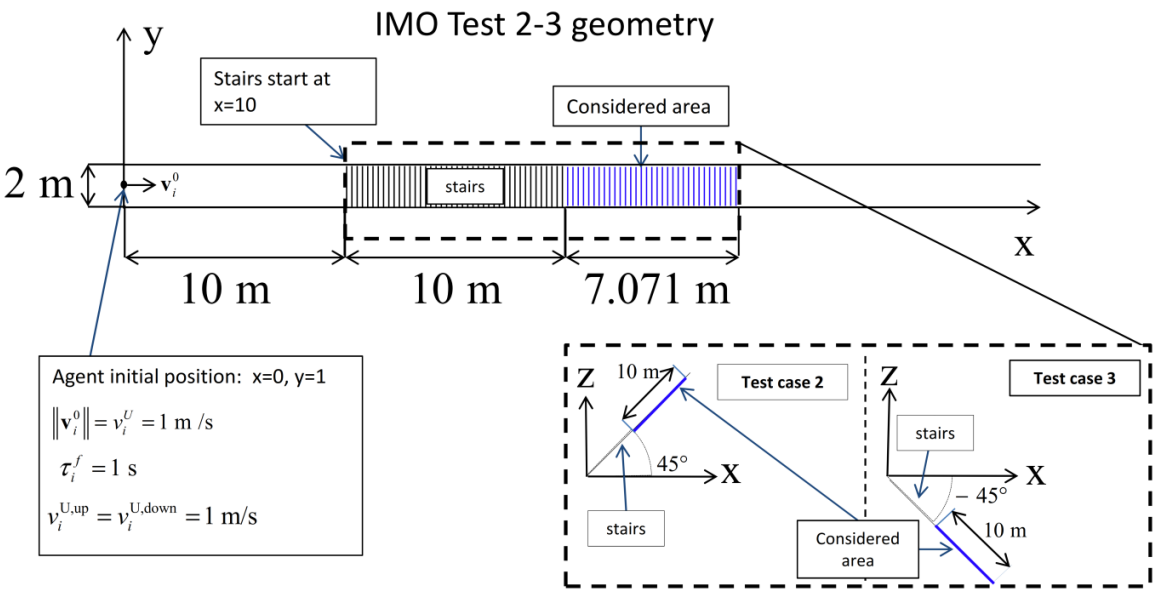

Figure 4.3: Geometry and parameters adopted for the IMO test cases 2 and 3.

The position of the agent along the x-coordinate as a function of time, as obtained from the simulations, is reported in Figure 4.4. In general, the only difference between the ascending and the descending case is due to the speeds on stairs $v_i^{U,up}$ and $v_i^{U,down}$ which are, usually, not equal (MSC.1/Circ.1533 [147], Table 4.1). However, in the two considered test cases, the speeds on stairs are set to be the same, therefore the relation between the x-coordinate and the time does not change if the subject is ascending or descending the stair, considering a fixed stair inclination angle. What, instead, changes, is the z-coordinate.

Specifically, an inclination angle of 45° degrees is considered when running this case. This value has been assumed, since it is not specified by the IMO test cases. It is however to be noted that it does not affect the results of the test. The area considered for the test case, measured along the x-axis, is, therefore, 7.071 m long, corresponding to a length of 10 m along the stairs incline when the incline is ±45° (Figure 4.3, Figure 4.4).

As it can be observed from Figure 4.4, the requirements from the test is fulfilled, as the agent travels the 10 m measured along the incline of stairs in 10 seconds.

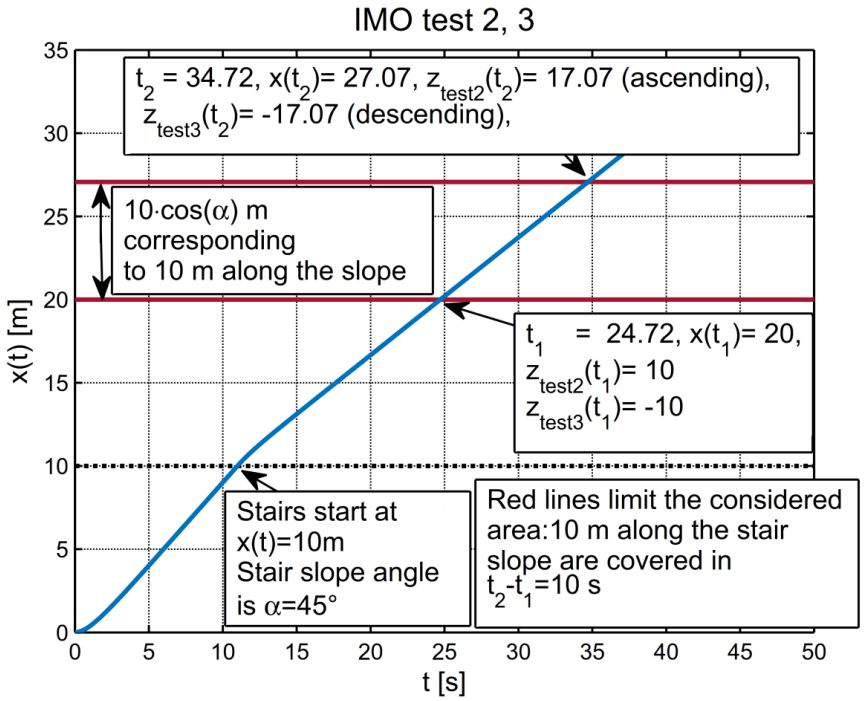

Figure 4.4: IMO test case 2. x-coordinate as a function of the time: the red lines limit the 10 m long segment of the staircase considered for the analysis.

4.2.3 IMO test 4 (Exit flow rate)

The description the test, according to MSC.1/Circ.1533, is as follows:

"100 persons [p] in a room of size 8 by 5 m with a 1 m exit located centrally on the 5 m wall. The flow rate over the entire period should not exceed 1.33 p/s."

The geometry of the test case is reported in Figure 4.5.

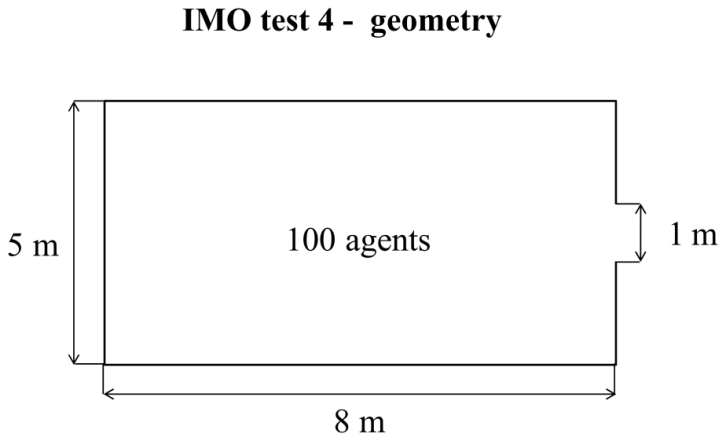

Figure 4.5: IMO test case 4. Geometry.

Agents unimpeded speeds, as well as gender distribution, are set in accordance to the population distribution specified by MSC.1/Circ.1533 [147]. Agents dimension are set according to distributions from the FDS+Evac "Male" and "Female" class ([112]).

In order to assess the effect of using different simulation tools, simulations for this test case have been carried out both using the evacuation tool developed herein, as well as by means of FDS+Evac version 6.3.2 and Evac version 2.5.1([112]).

Figure 4.6 presents results from the simulations. Instantaneous ensemble median, 25% and 75% percentiles of the number of people still in the room are calculated on the basis of 250 independent realizations. Results from the present tool are indicated as "UNITS". Results obtained with FDS+Evac are also reported, for comparison purposes.

Both tools fulfil the prescribed IMO Test 4 maximum exit rate, and the UNITS code shows a flow rate slightly higher than FDS+Evac. This difference can be due to the different counterflow models, which in the UNITS code is triggered when agents approach the exit door in opposite directions, and to the fact that the UNITS code implements a nervousness effect.

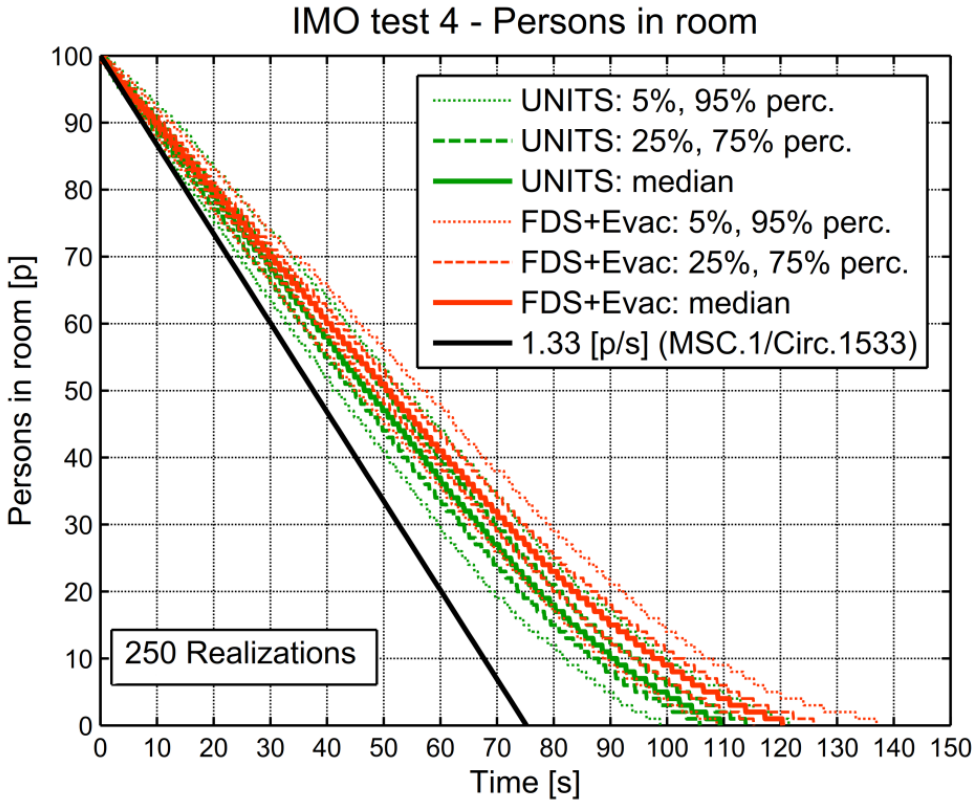

Figure 4.6: IMO test case 4. People in the room as function of time.

A snapshot from one of the simulations of this test case is reported in Figure 4.7. From the position and orientation of agents in the snapshots, the well-known arching phenomenon at a bottleneck is well visible in the simulation from UNITS. Differences in this respect can be noticed between FDS+Evac and UNITS. Such differences can be associated with the different routing algorithm in the two modelling. In fact, while UNITS agents are oriented towards the exit as a consequence of the positioning of a waypoint at the door, agents in FDS+Evac tend to orient themselves in accordance with an underlying flow-like field ([112]).

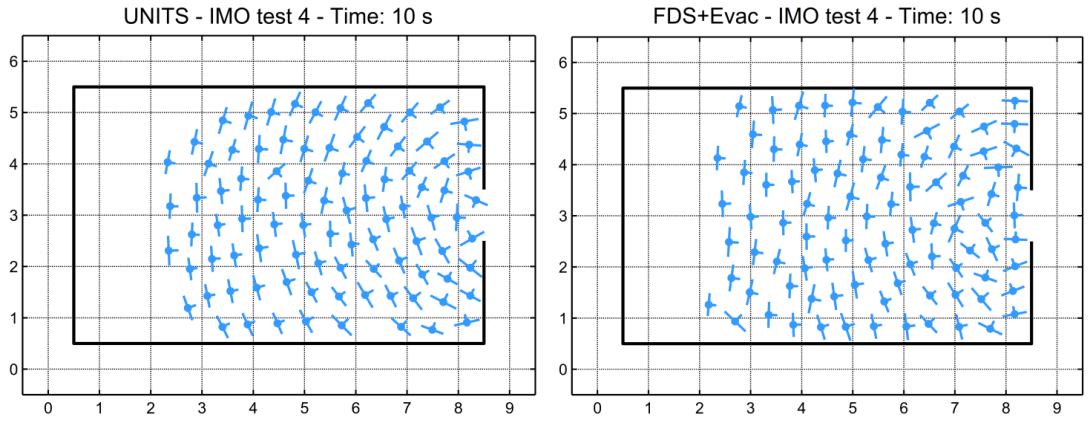

Figure 4.7: IMO test case 4. Snapshots from the simulations. Present tool (left) and FDS+Evac (right).

Looking at the outcomes reported in Figure 4.6, it can be noted that both tools fulfil the IMO requirement of a flow rate over the entire period not exceeding 1.33 p/s. It is however to be noted that the requirement may not be fulfilled if other distributions are used for agents unimpeded speeds. In this respect, it shall be underlined that in the experimental results reported by (Liao et al. [124]) related to the exit flow from a bottleneck, a specific flow rate higher than the limit of 1.33 p/s considered in this test was measured. The upper bound value of 1.33 p/s for the flow rate in the IMO guidelines may have been derived by the studies presented by Weidmann [223]. However, as several experiments were carried out after the ones by Weidmann [223] (e.g. [22]; [234]) an updated formulation for this test case might be necessary. The new formulation of the test case 4 should consider data and studies presently available about the flow through a bottleneck. Particular relevance should be given to the studies that followed the results presented by Weidmann [223] such as the one presented by Chattaraj et al.[22] and Zhang [234] which provide evidences that the specific flow might vary considerably in relation to the population properties and to the considered test conditions.

4.2.4 IMO test 5 (Response duration)

The description the test, according to MSC.1/Circ.1533, is as follows:

"Ten persons in a room of size 8 m by 5 m with a 1 m exit located centrally on the 5 m wall. Impose response durations as follows uniformly distributed in a range between 10 s and 100 s. Verify that each occupant starts moving at the appropriate time."

In the developed tool the response time for each agent is specified in the input file, together with the other agents properties, and the input files are generated by a series of scripts which have been developed separately from the main tool, within which the response time can be generated according to any arbitrarily specified distribution.

The test was, thus, carried out by imposing a uniform distribution for response times and randomly generating the agents. Figure 4.8 reports the length of travelled path by each agent as a function of time. It can be noticed that the travelled path is not zero

before the response time. This is associated with the fact that the model considers that usually people interact with each other even in a normal (non-evacuation) condition. In particular, when the response time is not yet reached, the desired speed is set to the null vector, meaning that the agent are assumed to desire to keep zero speed. At the same time, however, the repulsive forces between agents, the counterflow forces as well as the agent-wall interaction forces, are active as in case of desired speed different from zero. As a result, agents which have not yet started evacuating (time less than the corresponding response time) will however move to avoid contacts and clear the way for the other agents. This approach appears to be more realistic than, for instance, rigidly fixing the position of the agents before their response time. It shall be noted, however, that, as a hint for future research, it would be worth developing a model of social-forces more specifically intended for waiting/standing agents.

The instant agents start travelling towards the exit is clearly visible in Figure 4.8 and corresponds to a sharp increase of the travelled path as a function of time. Instead, the changes in the trend of the travelled path before the agents have reached their response time are due to the interaction between the agents. In such situations it can be observed that agents returns in an idle state after travelling a very short path, as a consequence of the damping effect of the social force.

In order to prove that the distribution of exit times is uniform and defined in the interval 10 s 100 s, it is, however, necessary to consider a larger number of agents. To this purpose 10^6 agents were generated and the resulting estimated probability density function (PDF) of response time from all the generated agents is reported in Figure 4.9. Results in Figure 4.9 prove that the generation of exit times is uniform and defined between 10 s and 100 s.

It is therefore proved that the developed tool passes the test. It is however underlined that the number of agents proposed by the IMO test condition (10) is clearly insufficient to obtain reliable information about the distribution of the response times from a single realization. It can therefore be suggested that this number is increased, or, equivalently, that the test is run a sufficiently large number of times in order to check the proper generation of response times from ensemble domain analysis.

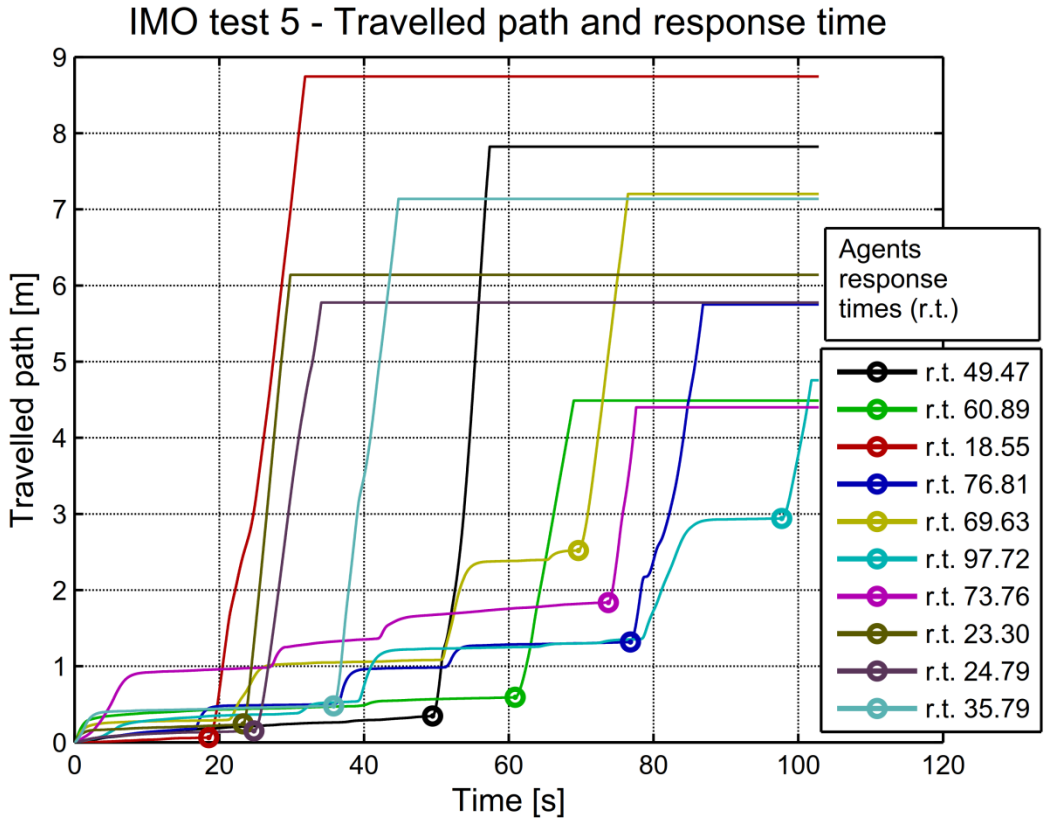

Figure 4.8: IMO test case 5. Travelled path of 10 agents as function of time. The response time for each agent is indicated in the figure.

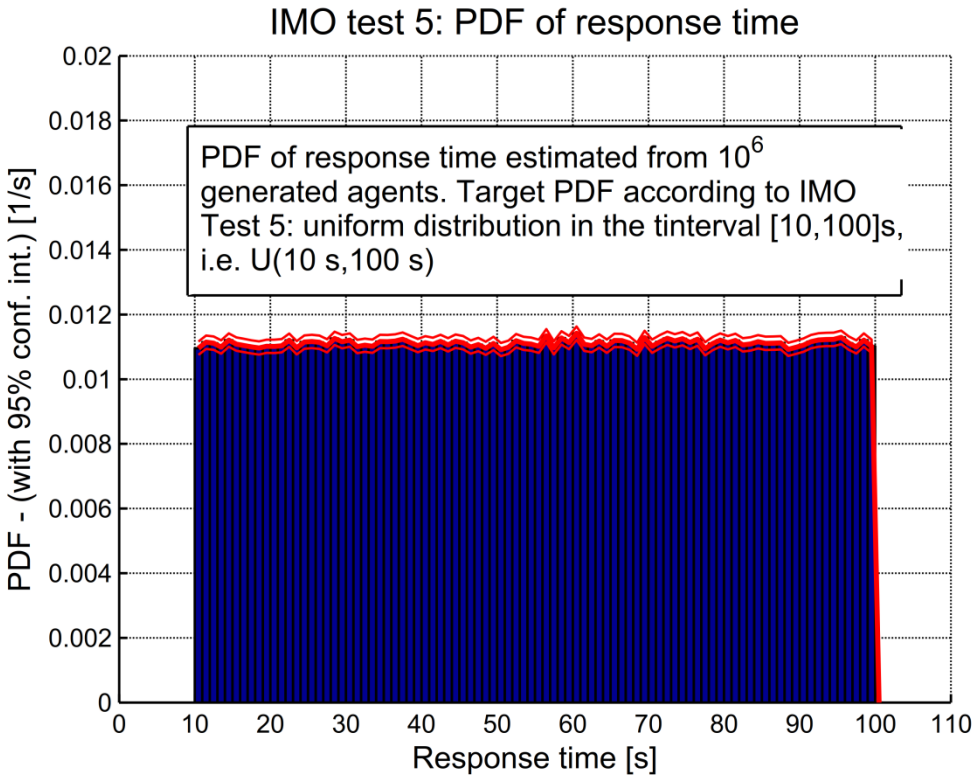

Figure 4.9: IMO test case 5. PDF of the response time calculated from 10^6 agents.

4.2.5 IMO test 6 (Rounding corners)

The description the test, according to MSC.1/Circ.1533, is as follows:

"Twenty persons approaching a left-hand corner will successfully navigate around the corner without penetrating the boundaries."

The geometry related to this test condition is reported in Figure 4.10.

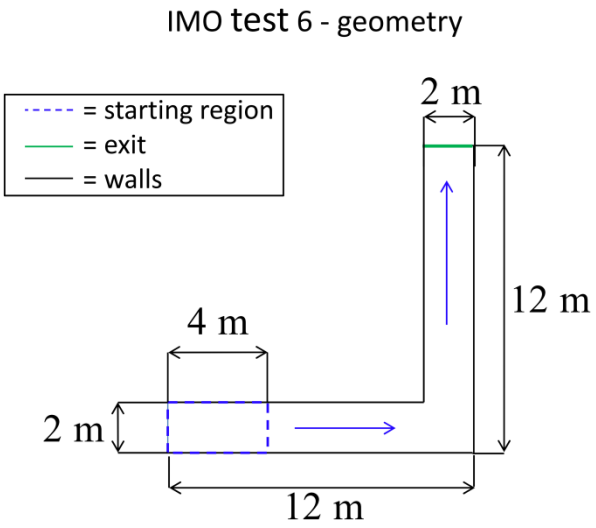

Figure 4.10 IMO test case 6. Geometry.

Two close triangular waypoints reported in Figure 4.11, were adopted for directing the behaviour of agents at corners, as such configuration of waypoints allow agents to modify their orientation in a progressive and more natural way during the turning. It is noted that, as an alternative, also the path finding algorithm might be used to effectively make agents moving around the corner. Modifications of the shape of waypoints have been checked in the analysis of this test case, and it was observed that changing the geometry of waypoints causes the paths of the agents to slightly change. However, the boundaries of the geometry are always respected and, thus, the requirement of the IMO test is always fulfilled.

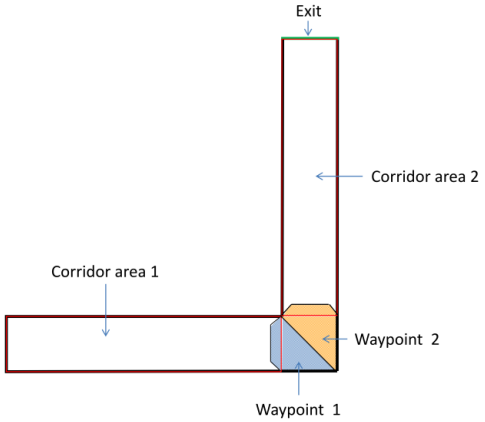

Figure 4.11 IMO test case 6. Waypoints.

A qualitative analysis is provided by the snapshots of the simulation reported in Figure 4.12 where agents can be seen navigating around the corner while a more detailed proof is reported in Figure 4.13, where the paths travelled by agents are reported all together. Although the figures report only the center position of the agents, the impenetrability condition is respected by the whole shape of the agent. In fact, if some agent enters in contact with a wall, the contact is resolved by the physics engine and the agent does not penetrate in the wall mesh with its volume.

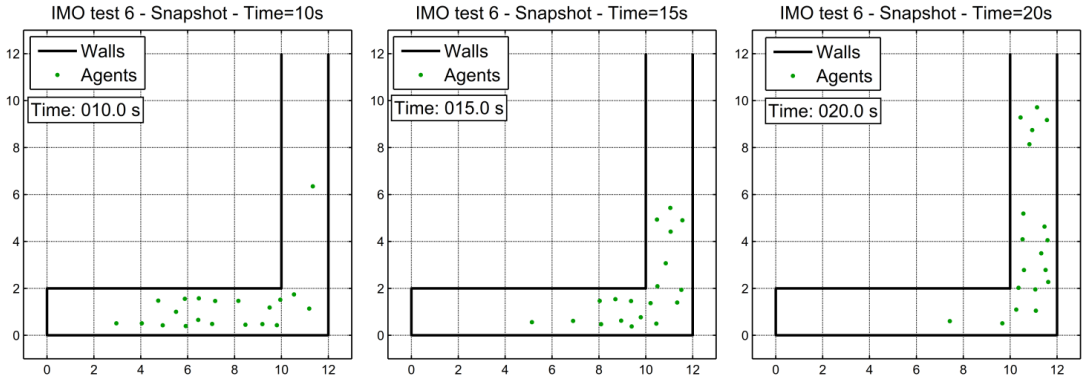

Figure 4.12: IMO test case 6. Snapshots.

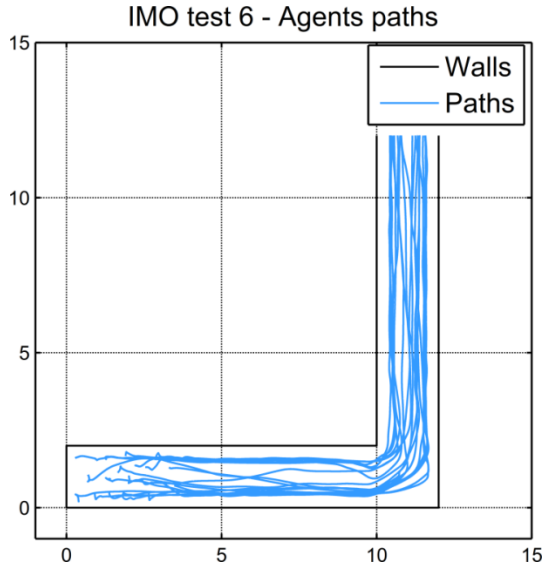

Figure 4.13: IMO test case 6. Paths travelled by the agents.

4.2.6 IMO test 7 (Assignment of population demographics parameters)

The description the test, according to MSC.1/Circ.1533, is as follows:

"Choose a panel consisting of males 30-50 years old from table 3.4 in the appendix to the *Guidelines for the advanced evacuation analysis of new and existing ships* and distribute the walking speeds over a population of 50 people. Show that the distributed walking speeds are consistent with the distribution specified in the table."

In accordance to the test case, 50 agents were generated and their speeds are plotted in Figure 4.14: it can be observed that the generated walking speeds are consistent with the provided distribution. The number of generated agents is, however, not sufficient to prove that the distribution is the one specified by the test case (i.e. uniform).

Herein the test case is generalized, to actually proving that the software is capable of generating the IMO population, as described in Table 4.1 and thus in accordance to the distribution provided by IMO for the unimpeded speeds and to the ones concerning the population compositions. To this end the theoretical parameters of the distribution (minimum, maximum, mean and standard deviation) are compared with the estimated parameters obtained from the generation of 50 and 10^6 agents. Results are reported in Table 4.3, from which it can be noticed that generation of parameters is in line with the target values.

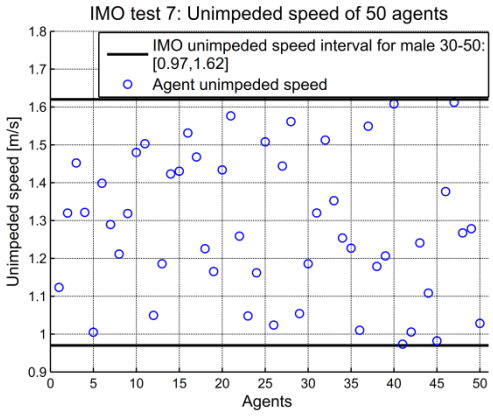

Figure 4.14: IMO test case 7. Unimpeded speed of 50 agents modelled accordingly to the test requirements.

Table 4.3: Comparison between target distributions of agents provide by the MSC.1/Circ1533 ([147]) and the distribution of the generated agents.

	G1	G2	G3	G4	G5	G6	G7	G8	G9	G10
Percentage of population	0.070 0.069 0.060	0.070 0.071 0.040	0.160 0.158 0.120	0.100 0.100 0.120	0.100 0.099 0.200	0.070 0.072 0.100	0.070 0.070 0.040	0.160 0.161 0.140	0.100 0.101 0.100	0.100 0.100 0.080
Minimum unimpeded speed [m/s]	0.930 0.930 1.035	0.710 0.710 0.963	0.560 0.560 0.643	0.430 0.430 0.448	0.370 0.370 0.438	1.110 1.110 1.190	0.970 0.970 1.075	0.840 0.840 0.853	0.640 0.640 0.646	0.550 0.550 0.697
Maximum unimpeded speed [m/s]	1.550 1.550 1.480	1.190 1.190 1.167	0.940 0.940 0.860	0.710 0.710 0.670	0.610 0.610 0.588	1.850 1.850 1.599	1.620 1.620 1.131	1.400 1.400 1.381	1.060 1.060 1.005	0.910 0.910 0.857
Mean unimpeded speed [m/s]	1.240 1.241 1.209	0.950 0.946 1.065	0.750 0.750 0.754	0.570 0.571 0.537	0.490 0.490 0.508	1.480 1.481 1.377	1.295 1.296 1.103	1.120 1.122 1.117	0.850 0.851 0.796	0.730 0.730 0.801
Standard deviation of unimpeded speed [m/s]	0.179 0.179 0.238	0.138 0.139 0.144	0.110 0.110 0.074	0.080 0.081 0.080	0.069 0.069 0.050	0.214 0.215 0.174	0.188 0.189 0.039	0.162 0.161 0.195	0.121 0.121 0.142	0.104 0.104 0.073

In each cell: Black = IMO unimpeded speed distribution (target values).
Red = Results considering 10^6 agents.
Blue = Results considering 50 agents.

G1: Females younger than 30 years; **G2:** Females 30-50 years old; **G3:** Females older than 50 years; **G4:** Females older than 50, mobility impaired (1); **G5:** Females older than 50, mobility impaired (2); **G6:** Males younger than 30 years; **G7:** Males 30-50 years old; **G8:** Males older than 50 years; **G9:** Males older than 50, mobility impaired (1); **G10:** Males older than 50, mobility impaired (2).

4.2.7 IMO test 8 (Counterflow – two rooms connected via corridor)

The description of the test, according to MSC.1/Circ.1533, is as follows:

"Two rooms 10 m wide and long connected via a corridor 10 m long and 2 m wide starting and ending at the centre of one side of each room. Choose a panel consisting of males 30-50 years old from table 3.4 in the appendix to the *Guidelines for the advanced evacuation analysis of new and existing ships* with instant response time and distribute the walking speeds over a population of 100 persons.

- **Step 1: One hundred persons move from room 1 to room 2, where the initial distribution is such that the space of room 1 is filled from the left with maximum possible density (see figure 2). The time the last person enters room 2 is recorded.**
- **Step 2: Step one is repeated with an additional ten, fifty, and one hundred persons in room 2. These persons should have identical characteristics to those in room 1. Both rooms move off simultaneously and the duration for the last persons in room 1 to enter room 2 is recorded. The expected result is that the recorded duration increases with the number of persons in counterflow increases."**

The geometry of the test case is reported in Figure 4.15**.**

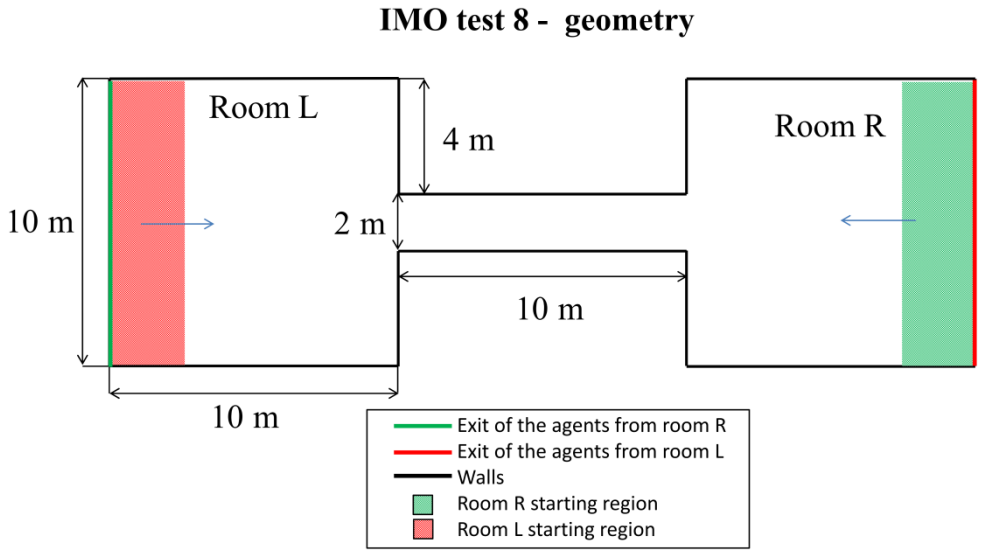

Figure 4.15: IMO test 8. Geometry.

Also for this tests, simulations have been run using the tool developed herein, as well as by means of FDS+Evac. Results from simulations regarding agents initially in room L are shown in Figure 4.16. A total of 250 independent realizations were carried out for each condition. The graphs show the 5%, 25%, 50%, 75%, 95% percentiles of the number of agents coming from room L and not yet in room R, as obtained from ensemble domain analysis at each time instant. It can be noticed that both tools (the one

developed herein, as well as FDS+Evac) pass the test, as it is observed that the egress duration increases with the number of counterflow agents.

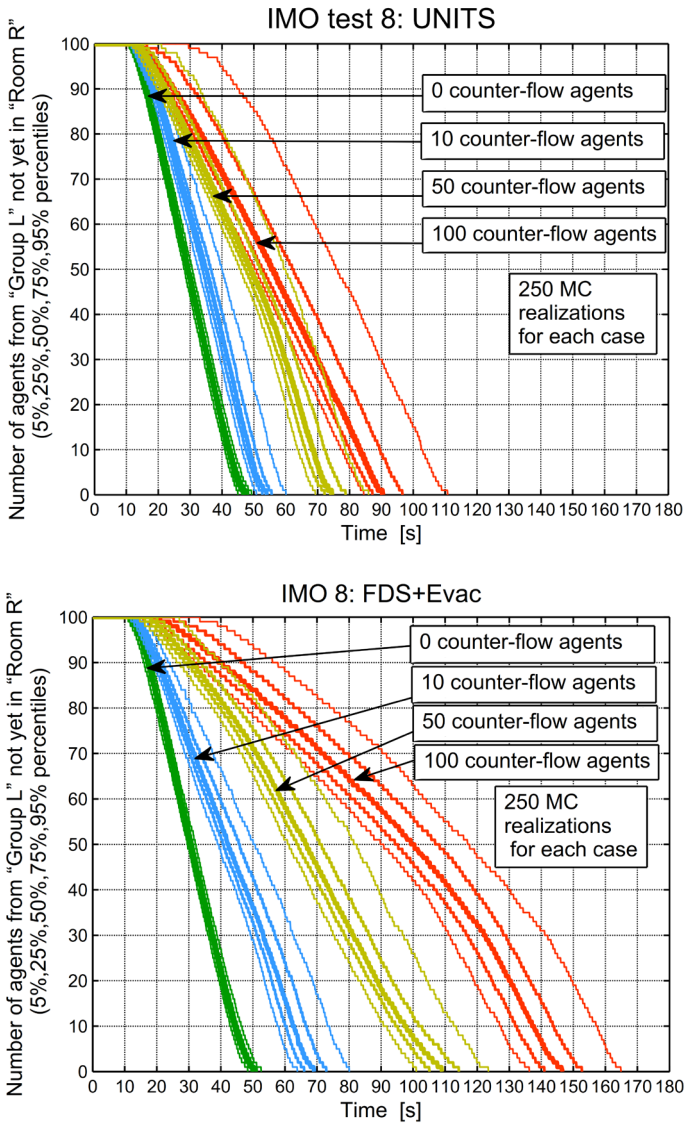

Figure 4.16: IMO test 8. Number of agents from "Group L" not yet in "Room R" as a function of time. UNITS (up) , FDS+Evac (down).

In general, results from UNITS code show a faster exit (here exit is meant as the arrival in room R from room L) compared to FDS+Evac. Looking at the curves of instantaneous ensemble percentile levels, it can be noticed that the 95% one is the farthest from the others, indicating a long tail of the instantaneous distribution for the number of agents. This means that, in certain, although limited, situations, the exit time can be significantly larger than the median exit time, and this indicates the importance of reporting, in a detailed way, the aleatory uncertainty associated with the results of an evacuation analysis. It can also be noticed that the exit time from FDS+Evac increases much more significantly that in case of UNITS as the number of agents in counterflow increases. From observation of the obtained simulations it could be noticed that this difference is due to the fact that in UNITS simulations the implemented counterflow

model tends to lead to the fast formation of two ordered lanes, which prevents the occurrence of jamming. Instead, the lane formation process in FDS+Evac simulations is slower and less organized, with a consequent increase of exit time.

In order to analyse the differences in the formation of the lanes between the two models, the graph clustering method described by Schaeffer [191] has been used, which was already used in the past also by Roggen et al. [178] to recognise group behaviour in crowds. According to this method, a graph is defined at each time instant of the simulations by connecting the agents. Two agents are connected if and only if the line connecting them does not intersect a wall. A disparity matrix is then obtained by considering the Euclidean distance between the agents in the graph. Subsequently, a hierarchical cluster structure is obtained with a bottom up clustering method. For any specified cut-off distance $d_{cut-off}$, the correspondent number of clusters can be determined. The number of clusters obtained according to this analysis is reported in Figure 4.17 as a function of time and of the cut-off distance. The agents considered in the analysis are only those coming from room L and moving towards room R, considering the case with 100 agents in counterflow. The reported number of clusters is the mean value across different realizations, at each time instant and for each considered cut-off instant.
For small values of the cut-off distance (less than about 1 m), the identified number of clusters depends more on the average distance between agents rather than on the actual number of groups which are actually formed by the agents. Larger cut-off distances, particularly in the interval $[1.5,3]m$, instead allow to actually identify groups of agents.
The presence of a large number of groups indicates that either the agents are not well organized in lanes or that the flow of agents is often interrupted. It can be noticed that, for the mentioned interval of cut-off distances, the number of identified groups is larger for FDS+Evac than for UNITS. It can therefore be deduced that FDS+Evac agents are less organized than UNITS agents and that the flow rate in FDS+Evac is often interrupted. Such results provide an explanation for the outcomes reported in Figure 4.16.

The application of this approach showed that FDS+Evac simulations are characterised by a more noticeable presence of separate groups compared to outcomes from the UNITS code, where agents tends to organise more orderly in lanes. FDS+Evac agents are therefore less organized than UNITS agents and the flow rate in FDS+Evac is often interrupted. The observed better organization behaviour arising in UNITS simulations is essentially due to the strength of the counterflow force and to the parameter regulating the preferred direction.

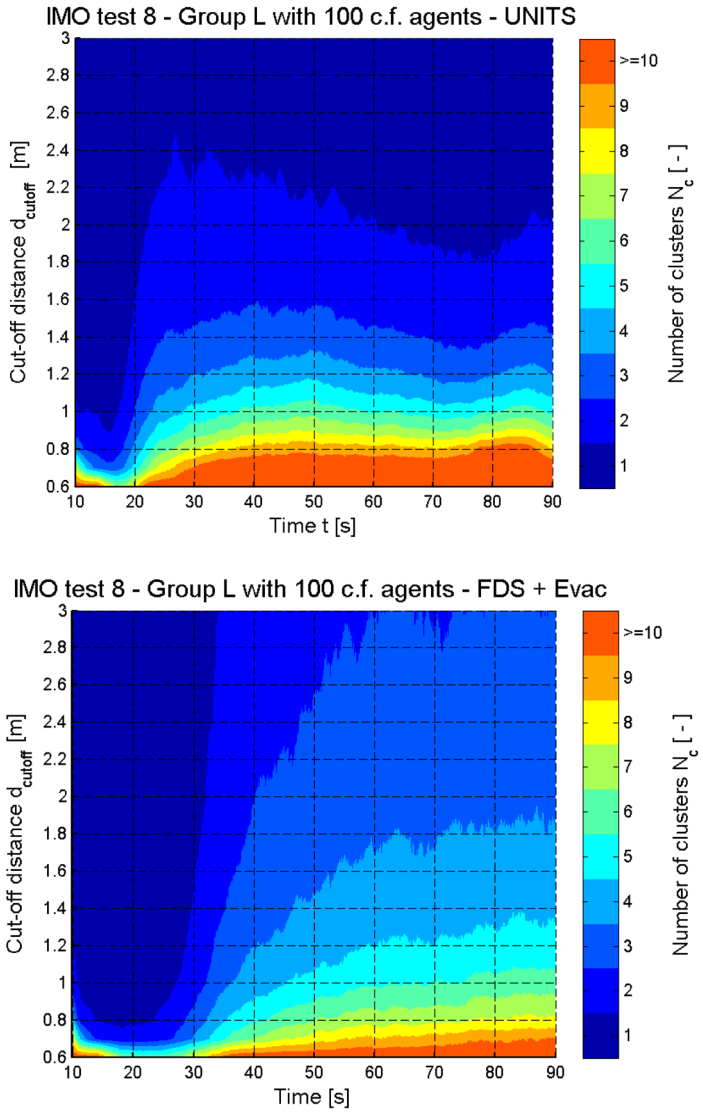

Figure 4.17: IMO test 8: Cluster analysis. The number of cluster N_C is reported in dependence of the time and of the cut-off distance $d_{cut-off}$.

The difference between UNITS and FDS+Evac results highlights the possibility of marked differences between two simulation models which are both passing the IMO test case 8, but it is not possible to decide on which model is more realistic in absence of experimental data. However, it is reasonable to suppose that experimental data could as well be influenced by variability of organizational skills depending on the tested population, similarly to what was observed by Chattaraj et al.[22] in case of tests related to flow-density relation analysis. The reported observations also highlight the value of assessing evacuation performance taking possibly into account different simulation tools.

4.2.8 IMO test 9 (Exit flow: crowd dissipation from a large public room)

The description the test, according to MSC.1/Circ.1533, is as follows:

"Public room with four exits and 1,000 persons (see figure 3) uniformly distributed in the room. Persons leave via the nearest exits. Choose a panel consisting of males 30-50 years old from table 3.4 in the appendix to the *Guidelines for the advanced evacuation analysis of new and existing ships* with instant response time and distribute the walking speeds over a population of 1,000 persons.

- **Step 1: Record the amount of time the last person needs to leave the room.**
- **Step 2: Close doors 1 and 2 and repeat step 1.**

The expected result is an approximate doubling of the duration to empty the room."

The geometry of the test case is reported in Figure 4.18.

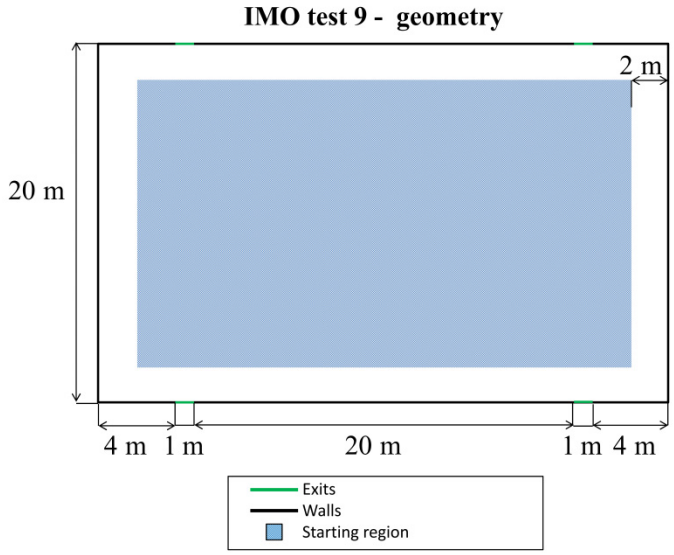

Figure 4.18: IMO test 9. Geometry.

The test case aims at assessing the capability of the software to simulate a large crowd and to correctly distribute all the possible targets to the agents. At the present stage of development, the software does not implement an internal logic for the dynamic choice of waypoints by the agents. The choice of waypoint is thus not influenced by behaviours such as herding as, for example, in case of the model presented by Helbing et al. [73] or by grouping or by communication between agents ([229]).

Each agent chooses the waypoint in accordance to its known pre-defined path. When the agent is in a region for which it has not a specified next waypoint, the closest waypoint among all waypoints connected to that region is chosen, at the condition that the closest waypoint is not the last one visited before entering the current area, if so the agent choses the second closest waypoint and so on.

In the present test case this logic assures that each agent at each time step is directed towards the exit which is closest to its instantaneous position. Each door is identified in

the simulation by an opening in the wall and a waypoint corresponding to the opening (see Chapter 2). Closed doors, instead, are considered in the same way as walls.

Snapshots from simulations of the two specified test conditions are reported in Figure 4.19. At the beginning of the simulation the agents are randomly positioned within the room. When the simulation starts, each agent directs towards the closest exit thus four discernible groups are formed in the condition with four exits whereas two larger groups are formed in the condition with two exits.

Clogging occurs at each of the exits and it is responsible of increasing the density and for slowing the exit rate. At the beginning of the simulations, the groups of agents close to each exit are not symmetrical with respect to the axis of the respective exit. However, the groups get more symmetrical as the time progresses and the dimension of the groups reduce. This feature is due to the way the agent desired direction is defined. Although experimental data are not available at the moment to clarify if this asymmetry represents a real behaviour, it is observed that this asymmetry is also present in the snapshots obtained with the model presented by Baochen et al. [5].

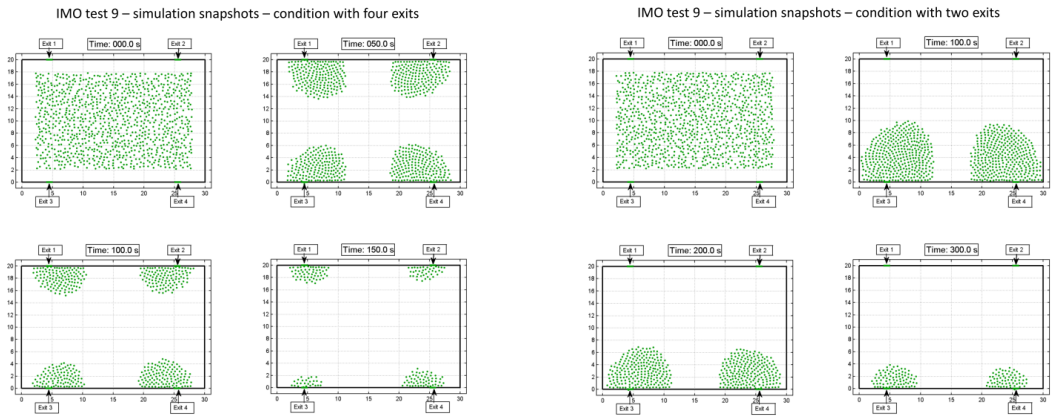

Figure 4.19: IMO test 9. Snapshots from single realizations of the two test conditions. Left: four exits, Right: two exits.

A total of 250 independent realizations for each test condition were performed. Figure 4.20 shows the median and the 5% and 95% percentiles of the number of agent inside the room at each time instant from ensemble domain analysis. The trend is almost linear although a slight non-linear behaviour can be observed at the beginning of the simulation, in the case with 2 doors, and at the end of the simulations in both cases. The exit rate in case of two doors, indeed, starts with a reduced value and then rises slightly to a steady value after the simulation around 30 s. This behaviour might be due to the action of the nervousness model. The decrease of the exit rate in correspondence of the end of the simulation has two main causes: firstly, the last agents are usually the slowest ones and, secondly, the last agents have no other pushing agents behind. This effect can be observed also in case IMO test 4 (see Figure 4.6).

Figure 4.21 shows a comparison between the exit time obtained by UNITS and those obtained by other tools. The results for other simulation tools were extracted from Baochen et al. [5].

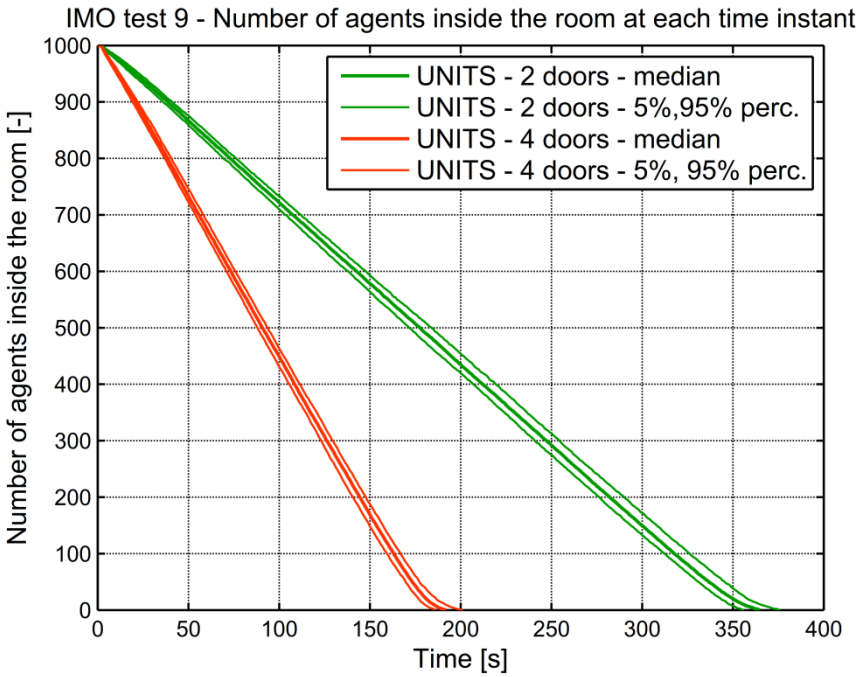

Figure 4.20: IMO test 9. Number of agents in the room as a function of time.

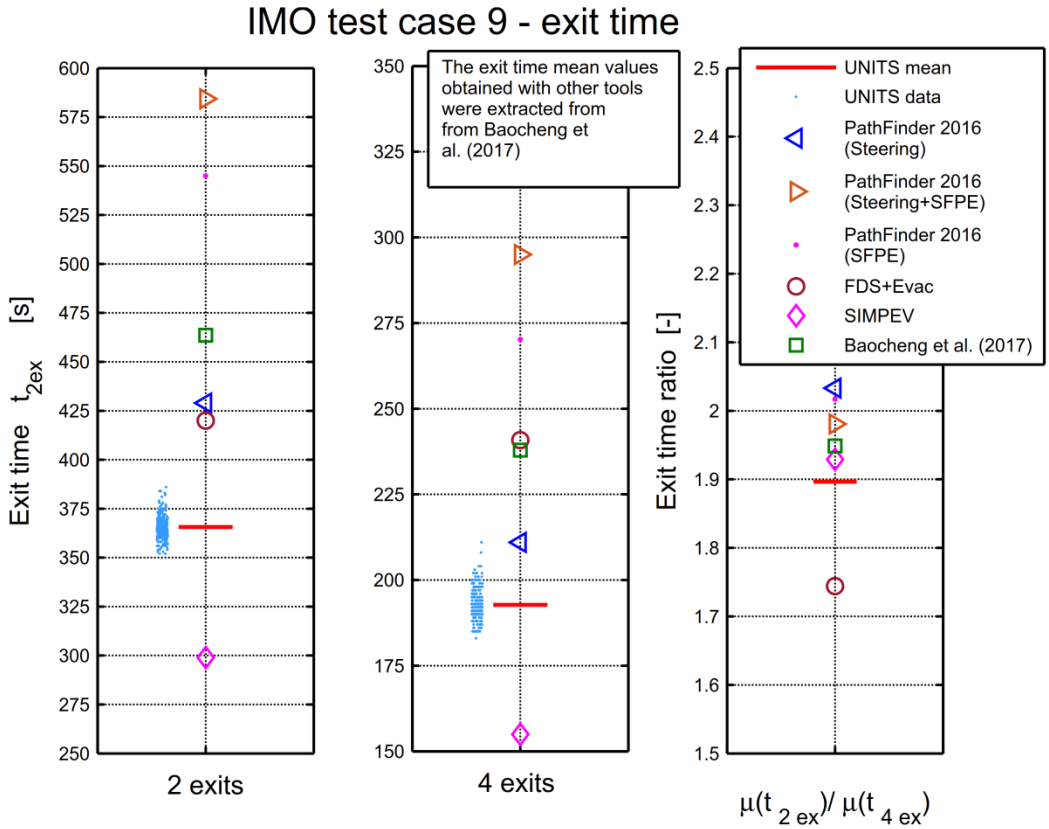

Figure 4.21: IMO test 9. Mean exit times.

From results in Figure 4.21, the difference between the simulate exit times among various tools is evident and considerable. The values obtained with by the tool developed herein are reasonably in line with those obtained with the other tools, although the exit time from present simulations tend to be shorter than most of the other tools.

This result might be explained by the combined effect of the social force model and of the nervousness model. On the one hand the social force model allows reproducing the pushing behaviour of back agents, therefore the speed of slower agents is increased as they are pushed by faster agents pushing from behind. On the other hand, the developed nervousness model also increases the flow by increasing the magnitude of the motive force in situation of prolonged congestion, as it is the case for the conditions simulated herein, particularly in case of only two exits.

The pushing behaviour has an effect also on the ratio between the exit times with 2 and with 4 doors available. This effect is due to the fact that in case with two doors the agents in front of the doors are more pushed by the social force of surrounding agents with respect to the other case. Due to the forces originated by the pushy behaviour, thus, the speed of the agents exiting the room might result increased in the case with two exits with respect to the case with four exits. This effect might change the ratio between the exit times, slightly decreasing the exit times related to the case with two exits.

The ratio found with FDS+Evac is, indeed, quite far from 2 (a value which would that indicate an exact doubling of the exit time). Instead, the ratio found with UNITS code is around 1.9, i.e. quite close to 2. It is interesting to underline this difference since both tools are based on the social-force modelling, although they differ in a series of aspects.

It is observed that, again, the lack of reference experimental data and of specific quantitative requirements in the IMO test case make impossible to establish which tools, among the reported ones, are better performing. Although it is clear that the exit time should increase in the case with only two exits with respect to the case with more exits, it is possible that the exit time dependence from the number of exits is not linear. Specifically, the flow might be increased by a rise of the density in the neighbourhood of the exits, when only a reduced number of exits is available. Moreover the nervousness of people and the pushing behaviour might also play a role in increasing the speed of the slowest agents when the number of exit is reduced. Considering these observations, the correspondence between the halving of the number of the exits and the doubling of the exit time might need additional experimental confirmations.

4.2.9 IMO test 10 (Exit route allocation)

The description of the test, according to MSC.1/Circ.1533, is as follows:

"Construct a cabin corridor section as shown in figure 4 populated as indicated with a panel consisting of males 30-50 years old from table 3.4 in the appendix to the *Guidelines for the advanced evacuation analysis of new and existing ships* with instant response time and distribute the walking speeds over a population of 23 persons. The people in cabins 1, 2, 3, 4, 7, 8, 9, and 10 are allocated the main exit.

All the remaining passengers are allocated the secondary exit. The expected result is that the allocated passengers move to the appropriate exits."

The geometry of the test case is reported in Figure 4.22, where also the distribution of persons (agents) in the cabins and the exits allocated to each person (agent) are reported.

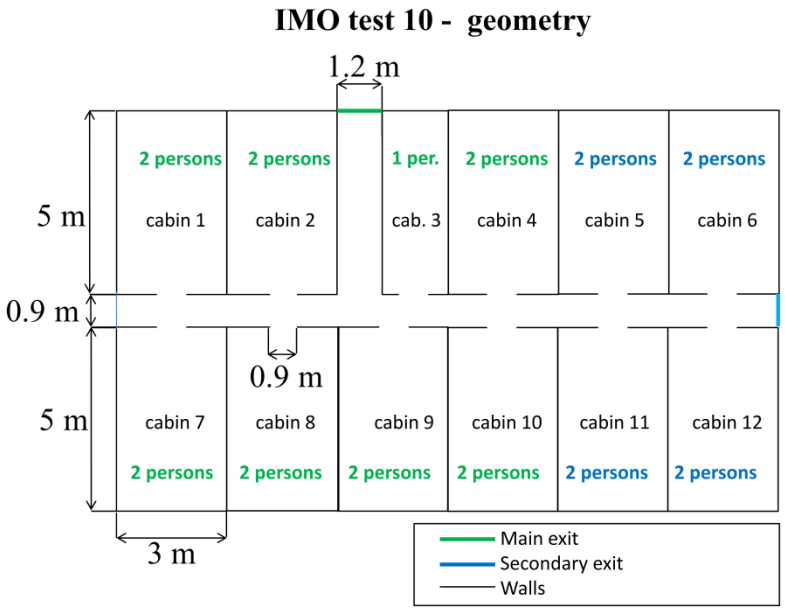

Figure 4.22: IMO test 10. Geometry.

The paths travelled by the agents are reported in Figure 4.23. The Figure 4.23 shows that each agent correctly travels towards the assigned exit. It can also be observed that paths are not straight, as agents interact with each other.

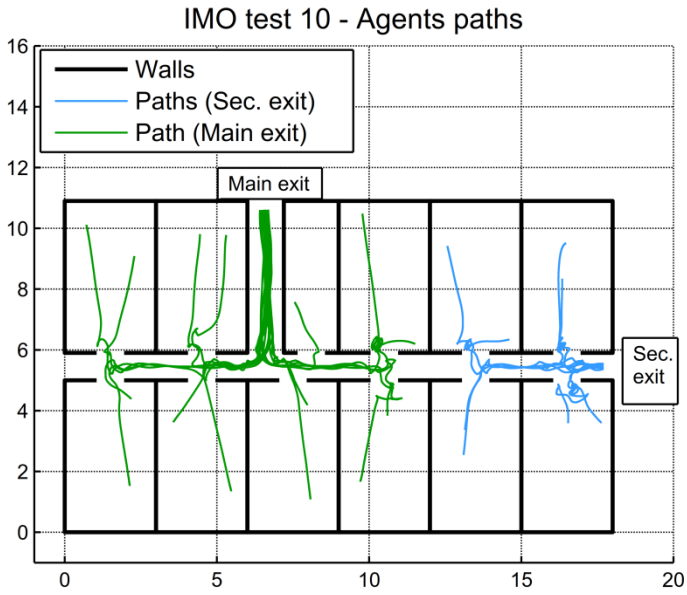

Figure 4.23: IMO test 10. Travelled paths.

4.2.10 IMO test 11 (Staircase)

The description the test, according to MSC.1/Circ.1533, is as follows:

"Construct a room connected to a stair via a corridor as shown in figure 5 populated as indicated with a panel consisting of males 30-50 years old from table 3.4 in the appendix to the *Guidelines for the advanced evacuation analysis of new and existing ships* with instant response time and distribute the walking speeds over a population of 150 persons. The expected result is that congestion appears at the exit from the room, which produces a steady flow in the corridor with the formation of congestion at the base of the stairs."

The test case is meant to assess the capability of the tool to correctly simulate the human behaviour in front of a stair entrance, and the geometry of the test is reported in Figure 4.24. However the IMO test case 11 does not specify the characteristics of the stair. Herein a nominal stairway is considered with projected length of 10 m (i.e. length parallel to deck) and height of 6 m, corresponding to an incline of 31°. In order to analyse the occurrence of congestion, time histories of agents' densities are calculated in areas A, B and C, as indicated in Figure 4.24.

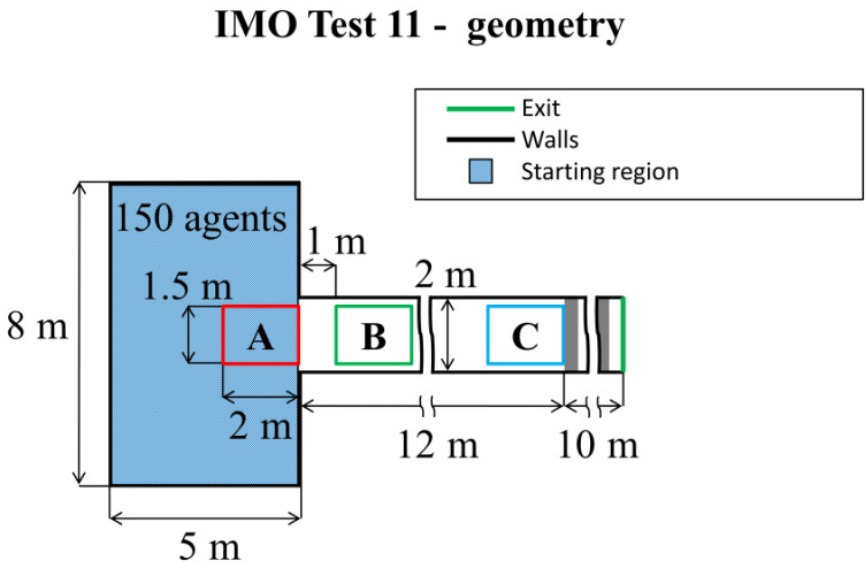

Figure 4.24: IMO test 11. Geometry.

Given a closed region Ω with area A_Ω $[m^2]$ the instantaneous density $\delta_\Omega(t)$ $[p/m^2]$ in the region Ω is determined as:

$$\delta_\Omega(t) = \frac{n_\Omega(t)}{A_\Omega} \tag{4.1}$$

where $n_\Omega(t)$ $[p]$ is the number of agents inside the region Ω at time t. The density $\delta_\Omega(t)$ has been analysed from UNITS and FDS+Evac simulations on the basis of 250 random realizations for each simulation tool, and results are reported in Figure 4.25.

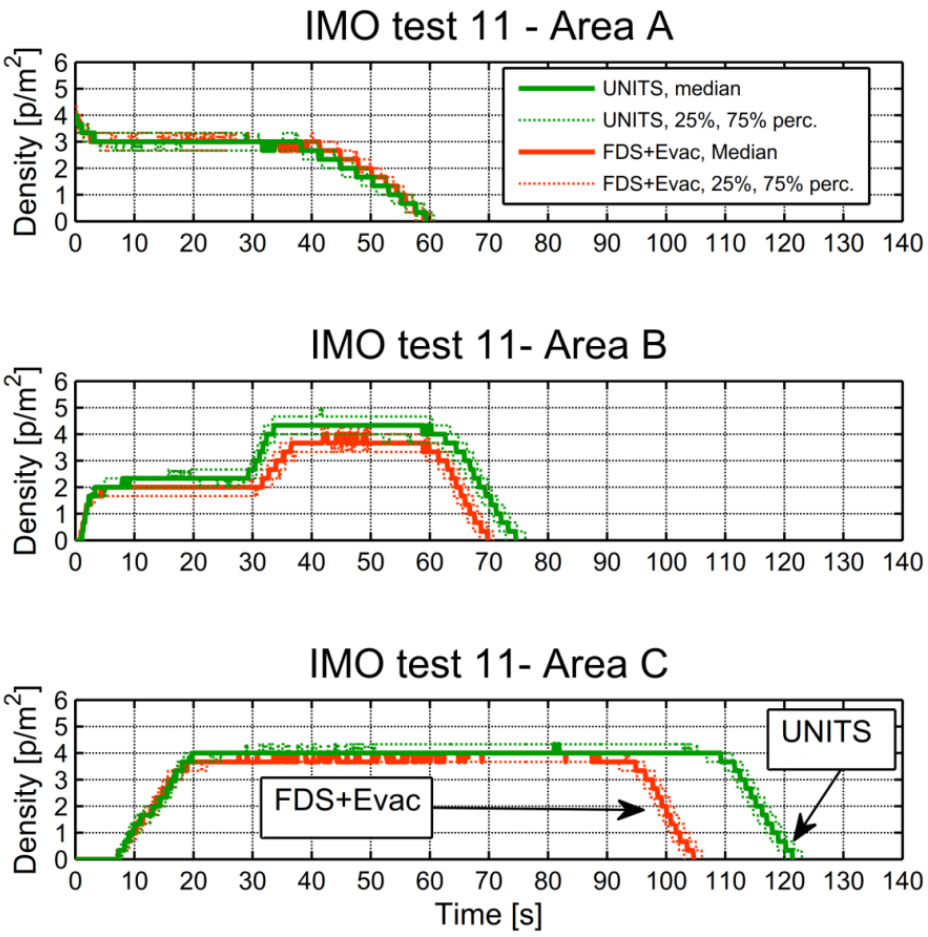

Figure 4.25: IMO test 11. Time-density relation for analysis areas A, B and C.

Results in Figure 4.25 indicate that, after the time necessary for the agents to reach the base of the stairs, the congestion is located only at the stairway entrance and the density in the corridor is low. As the simulation proceeds, the congestion spreads upstream along the corridor reaching region B causing a sharp rise of density (approximately after t=30 s). Afterwards, the density remains almost constant, until it decreases due to the fact that the room is progressively emptied. It can be noticed that the behaviour simulated by FDS+Evac and by the UNITS code is very similar, although FDS+Evac densities tend to be smaller. Furthermore, the total egress time from FDS+Evac is, for this test, shorter than that from the UNITS code.

Further insight into the time-space evolution of the density in the corridor can be obtained by results reported in Figure 4.26 as obtained from UNITS simulations. The figure shows the average density, over 250 realizations, in rectangular regions placed at different positions along the corridor. The region of analysis is 1.5 m wide and 2 m long, as those in Figure 4.25. The position of the measuring region is indicated by the coordinate x of its left edge, with $x = 0\,m$ corresponding to a region at the start of the

corridor. The analysis is carried out with regions shifted by $\Delta x = 0.1 m$, covering the entire corridor.

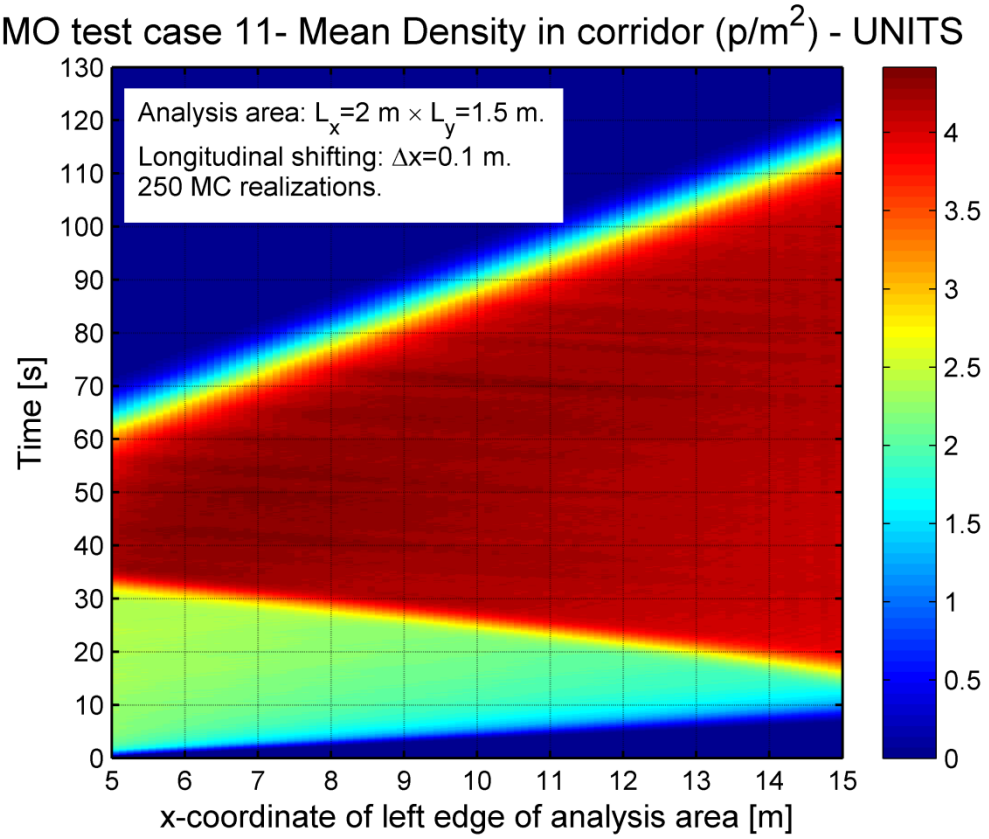

Figure 4.26: IMO test 11. Time-space analysis of average density in the corridor (250 realizations). UNITS results

Results in Figure 4.26 clearly show the spreading of the high-density region from the bottom of the stairs upstream throughout the corridor. The speed of this spreading, corresponding to the slope of region characterised by the sharp density rise is approximately 1.5 m/s. Horizontal bands of higher and lower density are visible in the region with higher density. These bands indicate oscillation of density in time and space, and subsequent observations of the simulation outcomes have shown that this is associated with the occurrence of stop-and-go effects as described by Helbing et al. [74].

4.2.11 IMO test 12(Flow-density relation)

The description the test, according to MSC.1/Circ.1533, is as follows:

"The software should be tested for a corridor without any obstructions. It should be demonstrated that the flow of persons in the corridor is generally smaller at very high population densities compared with that at moderate densities."

This test case was added in the revised version of the guidelines, as it was not present in the previous ones (see MSC.1/Circ.1238 [146]). The content of the test case appears to have been a topic of debate at IMO, as in SDC 3/WP.6 [193] the same test case was

more detailed, the title was different ("Fundamental diagram") and it proposed also a comparison between the simulation outcomes and the fundamental diagram reported in Weidmann [223]. The final version of the IMO test case is, instead, much more general.

The fundamental diagram was introduced by Weidmann [223] in order to describe the relation between the specific flow (the flow normalized by the width of the considered facility) and the density. Weidmann [223] assumed that this relation hold for different width of the facilities and in different situations and therefore a unique analytical definition of this relation could be obtained by fitting experimental data. It is however to note that more updated data concerning the flow density relation (e.g. [22], [234]) are present in literature. Moreover, Chattaraj et al. [22] highlights the marked differences among the fundamental diagrams available in literature based on experimental outcomes. This seems to indicate that the assumption from Weidmann [223] was too simplistic, and that the flow-density relation is dependent on the specific characteristic of the problem.

Nevertheless, the common feature among all the different experimental outcomes related to the flow-density relation seems to be the fact that specific flow rises with density up to a certain value (this limit density value is not equal for all experimental outcomes) and then decreases for higher density values. However, the value of density that maximizes the flow and the upper limit of density for which the flow becomes null are different from case to case, and might depend on the test condition and on the specific properties of the people involved.

The IMO test case 12 is therefore to be intended as a test to assess the capabilities of the software to correctly simulate those features of the flow-density relation which are qualitatively common to all experiments.

However in order to univocally reproduce the test condition by allowing quantitative comparisons between different simulations tools, a more detailed description of the case would be needed. A more detailed test should provide, in particular, the length of the corridor, the number of people, and two intervals of density quantifying the expressions "moderate densities" and "very high densities".

Another difficulty in reproducing this test case was found in the implementation of the initial condition. In microscopic models adopting repulsive forces, such as the social force model, it is difficult to create high density conditions at the very beginning of the simulation. In fact, due to the repulsive forces, agents get far one from another at the very beginning of the simulation causing the density to reduce. This behaviour is reasonable, as it is a common behaviour of people to occupy the available space in order to maintain a reasonable distance one from the other, when this is possible.

Indeed, the problem of creating a condition of a high but controlled density in a corridor is present also in the experiments performed with real people. Different solutions, aiming at creating controlled density experimental conditions, are described in literature. Seyfried et al. [196] presented an experiment where people walked around an elliptical corridor. The density could, thus, be considered constant and equal to the number of the subjects divided by the area of the corridor. In the experiment presented

by Zhang [234], instead, the density in the corridor was regulated by changing the width of the entrance and of the exit from the corridor.

The solution of the elliptical corridor allows keeping a constant density in the corridor during the whole experiment while in the other case the density fluctuates in accordance to the instantaneous flow of agents exiting end entering. However, in the first case the path followed by the people is not straight and the flow is thus affected by the change of direction. Presently there seems to be no sufficient data available in literature concerning the difference between the flow in a straight corridor and in a curved corridor.

It appeared, thus, more indicated to consider the method reported by Zhang [234] to obtain different density conditions for the IMO test case 12. The fundamental diagram obtained simulating the same experimental condition proposed by Zhang [234] considering the experiment of unidirectional flow is presented in the following section where also comparisons with outcomes of the software FDS+Evac and with experimental data are proposed. It is anticipated that the qualitative behaviour described in the IMO test case 12 concerning the flow-density relation is successfully reproduced by the model.

4.3 Flow-density relation and fundamental diagram

As observed before, relations between flow and density, or speed and density, play an important role in the estimation of evacuation performance of a designed ship arrangement and qualitative requirements for the flow-density relations are present in MSC.1/Circ.1533 [147].

Due to the discrete Lagrangian nature of microscopic model, the flow associated with a simulation run can be defined in different ways (Zhang [234]). Considering the situation of a unidirectional flow in a rectangular corridor, the definition adopted herein for the instantaneous flow $\Phi_{\Omega}(t)\,[p/s]$, associated with the rectangular measurement region Ω having the same width of the corridor, is described by the following equation:

$$\Phi_{\Omega}(t) = \delta_{\Omega}(t) \cdot \overline{v}_{\Omega} \cdot b_{\mathrm{CORR}} \tag{4.2}$$

where $\delta_{\Omega}(t)$ is the density $[p/m^2]$ as reported in equation (4.1), $\overline{v}_{\Omega}(t)$ $[m/s]$ is the mean speed component of agents along the corridor axis within Ω, and b_{CORR} $[m]$ is the width of the corridor.

Two test cases are considered in this section, for which experimental data are available, namely:

- A corridor ([234])
- A T-junction ([234], and see also [237])

Simulations are compared with available experimental data in the two mentioned cases in order to check that the expected qualitative behaviour for the flow-density relation is

reproduced, and to analyse, for validation purposes, the level of agreement between simulations and experiments. According to Zhang [234], in both experimental test cases the population was composed of young adults having free walking speed uniformly distributed in the interval 1.55 ± 0.18 m/s. Such speed has herein been taken as the unimpeded walking speed of agents. In both cases the dimensions of agents in the simulations are taken considering the "Adult" class reported in Table 4.2.

Simulations have been carried out and analysed in accordance with the experiments and corresponding data analysis from Zhang [234] and Zhang et al. [237]. The flow-density relation was estimated by determining the density and the correspondent flow only in the portion of the simulations where the flow could be considered sufficiently stationary, neglecting, therefore, transient regions. A total of 100 realizations were carried out for each test case and time windows of stationarity were manually determined for each test case by analysing the time histories of ensemble mean values of density and speed.

4.3.1 Flow-density relation in a corridor

The test case of evacuation through a corridor is of course relevant to the case of ship evacuation. Moreover, as one of the main targets of ship evacuation analysis is the detection of congestions (high density situations with low flow rate), the capability of an evacuation simulation tool to reproduce such congestions is clearly fundamental. Figure 4.27 shows the geometry of the test case by Zhang [234] characterised by a corridor width of 1.8 m. In order to change the density in the corridor, nine test conditions were considered by varying the room exit width b_R, the corridor exit width b_E and the number of people n, as reported in Table 4.4. Simulations have been carried out using both the tool developed herein as well as FDS+Evac, for comparison purposes.

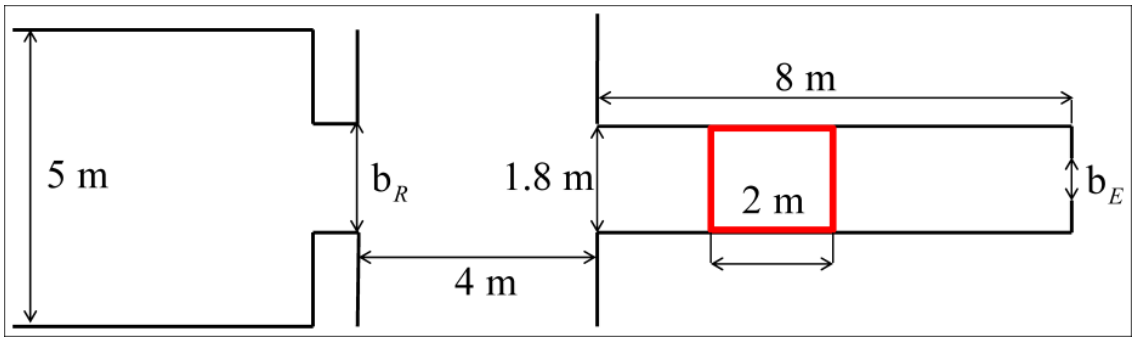

Figure 4.27: Corridor experiment by Zhang [234]. Geometry

Table 4.4: Corridor experiment by Zhang [234]. Main parameters for each experimental condition.

b_R (m)	0.50	0.60	0.70	1.00	1.45	1.80	1.80	1.80	1.80
b_E (m)	1.80	1.80	1.80	1.80	1.80	1.80	1.20	0.95	0.70
n	61	66	111	121	175	220	170	159	148

The flow–density relation as obtained by the UNITS code and by FDS+Evac are reported in Figure 4.28. In order to compare simulations with the experimental results presented by Zhang [234], data are reported in terms of actual flow (see (4.2)) instead of the more commonly used specific flow (i.e. flow normalised by the width of facility). To avoid an excessive number of curves, the figures report only median values conditional to the density, as derived from the flow–density data obtained from simulations. Since experimental data have been reported by Zhang [234] in terms of scatter plots, reference experimental data are herein reported as areas where scatter data from Zhang [234] are (approximately) present.

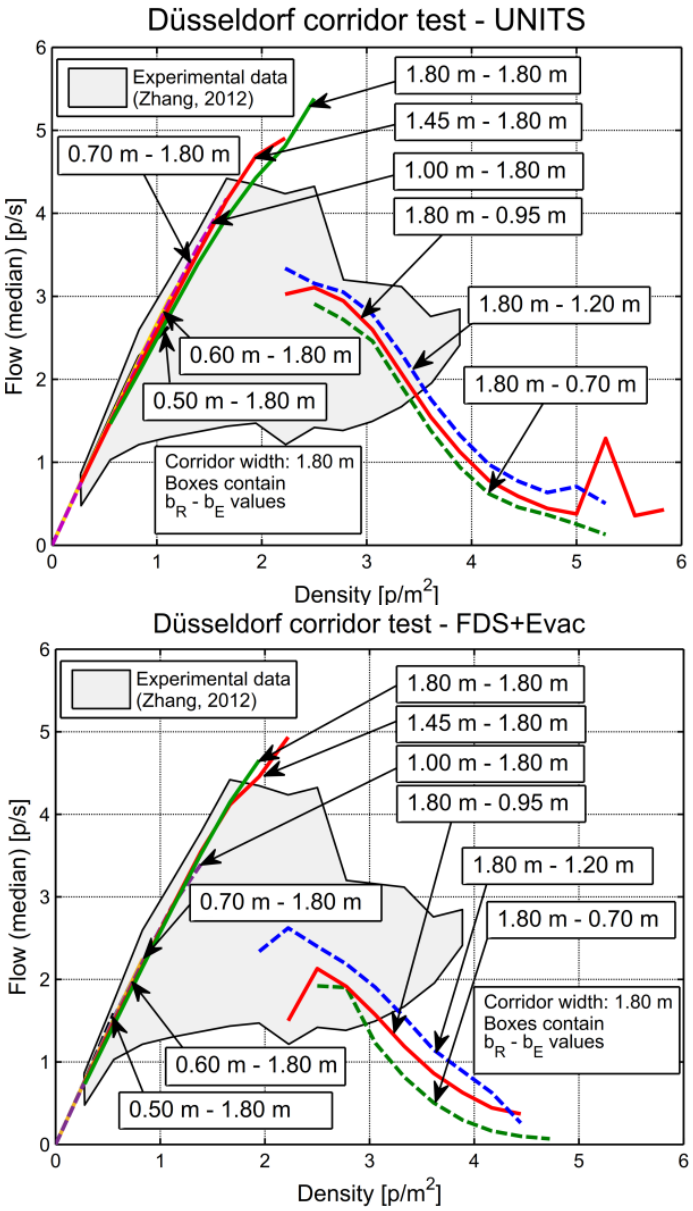

Figure 4.28: Corridor experiment by Zhang [234]. Flow as a function of the density for each simulation run. Only steady states are considered in the analysis. Simulation results are compared with the region of experimental outcomes as reported by Zhang [234]. Left: UNITS code, Right: FDS+Evac.

Results in Figure 4.28 show that the main patterns of the flow-density relation are reproduced by the simulations. The maximum flow corresponds to a density of approximately $2 \mathrm{p/m^2}$, which is in agreement with test results and with most of the fundamental diagrams presented by Chattaraj et al. [22].

There is a notable difference between the simulated flow rate of those situations where the exit has the same width as the corridor ($b_E = 1.8\,m$) and those where the exit is narrower than the corridor ($b_E < 1.8\,m$). These two conditions are also linked with the marked discontinuity, located approximately at density of $2 \mathrm{\ p/m^2}$, which can be clearly noticed in both UNITS and FDS+Evac results. The observed differences can be associated to the fact that when the exit width is narrower than the corridor width, agents have to organize to exit from the corridor, and this generates situations with high density but very low speed in both UNITS and FDS+Evac simulations. Instead, according to the scatter plots by Zhang [234], the actual behaviour from experiments seems to be smoother. Moreover experiments do not reach as high densities as those reached in the simulations. This might be due to the fact that humans can organize better than simulated agents when exiting from the bottleneck. It is also reasonable to think that people try to slow down in advance if they see a clogging ahead, and this behaviour might prevent the density from rising to very high values. Instead, in the social force models characterised by short-range interaction forces, agents slow down only when they are very close to other agents, and this results in higher density conditions.

A more detailed analysis is performed in Figure 4.29 which presents scatter plots from simulations with UNITS code, together with 5%, 25%, 50%, 75%, 95% percentiles (conditional to density). The observed spread of data indicates the difficulty in the quantitative determination of a representative flow-density relation with too few tests. The dispersion of flow data conditional to the density is smaller in low-density conditions while it is larger in high-density conditions. An increase of conditional dispersion of flow given density in high-density conditions can also be noticed in the experimental scatter plots from Zhang [234]. This behaviour shows that, while for relatively low densities the flow-density relation is well determined by the unimpeded speed and by the geometry, in high density conditions the capability of organization of people has an important effect and can lead to a high level of uncertainty.

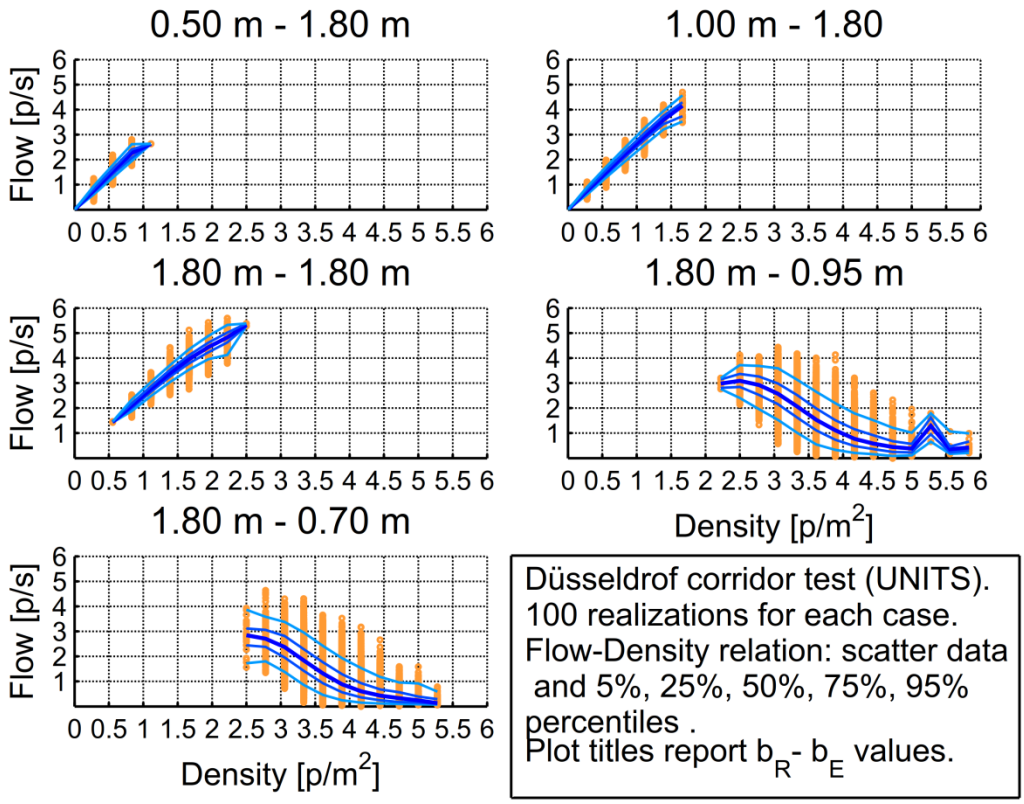

Figure 4.29: Corridor experiment by Zhang [234]. Data scatter plots together with 5%, 25%, 50%, 75%, 95%, conditional percentiles of flow given density for a set of different simulation conditions.

4.3.2 Flow-density relation in a T-junction

T-junctions are a type of element which is typically present in the arrangement of vessels (MSC.1/Circ.1533 [147]; SAFEGUARD Validation Data Set 2 [186]), especially in case of large passenger vessels with cabin areas (see, e.g., Figure 4.22). The flow-density relation inside a T-junction can be different from the one measured in a simple corridor, as observed by Zhang [234]and Zhang et al. [237]. Moreover the flow-density relation is also different depending on the specific measurement area in the T-junction. A comparison between data provided by Zhang [234] and Zhang et al. [237] and simulation results obtained from FDS+Evac and the UNITS code was therefore performed. Figure 4.30 shows the geometry of the T-junction used in the experiments by Zhang [234] and Zhang et al. [237]. The properties of the agents in the population used for the simulation are the same as the ones specified in for the corridor test case. The exit width b_E, the width b_R of entrances towards the corridor, and the number of people on each side were changed to obtain different density condition in accordance to Geometry
Table 4.5.

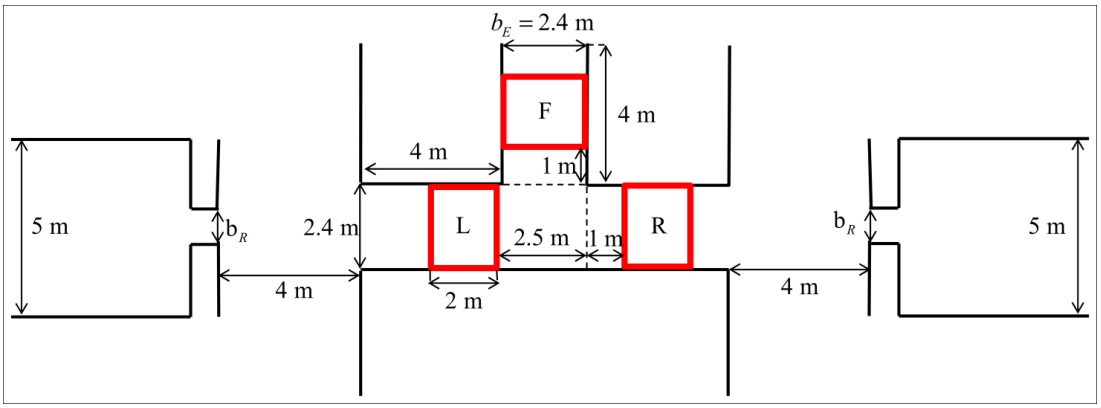

Figure 4.30: T-junction experiment by Zhang [234]. Geometry

Table 4.5: T-junction experiment by Zhang [234]. Main parameters for each experimental condition.

b_R (m)	0.50	0.60	0.80	1.00	1.20	1.50	2.40
n left	67	66	114	104	152	153	151
n right	67	66	114	104	153	152	152

In order to allow direct comparisons with the experimental data presented by Zhang [234] and Zhang et al. [237], results are reported in this section in terms of specific flow (flow normalized by the width of facility). Figure 4.31 reports UNITS results as conditional median specific flow for each test condition and for each region highlighted in Figure 4.30. A total of 100 Monte Carlo realizations were carried out, and, in the analysis of simulations, only data at stationary states were considered. The figure also reports an indication of the region of each graph corresponding to the experimental scatter data from Zhang [234] and Zhang et al. [237]for all values of b_R .

Results in Figure 4.31 show differences between the conditions leading to high-density ($b_R = 1.50\,m$ and $b_R = 2.40\,m$) and the other cases.

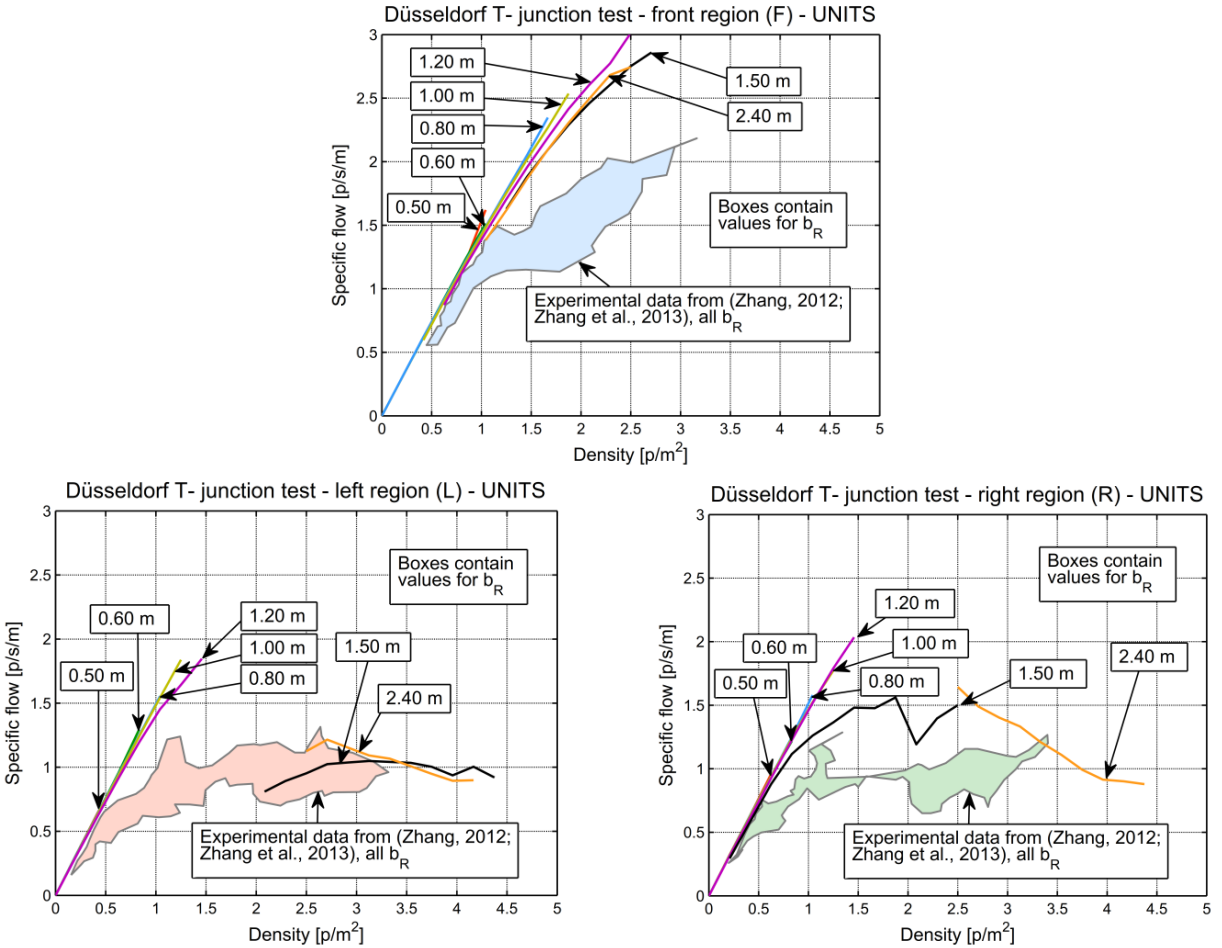

Figure 4.31: T-junction experiment by Zhang et al. [237]. Comparison between simulation results and experimental data regarding the relation between density and specific flow. The outcomes from 100 simulations for each experimental case are compared with the region obtained experimentally. Centre-up plot: front region (F), Bottom-left plot: left region (L), Bottom-right plot: right region (R).

This difference is very marked in the left region, with the occurrence of a discontinuity. The difference is marked, but without discontinuity, in the case of right region, and it is almost not present in the front region. Although simulation results do not match quantitatively well the experimental data, it looks like the trend is nevertheless qualitatively captured.

Figure 4.32 compares simulation results from both UNITS code and FDS+Evac with experimental data by Zhang [234] and Zhang et al. [237], by joining data from all conditions with different widths b_R. Outcomes from FDS+Evac and UNITS show flow rates which are in general higher than those obtained from the experiments, especially in conditions with intermediate density. However, it is to be noted that experimental values reported by Zhang [234] and by Zhang et al. [237] show that the speed of the subjects during the tests was lower than the average unimpeded speed, even in condition of very low density. This means that there was a tendency from the subjects, during the tests, to move slower than in unimpeded conditions even in situations without obstacles. This might be explained by the fact that people in a T-junction, knowing that they will eventually have to change their direction, tend to slow down with respect to a corridor situation. This type of behaviour is not modelled in the two simulation codes which embed mathematical models characterised by relatively short-range interactions among agents.

A qualitative difference in the specific flow-density diagram between the front and lateral (right and left) areas can be observed both from FDS+Evac and UNITS simulations. A qualitatively similar difference is present also in the experimental data, as visible in Figure 4.32 and as remarked also by Zhang [234] and Zhang et al. [237]. In the front area the specific flow-density diagram shows an almost linear behaviour both in case of FDS+Evac and UNITS, with a limited saturation at higher densities. Instead, experiments from Zhang [234] and Zhang et al. [237] show, first, an almost linear increase of specific flow with density (up to about $1\ \mathrm{p/m^2}$), and then a reduced increasing trend with an increase in the data dispersion. This particular characteristic from experimental data might be due to the fact that, in the real situation, people tend to change their desired speed when they see many other people coming from the opposite direction. This type of behaviour is not modelled in the two simulation codes which, as said before, are characterised by relatively short-range interactions among agents.

In the lateral (right and left) areas, the increase of specific flow with the density tends to saturate early, and simulations overpredict the initial growth of specific flow for low densities. FDS+Evac and UNITS codes show similar outcomes in the left region, whereas they more markedly differ in the right region. In the left region both UNITS and FDS+Evac show a sharp decrease, almost a jump, of specific-flow when the density exceeds approximately $1.5-2.5\ \mathrm{p/m^2}$, although such jump is more evident in case of UNITS. In the right region a jump is visible in FDS+Evac outcomes above a density of about $1\ \mathrm{p/m^2}$. Before this density experimental data are overpredicted, while the matching of FDS+Evac with experiments at higher densities is better. Instead, results from UNITS in the right region do not show such a jump, and the specific flow, after a first increases, remains almost invariant for densities in the range $1.0-2.5\ \mathrm{p/m^2}$, and then it slowly decreases. In general, UNITS simulations in the right region tend to

overpredict specific flow from the experimental data. This discrepancy between simulations from UNITS and experimental data might be due to the combination of two factors. Firstly, the unimpeded speed suggested by the experimental measurements could be too high for being used in the considered T-junction condition, and this possibility is particularly indicated by the results in the front region. Secondly, another source of discrepancy could be a too strong right preference in the counterflow model.

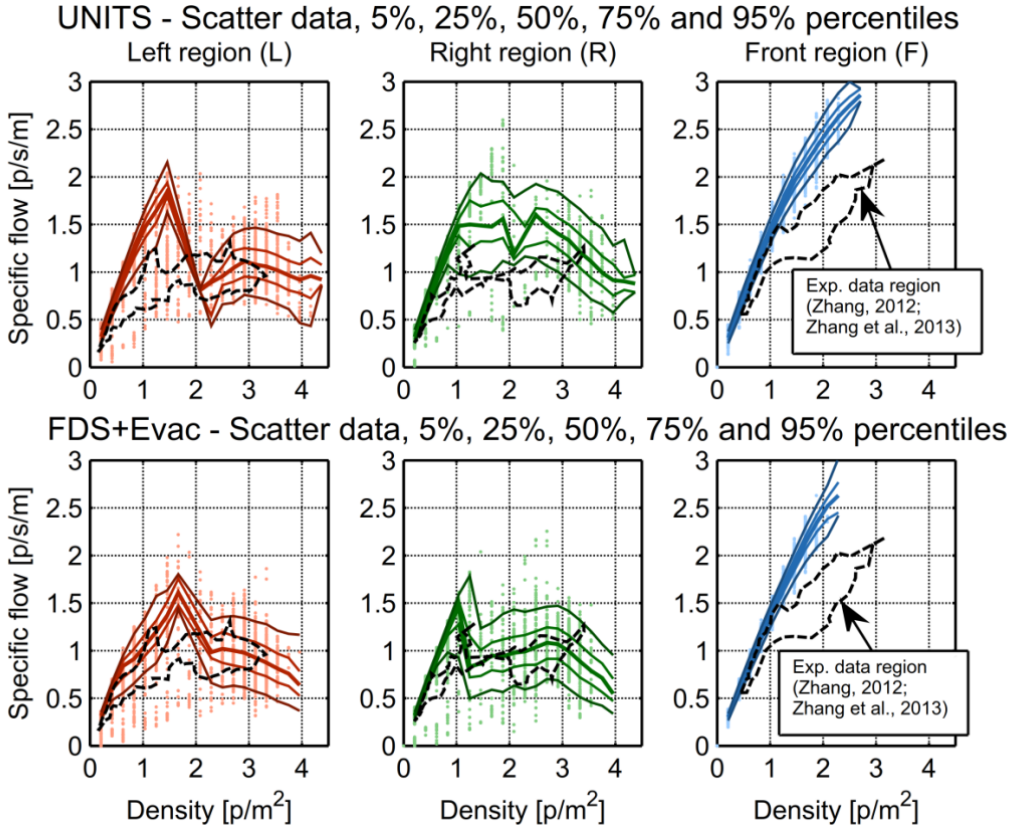

Figure 4.32: T-junction experiment by Zhang et al. [237]. Comparison between simulation results and experimental data regarding the relation between density and specific flow, joining data from all conditions with different width b_R. Top: results from UNITS code. Bottom: results from FDS+Evac.

Also for the present case of T-junction an analysis of scatter data was carried out, which, similarly to the case of unidirectional flow (see Figure 4.29), highlighted a larger dispersion in case of high density compared to the case of low density. Figure 4.33 shows the detail of such analysis.

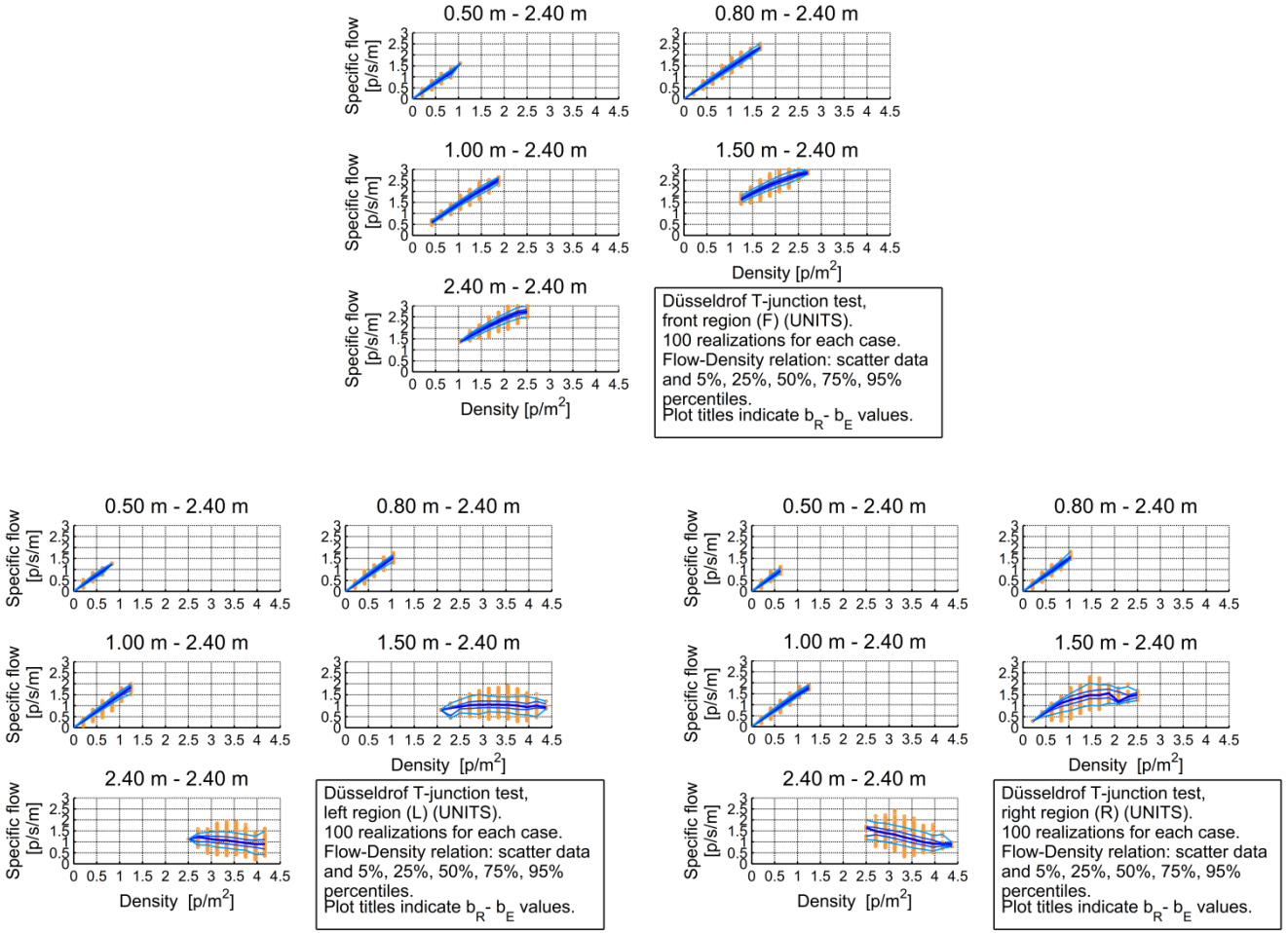

Figure 4.33: T-junction experiment by Zhang et al. [237]. Data scatter plots together with 5%, 25%, 50%, 75% and 95% percentiles of specific-flow given density for different combinations of width $b_R - b_E$. 100 Monte Carlo realizations for each test case. Centre-up plot: front region (F), Bottom-left plot: left region (L), Bottom-right plot: right region (R).

It is confirmed that the conditional dispersion of the specific-flow increases with the density. The effect is very evident by comparing the data related to the front region with the data related to the lateral regions (right and left). The front region is generally characterized by low density and high average speed. The agents, in these conditions, travel almost at their unimpeded speed, towards the same direction. As a result, the flow is almost linear with respect to the density and the spread of the flow data depend mostly on the adopted distribution for the unimpeded speed. The lateral regions, instead, are characterized by high density and reduced speed due to the interaction between agents coming from opposite directions. In such conditions agents are not free to travel to their unimpeded speed, and their speed is, instead, significantly modified by the occasional interactions with other close agents. As a result, the overall variability of data is higher in these conditions.

4.4 Bottleneck and impatient agents

Bottleneck conditions are common when evacuees have to exit from confined spaces. In a ship environment this could happen, for instance, in case of exiting of passengers from public spaces. As a result, investigating the capability of the mathematical model to properly reproduce crowd behaviour in such conditions is of practical importance if the evacuation simulation is to be used within a risk assessment framework. The IMO test case 4, discussed before, addresses a bottleneck condition, but it only provides an indication of a maximum expected flow (1.33 p/s with a 1 m wide exit, corresponding to a specific flow of 1.33 p/s/m). To further address this situation, reference is made in this section to the experimental data presented by Liao et al. [124], who report results from controlled laboratory experiments which was carried out in Düsseldorf in 2009 to investigate pedestrian behaviour through wide bottlenecks.

The geometry of the experiment from Liao et al. [124] is reported in Figure 4.34 taking also into account additional specifications reported by Liao et al. [124].. For consistency with the data analysis by Liao et al. [124], in this section the flow is defined as the number of agents initially the room (N_A), divided by the total exit time (T_E), i.e. the total time to empty the room.

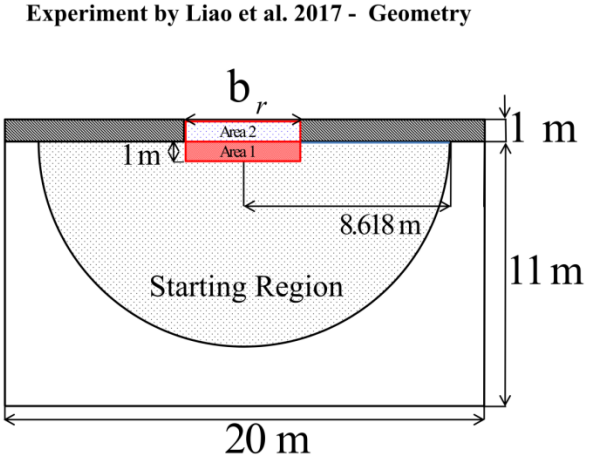

Figure 4.34: Bottle neck experiment by Liao et al. [124]. Geometry.

A first series of simulations have therefore been carried out with the developed tool to compare results with available experimental data. According to information from Liao et al. [124], the agents' unimpeded speed has been considered to be uniformly distributed in the interval 1.55 ± 0.18 m/s. For each condition, a total of 50 Monte Carlo realizations have been run. Results from these simulations are shown in Figure 4.35, both in terms of percentiles (5%, 25%, 50%, 75% and 95%) and also as scatter data. From the reported data, it is evident that the flow increases as the width of the exit increases, and it can be seen that the flow predicted by the UNITS software tends to be smaller than the experimentally measured one.

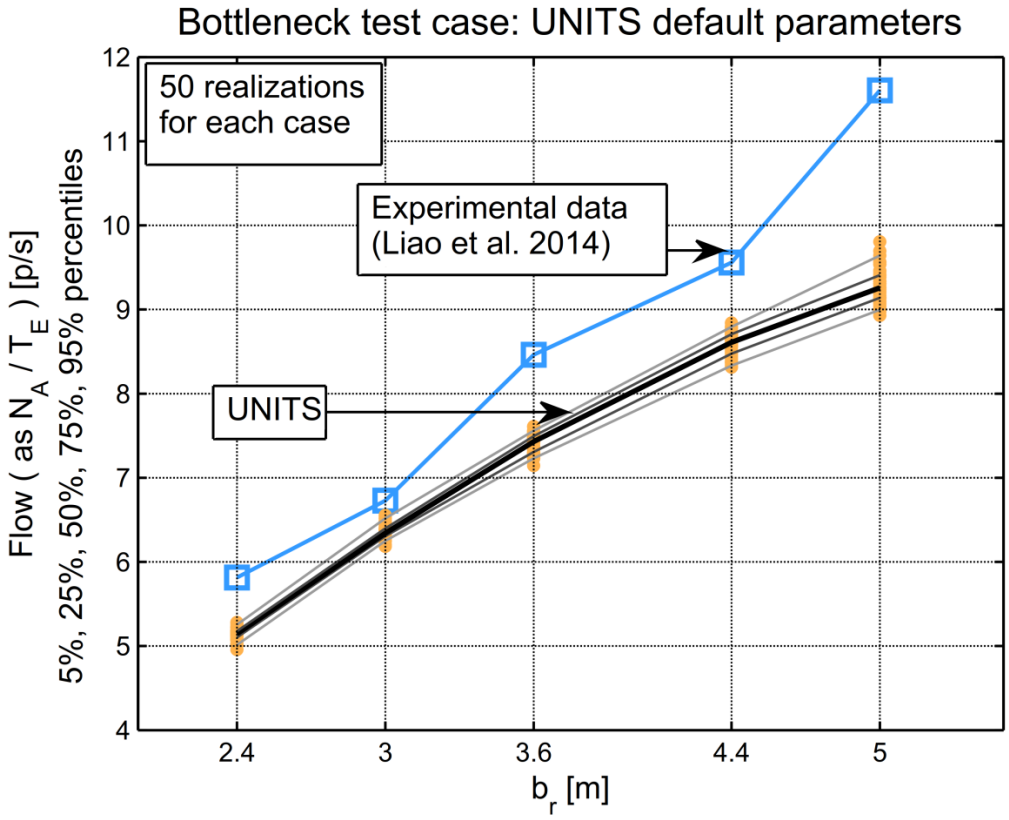

Figure 4.35: Bottle neck experiment by Liao et al. [124]. Flow (N_A / T_E) as a function of the width of the bottle neck b_r, as obtained from 50 realizations for each test case using UNITS code with default parameters. The flow obtained by Liao et al. [124] is also reported for comparison.

An underestimation of the experimental flow was also found by Liao et al. [124] when trying to validate FDS+Evac on the same experimental data from Liao et al. [124]. More specifically, Liao et al. [124] observed that the experimental evacuees speed was overestimated by the simulations and, conversely, the density in the experiments was underestimated by the simulations.

Figure 4.36 shows the density inside the region reported in Figure 4.34 for all test cases, as obtained from UNITS code. Results from Liao et al. [124] are reported for comparison. The model seems incapable of reproducing the high density peaks reported in the experiment. It is however to be noted that the high density peaks reached in the

experiments could also be a consequence of the fact that participants to the experiments were mostly young students, and it is therefore possible to imagine that, during the tests, there could have been a reduced tendency of maintaining sufficient distance between people and avoiding contacts.

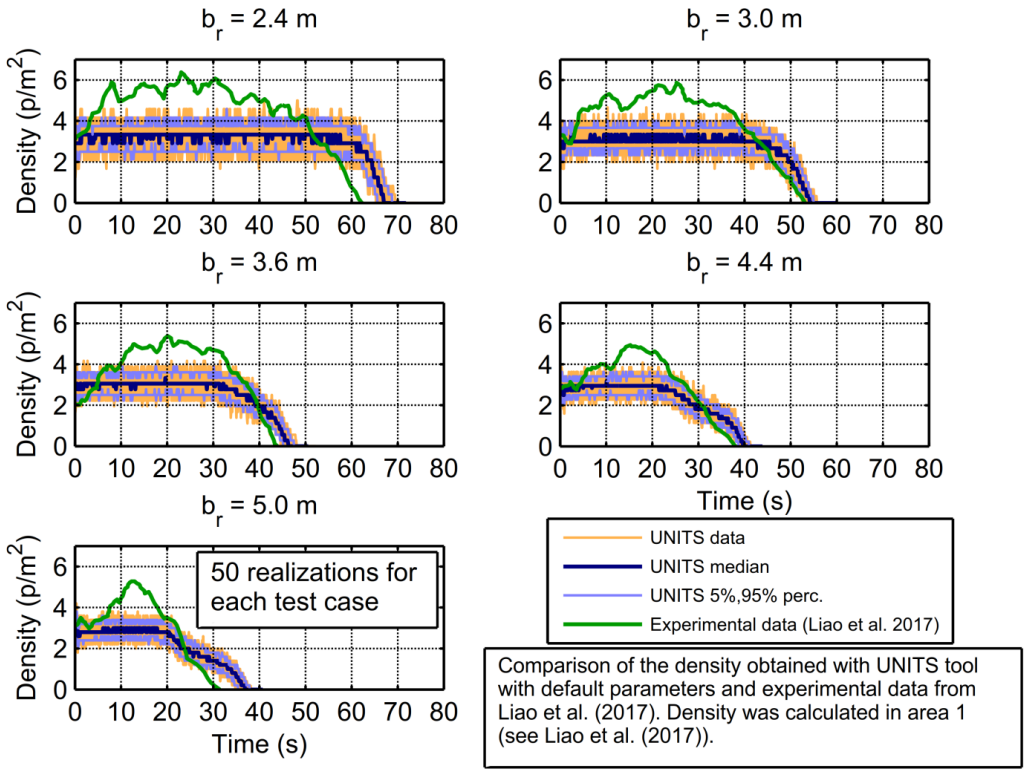

Figure 4.36: Bottle neck experiment by Liao et al. [124]. Instantaneous density as function of time, from 50 realizations using UNITS code with default parameters. Experimental data from Liao et al. [124] are reported for comparison.

In order to try to get a better matching with experimental flow, Liao et al. [124] modified the anisotropy parameter of the social force model λ_a. The resulting flow actually increased and better matched experimental results. However, it was observed that decreasing the anisotropy of the social-force model has the effect of increasing the force that an agent behind exerts on agent in front, and this leads to a tendency towards a sharp increase of the speed inside the bottleneck which was already overestimated by the default choice of parameter of the model. This effect could be reproduced also by the model developed herein. Figure 4.37, in particular, reports the average speed in area 2 considering the condition with bottleneck with of 3.6 m. The speed is reported for three cases with different parameter choices: the default choice of parameters ($\lambda_a = 0.3$, $A_a = A_w = 2000$ N), the case with modified anisotropy ($\lambda_a = 0.5$ and default values for all the other parameters), and the case with modified repulsive force intensity parameter ($A_a = A_w = 1000$ N and default values for all the other parameters). It is observed that while the modification of the anisotropy parameter causes an evident increase of the

average speed inside the area, the modification of the parameter $A_a = A_w$ allows maintaining the speed almost equal with respect to the situation of default parameter choice (see Figure 4.37).

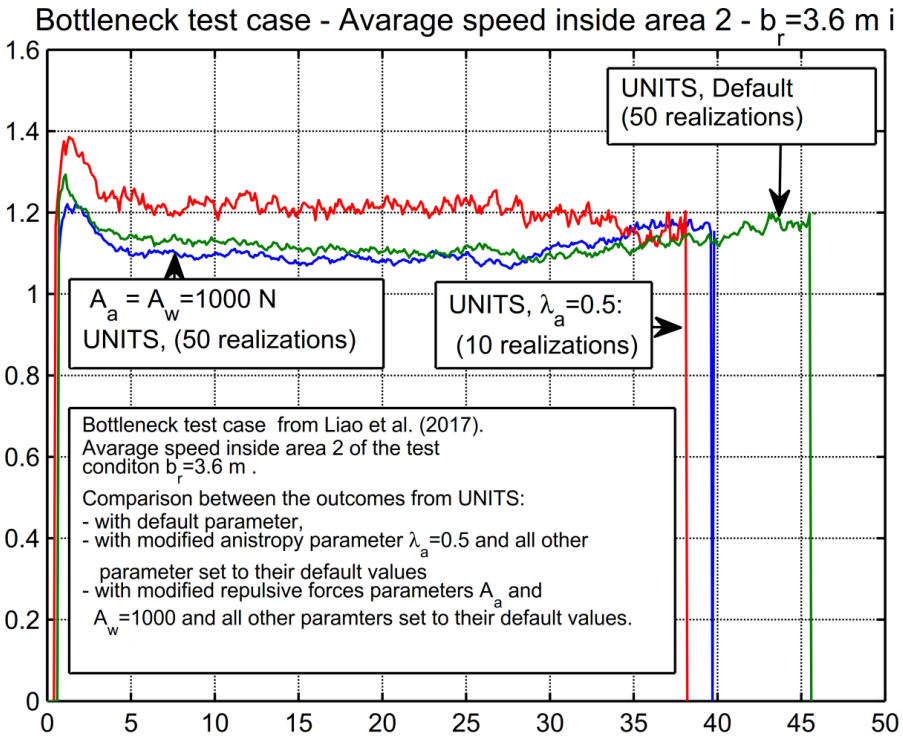

Figure 4.37: Bottle neck experiment by Liao et al. [124]. Effect of modification of the anisotropy parameter λ_a and of the parameters A_a, A_w of the UNITS model on the average speed inside Average speed inside area 2 for $b_r = 3.6\,m$.

Driven by these indications and considerations, it has therefore been decided to run another set of simulations with the intention of promoting an increase of density in the crowd without increasing the speed. To this end, agent-agent and wall-agent interaction forces parameters A_a and A_w have been halved compared to default values ($A_a = A_w = 1000$ N).

Simulation results obtained with such modified parameters are reported in Figure 4.38, which are to be compared with those based on default parameters and reported in Figure 4.35.

It can be noticed from Figure 4.38 that the modification (reduction) of the interaction forces, which allows achieving higher densities, significantly improves the matching between simulations and experiments. It is also worth noticing that a reduction in the agent-agent interaction force was also used by Heliövaara et al. [76], combined with a decrease in the relaxation factor τ_i^f of the motive force and an increase in the fluctuation of the random forces, in order to model agents which are considered to be "impatient".

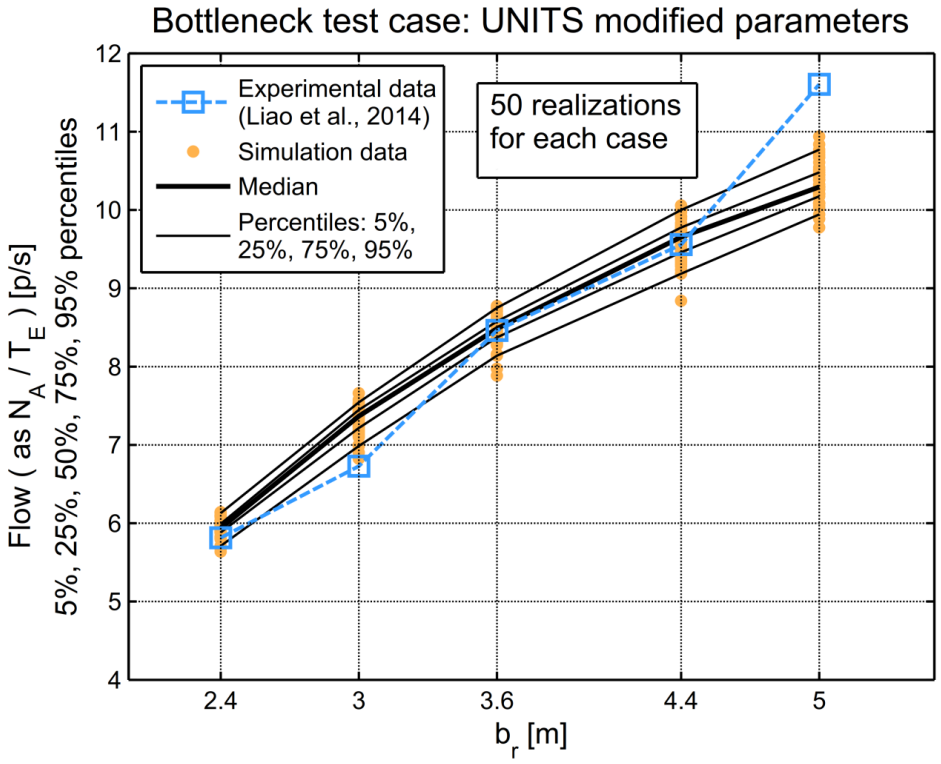

Figure 4.38: Bottle neck experiment by Liao et al. [124]. Flow (N_A / T_E) as a function of the width of the bottle neck b_r , as obtained from 50 realizations for each test case using UNITS code with modified parameters. The flow obtained by Liao et al. [124] is also reported for comparison.

A recent study by Liao et al. [125] suggests a similar modification of the parameters related to the repulsive forces. However, in results reported by Liao et al. [125] the spatiotemporal profile of density shows that the density in area 1 is quite low whereas a strange high density value is found in correspondence of the edges of the bottleneck. This unrealistic behaviour was observed by the authors and justified by an inappropriate agent routing algorithm used in the work. The agent routing algorithm, which, in the present model, is governed by the waypoint logic, is however fundamental in a bottleneck condition and the erroneous increase of density in correspondence to the edges of the bottleneck show that the model presented by Liao et al. [125], although allowing a reasonable flow rate, does not assure, globally, a realistic behaviour.

Driven by those observation an analysis related to the density in area 1 was carried out also in the condition of modified parameters A_a and A_w , and it is reported in Figure 4.39 (to be compared with Figure 4.36). The density obtained following the modification of parameters is closer to the experimental density, although the median is still below the measured experimental data.

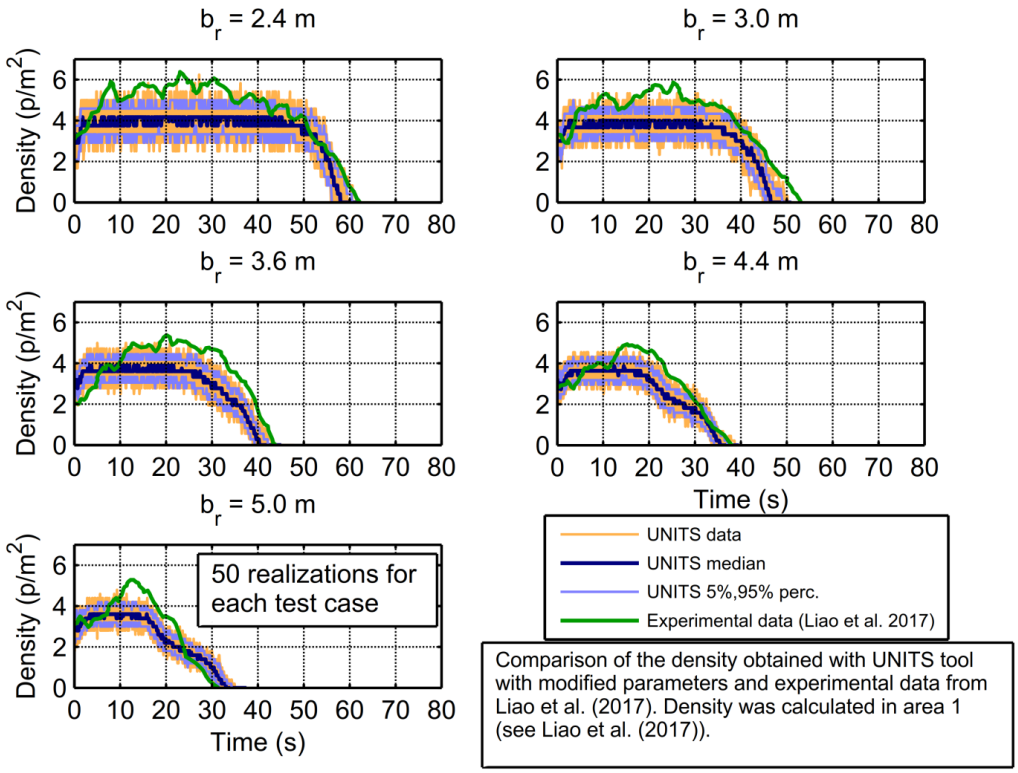

Figure 4.39: Bottle neck experiment by Liao et al. [124]. Instantaneous density as function of time, from 50 realizations using UNITS code with default parameters. Experimental data from Liao et al. [124] are reported for comparison.

According to the obtained results, the developed model looks like being capable of correctly simulating the exit from a bottleneck. However, the parameters of the model may need to be calibrated / modified in relation to the analysed population and to the test condition.

It is also interesting to observe that the specific flow resulting from the experiments from Liao et al. [124] is significantly higher than the reference value in the IMO test case 4. For example, the measured flow for b_r=2.4 m (the smallest width) is about 5.8 p/s corresponding to a specific flow of 2.4 p/s/m, which is 80% larger than the value 1.33 p/s/m which would correspond to the upper acceptable limit of flow indicated in the IMO test case 4. Reference parameters of UNITS model have been based taking into significant account requirements set by IMO Test cases. However, results of the comparison shown in this section, combined with the observed discrepancy between the IMO limit flow rate and the trend obtained by Liao et al. [124], indicate that further modelling improvements and, possibly, further experimental efforts would be worth being pursued.

4.5 A realistic test condition: evacuating behind aligned obstacles

In case of passenger ships, particularly ferries, passengers may sit on seats which can be arranged in lines. As a result, in order to evacuate, each passenger may have to wait for the passenger before him (see for example the geometry proposed in the SAFEGUARD validation data set 1 ([186])). Although this might seem a simple test condition, the comparison with experimental data presented in this section shows that this particular situation highlights some limitation of simulation tools.

The detailed experimental data used to analyse this situation, were not related to the maritime field, but, to the civil field, and have been presented by Santos et al. [188]. The experimental data were gathered during an evacuation exercise conducted at a teaching and research institute of Lisbon University, where 64 first year graduate students participated. During the evacuation exercises videos were recorded in order to analyse the students' behaviour. Moreover the students answered a questionnaire at the end of the activity. The answers to the questionnaire showed that the 46% of the students was motivated to do the activity and the 93% of them felt safer in the building after the evacuation exercise. Video records showed that some that students, however, did not maintain a correct behaviour during the exercise (they stopped for no apparent reason or they moved slowly or they waited for friends). The simulations performed through the developed tool of one of the evacuation situations described by Santos et al. [188] provided a further clarification of the effect of these behaviours on the exit time of the students.

The considered situation is the evacuation from a classroom where the desks were aligned and the evacuation drill started with the subjects sitting at the desks. The condition can be considered, however, similar to the one of passengers starting an evacuation sitting at aligned seats. Specifically the situation reproduced with the mathematical model corresponds to the evacuation exercises performed in Class 2 as it is indicated by Santos et al. [188]. The population of subjects in the experimental test consisted in 14 students mostly aged between 18 and 20 years. The intervals for the unimpeded speed of the modelled agents have been defined starting from those provided by MSC.1/Circ.1533 [147] for 'Males younger than 30' and 'Females younger than 30', and rescaled according to the average unimpeded speed of 1.06 m/s which was measured during the experiments. The mass of agents has been set according to the data acquired during the experiment, whereas the dimensions of agents have been obtained by rescaling in accordance to equations (2.10). In the simulations, 100 independent Monte Carlo simulations have been performed where the unimpeded speed varies according to the agents gender and initial position, while the mass and dimensions have been left unchanged.

The initial positions of the people and the geometry used for the simulation are reported in Figure 4.40.

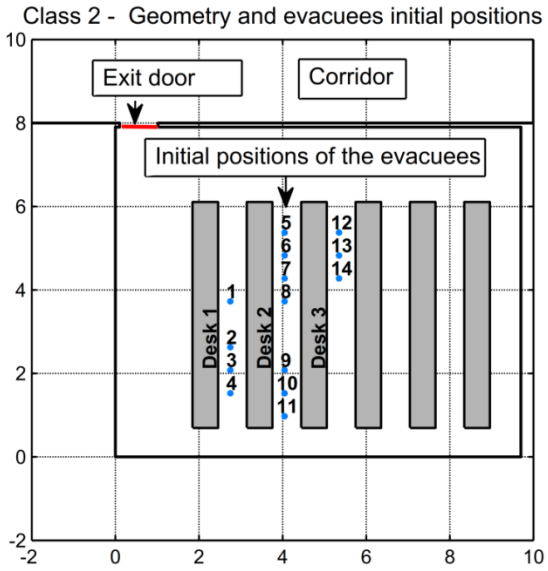

Figure 4.40: Experiment on exit from a classroom by Santos et al. [188]. Initial positions and geometry.

Figure 4.41 reports snapshots of one simulation. From the simulation a continuous flow towards the room exit can be observed, which is slowed down only by the bottleneck condition occurring at the door. However, from the recorded videos, it is clearly visible that the flow of students for this condition is often interrupted. These interruptions are either due to the presence of chairs in the room or by the fact that some students occasionally stopped, thereby blocking the flow.

This behaviour is confirmed by the analysis of exit times in Figure 4.42, which reports the exit time of each agent and compares them with the experimental exit time of the corresponding evacuee. The exit times resulting from the simulations match the experimental ones for more than half of the evacuees. In the other cases, instead, the evacuees exit time in the experiment is much longer than the one obtained from simulation. An explanation for the observed discrepancies can be given by looking at the recorded video. In fact, the video shows that evacuee 2 stops before the exit in order to wait for evacuees 3 and 4, since evacuees 3 and 4 were left behind because they stopped to take their own bags. Those kinds of behaviours might affect the overall time performance of the evacuation process, and they are not part of the modelling used in the simulations.

The phenomenon where, due to geometrical constraints, one evacuee slows down all the others in the row could, however, be observed also in the simulations outcomes. To this purpose those simulation where the evacuees 1, 5 and 12 obtain the largest exit time were highlighted in black, red and green respectively in Figure 4.42. The figure shows that in each desks line the exit time of the evacuees is affected by the reduced speed of the evacuee occupying the initial position of the line, as it was expectable.

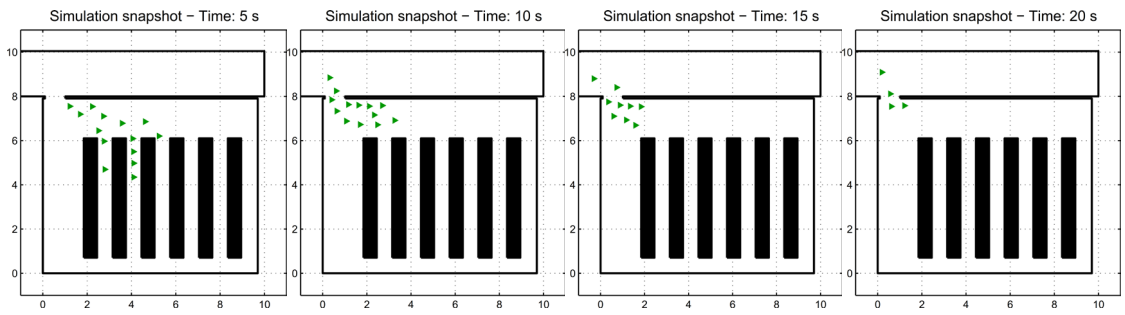

Figure 4.41: Experiment on exit from a classroom by Santos et al. [188]. Snapshots of one simulation at different time instants.

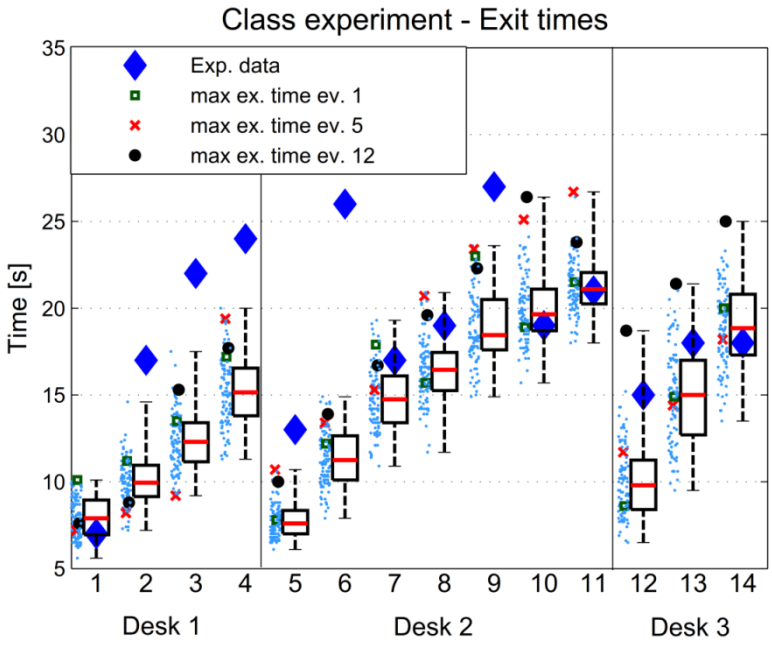

Figure 4.42: Experiment on exit from a classroom by Santos et al. [188]. Exit times resulting from 100 realizations. Simulation results are reported for each agent through box plots (min, 25%, 50% and 75% percentiles, max), scatter data. Experimental data are also reported. Some simulations are highlighted. In particular are highlighted the simulation outcomes associated with simulations having the maximum exit time for the evacuee 1 (green square), the evacuee 5 (red cross) and the evacuee 12 (black circle). Evacuees 1, 5 and 12 are the ones positioned initially at the beginning of their respective desk line, thereby their performance, in terms of exit time, affects also the performance of all the agents in the same line.

The effect, on the overall exiting performance, of the lack of complete modelling of evacuees behaviours can be better appreciated by looking at the exit time curve reported in Figure 4.43. Apart from an initial delay, it can be observed that the flow rate of the evacuees in the experiment matches well the one obtained from the simulations.

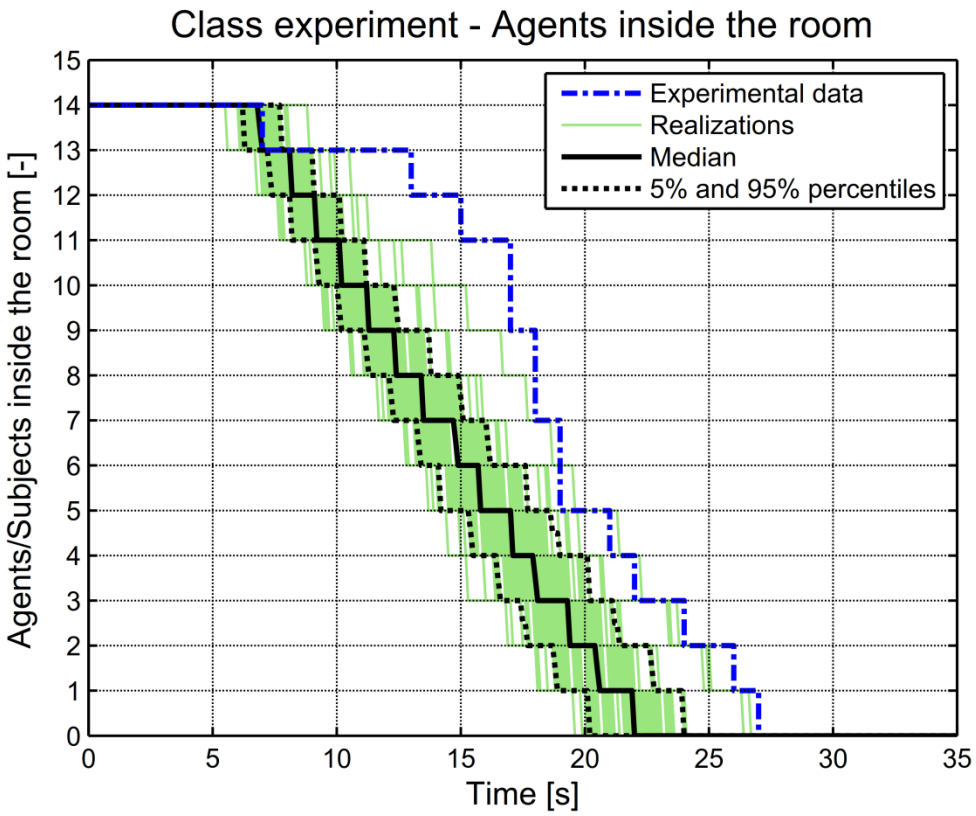

Figure 4.43: Experiment on exit from a classroom by Santos et al. [188]. Simulated exit time and comparison with experimental data. Outcomes from all realizations are reported together with ensemble median and 5% and 95% percentiles. Experimental results are also reported for comparison purposes.

As anticipated, it can be noted that, in Figure 4.43, early in the evacuation process, the experimental curve is shifted by some seconds with respect to the median of simulations. However, the exit rate in the subsequent part of the evacuation is very similar to that obtained from simulations. The initial shift is due to the initial slowdown of the evacuation process, which is present in the experiment but not in any of the simulations. This shift corresponds, in the video, to the situation of an evacuee stopping in front the exit while waiting for two others evacuees, as discussed before.

Behaviors such as stopping for apparently no reason or going in the opposite direction with respect to the exit are generally not considered when the assessment of evacuation time is performed through the use of simulators. For instance, there is no requirement by IMO concerning the modelling of these behaviours (MSC.1/Circ.1533 [147]). This is mainly due to the fact that models simulating these behaviours are very difficult to calibrate and validate. Moreover, such unpredictable behaviours might change drastically if considering a different population or different conditions (for example a real condition of danger).

Due to the relevance to the maritime field of a test condition with evacuees starting aligned behind some obstacles, an additional test could be suggested in the guidelines in MSC.1/Circ.1533 [147] dealing with this case. The condition of evacuation from cabins is, indeed, already proposed in IMO test 10. The additional test case might require that

the exit times reasonably reflect the initial position of the agents, as it is highlighted in Figure 4.42. Such a test could eventually assess the capability of the tool to correctly reproduce the human behaviour in narrow spaces.

4.6 Counterflow validation

The peculiarity of the counterflow condition has already been described in Chapter 3. The counterflow model has been calibrated through the experiments performed by Isobe et al. [89] and it has been tested through the IMO test case 8. Herein a comparison with other experimental results, provided by Kretz et al. [116], is proposed. The experimental condition is more similar to the IMO test case 8 than to the case presented by Isobe et al. [89] as also in this condition the groups of agents going in opposite direction are distant one from the other at the beginning of the simulation.

The geometry of the test condition is reported in Figure 4.44.

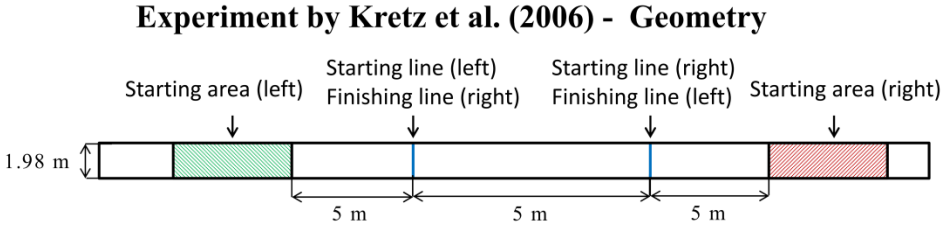

Figure 4.44: Counterflow experiment by Kretz et al. [116]. Geometry.

The subjects in the experiment were divided in two different groups, one starting on the left side of the corridor and the other starting on the right side. They were then invited to travel towards the opposite end of the corridor.

Herein only the cases where the number n of agents coming from left and from right is the same will be considered. Experiments were run for different values of n: $n = 5, 10, 15, 20, 25, 30, 35$.

The unimpeded speed of the subjects was derived from the experimental data concerning the speed of the first and the last person of the group in case $n = 5$ and without presence of counterflow agents. The unimpeded speed is thus considered to be uniformly distributed in the interval $[1.40, 1.66]$ m/s, whereas the dimension of the agents was set in accordance to the class "Adult" as reported in Table 4.2.

The experiment demonstrate that human organize in two or three lanes. This qualitative behaviour is reproduced by the simulation and is shown in Figure 4.45 where snapshots of one of the simulation runs with $n = 35$ is shown. The organizations in two lanes is present specifically for times 10 s 20 s.

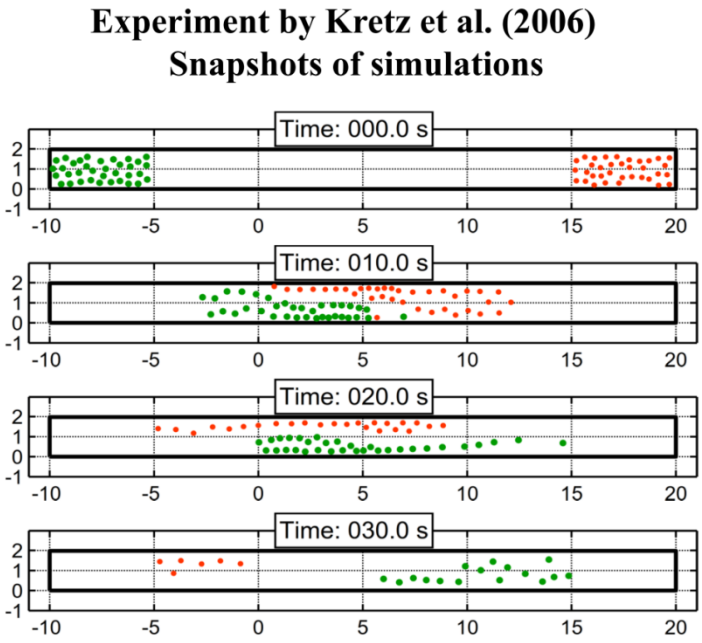

Figure 4.45: Counterflow experiment by Kretz et al. [116]. Snapshots from a simulation in the condition with 35 agents coming from left and 35 agents coming from right.

The experimental data by Kretz et al. [116] concern the time elapsed between the first agent of the group from left crossing the starting line of his group (starting line left in Figure 4.44) and the last agent of the same group from left crossing the finishing line of the group (finishing line left in Figure 4.44). Kretz et al. [116] performed a linear fitting of the data obtained in this test case using a least square linear regression method and obtaining that data were approximated by the line with equation $y = 0.622 \cdot x + 5.7003$ (see figure 6 [116]), where y is the time and x is the number of persons in counterflow. The linear regression obtained by Kretz et al. [116] is compared in Figure 4.46 with the analysis of outcomes from 100 Monte Carlo simulation runs, for each value of n, carried out with the UNITS code.

The simulation data match quite well the experimental data, although agents in simulations tend to be slower compared to experiments. This is probably due to the fact that, in reality, people react faster to people incoming from opposite direction when they are visible, and thus lanes form faster than in simulation. A further confirmation of this hypothesis is provided by the conclusion of Kretz et al. [116] that participant reacts quite early to even few people approaching. A similar outcome was observed in the experimental results obtained by Montecchiari et al. [141] through real-time user participation in virtual reality, as discussed in Chapter 6. In fact, also the experimental data gathered by Montecchiari et al. [141] with the use of virtual reality suggest that human obey to long range counterflow strategies. Chapter 5 herein will be described the adopted user interfaces for the virtual reality experiment while Chapter 6 will report the experimental outcomes.

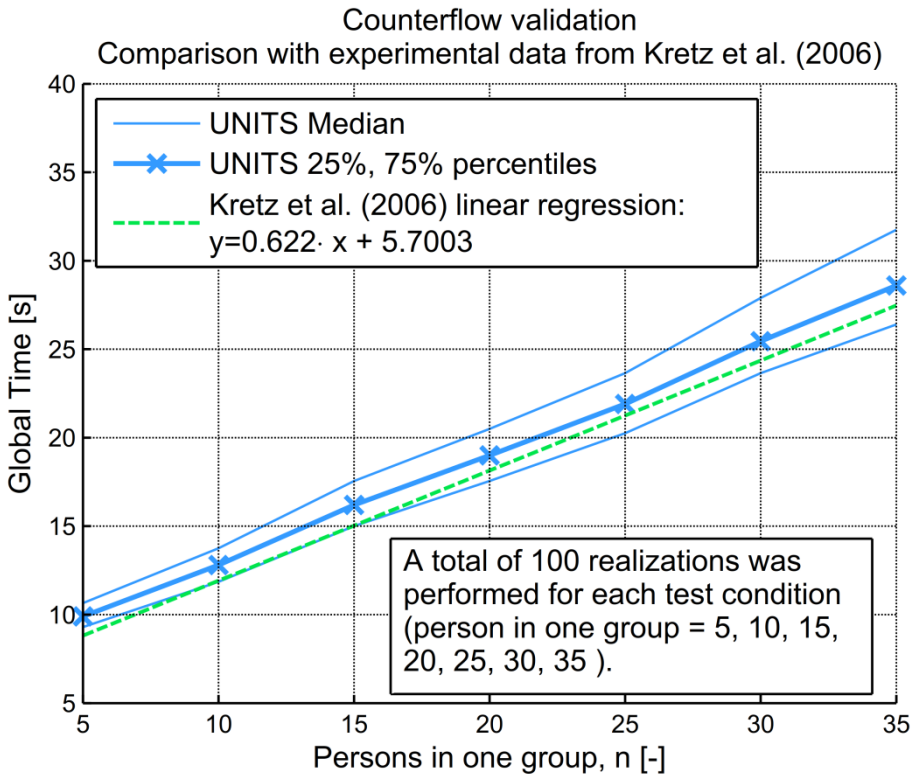

Figure 4.46: Counterflow experiment by Kretz et al. [116]. Global exit time as a function of the number of people in each group for each of the seven test conditions. The linear regression obtained by Kretz et al. [116] from the experimental data is also reported for comparison.

4.7 Final remarks

This chapter presented the process of verification and validation of the developed evacuation model. The tool was able to fulfil the requirements of all the test cases specified by MSC.1/Circ.1533 [147]. However, qualitative differences have been detected in the comparisons with the outcomes from other evacuation models, especially in IMO test 4, 8 and 11.

The capability of the developed model of correctly reproducing the flow density relation was assessed through comparisons with experimental data in two different test conditions: one considering the unidirectional flow in a corridor and the other one considering the flow in a T junction. The model proved to be able to qualitatively reproduce the experimental data in both conditions. Simulation results in unidirectional flow, however, showed a discontinuity in the flow-density graph which was not present in experimental data, and this might be due to the fact that humans can organize better than simulated agents when exiting from the bottleneck at the end of the corridor. A difference between simulations and experimental data, in the situation with the T-junction, was detected when considering the flow of the agents coming from the right side of the junction. The difference might be due to the parameter of the right preference: the default value of this parameter seemed to introduce a too marked right presence in relation to the outcomes of the T-junction test case.

The capability of the tool of correctly simulating the exit from a bottleneck was proved by comparison with experimental data. Although, qualitatively, the density and the flow followed the trend observed from the experiments, the model, with default parameters, tends to underestimate the density and to overestimate the speed. A possible modification of some of the model parameters was tested, which allowed a better match with experimental result.

Finally, the capability of correctly reproducing a counterflow condition was assessed by comparison with experimental data. The model correctly reproduced the qualitative behaviour observed in the experiments, and, in addition, quantitative experimental outcomes where also correctly reproduced.

This page is intentionally left blank

5 IMPLEMENTATION OF REAL TIME USER INTERACTION

As observed in the previous chapters, the execution of experiments aimed at gathering data for the validation and calibration of the evacuation process is surely complex. A promising field, in this direction is represented by the use of virtual reality, which can be implemented to study human behaviours in evacuation in a more controlled way.

The present chapter will provide an insight of the state of the art in the field of virtual reality applied to evacuation focusing also on the limits and problems presented by this approach. Subsequently the modelling and implementation of real time user participation in the evacuation process through the use of virtual reality will be presented. The adopted input and output interface will be carefully described and particular relevance will be given to a newly developed vibrotactile interface.

5.1 Introduction

Virtual reality has been adopted in the fields of evacuation and safety for different purposes. As an example it was demonstrated to be a valuable training tool in the experiments carried out by Kinateder et al. [107], Kinateder et al. [108].

Concerning the field of evacuation models, virtual reality offers an interesting opportunity to study specific controlled situations and to obtain detailed data without performing real experiments. This feature is highly interesting for the safety field as performing evacuation experiments is extremely onerous in terms of time and resources. This idea of applying virtual reality to obtain data for validation and calibration of experimental parameters was already presented and implemented by Shendarkar et al. [199] where an agent based model was developed starting from data acquired with virtual reality experiments.

More recently other studies adopted virtual reality to study crowd behaviour. Ronchi et al. [181], as an example, report a study where virtual reality is adopted to study the travelled path of people during an evacuation from a tunnel. Several more recent experiments performed with virtual reality showed analogies between users' behaviour in the virtual environment and in the real world. Olivier et al. [163] observed that humans tend to maintain approximately the same trajectories in virtual reality and in real conditions in the case of a simplified experiment while Olivier et al. [164] provides further evidences on the analogy between human behaviour in a real environment and in virtual reality.

Moussaïd et al. [143], instead, proposed a multi-user tool to study evacuation behaviour. The obtained results are encouraging because simulation outcomes well match experimental data. The experiment proposed by Moussaïd et al. [143] consisted in a simulated evacuation where all participants to the simulation were avatars controlled by human subjects. The number of avatars, however, was limited, in this case, by the number of available VR stations and volunteers. In case of more realistic large-scale experiments, involving a large number of pedestrians, there is the need to resort also to computer-controlled agents.

Approaches based on virtual execution of experiments, with participation of humans, allow a degree of control of experimental parameters (e.g. initial conditions, characteristics of participants) which is almost impossible for real experiments. A few experiments on the interaction between user-controlled avatars and agents have been carried out. In particular, Bode et al. [13] studied the decision-making process related to the route choice and the way it is affected by external factors. In this case a view from above (top-down) of the virtual field was used, which allows the user to view the whole situation. However, this kind of point of view is very different from the first person view a real person would have in reality. Moreover, in a high-density condition, users may fail to correctly identify the position of the avatar they are actually controlling. This type of view is similar to the one adopted by the software VELOS presented by Ginnis et al. [57]: this tool allows the user to impersonate an agent or a crewmember and interact with computer-controlled agents through a third person view.

However, human behaviour is greatly affected by the surrounding environment, in the evacuation process. It is therefore fundamental that the users totally identify themselves with the avatar they are controlling. To this end, a first person view is more appropriate and effective. The level of identification of the user with the avatar is called "presence" ([226]). While satisfying results can be obtained with the first person view without the use of full immersive hardware ([40]), the latter provides indeed a higher degree of presence.

The recent development of game engines such as Unity3D ([217]) or Unreal ([42]) allows a more straightforward implementation of the real time user interaction inside the simulation and a better user experience by the increase of frame rate. Moreover the newly developed virtual reality tools, (head mounted displays, CAVE system), have been proven to increases the feeling of presence in the user and the perceived usability of the software ([84]). This hardware should, thus, in principle, allow obtaining more realistic behaviours.

However, despite the use of this hardware, some limitations of the use of virtual reality to investigate crowd behaviour were encountered and highlighted in the experiments carried out by Kretz et al. [117]. One of the most important limitations is the reduced attitude to keep a reasonable distance from the simulated avatar. This problem arises in the experiment described by Kretz et al. [117]were an experiment performed in real conditions is reproduced with virtual reality. In this case, it is observed that high-density situations, where contacts are unavoidable, cannot be realistically reproduced in virtual reality. Kretz et al. [117] adopted a haptic interface in order to provide users with additional information about contacts and proximity to agents. This interface, presented by Kretz et al. [117], consists in a joystick that opposes to the users' hand the same force which models agents' contacts and repulsions. This haptic interface is however not sufficient to offer users a sufficient degree of immersion in situations of high density and further developments of the haptic interface are proposed by Kretz et al. [117].

A large variety of haptic interfaces has been used to enhance the degree of immersion in virtual reality (e. g. [48], [98]). The contacts with moving objects or obstacles are often reproduced with vibrotactile devices. Haptic interfaces providing those kinds of stimuli are usually in the form of gloves, jackets or belts. Gloves providing electro tactile stimuli are adopted by Pamungkas and Ward [165] and by Bloomfield and Badler. [11] to provide users with realistic perception of contacts in hands.

In the case of evacuation simulations, typically, the information about the positions of the other agents and walls are restricted to two dimensions as the mathematical model is 2-dimensional. To this purpose, haptic interfaces worn around the wrist and/or arms providing vibrotactile stimuli have been previously demonstrated to be efficient as way-finding systems by Ross et al. [183], Van Erp et al. [218], Bossman et al. [15] and have been applied to provide additional information about the environment to blind people (McDaniel et al. [134], Flores et al. [49]). A vibrotactile belt was also successfully used by Rosenthal et al. [182] for pedagogical purposes. Moreover, this type of haptic interface found its application as a guidance system also in virtual reality as described by Lindeman et al. [126]. The abovementioned studies suggest that this kind of haptic interface is effective in timely communicating two-dimensional information, especially about the surrounding environment. An easy-wearable vibrotactile interface providing information on the 2-dimensional position of obstacles, like the one proposed by McDaniel et al. [134], seemed therefore to be indicated also for the application in crowd studies.

The present background was considered in the choice of the user output interfaces adopted for the implementation of the real time user interaction in the simulation process. The detailed description of the input and output interface by which the user interaction is made possible will be the topic of the following sections. The first se

5.2 The modelling of the user-controlled avatar

Usually, in most of virtual reality applications, the avatar is controlled by the user by an instantaneous modification of the speed or of the position. This model allows indeed more comfort for the user with respect to implementing the avatar motion by means of forces as observed by Bowman et al. [16].

In this situation it was, however, chosen to model the control of the avatar in a similar way the agents are modelled, in particular considering the avatar as a rigid body moved by forces.

The translational motion of the avatar is due to the following force, where the user directly controls the instantaneous vector of desired velocity in terms of magnitude and direction through the right analog stick:

$$\mathbf{F}_a^{\text{control}}(t) = \frac{m_a}{\tau_a} \cdot \left(\mathbf{v}_a^0(t) - \mathbf{v}_a(t) \right) \tag{5.1}$$

where $\mathbf{F}_a^{\text{control}}(t)$ [N] is the control force exerted by the avatar at the time instant t [s], m_a [kg] is the mass of the avatar, τ_a [s] is the relaxation parameter, $\mathbf{v}_a^0(t)$ is the desired speed vector at the time instant t and $\mathbf{v}_a(t)$ is the instantaneous speed of the avatar. This force is specified as having the same mathematical expression of the motive force (see equation (2.11)). This specific control is intended to give the user the mathematical interface to express his/her complete behaviour when interacting with the other agents and with the obstacles, and allows to keep the underlying translational motion modelling, which is based on rigid-body dynamics. The presence of the dissipative term associated with $-\mathbf{v}_a(t)$ allows to damp the avatar speed when the user does not provide an "intention" to move forward through $\mathbf{v}_a^0(t)$.

The direction of $\mathbf{v}_a^0(t)$ is fully controllable. The user controls the avatar translation by setting its desired velocity $\mathbf{v}_a^0(t)$ through the use of an analog stick. In particular, the user sets the components of the vector $\mathbf{x}_a^0 = \left[x_a^0(t), y_a^0(t) \right], \left\| \mathbf{x}_a^0 \right\| \le 1$ respectively the values for the X-axis $x_a^0(t)$ and Y-axis $y_a^0(t)$, by moving the right analog stick. These two values are proportional, respectively, to the inclination of the analog stick with respect to the forward or to the lateral direction (considering the user reference system), and they represent the components of the 2-dimensional vector $\mathbf{x}_a^0 = \left[x_A^0(t), y_A^0(t) \right]$ determining the direction of the desired speed $\mathbf{v}_a^0(t)$ (see Figure 5.1).

In the implementation of the control of $\mathbf{v}_a^0(t)$ by the user, it is important, however, to bear in mind that, in virtual reality, the user cannot perceive, and is therefore not affected by physical limitations (such as, in particular, physical effort) as in a real condition. This lack of physical limitations may result in a user setting a "virtual desired speed" $\mathbf{v}_a^0(t)$ much higher than its real(istic) counter-part. In such case, the user would travel faster than any agent and the simulation would eventually lose consistency and become unrealistic. In order to cope with this issue, it has therefore been chosen to limit the maximum magnitude of $\mathbf{v}_a^0(t)$ which can be set by the user. Although this limit is in

principle arbitrary, it is considered relevant to set it to the maximum speed $v_A^{\max}$ of the category of agents the avataris assumed to belong to. The magnitude of the desired speed is hence determined following the equation:

$$\mathbf{v}_a^0 = \mathbf{x}_a(t) \cdot v_a^{\max} \tag{5.2}$$

Although the control of the avatar was developed to be in line with the previous described model of the agents, the comfort of the user should be considered as well. Following the results of Bowman et al. [16] showing that users are more comfortable with almost instantaneous accelerations, the relaxation coefficient τ_A^f in the control force for the human-controlled avatar is set to be equal to half the average value of the category the avatar is assumed to belong during the simulation. This reduction eventually results in a more responsive interface.

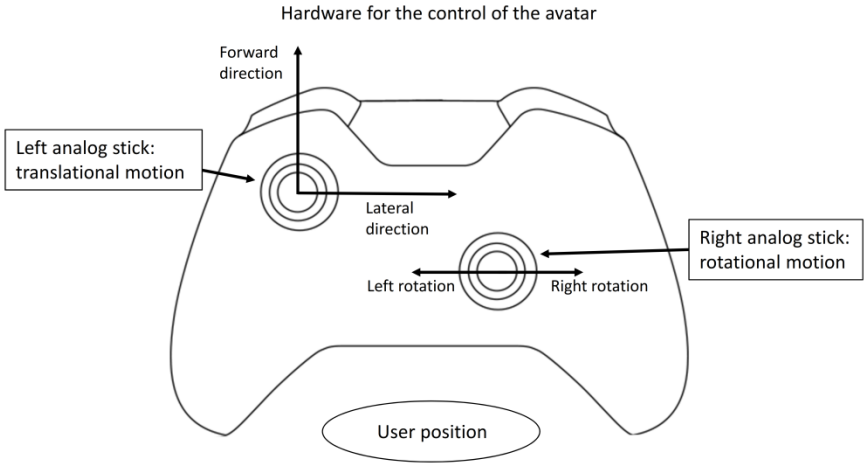

Figure 5.1: Hardware for the control of the avatar: the two analog sticks are indicated.

The above considerations are associated to the control of the translation. However, control of rotation (i.e. the orientation of the avatar) is an important issue in the virtual reality field, as the instantaneous orientation is associated with the direction where the user is looking to. For the avatar it was decided to keep separated the rotation of the head from the rotation of the body. In this way the user can walk towards a direction, while rotating the head to another direction to explore the space around him/her. While the head can rotate around all the three body-fixed axes, the body can rotate only around the vertical axis. This decision is mostly oriented to separating the orientation of the camera (i.e. where the user is looking to), which is a matter having to do with the exploration of the space, from the orientation of the body of the avatar, which is a matter having to do with the interaction between agents and avatar.

The orientation of the avatar is controlled with the left analog stick (see Figure 5.1). However, differently from the translator motion, the rotation of the avatar body is not governed by rigid body dynamics laws. Instead, the orientation is specified by the user through the control interface by indirectly specifying a rotational speed. This choice has been made because it was observed that, using torques for the control of the avatar angular dynamics, may result in making the virtual reality experience very unpleasant

for the user due to the resulting time lags induced by the system dynamics, with possibility of game-sickness. The importance of having a very responsive control of the orientation was also highlighted by Bowman et al. [16] in order to have a comfortable experience during the navigation of the virtual world.

While an experienced user can successfully adjust the rotation speed through the use of an analog stick, inexperienced/untrained users may fail in adjusting the rotation correctly, resulting in a too fast rotation of the view. This may give rise to unpleasant sensations of discomfort and nausea. To reduce this effect, it was decided to implement a nonlinear dependence between the rotation speed and the stick inclination with respect to the vertical axis of the stick. The relation is designed in such a way that responsiveness increases as the stick inclination increases, allowing a fast rotation only when it is required. The model governing the orientation of the avatar is therefore described by the following equation:

$$\phi(t+\Delta t) = \phi(t) + \Delta t \cdot k\left(t\right) \cdot \omega_0 \tag{5.3}$$

Where Δt (s) is the simulation time step. In order to avoid too fast rotations of the camera, which could lead to discomfort, ω_0 was set to $\pi/2\ rad/s$. The factor $k\left(t\right)$ depends nonlinearly on the controller signal (χ^x_{stick}), which is related to the inclination of the axis of the left stick with respect to the left-right direction. By design $\chi^x_{stick} \in \left[-1,1\right]$, with the limits being associated with the maximum inclination to each side. The relation between $k\left(t\right)$ and χ^x_{stick} has been defined as:

$$k\left(t\right) = \left|\chi^x_{stick}\left(t\right)\right|^{\alpha} \cdot sign\left(\chi^x_{stick}\left(t\right)\right) \quad \text{with} \quad \alpha = 4 \tag{5.4}$$

Finally, contacts between the avatar and the agents and between the avatar and the walls are resolved by the integrated physics engine, as for the case of agent-agent and agent-wall contacts (see section 2.2.10).

However, it was observed that applying a non-zero restitution coefficient for the avatar may result in unrealistic and undesired avatar movements. It was therefore chosen to use a restitution coefficient equal to zero (fully inelastic collision), while keeping a friction coefficient as the one adopted for computer controlled agents.

5.3 Visual output: rendering and hardware

The adopted development environment allows providing a first person visualization of the virtual environment starting from the meshes used to model the walls. Moreover it offers the possibility of creating humanoid animated agents that quite realistically resemble humans. In those cases, usually, the geometry adopted for rendering is not the same as the one that is instead used as reference for the underlying the mathematical model for the determination of contacts, distances, etc. This latter geometry is, in fact, far less complex.

The difference among rendered geometry and geometry adopted for the physics calculation and for the mathematical model may generate situations where the user incorrectly perceives the position of an agent, due to mismatches between the object used for the simulation model and the object used for the rendering of the agent. Those mismatches can be tolerated in video-games, where the main objective is the entertainment of the user. However, such mismatches cannot be tolerated within the scope of this research. As a result, for the purpose of this study, agents and obstacles are rendered with the same volume they actually implicitly occupy within the mathematical model used for the simulation (see Figure 5.2).

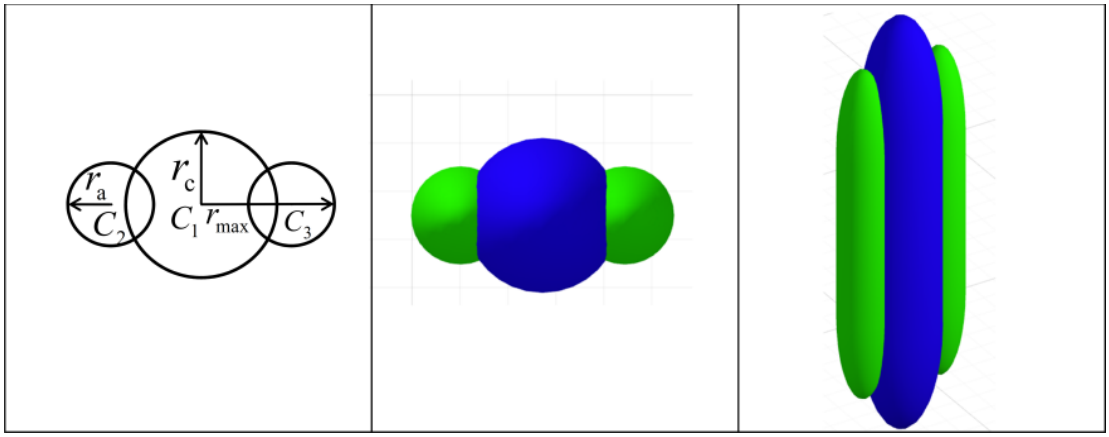

Figure 5.2: 2-D geometry of one agent as and corresponding 3-D rendering: (left) 2-D geometry of the agent as represented in the mathematical model, (centre) view from above of the rendered agents, (right) prespective view of the rendered agent.

An example of the rendering is reported in Figure 5.3 which shows a view from above, and the correspondent first person view of a simulation with user interaction. The figure shows the importance of using a first person view to allow a sufficient grade of immersion. The user, in third person view, has a complete picture of the geometry and of the position of agents and is thus able to choose the path considering all data available. In first person, instead, the user has access only to partial information on the positions of the agents in the scene and on the shape of the geometry.

To enhance further the feeling of immersion in the virtual world the full immersive virtual reality hardware Oculus Rift ([161]) was adopted. Oculus Rift offers a 3D rendering of the virtual environment in first person view and the possibility to rotate the view coherently with the head movements in addition to the control performed through the use of analog sticks described in the previous section.

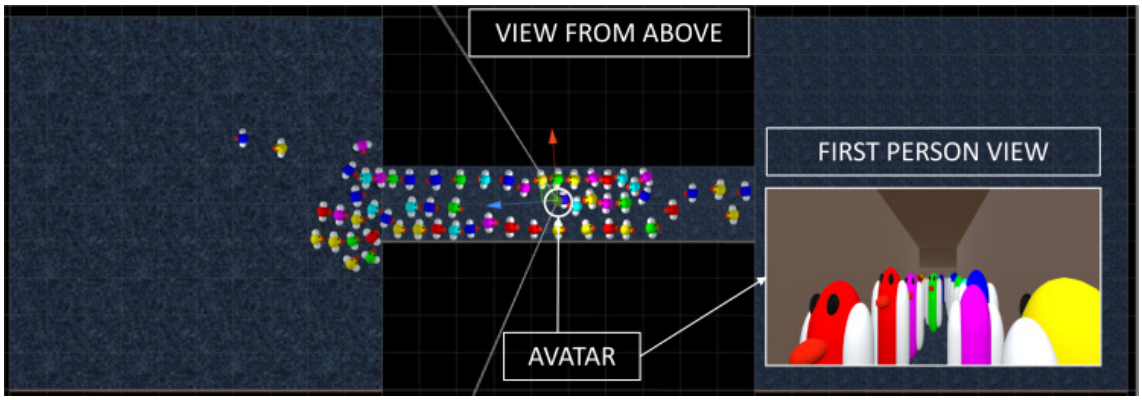

Figure 5.3: View from above and correspondent first person view of a simulation with user interation .

5.4 Audio and haptic outputs

Audio interfaces have been used to provide the user with additional information about the virtual environment.

A single step sound was played at a frequency depending on the speed of the avatar. This feature provides the user with additional information about the speed of the avatar. Moreover users were informed about the proximity of other agents by an “ouch” sound coming from the closest agents.

This sound was played every time an agent enters with its centre the audio area, at intervals of 3 seconds. The audio area has a width of about 0.4 m, centred in the avatar centre.

The haptic interface was meant to inform the user about the proximity of agents and about the contact with walls. It was made by three elastic stripes provided with 8 vibrating actuators. The users wear the longer stripe around the chest and the two smaller ones around the arms, as reported in Figure 5.4.

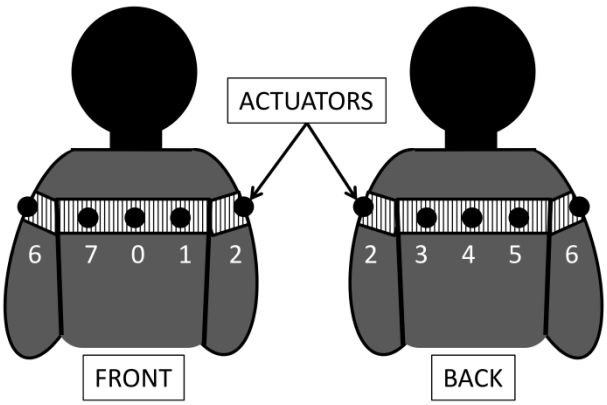

Figure 5.4: Sectors defining when the vibrators are activated and when the sound is played.

The design adopted is very similar to the one described by McDaniel et al. [134]. However, in this case the interface is worn around the chest and the arms, instead of around the waist. Indeed, as the area occupied by avatar in the mathematical model is obtained by an approximation of the area occupied by shoulders and chest of one person, positioning the actuators in these body parts guarantees consistency between the mathematical model and the location of the stimuli.
The actuators adopted for the experiment were coin eccentric mass vibration motor of the type used by McDaniel et al. [134] and by Scalera et al. [189]. They have 10 mm of diameter and thickness of 3.0 mm. They operate at a rated voltage of 3 V, drawing about 90 mA and providing a vibrating acceleration of almost 1 g at a frequency of 200 Hz. They were preferred to cylindrical vibrator motors of the type used by Bloomfield and Badler [11] because of their reduced weight and volume.

The computer controlling the haptic interface communicates with the one used for the virtual rendering and for the simulation through the UDP protocol and activates the actuators considering the position of the agents with respect to the avatar or the collisions with a wall (see Figure 5.4 and Figure 5.5).

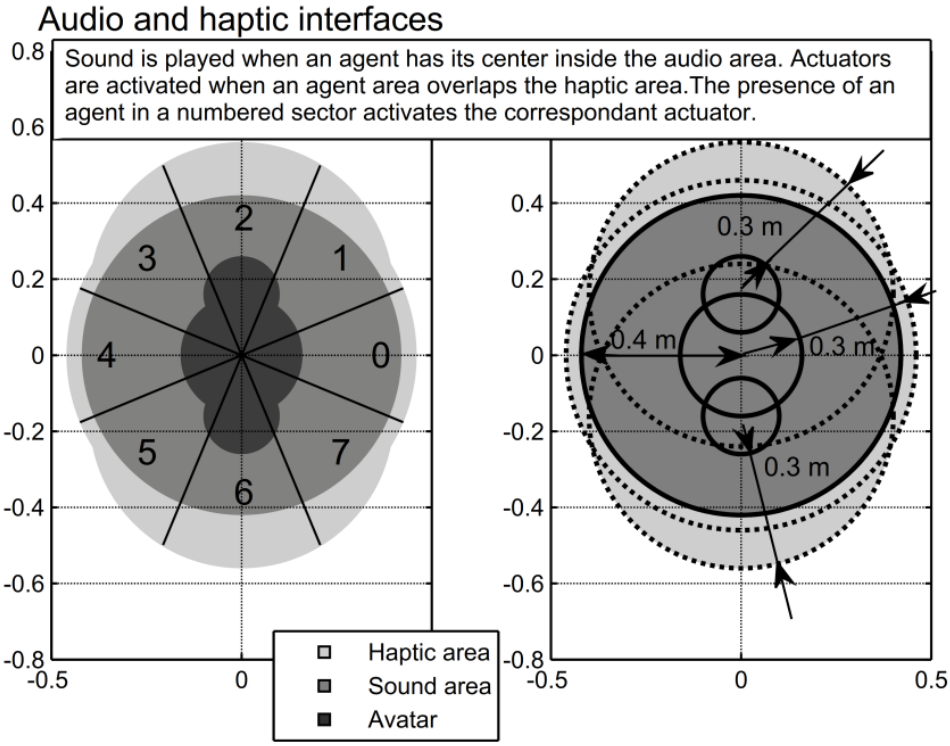

Figure 5.5: Sectors defining when the vibrators are activated and when the sound is played.

Finally, Figure 5.6 shows a user wearing all the presented interfaces and using the application.

Figure 5.6: User wearing all the presented interface while using the application.

5.5 Final remarks

The present chapter discussed the possibility of using virtual reality to acquire additional information on human behaviour in the evacuation process. A review of the topic was presented and the main advantages and limitations of the approach were discussed. Subsequently the modelling and implantation of the input and output interfaces allowing the user participation in the evacuation process where thoroughly described. Moreover the developed hardware and software concerning a haptic interface was presented. The haptic interface consists in a stripe with vibrators, developed to provide the users with a tactile feedback, informing them on the presence of close agents or contact with walls. The presented interfaces were adopted to set up an experiment with real time user interaction having the target of comparing user behaviour with the behaviour of the simulated agents and of assessing the effect of the haptic interface on users' behaviour.

The test case and its outcomes will be thoroughly described in the following chapter.

6 EXPERIMENTS WITH VIRTUAL REALITY: HUMAN BEHAVIOUR IN EVACUATION

The developed tool and user interfaces were adopted in an experiment where the subject was immersed in a virtual environment where he/she interacted with simulated agents. The experimental setup and the targets of the performed experiment will be carefully described in the first introductive session of the present chapter.

The second session of the chapter will be mostly focused on the comparison between the users' behaviour in the experiment and the behaviour of simulated agents.

Finally the third session will discuss the results concerning the implemented haptic interface, presenting the results of additional experiments which have been carried out to clarify the outcomes of the first one.

6.1 Introduction

In view of the studies on the application of virtual reality to the process of validation of an evacuation model, such as those reported by Moussaïd et al. [143] and by Olivier et al. [164], an experiment with the use of virtual reality was implemented to acquire data for the comparison with the developed evacuation model.

Moreover, the observation made by Kretz et al. [117] about the possibility of enhancing user perception of contacts through the use of a haptic interface suggested the introduction of this type of interface in the experiment. The data acquired during the experiments, in particular, were used also to assess the effect of the interface on users' behaviour.
Summarizing, the targets of the experiment were:

- Obtaining more information on human behaviour and compare human behaviour with the behaviour of simulated agents.
- Assess the effects of the developed haptic interface on users.

The following sub-section will provide a detailed description of the adopted geometry and condition for the experiment. Moreover exhaustive information will be provided about the population of the experiment and about the preparation of subjects which was performed before each test.

6.1.1 Geometry and test condition

The geometry adopted for the experiment Figure 6.1 was extracted from the IMO test 8 from MSC.1/Circ.1533 [147]. The test condition of IMO test 8 was chosen because allows a high grade of interaction between agents, due to the counterflow condition, while still being relatively simple and easy to analyse.

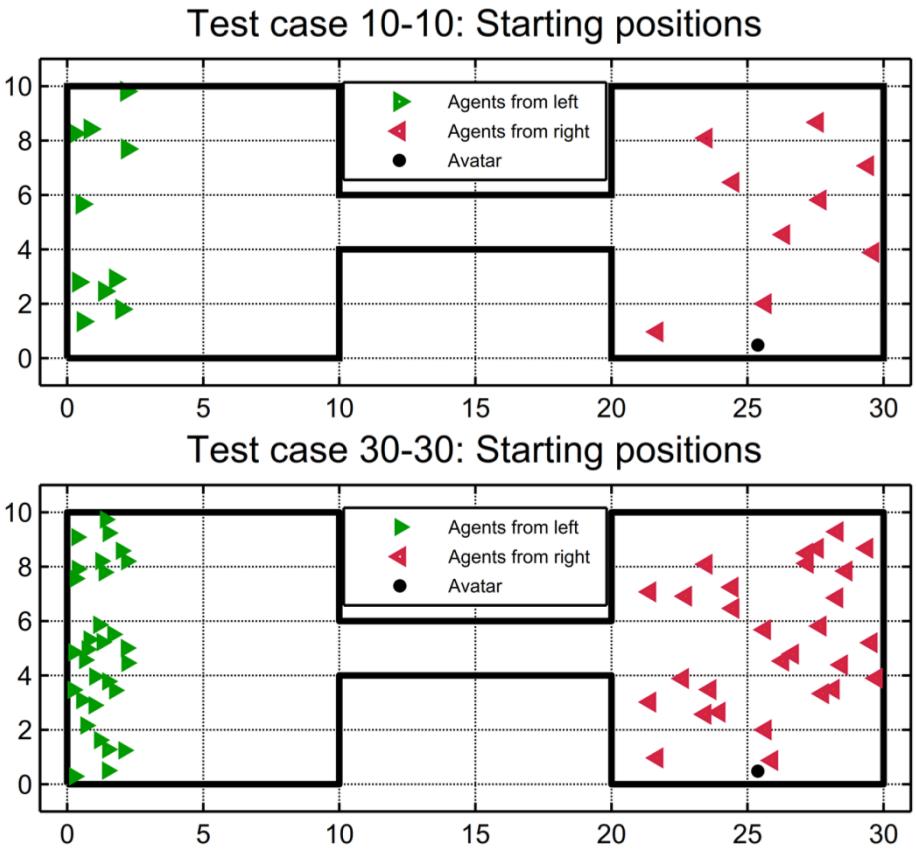

Figure 6.1: Starting conditions for the two different test cases.

Qualitatively, the situation of the test is the one described in MSC.1/Circ.1533 [147], where a group of agents start from the left and is directed towards the right exit, while another group starts from the right and is directed towards the left exit, in a typical counter-flow condition. Moussaïd et al. [143] and Olivier et al. [163] analysed an archetypal counter-flow situation, where the user is facing only one agent coming in the opposite direction. A counter-flow condition with a larger number of agents can be interesting as it leads to global phenomena, such as lanes formation ([236]).
Two different test conditions were considered, which differ only by the number of agents. In the first test case ("Case 10-10") there are 10 agents directed from left to right and 9 agents plus the user-controlled avatar directed from right to left. In the other test case ("Case 30-30") there are 30 agents going from left to right and 29 plus the user-controlled avatar going from right to left. Each test case was repeated two times by each user for a total of 4 test session per user. In particular, for each specific test case, during one session the haptic interface was enabled while during the other session it was disabled.

The order of the four test sessions was randomized for each user. This choice prevents experimental results from being dependent on the order of the sessions. The initial positions of the avatar and of each agent, as reported in Figure 6.1, were kept the same for all simulations and users.

Agents' unimpeded speeds were specified according to the distribution provided in the IMO test case 8 in MSC.1/Circ.1533 [147]. Agents' dimensions were distributed according to the "Male" class as reported in Table 4.2.

User controlled avatar parameters were kept the same for all simulations. In particular, the maximum unimpeded speed v_{0MAX}^{A} (see Chapter 5) was set to 1.62 m/s , which corresponds to the maximum speed of agents in this test case. The relaxation coefficient τ_{A}^{f} of the avatar control force was reduced to 0.5 s (see Chapter 5).

Finally, the avatar geometrical dimensions were derived by considering a fixed mass of 75 kg from equations (2.10).

6.1.2 Population of the experiment and preparation of the subjects

The experiment was performed on 30 students of the University of Trieste (7 females and 23 males) with age between 21 and 34. The size of the sample related to the present experiment (30 subjects), although not large in absolute terms, is, however, comparable to, e.g., [170] and [120].

Before the test subjects were invited to sustain a training session aimed to allow them gaining familiarity with the controller. During the training session, carried out without the use of the head mounted display, the subject was immersed in a simple room. The task was to reach in the shortest time amount a sphere appearing in different positions. The virtual environment and the software for the training were created specifically for this experiment.

The test was repeated two times without changing the positions of the sphere. Most of the subjects couldn't recognize that the positions of the sphere were unchanged in the two sessions. However, Figure 6.2 shows that the time required to complete the second session was reduced, in the average, with respect to the time required to complete the first, assuring the effectiveness of the training.

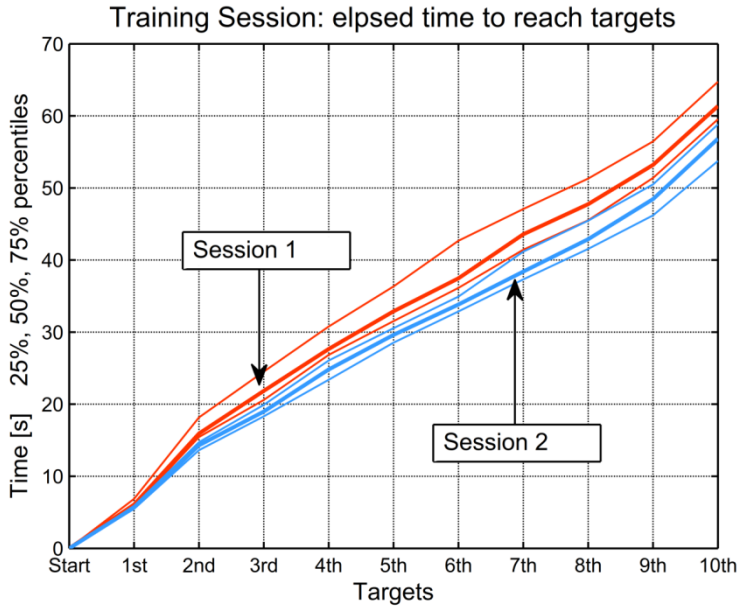

Figure 6.2: Outcomes from the training: in red the first session, in blue the second session.

To guarantee that all subjects receive the same information, the instructions for the test cases were provided to each user in written form. Also, subjects were not influenced regarding how to respond to stimuli received from the haptic interface.
The most relevant instructions provided to each subject can be summarised as follows:

- During the test the subject will be immersed in a virtual environment composed of two rooms connected by a corridor.
- The subject should reach the farthest wall of the room opposite with respect to the room the avatar is placed in at the beginning of the test.
- During the simulation the subject is invited to behave as if the evacuation situation was real.

The subject may perceive the actuators activating in some conditions. The perceived vibration is related to the closeness of an agent or to the contact with a wall.
The instruction provided to subjects where slightly modified to perform other additional experiments which will be described in the following section.

Experiment procedures were approved by the Ethical Committee of the University of Trieste. Informed consent was obtained by participants based on Ethical Committee requirements

6.2 Test result: Comparison between human subjects and agents

The position and speed of the avatar controlled by the user was recorded for each time instant of the simulation assuring the possibility of a detailed analysis of the experimental outcomes.

This section proposes different qualitative and quantitative comparisons between the outcomes from users from the experiment and from computer controlled agents.

Experimental results are compared with outcomes from 100 Monte Carlo fully-computer-controlled simulations, where the user-controlled avatar is substituted by a corresponding-computer controlled agent, with the same initial position and unimpeded speed as the user-controlled avatar. A total of 100 Monte Carlo realizations have been considered sufficient for obtaining reliable estimates for comparison with experimental data. Different quantities have been compared, aiming at offering an exhaustive interpretation of the experiment results.

Several differences have been found between humans and computer controlled agents. In particular, in general, the level of variability of outcomes was found to be higher for humans than for computer-controlled agents.

As the experiment was performed with and without the use of the developed haptic interface, an additional outcome of the test was also found in the experiment in relation to the use of the haptic interface. The comparison will be hence presented providing all the results of the experiment, from the cases with the haptic interface, without the haptic interface and from the simulations. The observations made concerning the comparison between the cases with and without the haptic interface inspired two other experiments that will be described in the next subsection.

6.2.1 Short distance time intervals

An analysis was carried out regarding the distribution of the length of the time intervals when the avatar is continuously close to another specific single agent (briefly “short distance time intervals”). The analysis of this quantity was initially aimed at assessing the effect of the developed haptic interface on users’ behaviour. However, it can also be used to assess the attitude of users to keep a reduced distance from the other agents and to compare this behaviour with the one embedded by the mathematical model in the computer-controlled agents.

For this analysis, two agents are considered at “short distance” when their skin-to-skin distance is less than a threshold, corresponding to the threshold value for the activation of the haptic interface. Each continuous interaction with a single agent identifies a different interval. The interval starts when the distance between the avatar and the agent gets smaller than 0.3 m (the threshold for the activation of the haptic interface (see Chapter 5) and ends when it gets larger. All intervals from all realizations of each specific test case are considered in the analysis.

An example identification of short distance time intervals is reported in Figure 6.5, where a representation of short distance time intervals is shown for an example realization corresponding to test case 30-30, with user participation. Each vertical line corresponds to one agent and agents are ordered by the distance from the avatar at the beginning of the simulation. Time is reported on y-axis and short distance time instants are marked. It can be noticed that the avatar firstly interacts with closest agents in the same room, while moving towards the corridor. Afterwards, the avatar interacts also with agents in counterflow coming from the opposite room. Multiple interactions can be seen to occur at the same time instant, for several different time instants. Furthermore, the length of short distance time intervals tends to be smaller when the avatar interacts with agents in counter-flow, and longer when the avatar interacts with agents going in the same direction.

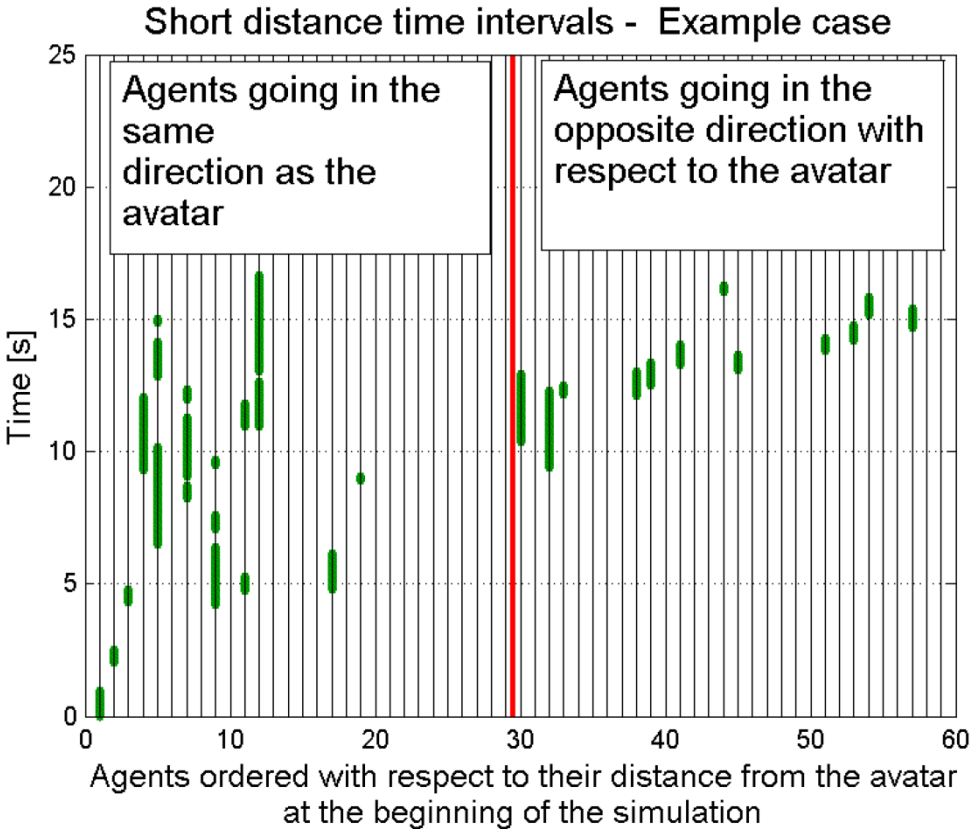

Figure 6.3: Example representation of short distance time intervals for one realization of the test case 30-30, with user participation.

Probabilities of exceedance $(1-cdf)$ for short distance time intervals, as estimated from experiments ("haptic", "non-haptic") and from fully computer-controlled simulations ("computer") are reported in Figure 6.4.

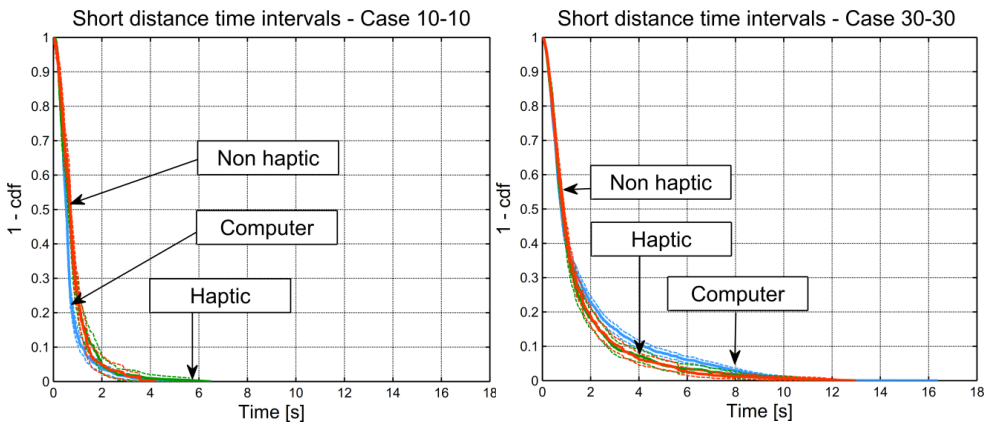

Figure 6.4: Estimated probability of exceedance (1-cdf) of short distance time intervals for cases 10-10 (left) and 30-30 (right)

In the case 10-10, the curve associated with the computer-controlled agent is below those associated with user controlled avatar (haptic and non-haptic). This means that, in case 10-10, the computer-controlled agent tends to stay at short distance to other agents for shorter time intervals compared to user-controlled avatars. This can be associated with the fact that, in this low density situation, the computer-controlled agent nearly instantly moves away from close agents due to the strong action of interaction forces. Instead, the reaction is not so immediate in the experiments. In particular, either the user response to the proximity to other agents is delayed or the user reaction is weaker compared to the computer-controlled agent.

The situation is, instead, opposite for the case 30-30, where the computer-controlled agent tends to stay at short distance to other agents for longer time intervals compared to user-controlled avatars. In this high-density condition the repulsive forces exerted on the computer-controlled agent from all the close agents basically balance each other. Therefore, computer-controlled agents tend to remain close to each other keeping the lane. On the contrary, it has been observed in the experiments, and later confirmed by the analysis of avatars' trajectories, that some users do not maintain a similarly ordinate behaviour and they try to overcome slow agents, without remaining in the lane.

The comparison of exceedance probabilities between experiments carried out with and without haptic interface does not show, instead, visible differences in both test cases. A possible explanation for this lack of difference could be that, in most cases, agents react to proximity to the avatar before the user does. As a result, the distribution of short distance time intervals could be determined more by the agents' model than by the users' behaviour.
The modification of the exceedance probability from case 10-10 to case 30-30 observed in the experiments is qualitatively reproduced by the simulations with computer-controlled agents.
A set of two-sample Kolmogorov-Smirnov tests have been also performed, separately for each test case, as reported in Table 6.1, to test the null hypothesis of equal distributions of short distance time intervals among the different conditions. The hypothesis test basically confirms the outcomes from visual observations of exceedance probabilities.

Table 6.1: Two-sample Kolmogorov-Smirnov test for short distance time intervals. Significance level: 0.05 Samples: Haptic - 290 (10-10), 752 (30-30); Non haptic - 259 (10-10), 798 (30-30); Computer-controlled: 792 (10-10), 2408 (30-30).

	Test Case 10-10	Test Case 30-30
Hapt. - Non hapt	ns	ns
Comp. - Hapt	<0.0001****	0.0475*
Comp.- Non hapt.	<0.0001****	0.0311*

6.2.2 Trajectories and travelled paths

Trajectories are often analysed in case of pedestrian dynamics, especially in case of counter-flow situations, as they offer valuable information about the way people maintain the lane formation (Zhang et al. [236]).

Herein we propose the analysis of the trajectory of the test case 30-30. Figure 6.5 shows all avatars' trajectories from experiments, as well as all paths from computer-controlled simulations.

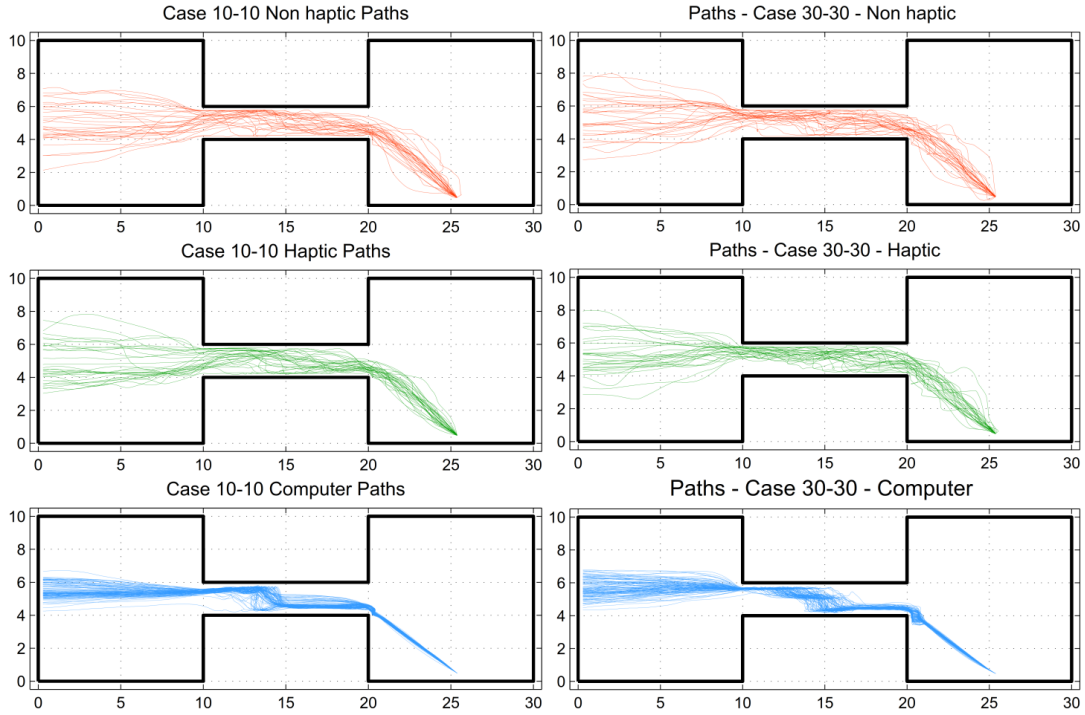

Figure 6.5: Test case 30-30. Trajectories. Test case 10-10(left), test case 30-30(right).

Mean trajectories for each time instant have also been determined, as shown in Figure 6.6. The instantaneous mean trajectory is calculated as the ensemble average position of the avatar/agent from all realizations. In order to reduce the scattering in the final parts of the calculated mean trajectories, the agents/avatars who have already reached the exit, and which in the simulations/experiments actually disappear from the environment, are instead assumed to remain fixed at their exit position.

The difference between experiments and computer simulation results is well marked. In particular, computer generated paths have much less variability than the user generated

ones. This greater variability can also be linked to the observed attitude of most of the users to try overcoming other agents, as discussed before.

It is evident, in Figure 6.5 and especially from the average trajectories plotted in Figure 6.6, that users start the lateral shift to avoid counter-flow agents sooner than the computer-controlled agents. This difference can be related to the fact that the counter-flow model for the agents has a short-range nature, while users seem to obey to a longer range counter-flow strategy.

Finally, in this case, the tendency to maintain the right when in counter-flow and to keep the lane, which was observed also experimentally by Zhang et al. [236], is not as marked for users as it is for the computer-controlled agents.

Concerning, instead, the influences of the haptic interface, the analysis of trajectories does not indicate any evident difference between the case with and without the haptic interface.

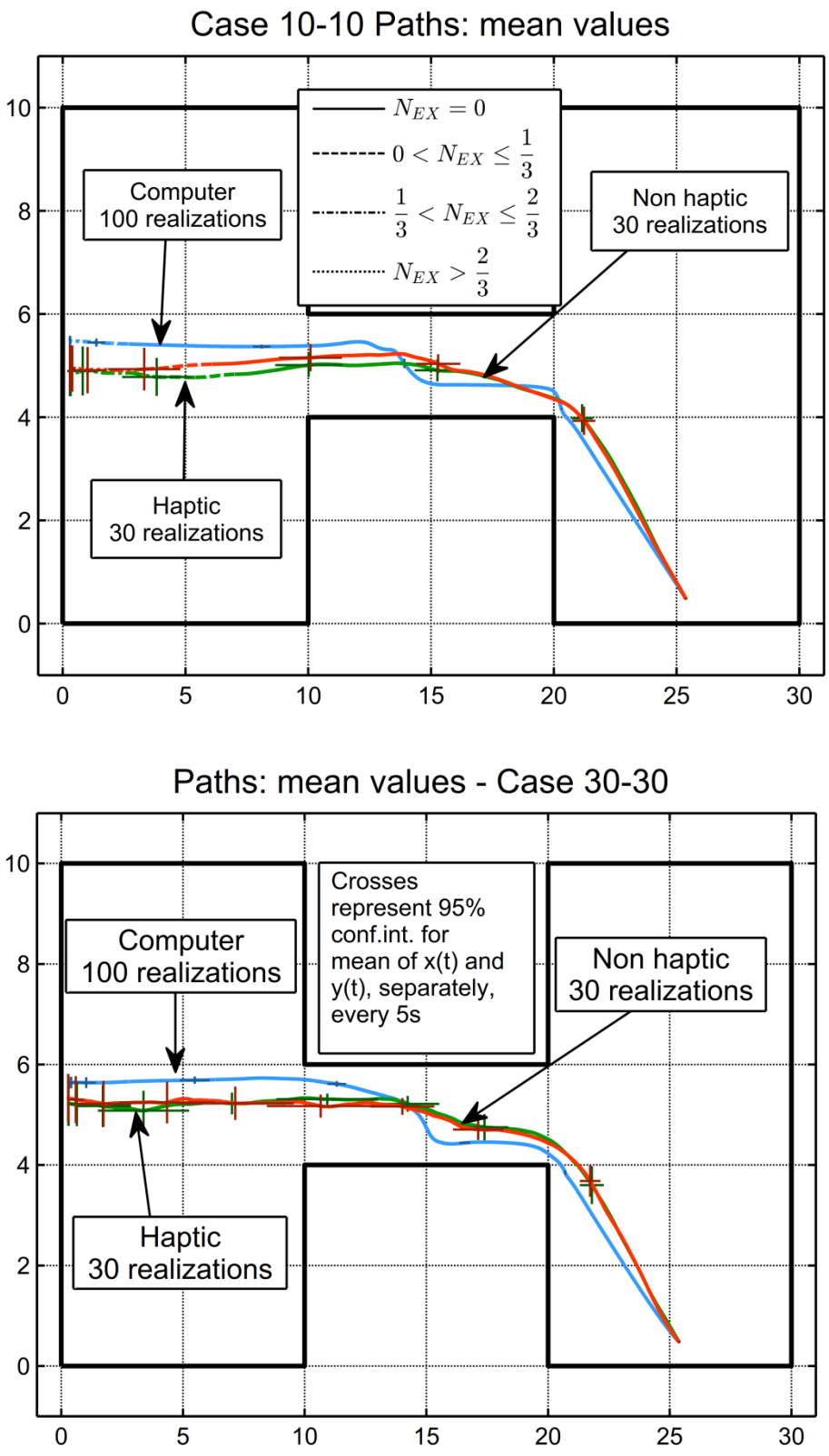

Figure 6.6: Mean of trajectories over time with 95% confidence interval for ensemble mean of $x(t)$ and $y(t)$. f_{EX} is the fraction among all realizations N_R of already exited avatars $N_{AE}(t)$ at each time instant (i.e. $f_{EX}(t) = N_{AE}(t) / N_R$). Test case 10-10 (left) and test case 30-30 (right).

In order to provide further analysis related to the path travelled by agents the total travelled path length was considered. The analysis aimed at determining how much the user and the agent are far from the minimum possible path corresponding to the shortest walkable distance from the target point. The obtained results are reported in Figure 6.7.

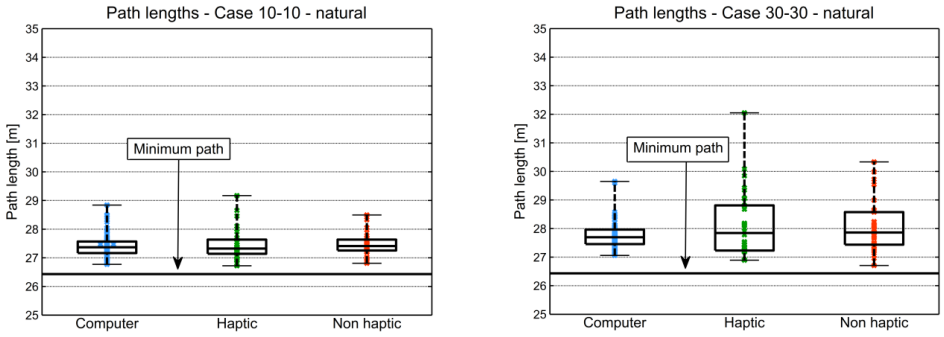

Figure 6.7: Travelled path lengths.

Although, due to the physics of the test case, all paths tend to have a similar length, the wider variability of user outcomes with respect to the computer controlled agent can be still observed.
The result is particularly evident in the test case 30-30. Moreover in this test case the data concerning the haptic condition seem to show variability larger than those concerning the non haptic condition. This might be due to the different response of the users to the haptic feedback.

6.2.3 Exit time analysis

The exit (arrival) times, were finally analysed and reported in Figure 6.8.

From a qualitative point of view, the dispersion in data from human-controlled avatars is larger than that obtained by computer-controlled agents. This is an additional indication that the variability in the modelled behaviour of agents underestimates the one in the behaviour of real humans.

The two-sample Kolmogorov-Smirnov test rejects the null hypothesis of equal distribution between computer-controlled agents and user controlled agents for all cases, with the exception of case 30-30 with haptic interface. Still, the null hypothesis, in the 30-30 case, is rejected when comparing computer and non-haptic results. However, this seems to be a random outcome due to sampling uncertainty, because a visual comparison of the estimated cumulative distributions of exit times shows that the difference between computer-controlled agents and users with haptic interface is quite evident also in this case.

The two-sample Kolmogorov-Smirnov test does not identify any statistically significant difference between haptic and non-haptic condition and indeed the distribution does not show evident difference.

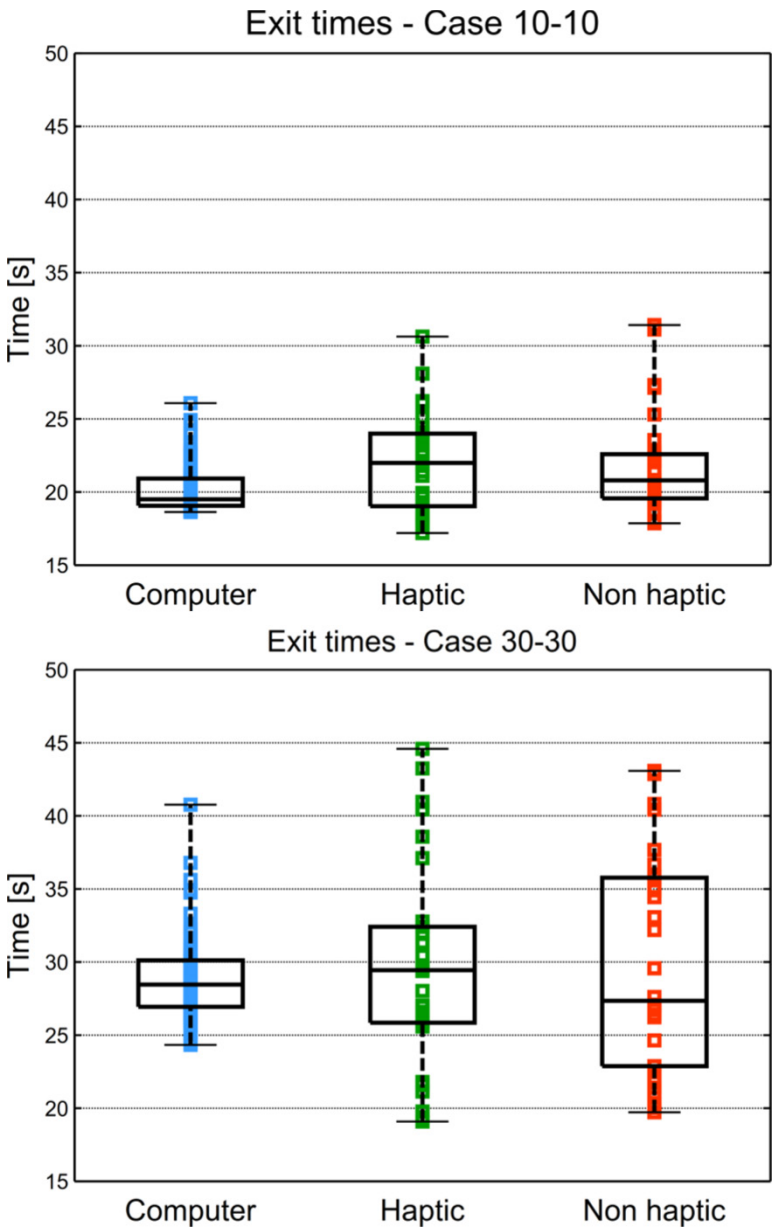

Figure 6.8: Exit times. Box plots (25%, 50% and 75% percentiles, plus min and max) with scatter of data.

6.2.4 Snapshots of avatar position

A more qualitative analysis is proposed herein. The aim of the analysis is summarizing the behaviours observed separately through the quantitative analysis performed before through a more exhaustive visualization of all experimental data.

To this purpose Figure 6.9 reports the position of the avatar controlled by users in each test and for each realizations performed with the computer controlled agent in the test condition 30-30. The positions are reported at intervals of 3 seconds of the simulation. The figure clearly shows that the dispersion in data from human-controlled avatars is larger than that obtained by computer-controlled agents (see, for example, the situation at 15 seconds), moreover the long range strategy adopted by user in counterflow condition is also observable (see the situation at 9 seconds) .

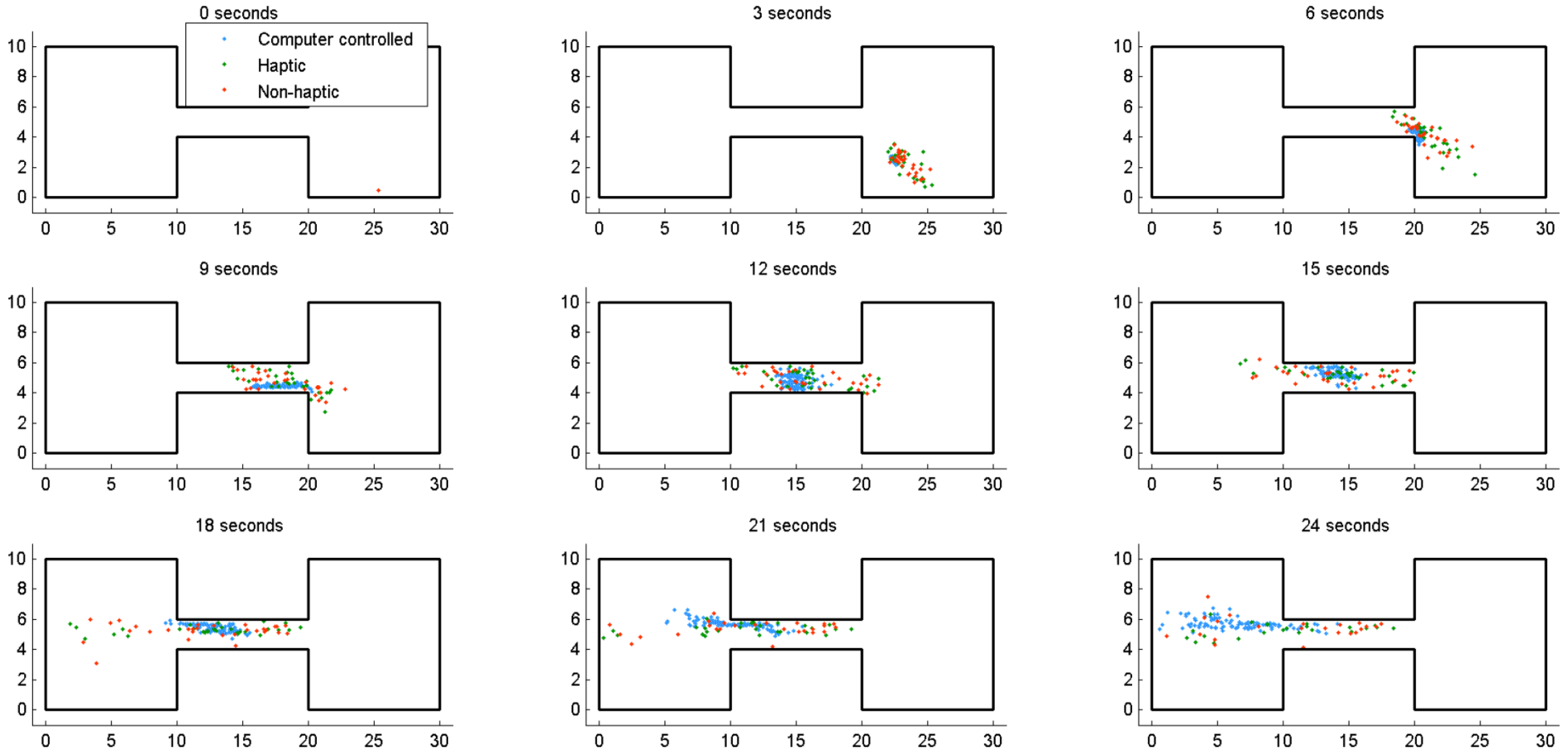

Figure 6.9: The position of the avatar for each realization is reported at intervals of 3 seconds.

The performed analysis still does not show evident effects of the haptic interface on users' behaviour.
The lack of statistically significant and/or evident effects of the haptic interface on users' behaviour in experiment requires further clarification. To this purpose, two different experiments were carried out in addition to the presented one and they will the topic of the following section.

6.3 Effect of haptic device on behaviour of human subject

The results presented in the previous chapter showed that the haptic interface had not visible effects on subjects behaviour.

The lack of statistically significant effects could be explained by two different hypotheses: either the haptic interface was not effective at all, or most users considered as a prior objective the reaching of the target destination in the minimum amount of time, without paying attention to the avoidance of contacts.
In order to clarify this point, two new experimental tests RA2, NA, were conceived and performed.
The differences between the three experiments are listed below:

- **RA1 (Rendered Agents 1)** Users were invited to behave naturally and computer-controlled agents were rendered.
- **RA2 (Rendered Agents 2)** Users were invited to avoid contacts with agents and computer-controlled agents were rendered.
- **NA (Not rendered Agents)** User were invited to avoid contacts with the agent and computer controlled agents were not rendered

The experimental case reported in the previous chapter, where users were invited to behave normally and agents were rendered will be called **RA1** (Rendered Agents 1) in the following.
The two-sample Kolmogorov Smirnov test is reported for each experiment and for each test case in
Resulting p-values from the two sample Kolmogorov-Smirnov test comparing haptic and non-haptic case are reported in Table 6.2.

Table 6.2: The two-sample Kolmogorov Smirnov test is reported for each experiment and for each test case. Resulting p-values from the two sample Kolmogorov-Smirnov test comparing haptic and non-haptic case are reported. The p-values indicating a statistically significant difference (95% significance level) are reported in bold. The symbol + indicates that the mean value for the haptic case is higher than the non-haptic whereas the symbol – indicates the opposite.

K-S test p-values:		**Test case 10-10**	**Test case 30-30**
Short distance time intervals mean	**RA1**	0.5372	0.7600
	RA2	0.3529	0.3481
	NA	0.3577	**0.0232 (-)**
Travelled path length	**RA1**	0.7600	0.7600
	RA2	0.6325	0.6325
	NA	**0.0232 (+)**	0.1349
Exit times	**RA1**	0.3420	0.5372
	RA2	**0.0231 (+)**	0.5465
	NA	0.2753	0.1349

6.3.1 Test case RA2: users invited to avoid contacts

This test case differs from the case RA1 only in relation to the instruction provided to the subjects. Specifically, subjects were invited to avoid being close to other agents.

The distribution of the short distance time interval length (see section 6.2.1) for the RA2 experiment is reported in Figure 6.10.

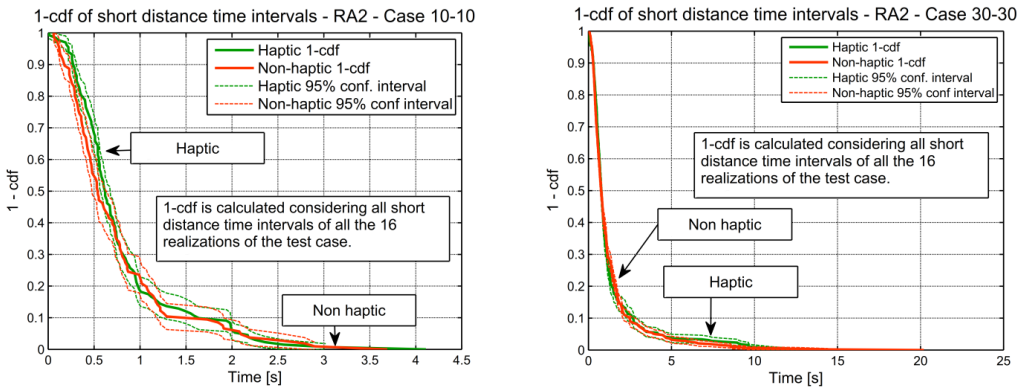

Figure 6.10: RA2: Estimated probability of exceedance (1-cdf) of short distance time intervals for cases 10-10 (left) and 30-30 (right).

With reference to the short distance time interval, there is no evident difference between the haptic and the non-haptic case also in this experiment even in this test condition. This is confirmed by the results of the Kolmogorov-Smirnov test performed on the mean short distance time interval length reported in Table 6.2.

The travelled path analysis shows no remarkable differences as well Figure 6.11 and the Kolmogorv-Smirnov test does not reject the null hypothesis of equal distribution in both the cases 10-10 and 30-30 (Table 6.2). The exit time comparison shows also no remarkable differences (Figure 6.12).

An evident difference between the haptic and non-haptic condition is present in the exit time analysis, in the case 10-10 Figure 6.12 (left). This difference is also statistically significant (Table 6.2).

However, the difference detected in Figure 6.12 (left) is not sufficiently marked to prove the presence of an evident effect of the haptic interface on the simulation. Moreover, this difference is restricted only to the case of exit times in a specific case, proving only a reduced impact on the overall users' behaviour.

Possible explanations for the reduced impact of the haptic device on the experimental tests are:

- either the vibrotactile interface does not provide the subject with proper haptic stimuli;
- visual stimuli are predominant with respect to the vibrotactile ones.

In order to investigate this research question raised by RA2, a last experiment set-up was proposed (NA), in which computer-controlled agents were not rendered. In this

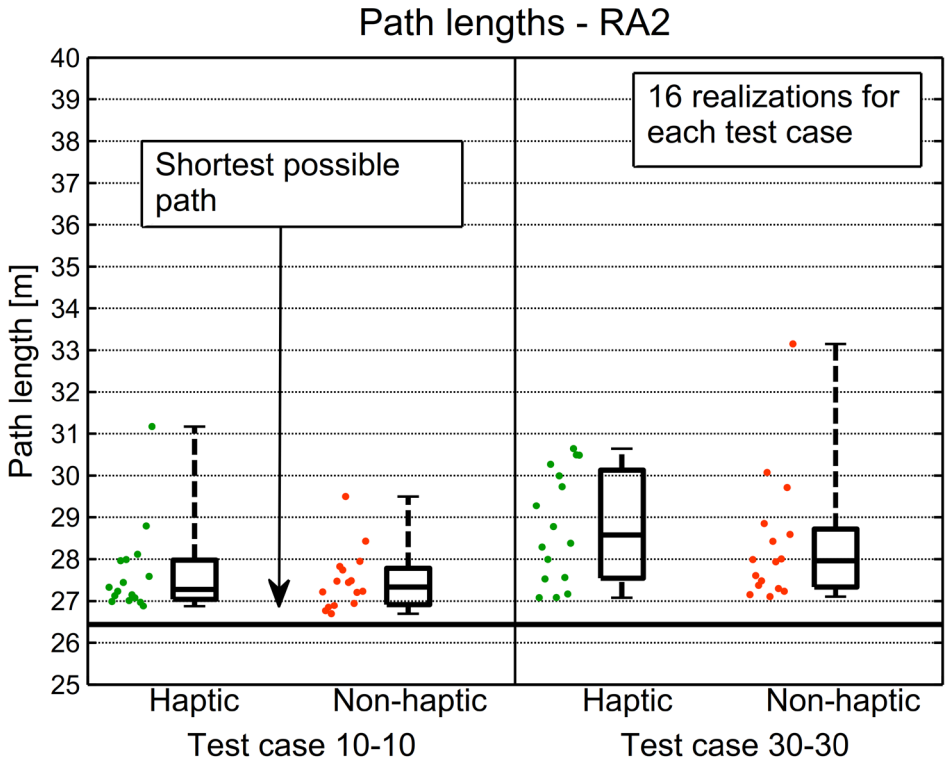

Figure 6.11: RA2: Travelled path lengths. Box plots (25%, 50% and 75% perc., min and max) with scatter of data.

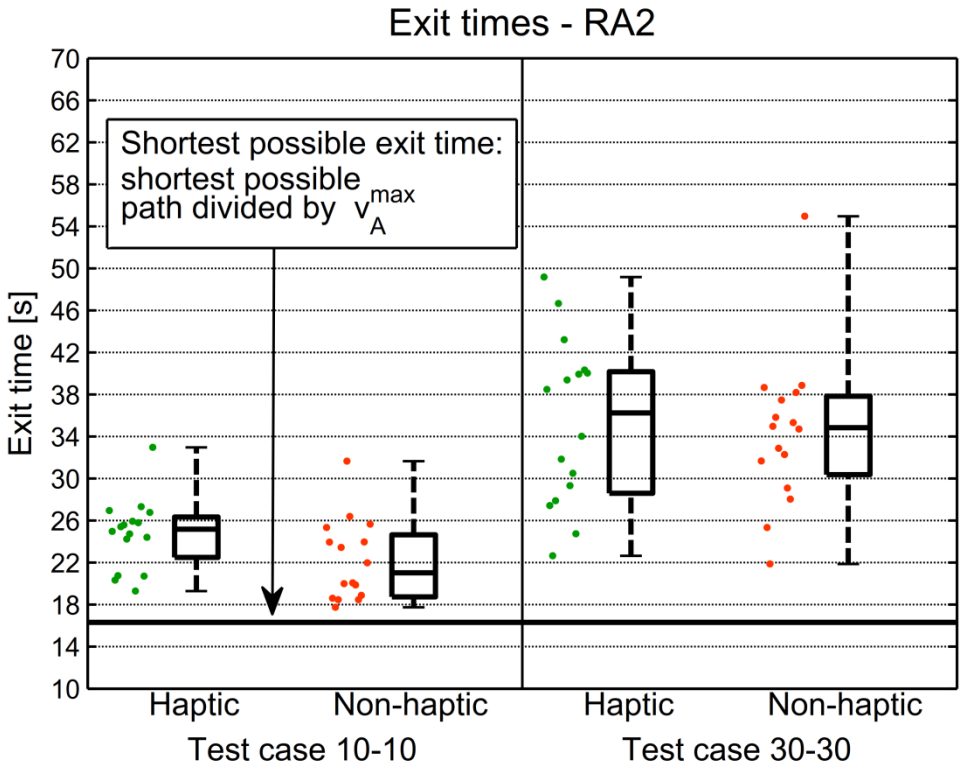

Figure 6.12: Exit times. Box plots (25%, 50% and 75% perc., min and max) with scatter of data.

6.3.2 Test case NA1: not rendered agents

As expected, this final analysis shows visible differences between the haptic and the non-haptic case.

Differences are observable in the comparison of short distance time interval probability of exceedance, as reported in Figure 6.13. The difference is marked in the case 30-30, whereas is not clearly visible in case 10-10. The different outcomes obtained between cases 30-30 and 10-10 might be due to the fact that in the condition of low density the number of interval is reduced with respect to the situation of higher density, leading to a more uncertain estimator of the true distribution.
The curve related to the haptic case in Figure 6.13 is systematically below the curve related to the non-haptic case, suggesting that in the haptic case the short distance intervals tend to be shorter than the ones in the non-haptic case.

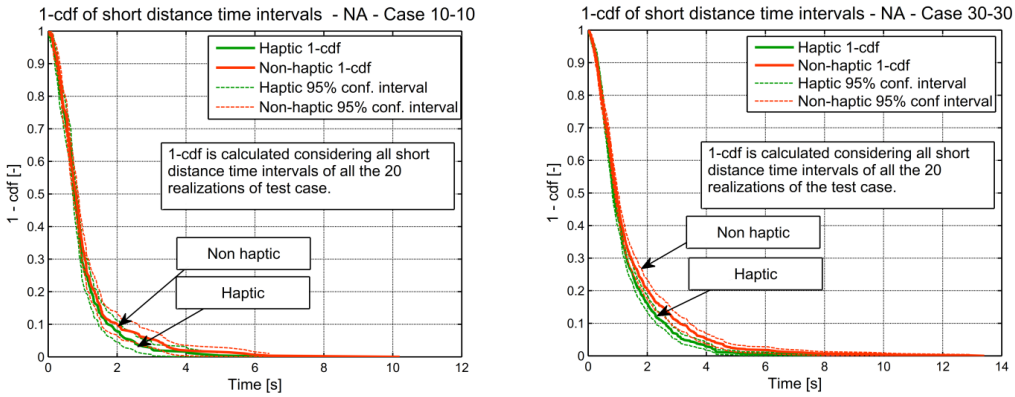

Figure 6.13: Probability of exceedance for short distance intervals of the experimental session NA for cases 10-10 (up) and 30-30 (down).

The difference is confirmed in the comparison of distribution of the mean short distance time interval length as reported in Figure 6.14(right). From the figure it can be observed that there is no marked difference between haptic and non-haptic in the case 10-10 (left). The difference in the median is instead marked in the case 30-30. The difference between the distributions is statistically significant according to the Kolmogorov-Smirnov analysis reported in Table 6.2 in this case.

The outcomes from this experiment show visible differences between haptic and non-haptic case also in relation to the analysis of the travelled path, as reported in Figure 6.15.

This experiment showed that the developed haptic interface is actually perceived by users and has effects on their behaviour. However, as proved by experiments RA1 and RA2, the effects of the interface are mitigated or annihilated in some cases by the visual perception.

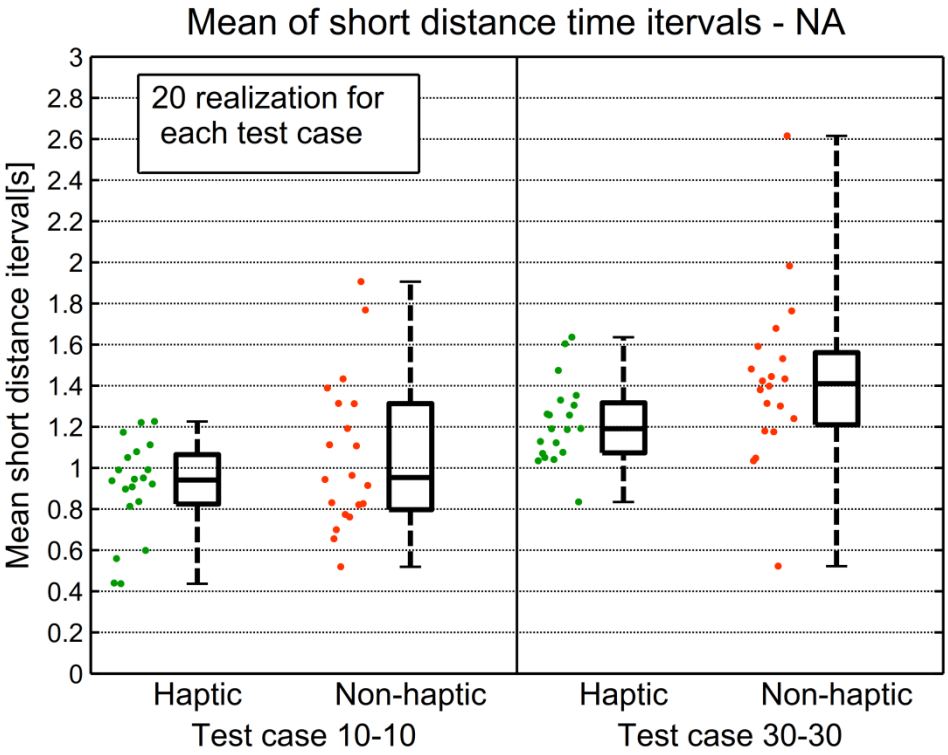

Figure 6.14: Exit times. Mean values of short distance intervals of the experimental session NA for cases 10-10 (left) and 30-30 (right), reported with the related boxplot.

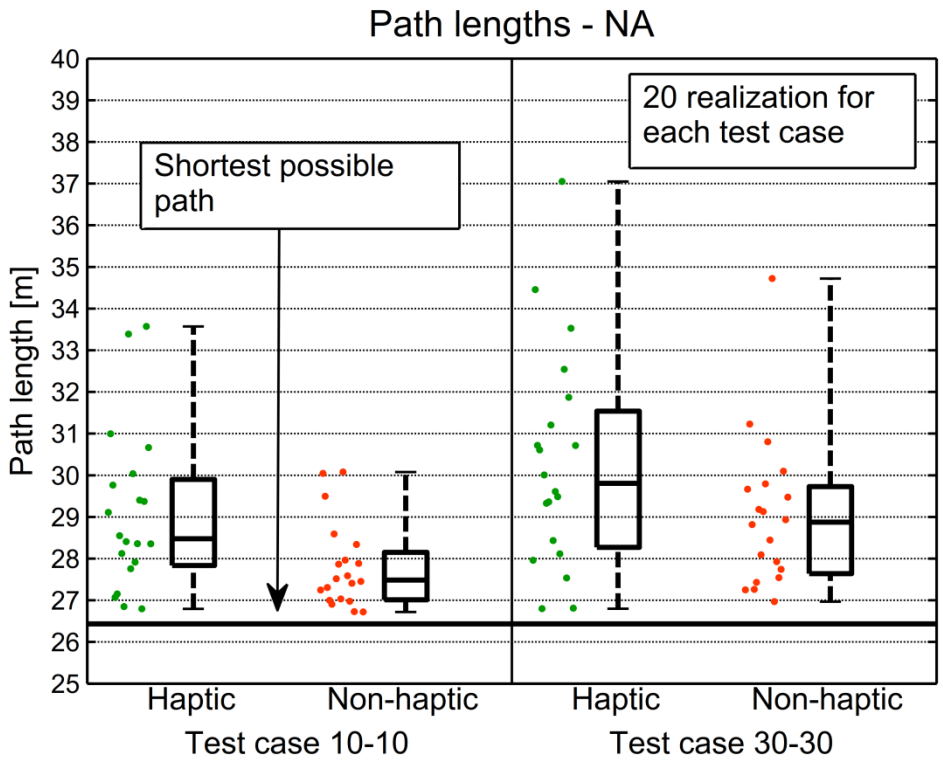

Figure 6.15: Travelled path lengths related to the experimental session NA for cases 10-10 (left) and 30-30 (right), reported with the related boxplot

The difference, in this case, is statistically significant only for the test condition 10-10 (Figure 6.15 (left), Table 6.2). In both cases we observe that the median of the haptic outcomes is above the median of the non-haptic, suggesting that users travel a longer path when they are informed of the presence of surrounding agents. However, in the case 30-30 user movement is impeded by the high density condition; users are therefore less free to modify their path in order to avoid agents.

In the analysis of exit time (Figure 6.16) no statistically significant difference was detected in the outcomes of this experiment (Table 6.2).

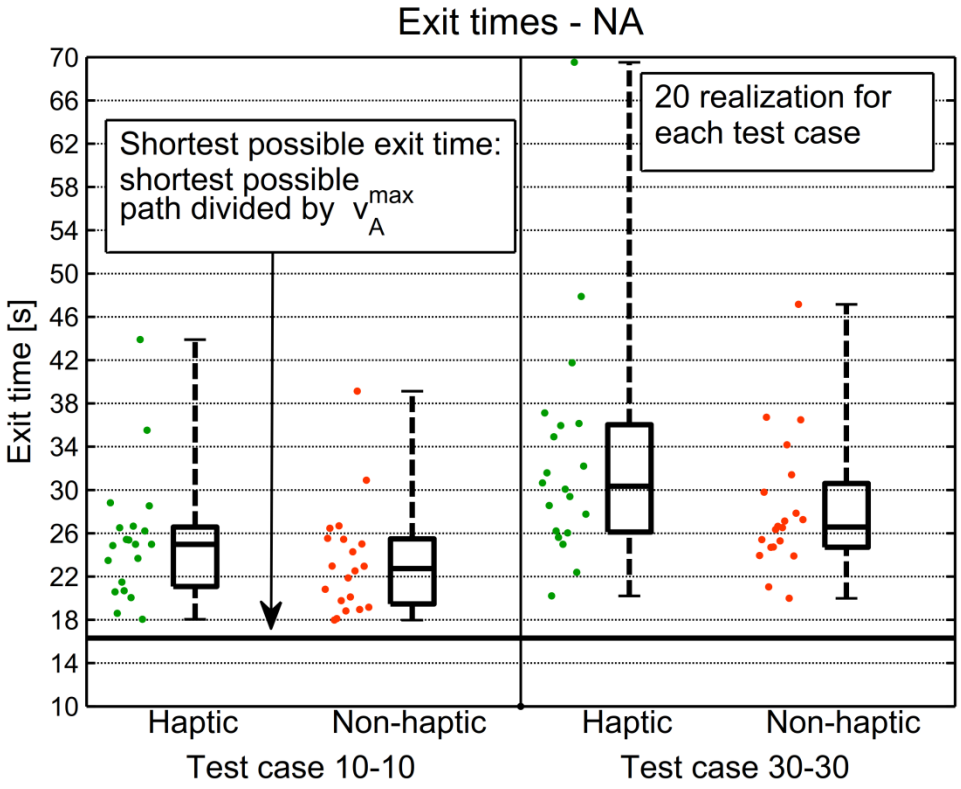

Figure 6.16: Exit times related to the experimental session NA for cases 10-10 (left) and 30-30 (right), reported with the related boxplot.

From Figure 6.16 it can be seen that median value related to the haptic case is above the one of the non-haptic case in both test conditions although the Kolmogorov Smirnov test does not reject the null hypothesis of equal distribution in both cases 10-10 and 30-30 (Table 6.2).

6.3.3 Use of movement interface: comparison between the experimental outcomes

This final analysis is related to the utilization of the analog stick made by users in the tests. This analysis differs from the others as it focuses on the user control rather than on the effects of this control on the avatar movement. The analysis, reported in Figure 6.17, is restricted to the 10 seconds right after the entrance of each user in the corridor in order to compare the users' behaviour in a similar condition. Data from all users are combined to arrive at a unique distribution for each test condition.
The probabilities of exceedance (1-cdf) obtained considering the value of the X-axis of the analog stick used for the movement are considered. A positive value of the X-axis corresponds to the forward direction, whereas a negative value corresponds to the backwards direction with respect to the avatar reference system.

From Figure 6.17 it can be seen that the probability of the X-axis being 1 is not null. The situation where the X-axis is equal to one corresponds to the maximum inclination of the analog: the user has selected the maximum speed as its desired speed. The difference among the curves is not marked in the experiment RA1 (Figure 6.17 (up-left)). In the experiment RA2 (Figure 6.17 (up-right)) a marked difference between the haptic and the non–haptic case is instead present, but only for the case 10-10. This difference is in accordance with the exit time analysis of the test case RA2 Figure 6.12 (left).

Finally, in the test condition AN (Figure 6.17 (down)), the differences are clearly visible in both the two test condition (10-10 and 30-30), in accordance with the results presented in Figure 6.13 – 1.15.

The fact that the curve for the haptic case is below the one for the non-haptic in the region of positive values shows that users tend to set the controller at the highest value when not perceiving the haptic stimuli. They instead modulate the inclination of the stick when perceiving the haptic stimuli.

The fact that the curve for the haptic case is below the one for the non-haptic in the region of positive values shows that users tend to set the controller at the highest value when not perceiving the haptic stimuli. They instead modulate the inclination of the stick when perceiving the haptic stimuli.

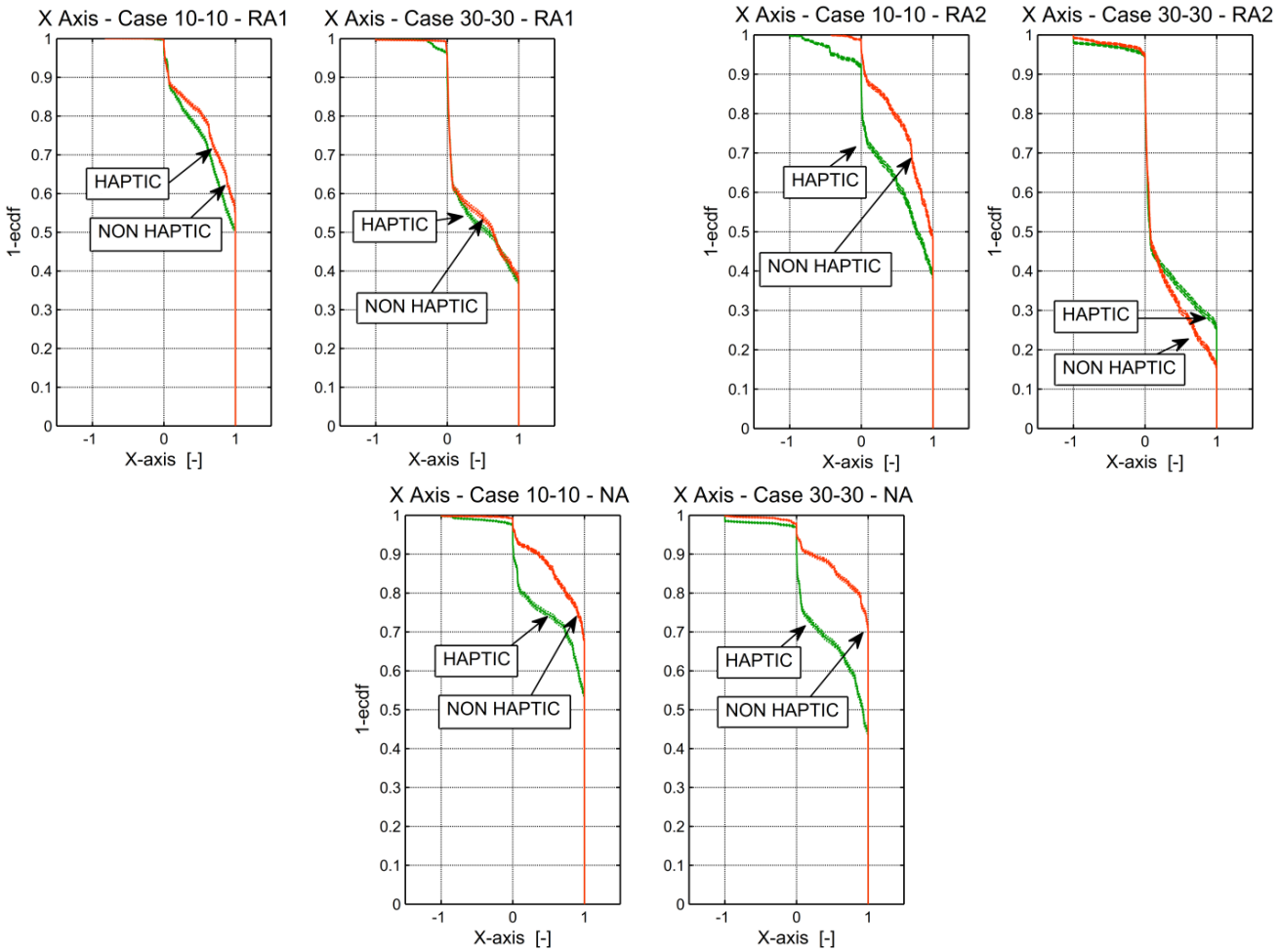

Figure 6.17: Probability exceedance (1-cdf) of controller X-axis, corresponding to the longitudinal direction of the avatar, evaluated for 10 s after the entrance in the corridor combining data from all users, for the test cases RA1 (up-left), RA2 (up-right) and NA (down).

6.4 Final remarks

Experiments using full immersive virtual reality and a haptic interface have been presented in the present chapter.

Three different experiments with respectively 30, 16 and 20 subjects aged between 21 and 34, were performed. The subjects were immersed in a virtual environment with other computer-controlled agents who interacted with the user as well as with other standard agents. In some experimental sessions users wore a haptic vibrotactile interface.

The objectives of the experiments were to obtain data regarding the behaviour of subjects in a counterflow condition to quantify the effect of the developed haptic interface, and to compare the behaviour of user-controlled avatars with that of computer-controlled agents. To this purpose different quantities, namely short distance time intervals, travelled path and global exit time where analysed.

The first experiment, where subjects were asked to behave naturally, showed a statistically significant difference between users and computer controlled agents in almost all cases. It was conjectured that the difference related to the short time distance interval analysis could be due to the attitude of most of the users to overcome slow agents and not respect lanes. Moreover the analysis of travelled path and trajectories showed that the dispersion is the most relevant difference between experimental and simulation data. This difference may indicate that the modelled behaviour of agents underestimates the actual variability in the behaviour of real humans. This hypothesis is confirmed also by the analysis of exit times, which also indicates no statistically significant difference between outcomes with and without haptic interface. In addition, the observation of the analysis of the trajectories showed that users seems to obey to a long range interaction behaviour which cannot be modelled by the short range interaction model developed herein.

The first experiment showed no statistically significant differences between the outcomes with and without the developed haptic interface.
One of the possible causes of absence of evident effects of the haptic interface in the presented test case may be the fact that users were not explicitly instructed to avoid agents. To further investigate the reason of the lack of effects of the haptic interface two other experiments where performed. One experiment was carried out directly instructing the subjects to avoid agents while in the other agents were not rendered. The experiments carried out with developed on the haptic interface showed that the utilization of the developed vibrotactile interface does not lead to evident differences in users' behaviour in evacuation simulation with virtual reality, when users are asked to behave naturally. A single slight difference was detectable when users where explicitly invited to avoid agents. A difference in users' behaviour is, instead, clearly present when the visual and audio interfaces do not provide information about the simulated agents positions and presence. The developed haptic interface is thus effective in informing the user about the proximity of agents. Moreover, the analysis of the differences on the way users utilize the controller showed analogies between the situation where agents were not rendered but perceived by means of the haptic interface

and the situation where agents were rendered. This suggests that users control the avatar in a similar way when perceiving agents presence only by vibration or only by vision. While the most marked difference between haptic and non-haptic outcomes in terms of use of controller was found in the test case with highest density, the test case with lowest density presented the sharpest difference in terms of travelled path. This can be explained by the fact that, in the situation of highest density, users are more constrained and thus unable to modify their path.
However, only further research might clarify if the present result is strictly related to the specific adopted haptic interface and to the considered test case, or it can be instead considered more generally applicable to evacuation experiments with virtual reality.

Another application of the hardware developed as haptic interface adopted for the experiment presented in this chapter will be described in Chapter 9 for an application with ship motions where also the problem of introducing motion effect on the avatar control will be addressed. The application of the haptic interface to ship motions is different from the one concerning contacts, as in this case the information provided by the user on perceived forces is uniquely provided by the haptic interface and not by other (visual or audio) stimuli.

The following chapter, instead, will address the introduction of ship motion effect in the mathematical model concerning the computer controlled agents.

7 EXTENSION OF THE SOCIAL FORCE MODEL TO ACCOUNT FOR SHIP MOTIONS

Modelling the evacuation process from a ship is extremely challenging. This is due not only to the complexity of the geometry of the vessel, but also to the presence of the ship motions, which might affect the evacuation performance. Nowadays, only a few evacuation tools implement a sub-model which allows considering ship motions in the simulation.

The present chapter will address the introduction of ship motion effects in the reference evacuation model based on social forces which has been previously described. The introductive section presents a review of available literature concerning models accounting for ship motion effects in the evacuation process and relevant experimental data.

The second section will present a new original sub-model capable of introducing the effects of ship motion on the evacuation not only as a reduction of speed (as it is most common), but also as a modification of the trajectory of agents through the application of instantaneous perceived forces as well as corresponding agent control forces. During the description of the sub-model particular attention will be paid to carefully reporting all relevant parameters.

Finally, the developed model will be embedded in the reference evacuation model described in the previous chapters, and will be adopted to assess the effect of ship

motions for the IMO test 4 (exit from bottleneck) and IMO test 8 (counterflow condition) from MSC.1/Circ1533 ([147]).

7.1 Introduction

One peculiarity of the evacuation in maritime field is the fact that the evacuation process might take place on a moving and/or statically inclined platform. The global perceived force per unit mass due to the combination of gravity and fictitious forces (due to ship motions) might have an important effect on the behaviour of the evacuees and might drastically increase the time required for the evacuation.

The effect of ship motion on evacuation has been documented through data acquired during casualties ([85]) and through controlled experiments such as the ones summarized by SLF 49/INF.5 [203] ([10], [18], [59], [145]) and those more recently performed by Sun et al. [207]or by Zhang et al. [233].

IMO has acknowledged the importance of the effects of ship motions on evacuation (MSC 78/INF.8 [145], SDC 2/INF.9 [192], SLF 49/INF.5 [203]), however, no standard test case with ship motion is specified, at the moment, in the MSC.1/Circ1533 [147]. A proposal of updating the MSC.1/Circ.1238 [146] with the addition of a series of test was already made in 2014 by Nicholl et al. [158]. However, the present revised guidelines on evacuation analysis, i.e. MSC.1/Circ.1533 [147] do not embed scenarios with heel, trim and/or dynamic ship motions. The delay in the development of a standardized test scenario with ship motions might be associated with the difficulty in having sufficient experimental data on the effect of ship motions on evacuation.

With reference to the pertinent literature, the effects of ship motion on the evacuation process can be summarized as follows:

- **Reduction of the unimpeded speed due to the perceived inclination of the ship**. The subjects reduce their desired speed when they perceive external forces. This is due to the difficulty of keeping balance while walking.
- **Modification of trajectory**. The forces per unit mass perceived by subjects due to the motions of the ship might affect the trajectory as well as the instantaneous speed.
- **Modification of the subject behaviour in case of ship motion**. Humans typically put in place some countermeasures to prevent consequences from loss of equilibrium, such as directing towards handrails or walls.

Among all the aforementioned behaviours, the reduction of the speed is the most documented effect of ship motion in literature. As reported in SLF 49/INF.5 [203] and by Meyer-König et al. [135], different research projects, indeed, were started to gather data on the effects of ship motion on the reduction of the unimpeded speed, especially in case of static inclinations. BMT Fleet technology performed tests using their motion simulator SHEBA (Glen [59]). A few tests on-board were conducted by KRISO (Korean Research Institute) (MSC 78/INF.8 [145]) and these results were considered in the development of the evacuation model IMEX ([106]). The Netherlands Organisation for Applied Scientific Research (TNO) performed the most complete series of test cases

aimed at studying human speed in different conditions: lateral or longitudinal inclinations with respect to the direction of the subjects, and with subjects ascending or descending stairs (Bles et al. [10])

Meyer-König et al. [135] presents all the aforementioned experimental results and summarizes them in the definition of a speed reduction factor. The experimental data summarised by Meyer-König et al. [135] provide information related to both the case of an inclination in the same direction of movement of the considered evacuee and the case of an inclination perpendicular to the direction of movement. Meyer-König et al. [135], therefore define two different speed reduction coefficients. One coefficient, r_l , depends on the longitudinal inclination angle γ_l (inclination in the same direction of movement of the person) and the other, r_t , depends on the transversal inclination angle γ_t (inclination in the perpendicular direction with respect to movement of the person).

Although the experimental results reported by Meyer-König et al. [135] have been obtained considering only conditions of static inclinations, it is observed by Meyer-König et al. [135] that the perceived force by subjects on a moving platform are the sum of fictitious forces parallel to the deck induced by dynamic motions of the ship and the real force generated by the component of gravity which is parallel to the deck. For an evacuee on a moving platform, from a dynamical perspective, there is no difference between the instantaneous effect of gravity due to inclinations and the effect of fictitious forces associated with dynamic effects. For this reason, in the model proposed by Meyer-König et al. [135], the speed reduction factor was considered to be dependent on the perceived inclination angle φ_{perc} (in either transversal or longitudinal direction), calculated as follows:

$$\varphi_{perc} = \varphi_{real} - \text{atan}\left(\frac{\ddot{\varphi}\cdot h}{g}\right) \tag{7.1}$$

where φ_{real} is the real inclination angle, $\ddot{\varphi}\ \left[\text{rad/s}^2\right]$ is the roll angular acceleration , h $\left[\text{m}\right]$ the height of the centre of mass of the subject with respect to the assumed centre of rotations and $g\ \left[\text{m/s}^2\right]$ is the acceleration of gravity. Equation (7.1) is used by Meyer-König et al. [135] in order to determine the longitudinal and transversal perceived angles, which herein will be referred to as γ_l and γ_t.

The model implemented in the tool VELOS ([113]) for the speed reduction is based on similar definitions as the one adopted by AENEAS, although the model by Kostas et al. [113] is based on different experimental data with respect to the one used by Meyer-König et al. [135].

Nicholl et al. [158] provides another interpretation of a subset of the same data used by Meyer-König et al. [135], summarizing them in a definition of speed reduction coefficients which considers not only the direction of the inclination with respect to the person's direction but also differentiates the reduction coefficient on the basis of the age of the subjects.

Figure 7.1 shows the dependence of the unimpeded speed reduction coefficient with respect to the perceived inclination angles γ_l and γ_t, which represent the longitudinal and the transversal inclinations perceived by the subject with respect to the subject direction. It is noted that the names "trim" and "heel" are used by Nicholl et al. [158] when addressing the angles γ_l and γ_t. This choice is surely misleading as the usual ship trim and heel angles do not depend on the agent desired direction. For this reason the notation γ_l and γ_t, which refers to the agent and not to the ship, will be preferred in the following.

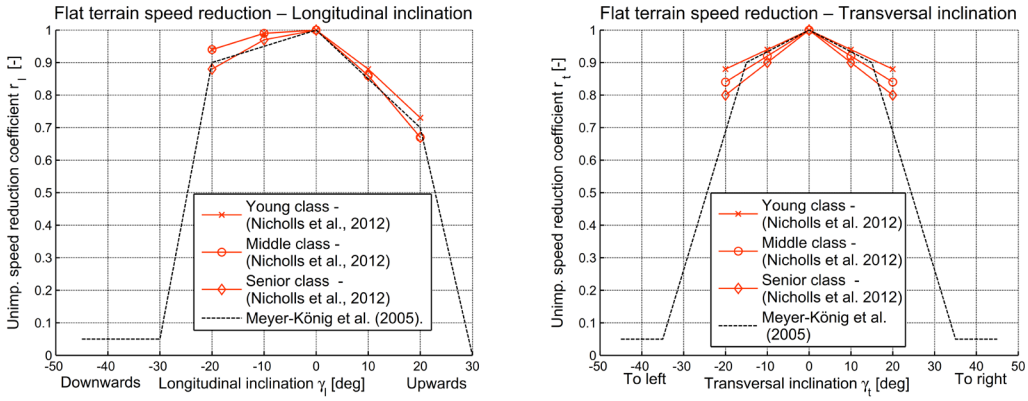

Figure 7.1: Reduction factor for longitudinal (left) and transversal (right) angle. Comparison between AENEAS modelling ([135]) and model by Nicholl et al. [158].

As reported in Figure 7.1, in the model proposed by Nicholl et al. [158] the reduction factor for transversal inclinations is not defined for inclinations larger than 20° , whereas in the model by Meyer-König et al. [135] it is defined for inclinations up to 45° (although the reduction factor goes to zero already at 35°). It is to be noted that the definition of the reduction coefficient was extended by Meyer-König et al. [135] above 20°, even though all the reference experimental data considered only inclinations up to 20°.

Very recently, new experimental data concerning the effects of ship inclination on the speed of subjects where carried on by Sun et al. [207] which also indicate maximum inclination angles above which subjects are unable to move. Sun et al. [207] observes that people fall and were unable to proceed for longitudinal inclination angles greater than 20° (both downwards and upwards) and transversal inclination angles greater than 15°. It is observed, however, that in the experimental results by Sun et al. [207], the walking speed seems not to decrease with transversal inclination like in the other studies and this behaviour seems to be inconsistent with the limit of 15° as the maximum acceptable transversal inclination angle assumed by Sun et al. [207]. These observations show that further experimental results are necessary for a correct determination of the maximum inclination angle in both longitudinal and transversal directions, although relevant experiments might be difficult to perform for safety reasons.

The experiments recently reported by Zhang et al. [233] and by Sun et al. [207], present some innovative aspect with respect to the ones discussed before.

Differently from the previously described experimental conditions, where the inclination was static, the experiments reported by Zhang et al. [233] are based on sinusoidal periodic motions. The experiment carried out by Zhang et al. [233] was aimed at analysing the human behaviour at different rolling amplitudes and periods, which were linked to wave heights and periods through a mathematical model. Motions used by Zhang et al. [233] were meant to be representative of ship rolling under the action of waves, however, it should be noted that their employed mathematical model for the prediction of motions is extremely simplified. Unfortunately Zhang et al. [233] provide only a qualitative commenting on the obtained results in presence of motions, without providing detailed quantitative information.

Although some experiments have been carried out before Zhang et al. [233] to assess the speed reduction in case of dynamic motion, a systematic analysis considering dynamic motion is not common in literature. There is thus a clear need for experimental data on this topic. Some quantitative data concerning the effect of dynamic motion are available from MSC 78/INF.8 [145], where a decrease from 10% to 20% is detected in the walking speed in presence of real motions generated, on the experimental facility, by natural wind and waves actions (roll period of the order of 13 s-14 s and maximum roll of the order of 5°-8°, depending on the condition). Bles et al. [10] conducted experiments in presence of sinusoidal pitch and roll motion considering five different conditions of amplitude and frequency. Although quantitative data are reported by Bles et al. [10] about the roll condition, the authors observe that the results should be considered only to identify the main effects of dynamic motions, as data were affected by the reduced length of the corridor. Moreover, as observed in SLF 49/INF.5 [203], the number of repeated tests performed by Bles et al. [10] in case of dynamic motions for each condition was limited, which increases the uncertainty related to the outcomes.

Sun et al. [207], systematically addressed the combined effect of longitudinal and transversal inclinations, which, to the best of author's knowledge, was not systematically addressed in previous works. The problem concerning the combination of the two inclinations was modelled by Meyer-König et al. [135] by the multiplication of the coefficients for the reduction of the speed. The comparison with data reported by Sun et al. [207] show that this assumption is approximately correct in most cases. Some differences are, however, detected between the results reported in Sun et al. [207] and those reported in all other works. In particular, in the results reported by Sun et al. [207], the measured speed is higher in the case with inclination of 10° directed downwards with respect to subjects' direction, compared to the one measured in the case without inclination. This behaviour is different from all other available experimental data and Sun et al. [207] explain it observing that the acceleration induced by gravity in the same direction of the person might increase the walking speed.

From a modelling perspective, however, might be clearer to differentiate between the effect of the speed increase due to the gravity acceleration, and the reduction coefficient of the desired speed. The desired speed reduction is, indeed, due to the effort in maintaining balance while walking. It is, thus, a response of the subject to the perceived force and it should be related to an instantaneous behaviour of the subject. However, the increase of the speed in case of inclination directed downward with respect to the subject direction is due, instead, to the fact that the perceived force is directly applied to the subject and modifies his motion. The force, thus, in this case, does not originate

from a subject behaviour. Keeping the distinction between forces originated by the subject and forces perceived by the subject helps maintaining a clear distinction between the modelled agent and the surrounding environment which is fundamental in agent based modelling.

The aforementioned distinction draws also the attention on the fact that perceived forces might directly affect subject motion due to the fact that the subject is not able to exert a control force strong enough to oppose to them. Perceived forces are, indeed, in reality, directly applied to subjects and thus might affect their instantaneous acceleration and eventually their speed, impacting also on the trajectory when the transversal component of the force with respect to the subject direction is not null. Unfortunately experimental data are limited, so far, to the analysis of the unimpeded speed reduction, thus neglecting the effects on the trajectories.

The effect of the perceived forces on agent trajectories requires additional modelling effort. Those effects, for instance, are not considered by VELOS ([113]) and they are not mentioned even in the computations performed by Nicholl et al. [158], perhaps due to the lack of experimental data. Some models in literature, however, embed this effect. Meyer-König et al. [135], in particular, consider the effect of the perceived force on agent trajectory in their Cellular Automata model. The motion of each agent in the Cellular Automata model by Meyer-König et al. [135] is determined by the probability of occupying the adjacent cells. The AENEAS model accounts for the perceived inclination by increasing the probability of occupying the cells placed in the direction of the perceived force vector, thus increasing the probability of moving towards that direction with respect to the condition without motion.

Modelling the effects of the perceived acceleration on trajectory is, apparently, more straightforward in social force models. In fact, in social force models, perceived forces can be directly applied to agents as agents are modelled as rigid bodies. As a result, different authors have proposed to modify the social force model by introducing the perceived force as an additional force to be applied to agents.

The study by Chen et al. [24], as an example, proposed a model which accounts for the perceived force in terms of modification of the instantaneous acceleration of the agents both in terms of magnitude and orientation. The model was used to assess the effect of horizontal motions on the trajectory and on evacuation time in harmonic forcing, both in the case where the direction of the agents is parallel with respect to the direction of the motions and the case where it is perpendicular, however no information related to the parameters of the considered harmonic motions are provided. Chen et al. [24] observe that the trajectory is affected only when the agent desired direction is perpendicular with respect to the ship sway motion (i.e. when the perceived transversal inclination angle γ_t is not null), whereas the speed is reduced or increased, but there is no change of direction, when the desired direction of the agent and the direction of motion aligned (i.e. when the perceived transversal inclination angle γ_t is null).

The simple application of the perceived force on agents cannot, however, be considered to produce results reasonably close to reality. This is due to the fact that, in reality, people try to balance the perceived forces. In the model proposed by Chen et al. [24], as

an example, the speed increases with the inclination angle in the case of longitudinal inclination which is downwards with respect to the agent direction. This behaviour was not observed in the vast majority of available experimental outcomes, with the exception of Sun et al. [207]. In particular, relevant experimental data identified in literature as those reported by Meyer-König et al. [135], MSC 78/INF.8 [145], SLF 49/INF.5 [203] and Sun et al. [207] agree that speed decreases when the inclination angle is greater than 10° for both upwards and downwards directions (Sun et al. [207] observe this decrease in relation to the "free speed" for angles of 15° and 20°). Humans, indeed, when perceiving an external force, usually exert an opposite force in order maintain equilibrium and their trajectory, and the effort required to exert this external force causes the unimpeded speed to reduce.

To reflect the aforementioned human behaviour, a rescaling of the perceived force is performed in the model presented by Balakhontceva et al. [4] and by Rybokonenko et al. [184], before applying the force to the agent. The effect of the control exerted by humans in this case is, thus, represented by the reduction coefficient applied to the perceived forces. Unfortunately, the parameters of the model by Balakhontceva et al. [4]are not available in the paper to allow a quantification of the performed reduction. The approach adopted by Balakhontceva et al. [4], however, does not maintain a clear differentiation between the forces exerted by the agents and does perceived as external by the agents. The effects of the control force exerted by the agent to oppose to the perceived force and the direct effects of the perceived force on agent are, indeed, in this case modelled with a unique rescaled force. However, it is advisable to maintain a clear differentiation by the forces exerted by agents, which are affected by limitations imposed by the subjects characteristics and by the physics condition (friction with the floor), and the perceived forces which in principle are not limited. The trajectory of the agent should, instead, be controlled by an additional control force with opposite direction with respect to the perceived force. In principle, it would be more physical to address the external force and the agent control force separately.

When control forces are not sufficient to balance the perceived forces, people would eventually lose equilibrium or would try to find a handhold in order to maintain balance. The attitude of people to direct towards the handrail is modelled in the tool EVI ([169]) which is based on a mesoscopic model. Balakhontceva et al. [4], introduce the latter behaviour in their microscopic force based model by inserting an attractive force towards possible close handholds when the external force reaches a threshold value. Although, in principle, this model is reasonable, the lack of experimental data related to the use of handrails in case of evacuation, makes the calibration and validation of the model presently not possible. It should be noted that, from a mathematical modelling perspective, such attractive force towards handholds might induce unrealistic behaviours, with agents which direct themselves at high speed towards walls and eventually bounce on them. It is believed that more experimental data are required in order to provide a consistent modelling of such a complex behaviour.

Finally another behaviour observed in people subject to dynamic ship motion is the so-called motion induced interruption. The motion induced interruption was initially defined addressing the situation of a crew member performing a given task on ship. The study addressed specifically the effects of the ship motions on the capability of the crew to perform the task. Motions induced interruptions (MII) effects are assessed by

determining those situations for which the subject loses balance due to tipping or sliding and, thus, needs to interrupt the job ([60], [61], [66]). Kostas et al. [113] propose to adapt this model to the evacuation by adjusting a number parameters of their behavioural model in accordance to the motion induced interruption model and parameters as reported by Graham [60] and by Graham et al. [61]. The motion induced interruption is modelled also in the software EVI ([169]) where a value of 0.243 for the tipping coefficient is used and the duration of the MII event is 3.56 s. The data were calibrated from the experimental observations presented by Crossland [29].

However, the parameters of the MII model refer to crew member and should thus be modified in case the model is applied to passenger. Unfortunately at the moment, no detailed experimental data sets are available in relation to the motion induced interruption effects on passenger evacuation.

The present review shows that, presently, the most documented, described and modelled effect of ship motion, both considering experimental results and evacuation models, is the reduction of the unimpeded speed. Some evacuation models (such as [4], [24], [135]) reproduce the effect of ship motions also on the agent trajectory, through sub-models which, however, tend to not transparently reflect the underlying physics of the system with reference to separation of different type of forces. Some of the models embedding the effect of perceived forces on agents trajectory implicitly introduce the concept of control forces, while in some other the perceived forces are applied entirely without any control force exerted by the agents. Moreover, in several cases, models reported in literature are, unfortunately, not presented with full details.

In the following, a newly developed sub-model will be presented which is intended to model the effects of ship motions on evacuees in a social force simulation framework. The model is capable of considering both the speed reduction and the modification of the trajectory of the agents due to ship motions. The model will be firstly presented in details. Afterwards, an analysis will be reported concerning the simulated effects of ship motions on the outcomes of two IMO test from MSC.1/Circ1533 ([147]). Scope of such analysis is to test the developed model and to provide information which, being based on simplified conditions may be used for direct comparison with other models.

7.2 A sub-model to add the effects of ship motion on the evacuation

The model presented in detail in the following considers the reduction of the unimpeded speed, the effects of the perceived forces and describes also the human attitude to oppose to the external forces. The presented model might be considered as a “quasi-static” one. In fact, the effects of ship motions on agents depend on the direction and magnitude of the instantaneous perceived force in a generic dynamic condition, but reference parameters are based on experiments carried out in static conditions. The description of the model will be carried out with a full characterization and justification of the adopted parameters.

7.2.1 Rigid body motions and perceived forces

The subject behaviour is affected, in case of ship motion, by the perceived forces per unit mass (or, briefly, "accelerations" in a general sense). When ship motions are not present, the only force perceived by a person is the gravity. When there are no heel and trim, moreover, the gravity is also perpendicular to the deck. However changes in the inclination of the ship originate an acceleration component parallel to the deck. Moreover, the motion might originate fictitious forces which are perceived by subjects.

The perceived force per unit mass $\mathbf{f}_i^{\text{perc}}\ \left[m/s^2\right]$ by an agent i having centre of mass $\mathbf{x}_i^{\text{cg}}$ in the ship fixed reference system, and the corresponding force $\mathbf{F}_i^{\text{perc}}$, can be determined as follows:

$$\begin{cases} \left(\mathbf{f}_i^{\text{perc}}\right)_S = -\left(\begin{array}{l} \underset{\Sigma\to S}{\mathbf{R}}\cdot\left(\ddot{\boldsymbol{\xi}}_O\right)_\Sigma + \left(\boldsymbol{\omega}'\right)_S \times \left(\mathbf{x}_i^{\text{cg}}\right)_S + \\ +\left(\boldsymbol{\omega}\right)_S \times \left(\left(\boldsymbol{\omega}\right)_S \times \left(\mathbf{x}_i^{\text{cg}}\right)_S\right) + 2\cdot\left(\boldsymbol{\omega}\right)_S \times \left(\mathbf{x}_i^{\text{cg}\prime}\right)_S \end{array} \right) + \underset{\Sigma\to S}{\mathbf{R}}\cdot\left(\mathbf{g}\right)_\Sigma \\ \left(\mathbf{F}_i^{\text{perc}}\right)_S = m_i\cdot\left(\mathbf{f}_i^{\text{perc}}\right)_S \end{cases} \tag{7.2}$$

where the variables in the equation are described in Table 7.1 and "×" is the cross product. The first term inside the parenthesis is a fictitious force due to the dynamic motions of the ship, whereas the second term is a real force which is due to gravity, as perceived in the ship fixed reference system. The dependence of the variables on the time is not indicated for brevity, but it is noted that only the earth fixed system of reference $\Sigma = \hat{\boldsymbol{\varepsilon}}, \hat{\boldsymbol{\eta}}, \hat{\boldsymbol{\xi}}, \Omega$ and the gravity vector $\left(\mathbf{g}\right)_\Sigma = \left(0,0,-g\right)^T$ are time independent. In the following, for brevity, $\left(\mathbf{f}_i^{\text{perc}}\right)_S$ will be denoted as $\mathbf{f}_i^{\text{perc}}$, since all evacuation simulations are carried out, naturally, in the ship fixed reference system. Finally the agent centre of mass $\mathbf{x}_i^{\text{cg}}$ is considered to be placed at the centre of the agent, at a height of 0.9 m from the deck, which is a reasonable height for the centre of gravity for the human body ([61]).

Table 7.1: Variables in equation (7.2).

$S = \hat{\mathbf{x}}, \hat{\mathbf{y}}, \hat{\mathbf{z}}, \mathbf{O}$	Ship fixed reference system.
$\Sigma = \hat{\boldsymbol{\varepsilon}}, \hat{\boldsymbol{\eta}}, \hat{\boldsymbol{\xi}}, \Omega$	Earth fixed reference system.
m_i	Mass of the agent.
$\underset{\Sigma\to S}{\mathbf{R}}$	Rotation matrix from earth fixed to ship fixed reference system.
$\left(.\right)_S$	Vector expressed in components in the ship fixed reference.
$\left(.\right)_\Sigma$	Vector expressed in components in the earth fixed reference.
$\mathbf{g}$	Gravitational acceleration (note: $\left(\mathbf{g}\right)_\Sigma = \left(0,0,-g\right)^T$).
ω	Angular velocity vector.
$\mathbf{x}_i^{\text{cg}}$	Position vector of centre of gravity of agent i with respect to the centre of the ship-fixed reference system.
$\ddot{\boldsymbol{\xi}}_O$	Acceleration vector of the centre of the ship fixed reference system.

As already observed the expression of the force is the sum of two quantities: the first term is the inertial force while the second term is the gravitational force as perceived in the ship system of reference. From the point of view of people on the ship, however, there is no difference between these two terms (at least if people do not have access to a visual perception of the horizon position). People on the ship estimate the ship inclination only by the perceived acceleration and they are, thus, not capable of distinguishing between inertial and real forces. Therefore, for the purpose of calculating the effect of the instantaneous motions and inclination on the agents, it is reasonable to consider in the same ways all the configurations which bring to the same value of $\mathbf{f}_i^{\text{perc}}$.

7.2.2 Agent behaviour in presence of external forces

7.2.2.1 Agent behaviour on flat terrain / on decks

The experimental data on the reduction of the unimpeded speed by Meyer-König et al. [135] concern angle of inclination in longitudinal and transversal direction with respect to the movement of subjects. However, the vertical movement of the ship (heave) is not considered.

The model presented herein will make use of experimental information based on static inclinations as those provided by Meyer-König et al. [135]. However, such information will be used in a quasi-static way considering the more general case of dynamic motions. All motions will be accounted for in defining, at each time instant, a couple of perceived inclination angles, γ_i^l and γ_i^t representing, respectively, the longitudinal and transversal (fictitious) inclination with respect to the desired direction of the agent. The proposed definition, which is based on the geometrical representation in Figure 7.2, generalizes the simplified one provided by Meyer-König et al. [135], as previously reported in (7.1).

To define the instantaneous values of the perceived inclination angles γ_i^l and γ_i^t, firstly a three dimensional agent-fixed reference system is defined. The reference system for the i-th agent is denoted as $A(i) = \hat{\mathbf{e}}_1, \hat{\mathbf{e}}_2, \hat{\mathbf{e}}_3$, with $\hat{\mathbf{e}}_1 = \left[\hat{\mathbf{v}}_i^0, 0\right]$ a vector parallel to the 2-dimensional unimpeded desired speed, $\hat{\mathbf{e}}_3 = \hat{\mathbf{z}}$ a vector parallel to the vertical axis of the ship fixed reference system and $\hat{\mathbf{e}}_2 = [\hat{\mathbf{t}}_i^0, 0] = \hat{\mathbf{e}}_3 \times \hat{\mathbf{e}}_1$ a vector perpendicular to the desired speed of the agent (note: here $\hat{\mathbf{v}}_i^0$ and $\hat{\mathbf{t}}_i^0$ are considered two-dimensional vectors in the x-y plane, i.e. on the deck plane). The component of $\mathbf{f}_i^{\text{perc}}$ along $\hat{\mathbf{e}}_1$ is defined as "longitudinal", the component along $\hat{\mathbf{e}}_2$ is defined as "transversal" and the component along $\hat{\mathbf{e}}_3$ is defined as "vertical". As a result, the concepts of "longitudinal" and "transversal" are now agent dependent. Accordingly, the longitudinal angle γ_i^l is the angle between the longitudinal component of the perceived force and the vector $\hat{\mathbf{e}}_3$, while the transversal angle γ_i^t is the angle between the transversal component of the perceived force and the vector $\hat{\mathbf{e}}_3$. The angle γ_i^l is conventionally considered positive when $\mathbf{f}_i^{\text{perc}} \cdot \hat{\mathbf{e}}_1 < 0$. This, in case of a static inclination, corresponds to an upwards

inclination with respect to $\hat{\mathbf{v}}_i^0$, and this convention is in accordance with the convention adopted by Meyer-König et al. [135]. The angle γ_i^t it is conventionally considered positive when $\mathbf{f}_i^{\text{perc}} \cdot \hat{\mathbf{e}}_2 < 0$ corresponding to an inclination upwards with respect to $\hat{\mathbf{t}}_i^0$ direction (to right considering $\hat{\mathbf{v}}_i^0$). It is underlined that γ_i^l and γ_i^t are, in general, time dependent, because the reference system $A(i) = \hat{\mathbf{e}}_1, \hat{\mathbf{e}}_2, \hat{\mathbf{e}}_3$ may have, and typically has, a time dependent orientation, and because $\mathbf{f}_i^{\text{perc}}$ is, in general, time dependent if dynamic motions are present. In case of static inclinations, instead, $\mathbf{f}_i^{\text{perc}}$ is time independent.

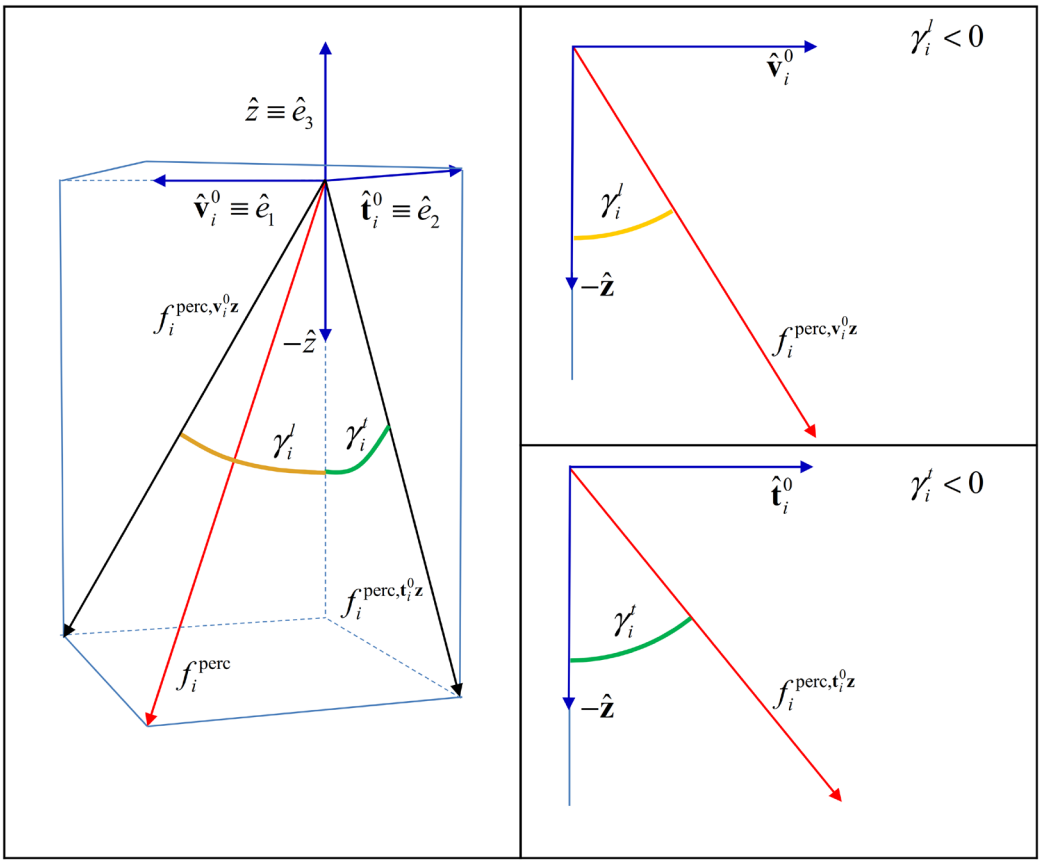

Figure 7.2: Definition of the perceived inclination angles γ_i^l and γ_i^t.

As a reference, the experimental data summarized in the model presented by Meyer-König et al. [135] for the reduction factor of the unimpeded speed was adopted for the determination of the unimpeded speed reduction coefficient also in the present model. Figure 7.3 shows, on the left, the dependence of the longitudinal reduction factor $r_l = r_l\left(\gamma_i^l\right)$ with respect to the perceived inclination angle γ_i^l, and it shows, on the right, the dependence of the transversal reduction factor $r_t = r_t\left(\gamma_i^t\right)$ with respect to the perceived inclination angle γ_i^t.

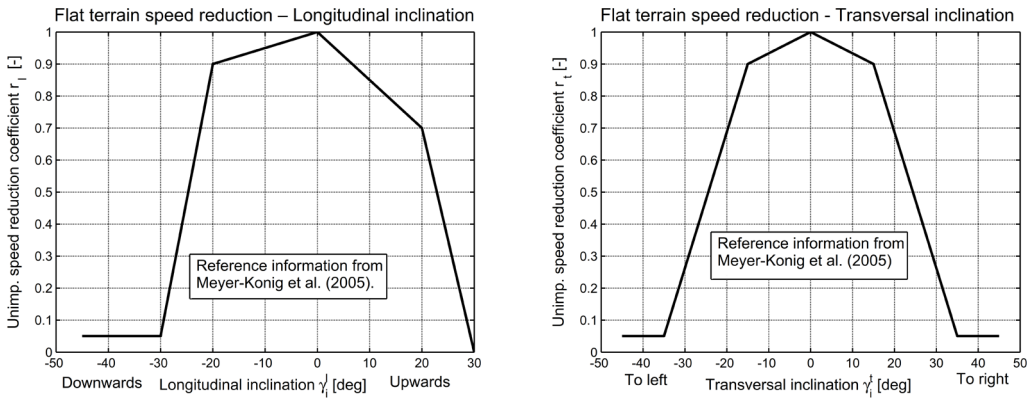

Figure 7.3: Speed reduction factors $r_l = r_i^l\left(\gamma_i^l\right)$ (left) and $r_t = r_i^t\left(\gamma_i^t\right)$ (right).

For the generic i-th agent, the instantaneous unimpeded speed reduction factor r_i on flat terrain is calculated by multiplying the two reduction factors r_i^l and r_i^t. The instantaneous desired speed affected by ship motions $v_i^{0,\mathrm{sm}}\left(t\right)$ is hence obtained by multiplying the desired speed v_i^0 for the case without motion by the instantaneous reduction coefficient r_i, as follows:

$$\begin{cases} v_i^{0,sm}\left(t\right) = v_i^0\left(t\right)\cdot r_i \\ r_i = r_i^l\left(\gamma_i^l\left(t\right)\right)\cdot r_i^t\left(\gamma_i^t\left(t\right)\right) \end{cases} \tag{7.3}$$

7.2.2.2 Agent behaviour on stairs

The reduction of the speed due of ship motion of agents on stairs is treated separately, referring to the available experimental data reported in Meyer-König et al. [135] for this condition.

In the case without ship motion, when the agent is on a stair, the magnitude of its 3-dimensional instantaneous desired speed $\mathbf{v}_i^{03d}\left(t\right)$ (laying on the stair plan) $v_i^{03d}\left(t\right)$ depends on the agent orientation with respect to the stair-fixed reference system and on the parameters $v_i^{U,\mathrm{up}}$, $v_i^{U,\mathrm{down}}$ and v_i^U which determine the speed of the agent on the stair, as it is described in section 2.2.8.

When ship motions are present, the 3-dimensional desired speed vector $\mathbf{v}_i^{03d,sm}\left(t\right)$ on stairs is determined as a correction of the nominal desired speed vector $\mathbf{v}_i^{03d}\left(t\right)$ calculated with the same method adopted without ship motion. The 3-dimensional desired speed vector $\mathbf{v}_i^{03d,sm}\left(t\right)$ on stairs has the same direction as $\mathbf{v}_i^{03d}\left(t\right)$ while its magnitude $v_i^{03d,\mathrm{sm}}\left(t\right)$ is obtained by multiplying $v_i^{03d}\left(t\right)$ by the speed reduction factor on stairs, as follows:

$$v_i^{03d,sm}(t)=\begin{cases} v_i^{03d}\cdot r_{\text{st,l,up}}\left(\gamma_i^{l,st}\right)\cdot r_{\text{st,t}}\left(\gamma_i^{t,st}\right) & \text{if } \left\langle \hat{\mathbf{v}}_i^{03\text{d}},\hat{\mathbf{z}}\right\rangle > 0 \quad (\text{ascending stair}) \\ v_i^{03d}\cdot r_{\text{st,l,down}}\left(\gamma_i^{l,st}\right)\cdot r_{\text{st,t}}\left(\gamma_i^{t,st}\right) & \text{if } \left\langle \hat{\mathbf{v}}_i^{03\text{d}},\hat{\mathbf{z}}\right\rangle < 0 \quad (\text{descending stair}) \end{cases} \tag{7.4}$$

where $r_{\text{st,l,up}}$, $r_{\text{st,l,down}}$ and $r_{\text{st,tr}}$ are the desired speed reduction coefficients on stairs related, respectively, to the longitudinal inclination when the agent is ascending, to the longitudinal inclination when the agent is descending and to the transversal inclination (both in ascending and descending conditions), and $\hat{\mathbf{z}}$ is the perpendicular versor to the deck plane.

The coefficients $r_{\text{st,l,up}}$, $r_{\text{st,l,down}}$, $r_{\text{st,tr}}$ depend on the longitudinal inclination angle $\gamma_i^{l,st}$ and on the transversal inclination angle $\gamma_i^{t,st}$ of the stair, as perceived by the i-th agent. The perceived inclination angles $\gamma_i^{l,st}$ and $\gamma_i^{t,st}$ on stairs are defined with the same method adopted for the flat terrain (see Figure 7.2), but using a modified reference system which is, now, fixed with respect to the stair. The adopted stair-fixed reference system $S=\left(\hat{\mathbf{e}}_1,\hat{\mathbf{e}}_2,\hat{\mathbf{e}}_3\right)$ is defined considering the stair orientation as shown in Figure 7.4. The versor $\hat{\mathbf{s}}$ in Figure 7.4 determines the orientation of the stair from its lowest point to the highest point along the main stair direction. The versor of the first axis of the stair-fixed reference system is defined as $\hat{\mathbf{e}}_1=\hat{\mathbf{s}}^{xy}/\left\|\hat{\mathbf{s}}^{xy}\right\|$ (where $\hat{\mathbf{s}}^{xy}$ is the projection of $\hat{\mathbf{s}}$ onto the deck plane). The vector $\hat{\mathbf{e}}_3$ is normal with respect to the deck and directed upwards, i.e. $\hat{\mathbf{e}}_3=\hat{\mathbf{z}}$. Finally $\hat{\mathbf{e}}_2$ is defined as $\hat{\mathbf{e}}_2=\hat{\mathbf{e}}_3\times\hat{\mathbf{e}}_1$. The adopted convention is coherent with Bles et al. [10].

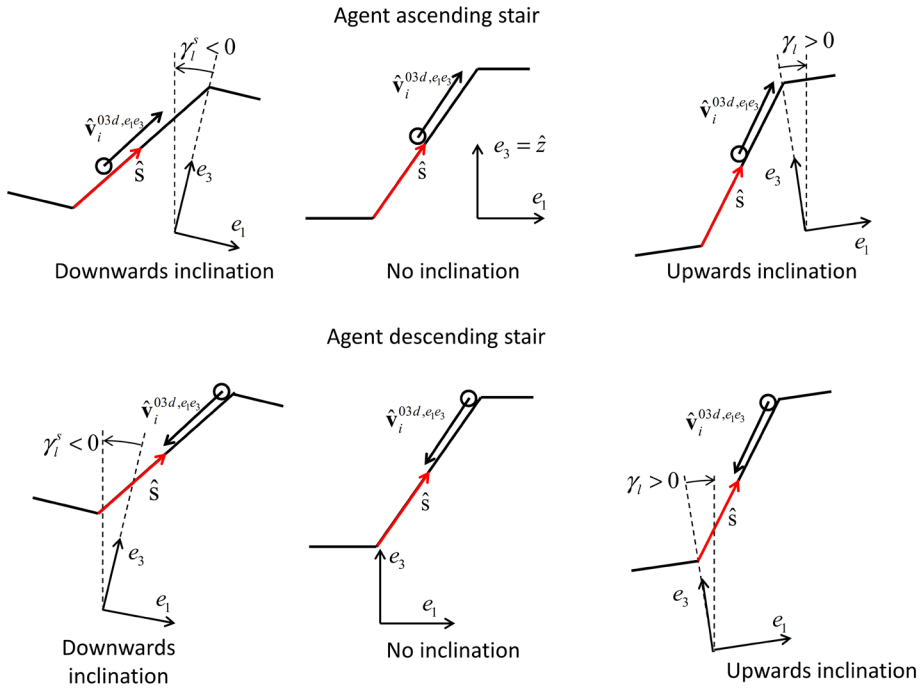

Figure 7.4: Definition of stair-fixed reference system $S=(\hat{\mathbf{e}}_1,\hat{\mathbf{e}}_2,\hat{\mathbf{e}}_3)$ and of sign convention used for the perceived longitudinal tilt angle angle $\gamma_i^{l,st}$.

The reduction coefficients $r_{\mathrm{st,l,up}}$ is obtained by interpolation of the functions reported in Figure 7.5 (left) using $\gamma_i^{l,st}$, where the appropriate reduction coefficient is chosen depending on whether the agent is ascending or descending the stair (see (7.4)). Similarly, the coefficient $r_{\mathrm{st,t}}$ is obtained by interpolating the function reported in Figure 7.5 (right) using the transversal inclination angle $\gamma_i^{t,st}$, and in this case the same speed reduction coefficient is used both for ascending and descending agents.

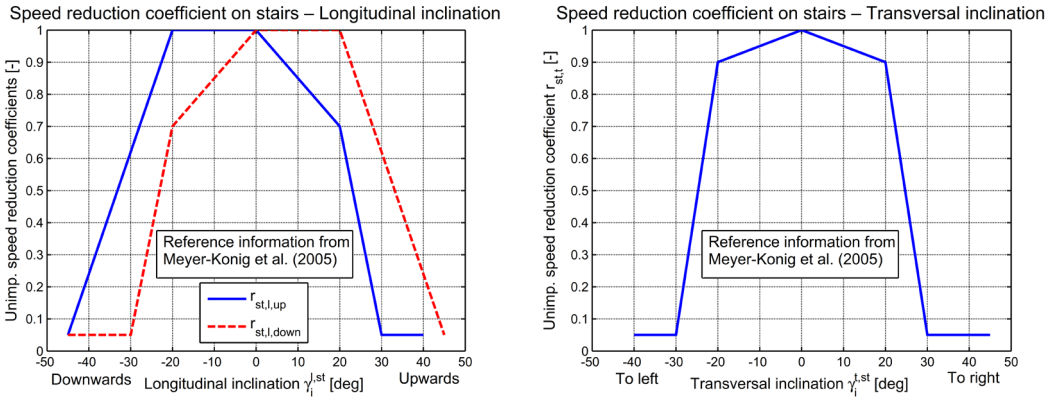

Figure 7.5: Speed reduction coefficients on stairs $r_{\mathrm{st,l,up}}$, $r_{\mathrm{st,l,down}}$, $r_{\mathrm{st,tr}}$.

It is observed that equations (7.4) are not defined when $\left\langle \hat{\mathbf{v}}_i^{03d}, \hat{\mathbf{z}} \right\rangle = 0$. This situation corresponds to the case of an agent having desired direction which is perpendicular with respect to the stair main direction, meaning that the agent desires to move transversally with respect to the main stair direction. However, in vast majority of conditions (actually all conditions addressed herein) agents are either strictly ascending ($\left\langle \hat{\mathbf{v}}_i^{03d}, \hat{\mathbf{z}} \right\rangle > 0$) or strictly descending ($\left\langle \hat{\mathbf{v}}_i^{03d}, \hat{\mathbf{z}} \right\rangle < 0$) the staircase. Moreover, their desired nominal directions $\hat{\mathbf{v}}_i^{03d}$ are almost parallel to $\hat{\mathbf{s}}$. Nevertheless, for robustness of the code, it was decided to treat the condition where $\left\langle \hat{\mathbf{v}}_i^{03d}, \hat{\mathbf{z}} \right\rangle = 0$ as if the agent were descending the stair, and thus a descending agent is nominally redefined as an agent for which $\left\langle \hat{\mathbf{v}}_i^{03d}, \hat{\mathbf{z}} \right\rangle \leq 0$.

7.2.2.3 Agent control force

The reduction of the unimpeded speed mimics human attitude to reduce the desired speed when the ship is inclined and/or is moving. This may be considered as a sort of behavioural effect. However, the direct mechanical effect due to the application of the force per unity of mass $\mathbf{f}_i^{\text{perc}}$ on the agent should also be reproduced.

Due to the fact that in the present model the vertical movement of agents is not considered from the point of view of rigid body dynamics, and agents are represented as two dimensional rigid bodies, only the component of the perceived force which is parallel to the deck plane, namely $\mathbf{F}_i^{\text{perc,xy}} = m_i \cdot \mathbf{f}_i^{\text{perc,xy}}$ $\left[\text{N}\right]$, is applied to the agents, where $\mathbf{f}_i^{\text{perc,xy}}$ is the component of $\mathbf{f}_i^{\text{perc}}$ parallel to the deck.

$\mathbf{F}_i^{\text{perc,xy}} = \left(f_i^{\text{perc,x}}, f_i^{\text{perc,y}}, 0 \right)$ is, in principle, a 3-dimensional vector, however, in the following, the same notation will be adopted, for simplicity, also to indicate the corresponding 2-dimensional vector as obtained by neglecting its third, null, vertical component. Following this flexible nomenclature, the vector $\mathbf{F}_i^{\text{perc,xy}}$ can thus be directly applied to the two dimensional rigid body equations modelling the motion of the agents. The same will hold in the following for all the projections of $\mathbf{F}_i^{\text{perc}}$ on vectors which are parallel to the deck plane.

However, the simple application of the perceived force $\mathbf{F}_i^{\text{perc,xy}}$ to agents, brings to unrealistic behaviours and leads to a modification of the agents trajectory even for very low perceived forces. This is due to the fact that people cannot be modelled as a simple free rigid bodies affected by external forces. It is reasonable, instead, to suppose that people oppose some reaction to the perceived external forces, in order to try maintaining their trajectory. This behaviour might be modelled either as an increase of the motive force or by the introduction of an additional control force.

In order to completely model the agent behaviour in presence of ship motions, i.e. in order to model the modification of the agent speed and its opposition to the external forces $\mathbf{F}_i^{\text{perc,xy}}$ a global control force $\mathbf{F}_i^{\text{c}}$. $\left[\text{N}\right]$ is introduced. The control force is then split in two components:

$$\mathbf{F}_i^{\mathrm{c}} = \mathbf{F}_i^{\mathrm{c},l} + \mathbf{F}_i^{\mathrm{c},t} \tag{7.5}$$

The first component, $\mathbf{F}_i^{\mathrm{c},l}$, is directed longitudinally whereas the second one, $\mathbf{F}_i^{\mathrm{c},t}$, is directed transversally, with respect to the desired direction $\hat{\mathbf{v}}_i^0$.

In order to better understand the purpose of the control force, a simplified condition is now considered, namely the archetypal condition of an agent i which is travelling along a corridor inclined in the direction of the agent motion. The equation of motion of the agent in this condition is the following:

$$m_i \cdot \ddot{x}(t) = \frac{m_i}{\tau_i}\left(v_i^0(t) - v_i(t)\right) + F_i^{\mathrm{perc,l}}(t) + F_i^{\mathrm{c,l}}(t) \tag{7.6}$$

where the effects of ship motion are restricted to the longitudinal force component $F_i^{\mathrm{perc,l}}(t)\,[\mathrm{N}]$ and are counteracted by $F_i^{\mathrm{c,l}}(t)\,[\mathrm{N}]$, the longitudinal component of the agent control force.

The available experimental data for this condition as presented by Meyer-König et al. [135] allow setting a stead speed for this simple case. This steady speed is the desired speed $v_i^{0,\mathrm{sm}}(t)$ as modified in case of ship motion according to equation (7.3). Therefore, in order to achieve the required speed at steady state, the component longitudinal control force, in this case, should be defined as:

$$F_i^{\mathrm{c,l}}(t) = \frac{m_i}{\tau_i}\left(v_i^{0,\mathrm{sm}}(t) - v_i^0(t)\right) - F_i^{\mathrm{perc,l}}(t) \tag{7.7}$$

In the considered archetypal case, the aforementioned definition might be generalized considering the non-linear motive force defined in (2.12). When considering only longitudinal incline with respect to the agent, the sum of motive force and longitudinal control force can thus be defined as follows:

$$\mathbf{F}_i^{\mathrm{c,l}}(t) + \mathbf{F}_i^{\mathrm{mot}}(t) = \frac{m_i}{\tau_i} f_{mot}\left(\left\|\mathbf{v}_i^{0,\mathrm{sm}}(t) - \mathbf{v}_i(t)\right\|\right) \cdot \frac{\mathbf{v}_i^{0,\mathrm{sm}}(t) - \mathbf{v}_i(t)}{\left\|\mathbf{v}_i^{0,\mathrm{sm}}(t) - \mathbf{v}_i(t)\right\|} - \mathbf{F}_i^{\mathrm{perc,l}}(t) \tag{7.8}$$

where f_{mot} is the function calculating the non-linear motive force as reported in (2.12). The right hand side of the equation is composed of two terms. The first term might be interpreted as a modified motive force having steady desired speed $v_i^{0,\mathrm{sm}}(t)$, whereas the second term is the control force exerted by the agent which is counterbalancing the longitudinal component of the external force.

Some preliminary simulations showed, however, that for large longitudinal inclinations, the control force component opposed to the external forces as defined by (7.8) may become too large with respect to the other social forces. This may lead, in some situations, to an unnatural behaviour of agents which are no longer avoiding contacts. In addition, if there is no limit to longitudinal component of the control force, it might

happen that the agents can compensate the force even for extremely large inclinations even though people, in a real condition, would eventually slide in the direction of the inclination. For this reason, a bound $F_i^{\mathrm{c,l,\,lim}}$ [N] was set in order to prevent the control force from reaching unnatural magnitudes. The value $F_i^{\mathrm{c,l,\,lim}}$ was set by considering that the speed reduction factor for the longitudinal case in Meyer-König et al. [135] reaches 0 when the longitudinal inclination angle γ_i^l is 30° (upwards with respect to the agent direction). The magnitude of the desired speed of the agent $v_i^{0,sm}(t)$ is, thus, null when $\gamma_i^l = 30°$. Moreover, in such a condition, $\mathbf{F}_i^{\mathrm{c,l}} = -\mathbf{F}_i^{\mathrm{perc,l}}$, i.e. the longitudinal control force and the longitudinal perceived force compensate each other. The condition is, thus, the one of an agent which is able to oppose enough force only to compensate the perceived force, but not to move forward. By considering a static inclination of 30° the parameter $F_i^{\mathrm{c,l,lim}}$ was defined as follows:

$$F_i^{\mathrm{c,l,lim}} = m_i \cdot g \cdot \sin(30°) = 0.5 \cdot g \cdot m_i \tag{7.9}$$

were m_i [kg] is the mass of the agent and g [m/s^2] is the acceleration of gravity.

The final equation describing the sum of the motive and of the control force when considering only the longitudinal direction, is, hence, as follows:

$$\mathbf{F}_i^{\mathrm{c,l}}(t) + \mathbf{F}_i^{\mathrm{mot,}}(t) = \frac{m_i}{\tau_i} f_{mot}\left(\left\|\mathbf{v}_i^{0,\mathrm{sm}}(t) - \mathbf{v}_i(t)\right\|\right) \cdot \left(\frac{\mathbf{v}_i^{0,\mathrm{sm}}(t) - \mathbf{v}_i(t)}{\left(\left\|\mathbf{v}_i^{0,\mathrm{sm}}(t) - \mathbf{v}_i(t)\right\|\right)}\right) + \\ + \min(\max(-F_i^{\mathrm{perc,l}}, -F_i^{\mathrm{c,l,lim}}), F_i^{\mathrm{c,l,lim}}) \cdot \hat{\mathbf{v}}_i^0 \tag{7.10}$$

The case of transversal control force is treated similarly. However, there are not sufficient experimental data to set a bound for the transversal component of $\mathbf{F}_i^{\mathrm{perc,t}}$. SLF 49/INF.5 [203] reports that up to inclinations of 15° degrees, there are no appreciable differences in the behaviour of subjects with respect to the situation without inclination. The model proposed herein assumes, thereby, that the agent is able to completely balance the lateral component of the external force with a control force until the angle γ_t is equal 15° . For larger transversal angles, the external lateral is, therefore, only partially compensated by the agent control force.

The component of the lateral control force is therefore defined as follows:

$$F_i^{\mathrm{c,t}} = \min(\max(-F_i^{\mathrm{perc,t}}, -F_i^{\mathrm{c,t,lim}}), F_i^{\mathrm{c,t,lim}}) \tag{7.11}$$

where the limit transversal control force, $F_i^{\mathrm{c,t,lim}}$, is calculated as follows:

$$F_i^{\mathrm{c,t,lim}} = m_i \cdot g \cdot \sin(15°) \approx 0.256 \cdot g \cdot m_i \tag{7.12}$$

The combination of the agent control force and of the modified motive force in presence of ship motions is therefore modelled as follows:

$$\begin{aligned}\mathbf{F}_i^{\mathrm{c}}(t)+\mathbf{F}_i^{\mathrm{mot},}(t)=&\frac{m_i}{\tau_i}f_{mot}\left(\left\|\mathbf{v}_i^{0,\mathrm{sm}}(t)-\mathbf{v}_i(t)\right\|\right)\cdot\left(\frac{\mathbf{v}_i^{0,\mathrm{sm}}(t)-\mathbf{v}_i(t)}{\left(\left\|\mathbf{v}_i^{0,\mathrm{sm}}(t)-\mathbf{v}_i(t)\right\|\right)}\right)+\\&+\min(\max(-F_i^{\mathrm{perc,l}},-F_i^{\mathrm{c,l,lim}}),F_i^{\mathrm{c,l,lim}})\cdot\hat{\mathbf{v}}_i^0+\\&+\min(\max(-F_i^{\mathrm{perc,t}},-F_i^{\mathrm{c,t,lim}}),F_i^{\mathrm{c,t,lim}})\cdot\hat{\mathbf{t}}_i^0\end{aligned}\tag{7.13}$$

This model represents the reference model embedding the effect of ship motions from the point of view of agent control force and modified motive force. However, some tests performed with the present model indicated that agents may present difficulties when exiting from narrow exits in presence of ship motions. In particular, by analysing some specific situations, it was observed that the present model might lead to situations of impasse. A modification to this basic model has therefore been introduced, as described in the next section.

7.2.2.4 Model modification to address abrupt changes of desired direction

As anticipated in the commenting to equation (7.13), some tests performed with the basic model indicated that, in specific situations, situations of impasse may occur. An example of these peculiar situations is the one of an agent exiting from a cabin and entering a corridor which is perpendicular to the exit, as shown in Figure 7.6, in presence of ship motions. In this clarification example it is assumed that a static inclination larger than 15° is present, which is directed downwards from the corridor towards the cabin. In such a condition, at a generic time instant t_1, the agent, while in the way-area placed at the exit of the cabin, has a desired direction $\hat{\mathbf{v}}_i^0(t_1)$ perpendicular to the corridor. In such a situation the agent exerts a control force to compensate the external force due to the inclination of the vessel, and this force is directed, basically, in longitudinal direction with respect to the agent. When the agent exits the waypoint area and enter the corridor at a later time instant t_2, the desired direction abruptly changes to $\hat{\mathbf{v}}_i^0(t_2)$, with an abrupt rotation of 90°.

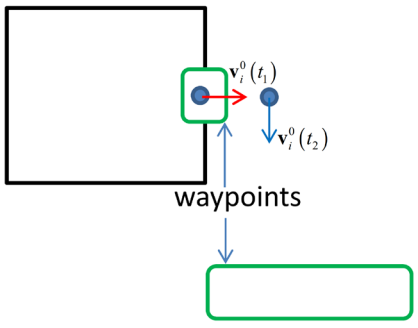

Figure 7.6: Reference geometry associated to an impasse situation in case of ship motions.

The abrupt change of direction leads to an abrupt modification of the control force. This is due to the fact that the control bounds of the control force are applied to components of the control force which are defined considering the agent direction (longitudinal or

transversal, see (7.9) and (7.12)). When the perceived force is longitudinal with respect to the agent direction, the agent is able to balance the effect of relatively large external forces and, then, it is able to move forward. Instead, when the agent desired direction rotates, and the external force become transversal with respect to the agent desired direction, the agent is no longer able to balance the external force due to the fact that the maximum transversal control force component is smaller than its longitudinal counterpart, i.e. $F_i^{\mathrm{c,t,lim}} < F_i^{\mathrm{c,l,lim}}$ (compare (7.9) and (7.12)). As a result, immediately after the rotation of the desired direction, the agent is pushed back to the waypoint area due to the drop in the force which is counteracting the perceived forces. At this stage, the agent changes again its desired direction and this situation repeats. The reason for the creation of this impasse situation is, hence, the sudden drop of the control force in terms of components with respect to the ship fixed reference system.

However, it is reasonable to assume that, when sharply modifying their direction, people tend to increase also the lateral control force, at least for a limited time interval, in such a way that situations of the type described above do not actually occur. According to this reasoning, the model has been modified in order to take into account the variation of the unimpeded speed direction. To this end, reference has been made to the angular speed ω_i^0 [rad/s] of the versor of the desired speed, which can be defined as follows:

$$\omega_i^0(t) = \frac{d\,\hat{\mathbf{v}}_i^0(t)}{dt} \cdot \left(\hat{\mathbf{e}}_3 \times \hat{\mathbf{v}}_i^0(t)\right) \tag{7.14}$$

It is noted that, being $\hat{\mathbf{v}}_i^0(t)$ a unit planar vector on the deck plane, the angular speed vector is always directed along $\hat{\mathbf{e}}_3$ and the derivative of $\hat{\mathbf{v}}_i^0(t)$ is orthogonal to $\hat{\mathbf{v}}_i^0(t)$.

In order to allow the possibility of temporarily increasing the bound of the transversal control force, the idea is to monitor the magnitude of ω_i^0 in a past time window. The presence of large ω_i^0 is assumed to indicate the presence of sharp turning which should be allowed to be accompanied by an increase of the bound of the lateral control force.

To this end, the maximum magnitude $\bar{\omega}_i^0$ of the angular velocity, referred to an interval is defined as follows:

$$\bar{\omega}_i^0(t) = \max_{\tau \in [t - T_\omega, t]} \left| \omega_i^0(\tau) \right| \tag{7.15}$$

where $\omega_i^0(\tau)$ [rad/s] is the instantaneous angular speed at the time instant τ, and T_ω [s] is a parameter representing the length of the analysis time window in the past. The parameter T_ω, however, needs to be specified, and this has been done as described in the following.

The initial idea was to set a common value of T_ω for all the agents. However, preliminary simulations for the archetypal case reported in Figure 7.6 showed a very

different behaviour between different agents when a common T_ω was used. In particular, some agents remained blocked inside the waypoint, whereas some others maintained an increased bound for the lateral control force even when travelling through the corridor, which was not the desired behaviour. This was due to the fact that, due to the randomness in the population, different agents may have very different unimpeded speeds and they can therefore travel different path lengths in the same time window.

In order to overcome this problem, the parameter $T_{\omega,i}$ was defined depending on the agents characteristics, as follows:

$$T_{\omega,i} = \sqrt{\frac{2 \cdot \tau_i^f \cdot D_\omega}{v_i^U}} \tag{7.16}$$

where $\tau_i^f \ \left[s\right]$ is the relaxation parameter of the motive force of the agent, $v_i^U \ \left[m/s\right]$ is the agent unimpeded speed and $D_\omega \ \left[m\right]$ is a new parameter that needs to be specified. It is observed that equation (7.16) represents the time it takes for the agent to cover the distance D_ω starting from rest if the agent is in a free field and if the dissipative term of the motive force is neglected. In such case, in fact, the agent motion would be governed by $\ddot{x} = v_i^U / \tau_i^f \Rightarrow x(t) = \left(v_i^U \cdot t^2\right) / \left(2 \cdot \tau_i^f\right)$. Considering this interpretation, a value $D_\omega = 1.5$ m was considered to be reasonable.

The time dependent transversal force bound $F_i^{\mathrm{c,t,lim}}\left(\overline{\omega}_i^0(t)\right)$ is defined as follows:

$$F_i^{\mathrm{c,t,lim}}\left(\overline{\omega}_i^0\right) = \begin{cases} F_i^{\mathrm{c,t,lim}} & \text{if} \quad \left|\overline{\omega}_i^0\right| < \psi_1 \\ \dfrac{\left|\overline{\omega}_i^0\right| - \psi_1}{\psi_2 - \psi_1} \cdot F_i^{\mathrm{c,l,lim}} + \dfrac{\psi_2 - \left|\overline{\omega}_i^0\right|}{\psi_2 - \psi_1} \cdot F_i^{\mathrm{c,t,lim}} & \text{if} \quad \psi_1 \le \left|\overline{\omega}_i^0\right| \le \psi_2 \\ F_i^{\mathrm{c,l,lim}} & \text{if} \quad \left|\overline{\omega}_i^0\right| > \psi_2 \end{cases} \tag{7.17}$$

were the parameters ψ_1 and ψ_2 (rad/s) need to be specified.

Determining the two parameters ψ_1 and $\psi_2 \left[\text{rad/s}\right]$ is complex as they are not directly related to physically measurable quantities: this is due to the fact that the vector $\hat{\mathbf{v}}_i^0(t)$ models the attitude of the agent to be oriented towards a target but not its real orientation.

However, the previously described conceptual approach was adopted in the present model, in order to identify the limit condition of a discontinuity related to the

orientation of $\mathbf{v}_i^0(t)$, which is actually the case in the archetypal case in Figure 7.6. A discontinuity in $\mathbf{v}_i^0(t)$ can be represented as follows:

$$\lim_{\varepsilon \to 0^-} \mathbf{v}_i^0(t+\varepsilon) \neq \lim_{\varepsilon \to 0^+} \mathbf{v}_i^0(t+\varepsilon) \tag{7.18}$$

In such a situation, there is a sharp instantaneous change in the direction of the desired speed versor. If the change in the direction is by an angle Δ_α, the angular velocity $\omega_i^0(t)$ becomes locally singular and can be locally represented as follows:

$$\lim_{\varepsilon \to 0} \int_{t-\varepsilon}^{t+\varepsilon} \omega_i^0(\tau) d\tau = \Delta_\alpha \;,\; \omega_i^0(\tau) = \Delta_\alpha \delta(t-\tau) \tag{7.19}$$

where $\delta(x)$ is the Dirac delta function.

The Dirac delta function cannot be represented numerically, thus, under the assumption of the presence of orientation discontinuity of the vector $\mathbf{v}_i^0(t)$, the parameters ψ_1 and ψ_2 cannot directly be used.

However, considering the fact that simulations are carried out with a discretized time, and assuming that the integration time step, as in the present model, has a constant value Δt, a maximum (numerical) angular speed can be defined as follows, depending on a specified threshold angular variation Δ_α for the direction of $\mathbf{v}_i^0(t)$:

$$\psi_u = \frac{\Delta_{\alpha_u}}{\Delta t} \; u = 1,2 \tag{7.20}$$

where Δ_{α_u} $u = 1,2$ are the limit angular variations which are used to identify sharp variations in the orientation of the desired velocity. The parameters $\Delta_{\alpha_1} = 30°$ and $\Delta_{\alpha_2} = 60°$ were adopted after a tuning carried out considering the archetypal condition reported in Figure 7.6.

The described modification of the transversal control force bound has very reduced effect in case the external forces are weak, but it has considerable effects in conditions of very large heel or trim angles. The present model allows in particular the slow agents to maintain a large magnitude of the lateral control force for a sufficient time interval, allowing them to modify their direction with sharp turns also in presence of relatively large external forces.

7.2.2.5 Further modelling considerations

In addition to the modelling characteristics already described, some further effects are taken into account, as described as follows.

Forces intended to control effects from ship motions are not clamped to the global force limit of 3 m/s^2 (force per unit mass) as the other social forces (see equation (2.9)), since this limit is too low. In fact, considering the situation of a static inclination, in case the 3 m/s^2 limit were applied to control forces, agent would stop and start moving in the opposite direction when the inclination exceeds 17.8° (corresponding to $\arcsin(3/g)$). Instead, agents should be capable of keeping moving in the desired direction up to a maximum inclination of 30° considering an upwards inclination.

In reality, humans' movement is based on the generation of forces through friction with the floor. The maximum possible friction force depends on the force orthogonal to the deck and it is hence constant when the deck is not inclined and the ship is not moving. This condition corresponds to the situation where the vertical component $\mathbf{f}_i^{\text{perc},z}\left[\text{m/s}^2\right]$ of the perceived force per unit mass is equal to the gravitational acceleration and it is directed perpendicular to the deck. In a more general condition the maximum possible friction force per unit mass can be estimated as follows:

$$f_{fd,i,\max} = \begin{cases} 0 & \text{if } f_i^{\text{perc},z} \geq 0 \\ -f_i^{\text{perc},z} \cdot \mu & \text{if } f_i^{\text{perc},z} < 0 \end{cases} \tag{7.21}$$

where $f_i^{\text{perc},z}\left[\text{m/s}^2\right]$ is the vertical component of the perceived force and μ is the friction with the floor, which can be estimated of the order of 0.7. It is however to be underlined that, in typical cases where ship motions are not extreme it is $f_i^{\text{perc},z} < 0$, i.e. the normal-to-deck component of the perceived force is towards the deck and there are no airborne conditions. The maximum magnitude of horizontal force that an agent can generate to control its movement should therefore be limited to $f_{fd,i,\max}$.

Finally, the applied (two dimensional) force $\mathbf{F}_i^{\text{app}}$ to the agent i is defined as follows:

$$\mathbf{F}_i^{\text{app}} = \min\left(\left\|\mathbf{F}_i^{\text{g}} + \mathbf{F}_i^{\text{c}}\right\|, f_{fd,i,\max} \cdot m_i\right) \cdot \frac{\mathbf{F}_i^{\text{g}} + \mathbf{F}_i^{\text{c}}}{\left\|\mathbf{F}_i^{\text{g}} + \mathbf{F}_i^{\text{c}}\right\|} + \mathbf{F}_i^{\text{perc,xy}} \tag{7.22}$$

where $\mathbf{F}_i^{\text{g}}$ is the global force, sum of all social forces without ship motion model as described by (equation (2.9)), $\mathbf{F}_i^{\text{c}}$ is the control force related to ship motions as defined in equation (7.13), $f_{fd,i,\max} \cdot m_i$ is the maximum friction force per unit mass with $f_{fd,i,\max}$ defined by equation (7.21), and $\mathbf{F}_i^{\text{perc,xy}}$ is the component of the perceived force vector $\mathbf{F}_i^{\text{perc}}$ parallel to the deck.

However, in addition to the above, some preliminary simulations showed that some of the definitions related to the social forces without ship motions required some modification in order to be consistent with the introduction of ship motions. In fact, the module v_i^0 of the desired speed is usually almost constant in absence of ship motions.

However in presence of ship motions v_i^0 might significantly reduce becoming very close to 0 due to the speed reduction factor.
The nervousness paramters ξ_{inst} (see section 2.2.7) and the parameters determining the magnitude of the repulsive interaction forces $A_i^a(t)$ and $A_i^w(t)$ are not defined when $v_i^0 = 0$.
In order to keep consistency also in the case $v_i^0 = 0$, the nervousness sub-model is not applied when the desired speed is less than 10% of the unimpeded speed i.e. when the following inequality holds:

$$v_i^0 < 0.1 \cdot v_i^U \tag{7.23}$$

where v_i^U is the unimpeded speed of the agent and v_i^0 is the desired speed after performing the reduction.

The parameter $A_i^a(t)$ instead is newly redefined by introducing an upper bound $A_{a,\max} = K_{a,\max} \cdot A_a$. The new instantaneous parameter $A_i^a(t)$ is hence calculated as follows

$$A_i^a(t) = \min\left(\max\left(v_i(t)/v_{i,0}(t), 0.5\right), K_{a,\max}\right) \cdot A_a \tag{7.24}$$

where $K_{a,\max}$ is a parameter that needs to be set. The parameter $K_{a,\max}$ was set in order to be greater than the maximum values reached by the ratio $v_i(t)/v_i^0(t)$ in simulations without ship motions. This choice was made in such a way that the modelling introduced in (7.24) to account for the presence of ship motions is not going to affect cases where ship motions are not present. The test IMO 8 and IMO 11 where used to determine reasonable maximum values reached by the ratio $v_i(t)/v_i^0(t)$. This choice was made since in those test conditions the agent speeds are likely to reach values higher than $v_i^0(t)$. This happens in IMO test 8 because the counterflow force might increase the instantaneous speed above $v_i^0(t)$. Instead, in IMO test 11 this happens because, when the agent starts walking on the stairs, its target speed $v_i^0(t)$ is abruptly reduced while it takes some time for its speed $v_i(t)$ to reduce as well. As a result, in IMO test 11, there is an abrupt increase of the ratio $v_i(t)/v_i^0(t)$ for agents just entering the stair. The maximum values of the ration $v_i(t)/v_i^0(t)$ found in IMO 8 where, however, greater than those found in IMO test 11. Figure 7.7 reports the value of the ratio for each agent and for each time step in 10 runs of IMO test 8 (case with highest density value).

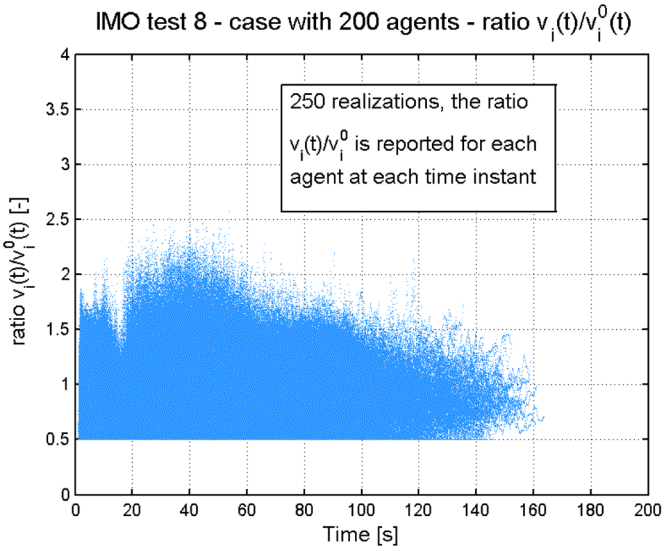

Figure 7.7: Ratio $v_i(t)/v_{i,0}(t)$ for each agent and each time instant from 250 simulation runs of IMO test 8 case.

Using, as a reference, data reported in Figure 7.7, the parameter $K_{a,\max}$ was thus set to $K_{a,\max} = 2.5$, in order not to affect simulations results in cases without ship motions.

7.3 IMO tests considering the presence of ship motions

The IMO tests reported in the MSC.1/Circ.1533 [147] have already been useful for sensitivity analysis and calibration of the parameters in the model without ship motions. Herein the geometries and the test conditions of IMO test 4 (bottleneck) and IMO test 8 (counterflow) will be adopted to analyse the effects, on evacuation, of regular (periodic) ship motions.

For simplicity, the generated regular motions are supposed to refer to a point positioned at a hypothetical waterline. The geometry of each test is assumed to be positioned at 15 m above the centre of rotation, i.e. at 15 m above the waterline. This value was taken as an approximation of the height above waterline deck 5 in the SAFEGUARD Validation Data Set 2 (Galea et al. [54], [186]). In addition, the geometry of the IMO test are considered to be oriented from stern to bow. By convention, in the following, a positive trim angle indicates a trim by stern, whereas a positive heel angle indicates a heel angle to starboard.

A total of 50 realizations were run for each motion condition. The motions were derived by a systematic variation of the roll amplitude, of the heel and of the trim .The period of roll motion was set to a constant value of 20 s (typical order of magnitude of roll period for large cruise vessels, adopted also by Nicholl et al. [158]) for each simulation condition.

Table 7.2 show motion parameters used to generate all the test conditions. A total of 45 test conditions, corresponding to the set of all the possible combinations of the reported values, was generated.

Table 7.2: Motion parameters.

Roll amplitude	0°, 5°, 10°
Roll period	20 s
Heel	0°, 15°, 20°, 25°, 30°
Trim	-10°,0°,10°

In the simulation campaign, it was necessary to set an absolute maximum duration time for the simulations, and this time was set to $t_{\max} = 1800\,s$ of 1800 s. This was necessary as in some cases with very large heel angle not all agents were able to achieve the exit, and the simulation had to be forcedly stopped.

7.3.1 IMO test 4 with regular ship motions

The exit from the bottleneck is one of the most important evacuation situations and it is thus necessary to analyse how it is affected by ship motions.

Snapshots related to five different simulations with different heel angles are reported in Figure 7.8. The figure shows that the trajectory of agents is affected by the heel angle. In particular, agents move towards the side of the room corresponding to direction of the inclination. The action of the heel angle on the trajectory increases the difficulty in exiting from the bottleneck. As a result, the exit time is affected not only by the reduction of the unimpeded speed, but also by the application of the perceived force to each agent.

The exit time was analysed for each combination of applied motions, and Figure 7.9 shows the statistical analysis of exit times based on 50 realizations for each case.

Results in Figure 7.9 clearly show that the exit time increases with the heel angle and the increase is very sharp when the heel angle becomes larger than 20°. This behaviour, which is due to the model used for defining the speed reduction coefficient of the unimpeded speed (see Figure 7.3), was definitely expectable by "model design".

The observed behaviour concerning roll angles, is, instead, more unexpected. The introduction of a rolling amplitude, with long rolling period, tends to reduce the exit time when the heel angle is larger than 20°. This effect is due to the fact that, while in the static condition agents have a constant and very large reduction of the unimpeded speed; in case of dynamic conditions, the unimpeded speed increases when dynamic roll tends to compensate the heel, and this gives the opportunity to agents to reach a higher speed. Moreover, the periodic motions increase the opportunity to overcome impasse situations occurring at the bottleneck, reducing the clogging. This behaviour, although reasonable from the point of view of consistency with the underlying modelling, should be taken with caution and would require checking through experimental data, which are not available at the moment.

The effect of trim is also marked. Negative trims (meaning that user perceive an inclination going downwards with respect to their desired direction) has the effect of increasing the exit time when the heel angle is low. In case of large heel angles (>20°),

instead, the effect is opposite: the presence of a negative trim reduces the exit time as agents are pushed towards the exit.

Finally the dispersion of exit times seems to increase with the heel angle. In particular, there is a marked difference between the cases with heel smaller or equal to 20°, where the dispersion is relatively small, and those where heel is larger than 20°, where, instead, the dispersion of data becomes very marked.

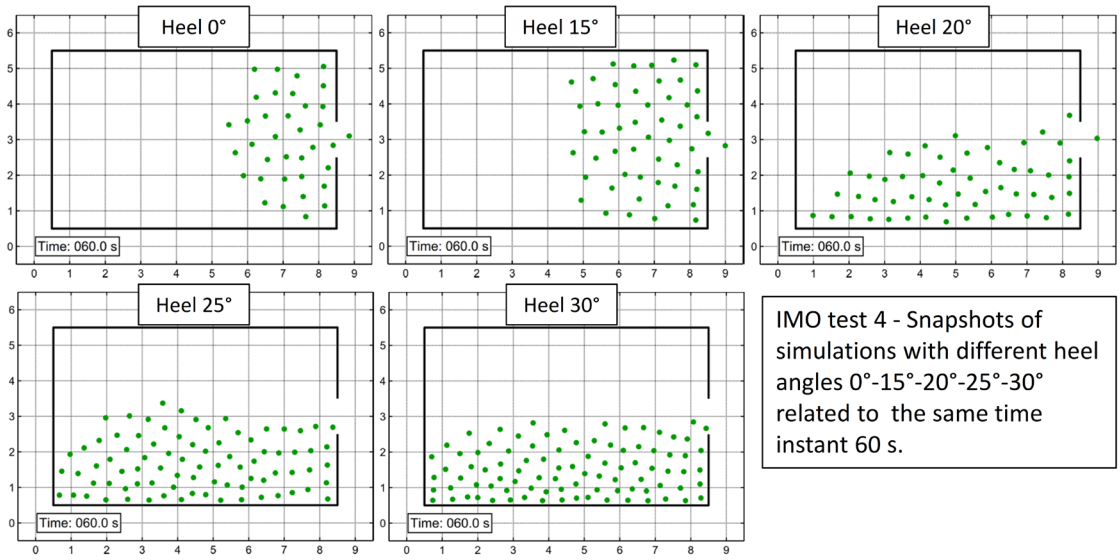

Figure 7.8: IMO test 4. Snapshots of simulations with different heel angles (0°, 15°, 20°, 25°, 30°) showing the progressive tendency of agents to move towards the side of the room in the direction of the inclination of the ship.

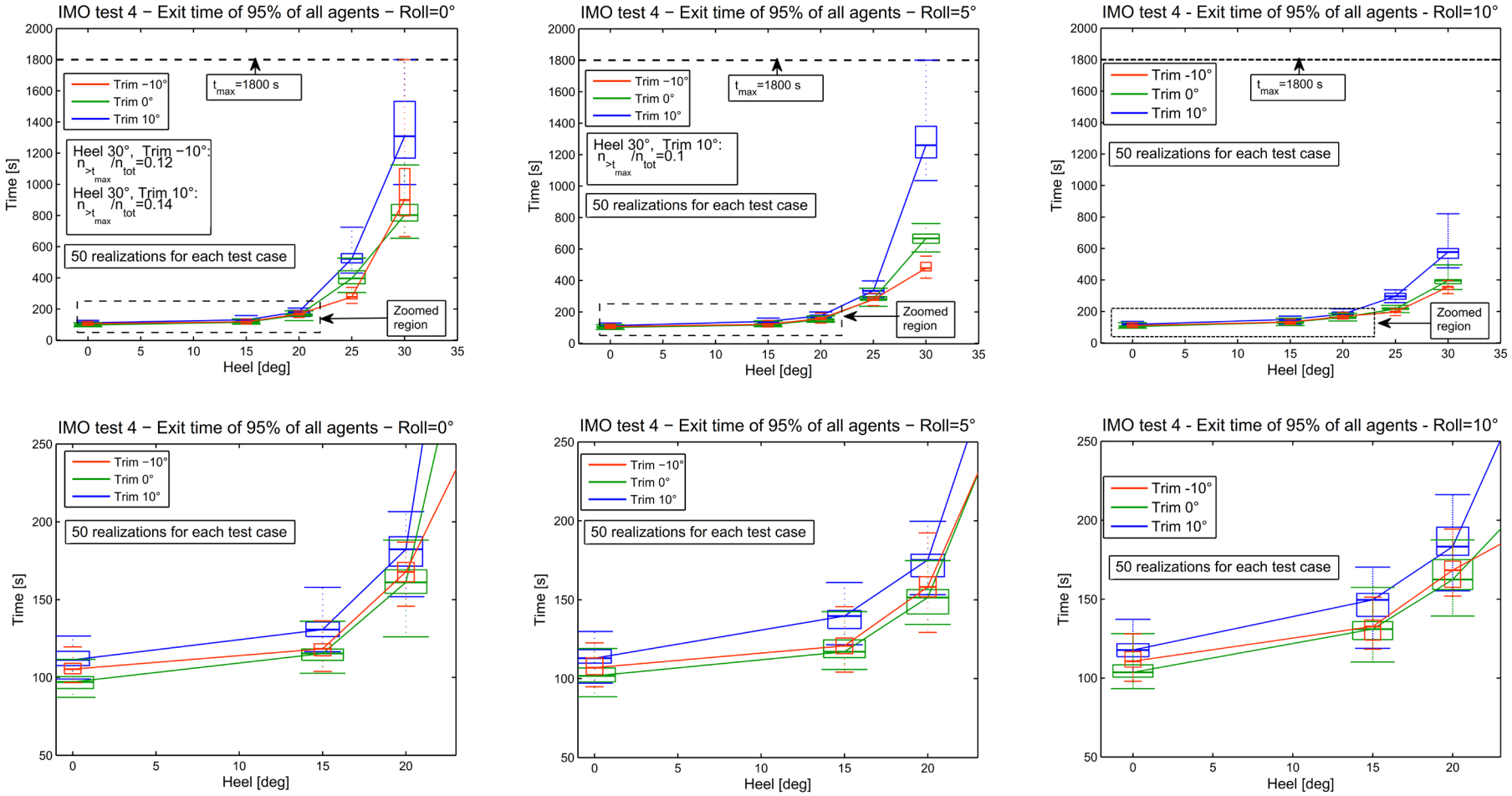

Figure 7.9: IMO Test 4. Analysis of exit time of 95% of agents in presence of ship motions. Box plots report minimum, maximum and 25%, 50% and 75% percentile values. $n_{>t_{\max}}$ is the number of simulations, on a total of $n_{tot} = 50$, where less than 95% of all agents exited the room within $t_{\max} = 1800$ s Top: full data. Bottom: zoomed regions.

7.3.2 IMO test 8 with regular ship motions

The condition of a reduced group of crew members going in counterflow with respect to evacuating passengers can frequently appear in evacuation situations (MSC.1/Circ.1533 [147]). Such a condition is effectively represented by IMO test 8, considering the test situation with 10 agents in counterflow. The effect of ship motion was thus tested in this specific counterflow condition.

The qualitative effect of the different heel angles is observed in the snapshots presented in Figure 7.10. The positive heel angle has the effect of originating a perceived force which has the same direction as the preferred direction in case of agents coming from the left and opposite direction in case of agents coming from the right. As a result, the agents coming from the right have difficulty in forming the lane in the case with heel equal to 20°. Moreover, it can be observed that agents occupy the whole corridor in the case without heel as the agents coming from right form two parallel lanes. However, in the case with heel angle equal to 20°, the agents coming from right form only one lane and the corridor is not fully occupied.

Finally, the phenomenon described by Duives et al. [41] concerning the widening of the lane width at the exit from bottlenecks (due to the increase of the distance between agents) is observed in the case without heel whereas it is not present in the case with heel equal to 20° where agents exit the bottle neck in a single line.

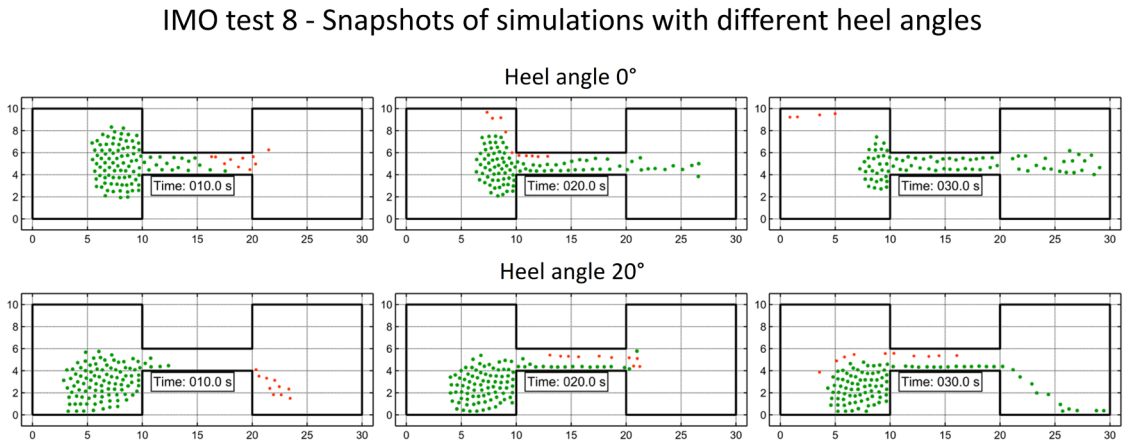

Figure 7.10: IMO test 8. Snapshots of simulations without heel (top) and with 20° of heel (bottom) for three different time instants (from left to right).

Figure 7.11 reports a quantitative analysis of the exit time of 95% of the agents coming from the left room, as obtained by 50 realizations of each test, for the considered heel and trim angles.

The same effect of roll as previously observed for the IMO test 4 is present also in this case: the presence of dynamic roll increases the exit rate by generating instantaneous situations of reduced inclinations during which the agents are capable of moving towards the exit.

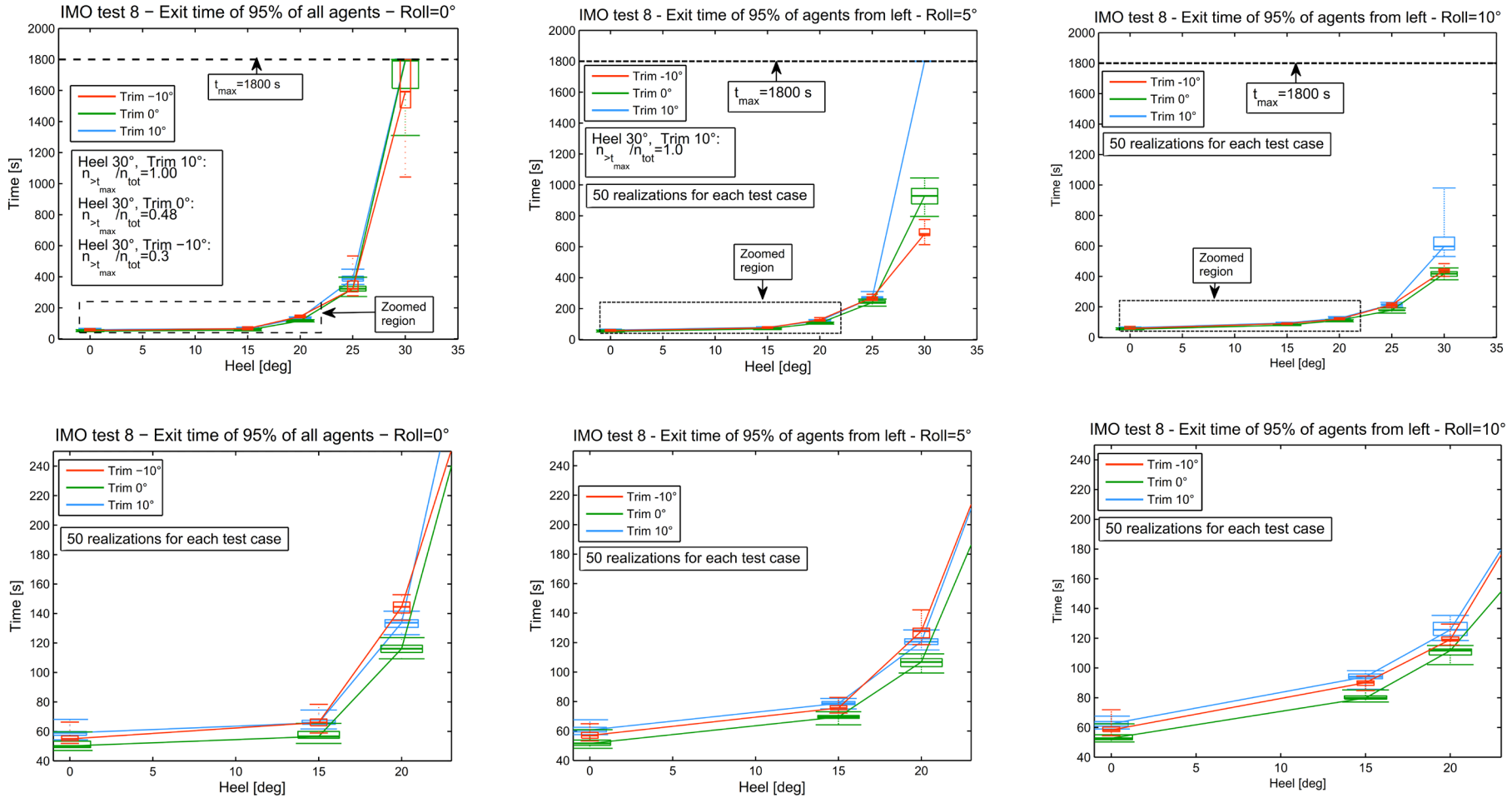

Figure 7.11: IMO Test 8. Analysis of exit time of 95% of agents from left room in presence of ship motions. Box plots report minimum, maximum and 25%, 50% and 75% percentile values. $n_{>t_{max}}$ is the number of simulations, on a total of $n_{tot} = 50$, where less than 95% of all agents exited the room within $t_{max} = 1800$ s . Top: full data. Bottom: zoomed regions.

The effect of roll seems, however, to be very limited when the heel angle is small. Instead, the effect of dynamic roll becomes more important for heel angles equal to 25° or 30°.

The effect of trim in this test condition is more complex due to the asymmetry of the situation. It can be observed that, generally, for small heel angles (<25°), the presence of trim, irrespective of its direction, seems to slightly increase the exit time of the agents from left. A positive effect of trim is, instead, detected when heel reaches 30°. In this case an inclination towards the direction of the agents coming from left (negative trim according to the used convention) seems to allow a faster evacuation.

The cases with heel 25° and 30° should, however, be considered as as conditions where the model is possibly stretched above its foreseeable applicability, as the present model which currently does not consider situations where people fall. It is reasonable to think that in the condition of heel equal to 30°, the behaviour of people is affected by other factors such as panic and loss of equilibrium that might cause a completely different behaviour compared to that of an orderly evacuation. Data presented herein are, nevertheless, useful to better understand the effects and limitations of the proposed model.

7.4 Final remarks

The present chapter addressed the problem of considering ship motions in evacuation models. An overview of the state of the art on this topic was presented at the introduction of the chapter, where experimental data available in literature have been referred to and commented.

A new model capable of considering the effects of ship motions not only as a reduction of the desired speed of the agents, but also as a modification of their trajectory, has been developed and presented. The model has been described in detail with all the associated parameters.

Finally, an implementation of the developed model was presented. In particular, results from IMO test 4 and test 8, performed with different periodic ship motions and different heel and trim angles have been reported. It is observed that in IMO test 4 the presence of heel has the effect of increasing the exit time. Trim has also the effect of increasing the exit time in most of the cases, except when the heel angle gets larger than 25°: in this condition a trim directed downwards with respect to the exit of the room has the effect of decreasing the exit time. Finally it was observed that the effect of heel is not limited to a reduction of speed, but heel also modifies the trajectories of the agents. The IMO test 8 showed similar outcomes. However, in this test condition, the effect of trim was more complex due to the asymmetry of the considered situation.

From a qualitative analysis of the obtained results it is observed that in both tests, the behaviour of agents is affected by perceived forces in terms of change of trajectory when the heel angle is sufficiently large. More specifically, in the IMO test 4 agents are observed to move towards the wall placed in the direction of the inclination, whereas in IMO test 8 the lane formed by the agents is observed to become thinner when heel increases.

A more realistic test case, consisting of two cabin decks, will be presented in the next chapter. The test will be run with and without the presence of ship motions. Moreover, in such case, motions for a notional cruise vessel deriving from an irregular beam waves condition, will be also considered.

This page is intentionally left blank

8 A TWO-CABIN-DECK TEST CASE

This chapter proposes a test case which, while keeping a sufficiently reduced level of complexity, can be considered to be a realistic scenario for the maritime field. In particular, a two-cabin-deck test case is presented, which is the result of simplification of a portion of geometry of an existing cruise vessel. Firstly, the motivations of the study are presented, with reference to existing standardized evacuation test cases related to the maritime field. The proposed test geometry and is then described in detail, providing all the information for allowing its reproduction, and a description is given of the main quantities considered in the subsequent analysis of evacuation simulations. Evacuation simulations for the proposed geometry are then carried out considering, firstly, the vessel as fixed and upright. Afterwards, standard notional conditions of static (heel, trim) and periodic dynamic motions (roll) are considered, and the effects on the evacuation process are assessed. The same geometry is then used for evacuation simulations using more realistic ship motions which have been computed considering that the test geometry is placed onboard of a notional cruise vessel, and considering long-crested irregular beam waves. The notional sample vessel is described in details, together with the methodology for the calculation of ship motions. Evacuation simulations are then carried out, and results from the analysis are reported and commented. Some final remarks are then provided.

8.1 Introduction

Results of simulations as discussed in Chapter 4 highlight the importance of carrying out comparisons among different evacuation models and show that non-negligible differences among models can be observed also when referring to very simple test cases. This indicates that the importance of relative comparisons of different evacuation models may even increase when considering more complex and realistic cases. However, it is a fact that very few realistic geometries specifically relevant to the

maritime field are available in the public literature, with all the necessary details to carry out systematic comparative analyses and, possibly, benchmarks. As an example, the only test proposed by the MSC.1/Circ.1533 [147] which is based on a non-archetypal geometry, but on a geometry which is specifically related to the maritime field is the IMO test 10, where a small portion of a cabin deck is reproduced.

A valuable contribution to the creation of a set of realistic benchmark geometries and experimental data related to the maritime field has been produced during the project SAFEGUARD ([186]). During SAFEGUARD, two full-scale evacuation trials were performed, one regarding a ro-ro passenger ship and the other one regarding a large cruise vessel. Data concerning evacuation time, response time and passengers positions have been collected during the project and then reported by Deere et al. [33], Galea et al. [54] and Brown et al [17]. The two SAFEGUARD validation data sets represent a very unique source of information in the process of validation of an evacuation simulation tool. Moreover, very detailed data concerning the population and the geometry of the ship are available ([186]). A comparison between simulation and SAFEGUARD data has been carried out by Park et al. [167], the comparison showed that the software SIMPEV satisfyies the acceptance criteria of the two validation data sets provided by the SAFEGUARD project ([186]).

However the geometries of the test cases available in [186] are quite complex and their use can therefore become difficult, especially in the early development phases of an evacuation model and/or a software tool. Moreover, the complexity of the geometry may require additional modelling functionalities embedded in the simulation tool for the representation of the real layout, which may influence the final results of the simulations. For such reasons, the SAFEGUARD Validation Data sets, while representing a unique resource for validation and testing of tools and models at an advanced stage of development, might not represent a first choice for a quantitative comparison of different tools.

A test case of reduced complexity concerning, specifically, the maritime field, would therefore be useful. In particular, the geometry of such a test case should be sufficiently realistic to highlight the most important phenomena which may occur during the evacuation process in order to perform informative comparisons among evacuation simulation tools. At the same time, the geometry should be still sufficiently simple for implementation, in order not to require significant geometrical processing which may affect the final results.

For the above reasons, a simple test case is presented in this chapter, which has been derived from the geometry of the SAFEGUARD Validation Data Set 2 (SGVDS2), which pertains a cruise vessel. Although relatively simple, the test case embraces some important layout characteristics, which are very common in the maritime field, such as the exit from cabins and subsequent entering in narrow corridors, the clogging occurring at the bottom of staircases, and the situation of merging of flows of evacuees.

In the following, the developed test case is firstly described. Then, a series of evacuation simulations have been carried out considering the geometry as fixed. Subsequently, Simulations are presented, which were run in presence of ship motions to

assess their effects on the evacuation process. To this end, results are firstly shown which are based on notional periodic motions, as suggested by Nicholl et al. [158].

In order to assess the effect of more realistic ship motions, the proposed geometry was also used to simulate evacuation in presence of ship motions due to irregular beam waves. For the generation of motions, a notional cruse vessel has been considered, and the developed test geometry has been assumed to be placed in a specific position on the vessel. Although the considered cruise vessel is a notational one, her characteristics are in line with those of the cruise vessel relevant to the SAFEGUARD Validation Data Set 2 (SGVDS2, [186]) (see [185]). Before reporting results from evacuation simulations in presence of irregular waves, the approach used for the generation of ship motion, which is based on linear seakeeping calculations with the superposition of steady heel and/or trim, will also be carefully described.

8.2 Description of the test case

In the following section the developed test case is described in detail, with particular emphasis on the population characteristics and on the geometry, which was extracted from the SafeGuard Validation Data Set 2 (SGVDS2, [186]). The second part of this section describes the quantities that have been considered in the analysis of simulation outcomes, which will be presented in the subsequent sections.

8.2.1 Geometry, initial conditions and population

The proposed geometry was derived as a direct simplification of the geometry from the SAFEGUARD Validation Data Set 2 (SGVDS2 - Galea et al. [54]), which corresponds to the case of a cruise vessel. For the development of the simplified geometry, the aft parts of decks 5, 6, 7 of the entire SGVDS2 were considered. For simplicity of notation, decks 5, 6, 7 from SGVDS2 are herein renamed as deck 1, 2, 3. The positioning, on the vessel, of the considered geometry is schematically indicated in Figure 8.1. For the purpose of simulations in presence of ship motions, deck 1 was assumed to be placed at a height of 15 m above the waterline and, considering a typical draught of 8m for a cruise vessel, this corresponds to a height of 23 m from the ship bottom. Conventionally, herein, for sake of simplicity, the aft end of the test geometry has been assumed to coincide with the aft perpendicular. Although in a real vessel there would be a shift aft in order to have the balconies coinciding with the extreme end of the vessel, the effect of such a shift, for the calculations presented herein, is deemed to be minimal.

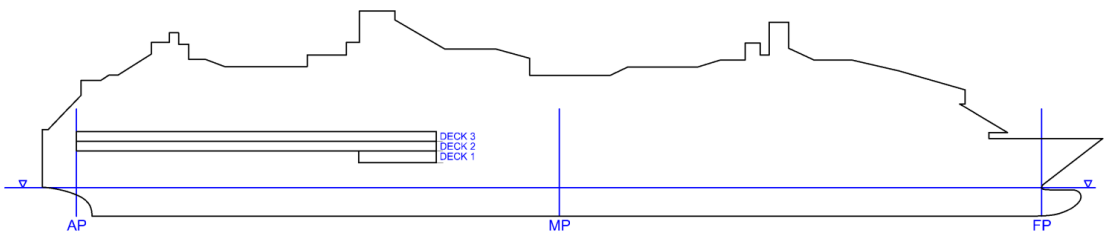

Figure 8.1: Reference positioning of the test case on the vessel.

Figure 8.2 shows the details of the whole geometry developed for this test case as well as the indication of areas which will be used for the analysis of simulations, while

Figure 8.3 shows a detailed view close to the staircase. Deck 2 and deck 3 are cabin decks having the same layout, while an assembly station is assumed to be placed on deck 1, as a simplification of the corresponding one on deck 5 of SGVDS2.

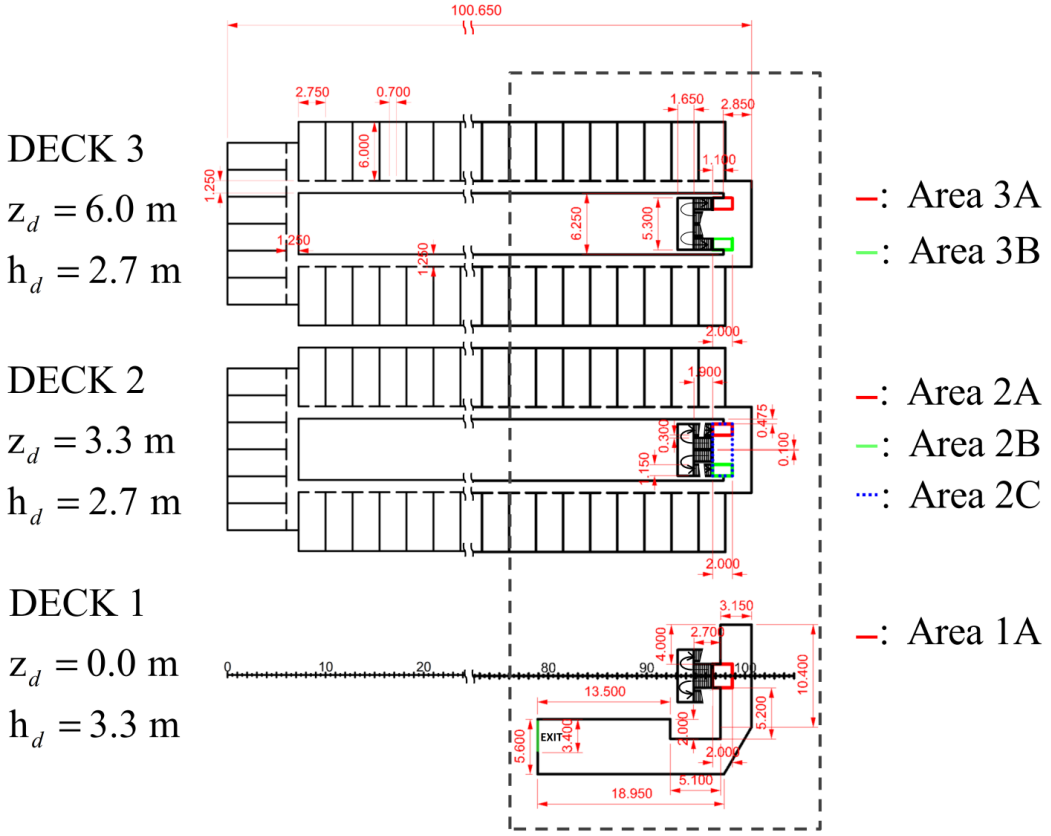

Figure 8.2: Arrangement of the two-cabin-deck test case. The variable z_d indicates the vertical coordinate of each deck plane, starting with $z_d = 0\ m$ at deck 1, while h_d indicates the height of each deck. Areas used for the analysis of evacuation simulations are indicated as 1A, 2A, 2B, 2C, 3A and 3B.

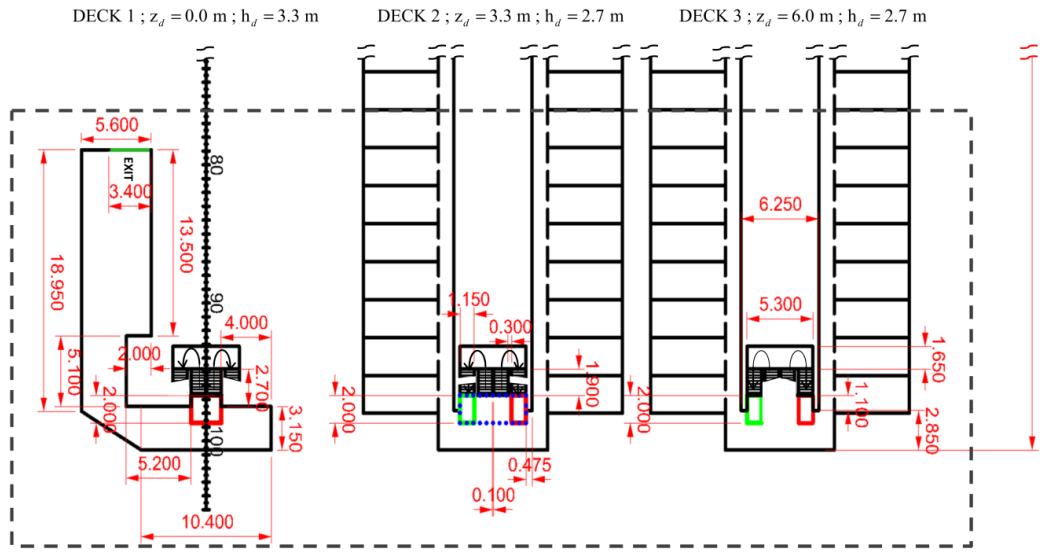

Figure 8.3: Arrangement of the two-cabin-deck test case. Detailed view close to the staircase.

The connection between the decks is made through a single staircase that rises from deck 1 to deck 3, and this staircase corresponds to stairs 8, 10 and 12 from the SGVDS2 geometry. For sake of simplification, all cabins in the test case have the same dimensions and the exit of each cabin is placed in the middle of the corresponding side. The dimensions of stairs and landings, as well as the heights of the decks are the same as those reported by Galea et al. [54]. All landings are positioned at mid-height between the corresponding upper and lower decks.

An evacuation scenario has then been setup. In order to observe clogging phenomena and clearly identify conditions of high density, two agents are placed within each cabin at the starting of the simulation, for a total of 288 agents.

- The total population is divided in 10 different classes in accordance to MSC.1/Circ.1533 [147]. The population was generated randomly for each realization, following the classes composition specified in MSC.1/Circ.1533 [147] as reported in Table 4.1.
- The unimpeded speed of each agent was randomly generated in accordance to the distribution of unimpeded speed specified for the class the agent corresponds to, following MSC.1/Circ.1533 [147] as reported in Table 4.1.
- The distribution for the dimensions for each agent depends on the gender (Male or Female) which is specified by the IMO class the agent belongs to. As no information is provided in MSC.1/Circ.1533 [147] regarding agents dimensions, the data reported in Table 4.2 are used.
- For sake of simplification, the response time was set to zero for all agents, and therefore all agents start moving at the same time, corresponding to the beginning of the simulation.

8.2.2 Analysed quantities

The outcome of each simulation is very detailed as it consists in the position and speed of all the agents at each time instant. It is therefore necessary to limit the set of quantities subject to the analysis. In this respect, reference was made to MSC.1/Circ.1533 [147], which specifies the main objectives of the evacuation analysis, which are summarized in the following:

- Assessing the effectiveness of the evacuation process, principally by analysing the overall duration of the evacuation.

- Identifying congestion points and/or critical areas (e.g. areas of intense cross or counter flows). According to MSC.1/Circ.1533 [147], congestions can be identified within regions having local population densities exceeding 4 p/m^2 for significant duration.

Accordingly, the total assembly duration and the density are the most important quantities to be analysed.

However, although global quantities are the ones used in the assessment of the evacuation process, instantaneous quantities such as the number of agents still to be evacuated at each time step, or the number of agents inside decks or stairs, provide

additional useful information on the evacuation process, by offering a detailed insight of the phenomena occurring during the evacuation.

Due to these observations the analysis of the outcomes from the simulations, as reported hereinafter, focuses on the following quantities:

- **Total assembly duration**. The total assembly duration , in this case, corresponds to the time elapsed between the beginning of the simulation and the time instant the last agent arrives at the designated assembly station by exiting from the exit on deck 1 (see Figure 8.2 and Figure 8.3). The total assembly duration is analysed as a random variable, in terms of its cumulative distribution and probability density function.

- **Density at the stair entrance.** Congestions often occur at the entrance of staircases and it is, thus, fundamental for an evacuation tool to effectively reproduce this phenomenon. The IMO test 11 in MSC.1/Circ.1533 [147] assesses the capability of the model to reproduce congestion at the entrance of staircases in an archetypal condition. However, a more complex condition is, instead, analysed in this test case. Therefore, herein, the instantaneous density is calculated in six different regions (3A, 3B, 2A, 2B, 2C and 1A), which are represented in Figure 8.2, for each simulation run. Densities will be considered as stochastic processes, and their time dependent instantaneous distribution will be reported in terms of percentiles curves as estimated, in ensemble domain, from all the available simulations.

- **Number of agents.** In order to have an insight of the occupation of facilities during the evacuation process and on the overall passenger flow, it is useful to analyse the number of agents in each deck, in the assembly and in each staircase, at each time instant. The instantaneous number of agents in each considered region, similarly to the density, is, therefore a stochastic process. Accordingly, also in this case, the corresponding time dependent instantaneous distribution will be reported in terms of percentiles curves as estimated, in ensemble domain, from all the available simulations.

8.3 Results with fixed geometry and using standard motion conditions

The present section will report the results obtained considering fixed geometry in upright conditions and standard motion conditions. Firstly the condition without ship motion is analysed. Subsequently, four standard conditions of motion will be prescribed, considering heel, trim and roll, as suggested by Nicholl et al. [158].

8.3.1 Condition without ship motion

The test case without ship motions is considered in the following. The analysis of all quantities is performed considering data from a total of 250 Monte Carlo realizations.

The total assembly duration is analysed considering the cumulative distribution and the corresponding probability density function, as reported in Figure 8.4.

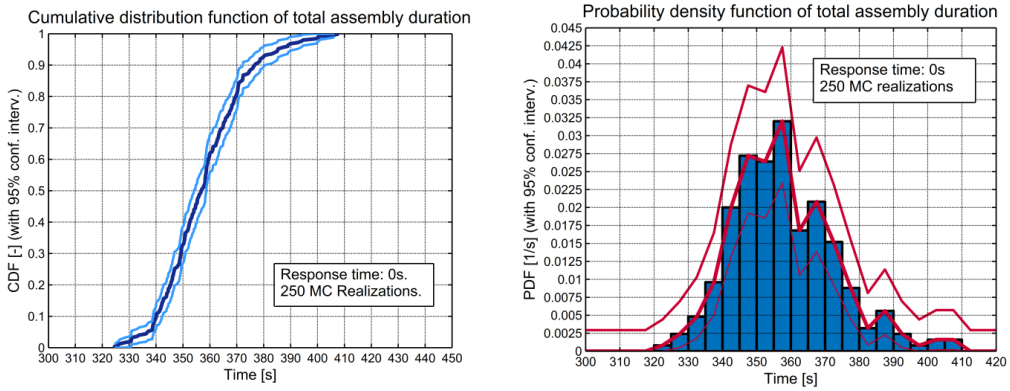

Figure 8.4: Two-cabin-deck test case. Case without ship motion. Estimated cumulative distribution (CDF), left, and probability density function (PDF), right, of total assembly duration.

The total assembly time from the simulations, as shown in Figure 8.4, shows a significant dispersion when considering, particularly, extreme values. Data are characterised by a median of 357 s, 10% percentile of 340 s, 90% percentile of 377 s, observed minimum 325 s, observed maximum of 408 s, and most probable value approximately around 355 s.

The density in areas 1A, 2A, 2B, 2C, 3A and 3B (see Figure 8.2) is analysed in Figure 8.5, and it can be noticed it rarely exceeds 3.5 p/m^2, and it did not exceed 4.0 p/m^2. As a result, following the definition from MSC.1/Circ.1533 [147], in the considered test scenario there were no congestions in the considered regions. Nevertheless, situations of high density could be identified at the entrance of stairs, particularly in regions 3A and 3B on the uppermost deck. Such regions of high density are the most likely to become congestion regions in situations of panic and nervousness.

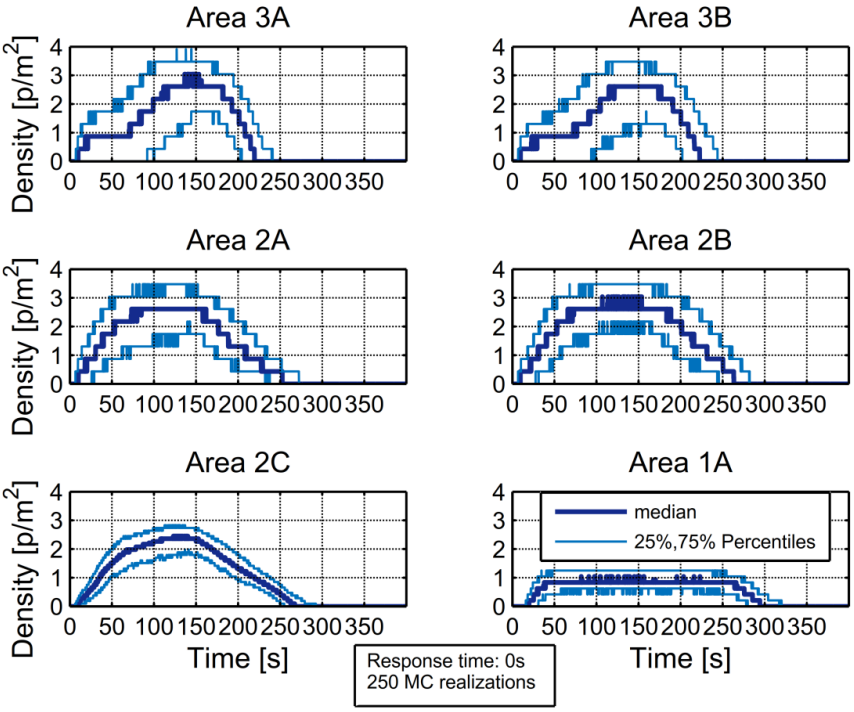

Figure 8.5: Two-cabin-deck test case. Case without ship motion. Density inside each area in front of the stairs. The curves report the ensemble 5%, 50% and 95% percentiles for each time instant.

Looking at results in Figure 8.5 it can be noticed that the density increases at the entrance of the staircases. The lowest densities are observed for the area 1A, because agents in that region are exiting from the stairway already organized in ordered lanes and no clogging occurs. The density in area 1A, after a first raising, then remains, on average, constant, until the evacuation has completed. On the other hand, regions at the entrance of stairs (areas 2A, 3A, 2B, 3B) all show an initial strong increase of density which then decreases as the decks and the staircase progressively empty. While for areas 3A and 3B there are no long stationarity time windows, stationarity time windows can be identified for areas 2A and 2B in correspondence to the highest density. It is also worth noticing that, for areas 3A and 3B, the rise of density occurs in two phases. In a first phase the density increases slightly, while in a second phase the density increases faster up to the maximum value, after which it sharply decreases. The density in the area 2C is lower than the ones measured in area 2A and area 2B, particularly in the time window where densities are increasing. This is due to the fact that area 2C comprises also the region in front of the stairs descending from deck 3, where the density is low as descending agents are already organized in ordered lanes. The stationarity time windows with high density in areas 2A and 2B are longer than those in areas 3A and 3B. This might be due to the situation occurring at the entrance of the stairs leading from deck 2 to deck 1. In fact, in such region, agents descending from deck 3 and arriving on deck 2 compete for the occupancy of the stairs with agents coming from the cabins on deck 2.

The overall flow of passengers can be better understood by considering the distribution of the number of people inside each deck and staircase, at each time instant, as reported in Figure 8.6.

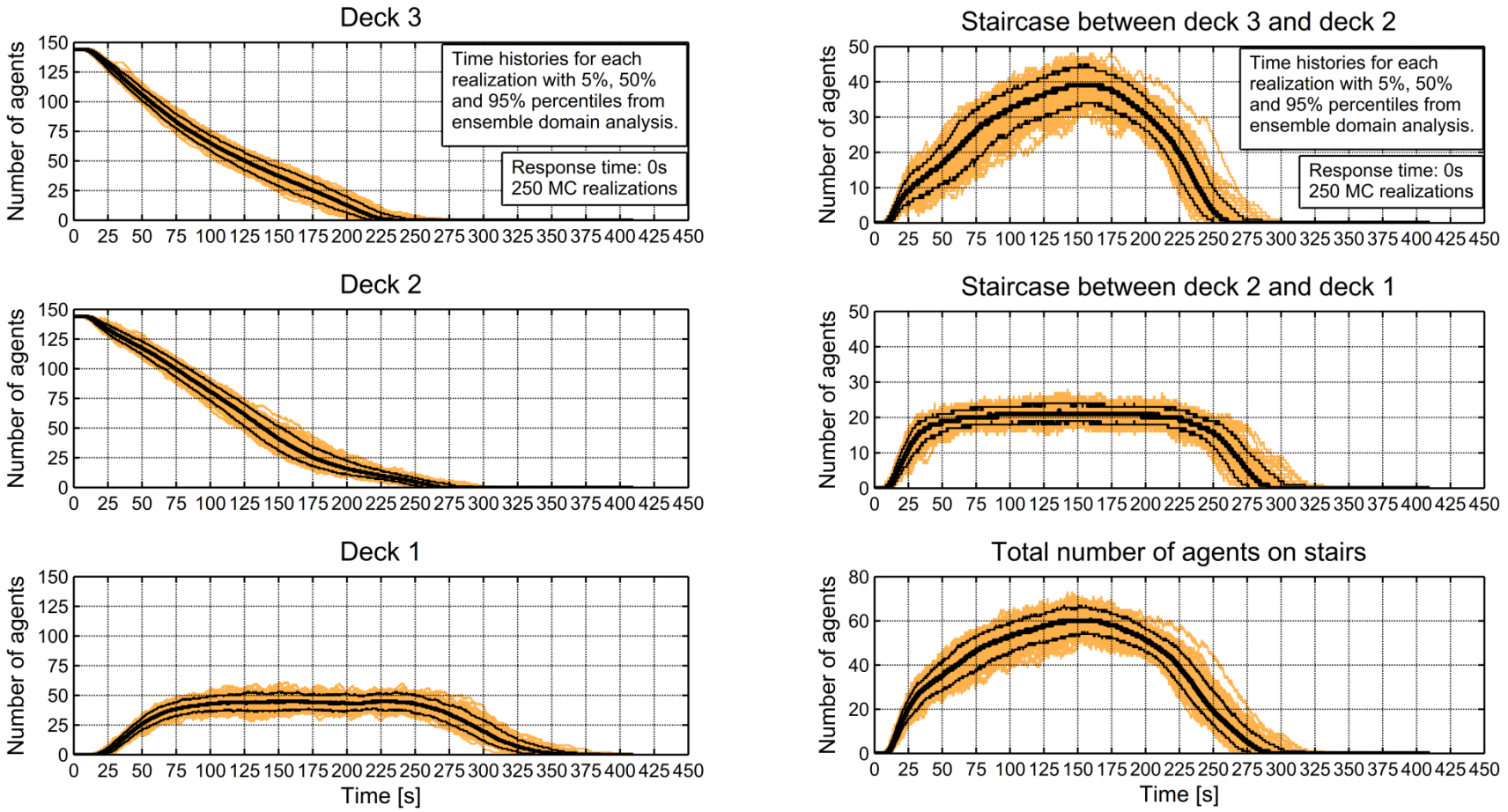

Figure 8.6: Two-cabin-deck test case. Case without ship motion. Number of agents on decks (left) and on stairs (right). Figures report time histories from each single realization, as well as 5%, 50% and 95% percentiles from ensemble domain analysis at each time instant.

From the results in Figure 8.6 it can be noticed that, while the flow is similar for agents in deck 2 and deck 3, there is a very marked difference between the staircase between deck 3 and deck 2, and the staircase between deck 2 and deck 1. The large number of agents inside the staircase between decks 3 and deck 2 is due to the fact that agents descending from deck 3 compete to access the staircase between deck 2 and deck 1 with agents coming from cabins in deck 2, as previously highlighted. This situation of competition for the use of the facility slows down the flow of agents inside the staircase between the deck 3 and deck 2 (occasionally blocking the flow) and originates a situation of high density inside the staircase. This observation is in agreement with the behaviour of the density as presented in Figure 8.5. In general, this type of information, when reported for real ship arrangements, can be useful for better understanding the capacity of the facilities and for driving design choices, such as the selection of stairs width, aimed at optimizing the evacuation performance of the ship arrangement.

Finally, Figure 8.7 summarises the global flow of agents in the considered evacuation scenario, by reporting the distribution of number of exited agents at each time instant from the ensemble domain analysis. It can be noticed that, despite the previously large variability of behaviour in different regions in different decks, the global exit rate is almost constant for a large portion of the simulation time.

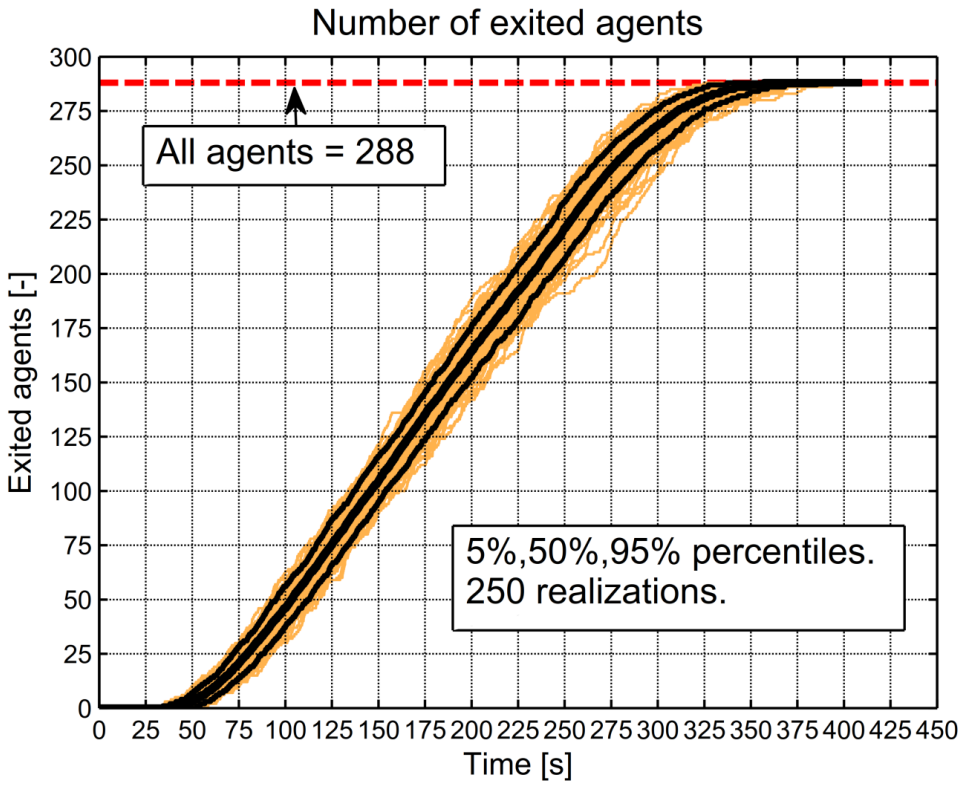

Figure 8.7: Two-cabin-deck test case. Case without ship motion. Analysis of time dependence of number of exited agents. The figure reports time histories from each single realization, as well as 5%, 50% and 95% percentiles from ensemble domain analysis at each time instant

8.3.2 Standard static and dynamic motion scenarios

Herein, evacuation performance for the described two-cabin-deck test case are considered assuming notional simplified ship motions conditions (both static and

dynamic), which can be referred to as a set of "standard motion scenarios". Firstly, motion scenarios proposed by Nicholl et al. [158] are considered. Afterwards, a combined heel and trim scenario is considered as well combining two of the SAFEGUARD scenarios.

8.3.2.1 SAFEGUARD motion scenarios

Four different test conditions, two static conditions and two periodic harmonic motion conditions, are defined following the ship motion scenarios proposed by Nicholl et al. [158]. The motion scenarios are summarized in Table 8.1.

Table 8.1: SAFEGUARD motion scenarios.

	Heel Condition	**Trim Condition**	**Roll Condition 1**	**Roll Condition 2**
Heel	20°	-	15°	Varying linearly from 0° to 15° in 1 hour, then static at 15°
Trim	-	10°	-	-
Roll amplitude	-	-	5°	5°
Roll period	-	-	20 s	20 s

As a convention, in the following, a positive heel is considered to correspond to an inclination to starboard and a positive trim is considered to correspond to a trim by stern. In case of harmonic roll motions, the phase was the same for all realizations, and roll motion was conventionally defined as:

$$\phi(t) = A_{roll} \cdot \sin(\omega_{roll} \cdot t) \tag{8.1}$$

where A_{roll} [deg] is the assumed rolling amplitude and ω_{roll} [rad/s] is the assumed rolling frequency.

In is anticipated, already at this stage, that obtained results show that ship motions not only affect the total assembly duration, but have also a large impact on the density at the stair entrance and on the use of the facilities. Such effects could be simulated herein thanks to the model developed in Chapter 7 which considers fictitious forces directly applied to agents. At the same time, it is necessary to highlight that the routing strategy of agents, i.e. the list of waypoints that the each agent should follow to arrive at the target exit, is not affected, in present simulations, by ship motions. This means, in particular, that agents do not change their designated staircase entrance in case of, e.g., a heeled vessel, and this has likely an effect on the final outcomes. Such effect should be quantified by introducing a re-routing strategy, which, however, has not been pursued herein.

As first result, the total assembly duration of the static conditions (static heel or trim) is reported in Figure 8.8.

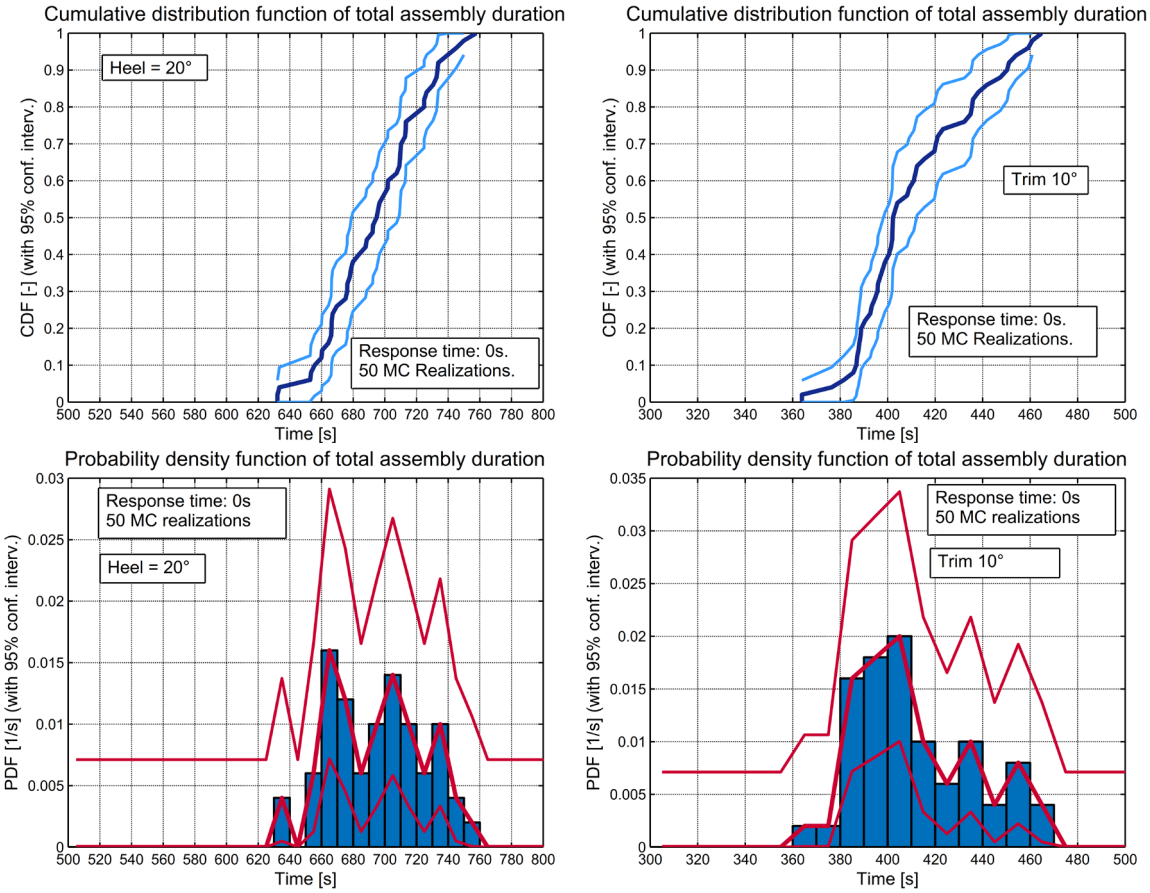

Figure 8.8 Two-cabin-deck test case. Heel condition (left) and trim condition (right). Estimated cumulative distribution (top) and probability density function (bottom) of total assembly duration.

Figure 8.8 shows that the total assembly duration is much more affected in the heeled condition. In this condition, indeed, the maximum assembly duration from the considered 50 random realizations is 758 s while the minimum is 632 s. The median of 696 s corresponds to an approximate doubling of the median total assembly duration with respect to the condition without ship motion (see Figure 8.4). The 25% percentile is 670 s while the 75% percentile is 713 s, leading to an interquartile range of 43 s. The large impact of heel is due both to the decrease of the unimpeded speed and also to the fact that control forces, in this condition, cannot totally counterbalance the external forces (see Chapter 7) and agents trajectories are, thus, modified by external forces.

The total assembly duration is, instead, only slightly affected in the trim condition. Although there is still a reduction of the unimpeded speed in this condition, the trajectory is not modified since agents control forces can completely counterbalance the external forces with the considered 10° of trim (see Chapter 7). The maximum assembly duration obtained in this condition is 465 s and the minimum is 364 s. The obtained median of 403 s corresponds to an approximate increase of 13% with respect to the condition without ship motions. The 25% and the 75% percentiles, respectively 393 s and 433 s, show that the absolute dispersion (40 s of interquartile range) in this test condition is close to that in heeled condition, despite the difference in the direction of inclination and in the magnitude of the inclination.

Figure 8.9 shows the analysis of the total assembly duration for the roll conditions 1 and 2 (see Table 8.1).

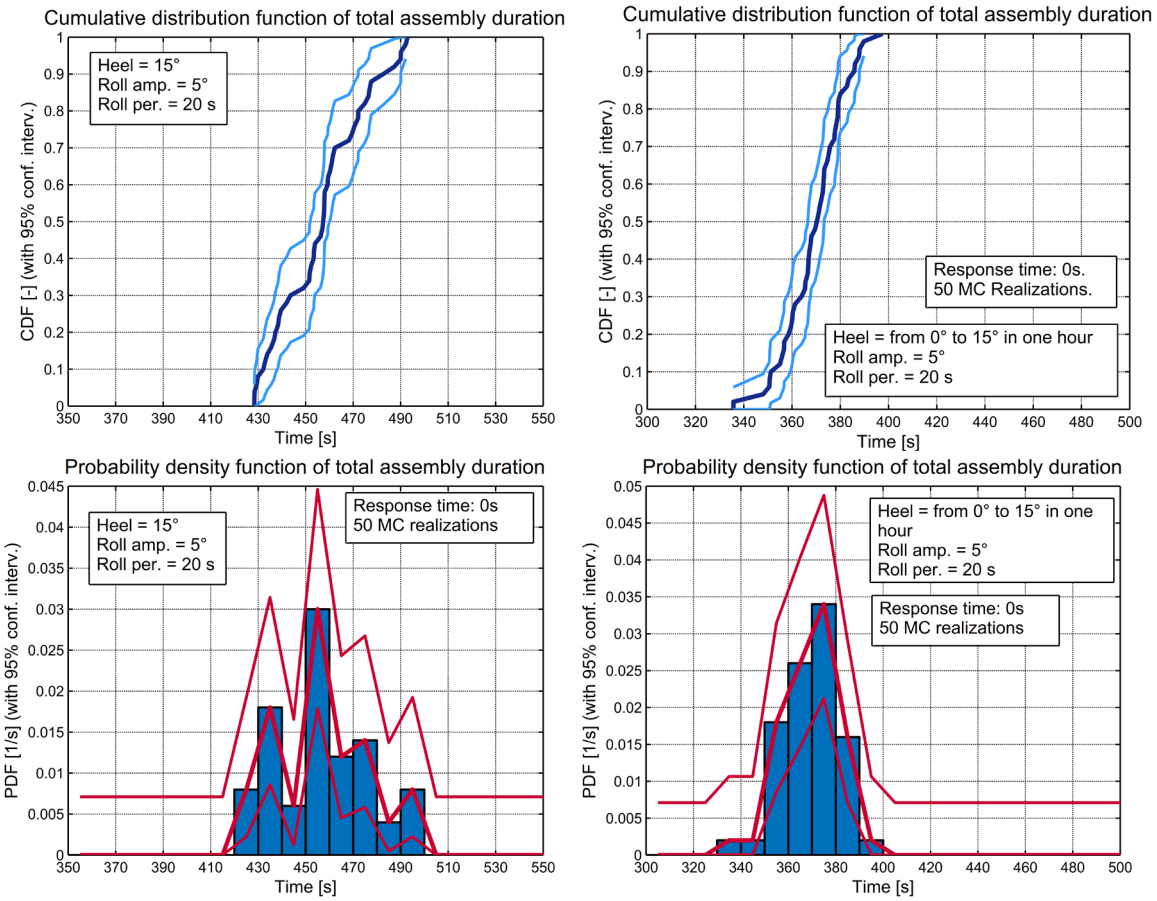

Figure 8.9: Two-cabin- deck test case. Roll condition 1 (top) and roll condition 2 (bottom). Estimated cumulative distribution (left) and probability density function (right) of total assembly duration.

The total assembly time, in the roll condition 1, is still reduced with respect to the condition without motions and this is mainly due to effect of the assumed static heel. Indeed, in this condition the maximum value is 493 s and the minimum value is 428 s. The median is 458 s, corresponding to an approximated increase of 25% with respect to the measured median without ship motions.

The roll condition 2, instead, shows a maximum value of 398 s and a minimum of 336 s. The median is 371 s with a 25% percentile of 360 s and a 75% percentile of 378 s. In this case the increase of the exit time is very small with respect to the case without ship motions. This is due to the fact that heel increases slowly (linearly from 0° to 15° in one hour) and the effects of dynamic roll motions are quite reduced as a consequence of the assumed small roll amplitude and long roll period.

The analysis of density at the stair entrance, calculated in the areas indicated in Figure 8.2, is reported in Figure 8.10.

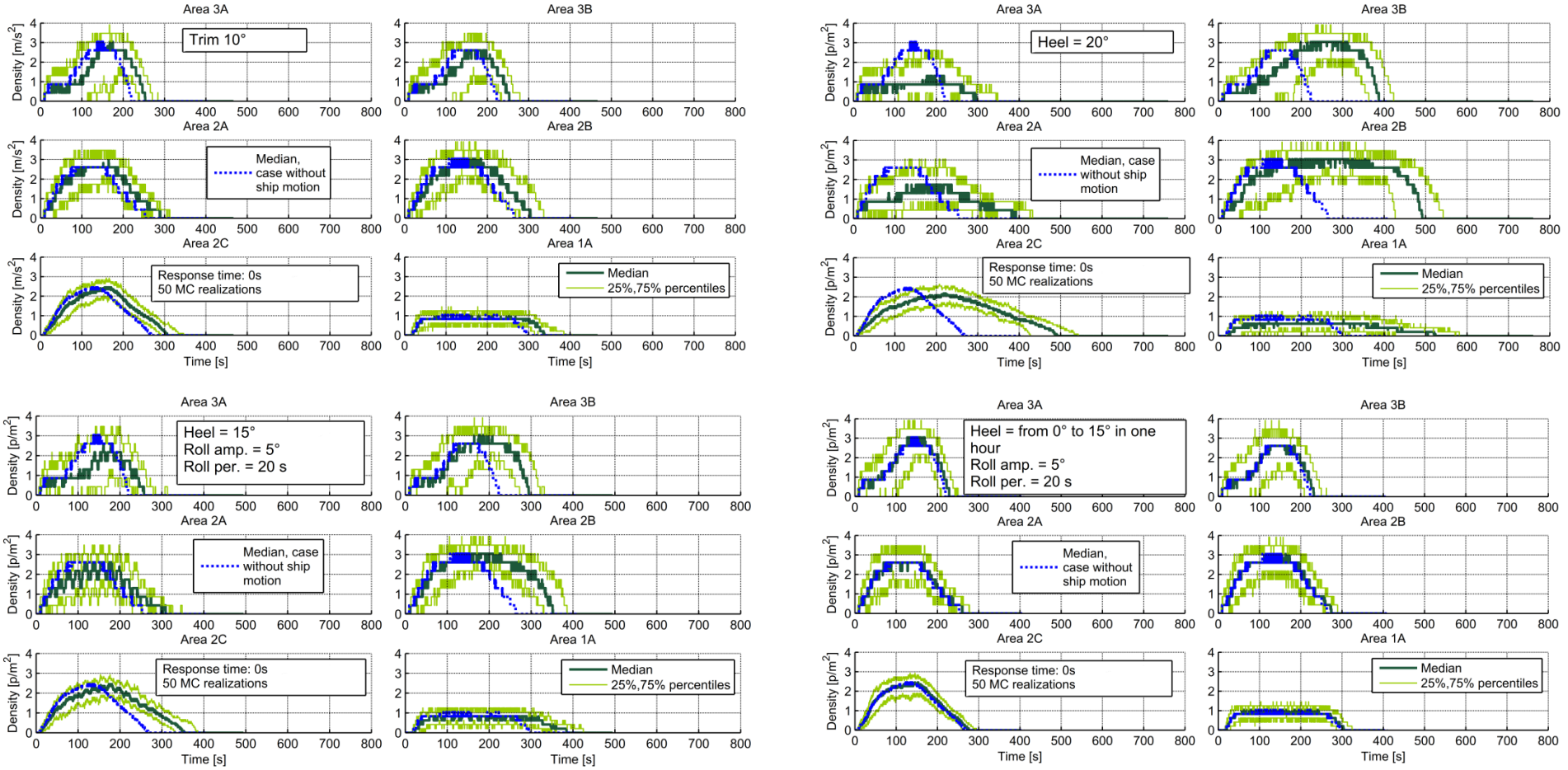

Figure 8.10: Two-cabin-deck test case. Heel condition (top-left), trim condition (top-right), roll condition 1 (bottom-left), roll condition 2 (bottom-right). Density inside each area in front of the stairs. The curves report the ensemble 25%, 50% and 75% percentiles for each time instant. Total number of Monte Carlo realizations: 50 for each test condition. The median of the case without ship motion is also reported, for comparison.

The analysis of the density in Figure 8.10 shows the effects of the direct application of external forces on agents in the heel condition. Heel, indeed, affects the density at the stairs entrance both in terms of duration (the occupation time of the area is increased) and in terms of magnitude. It is particularly relevant to highlight that the density is lower in regions 2A and 3A, positioned on the port side, and thus upwards with respect to the ship inclination (heel is positive, i.e. to starboard), with respect to regions 2B and 3B, which are positioned on the starboard side, and thus downwards. This effect is still present, but with reduced magnitude, in the roll condition 1 as a consequence of the superimposed heel. Instead, the effect is not present in the other two cases. Overall, the trim condition appears to have limited impact. Similarly, the effect of dynamic roll with the considered characteristics, appear to be very limited.

The analysis of the number of agents on each deck and on stairs, as reported in Figure 8.11, provides more detailed information on how ship motion might affect the overall evacuation progress in case of presence of heel or trim.

Results in Figure 8.11 show the significant impact of the considered heel condition, particularly regarding the number of agents on decks. Each deck and each staircase is continuously occupied by agents for a longer duration when heel is present, and this is of course linked with the increase of the assembly time. Moreover in the heel condition, the maximum number of agents on deck 1 reaches a value of approximately 70, whereas a maximum of approximately 50 was reached in the case without motion. This is due to the effect of the perceived force which modifies the agents trajectory increasing the difficulty of exiting from deck 1 through the final exit. In fact, due to the positive heel (i.e. heel to starboard) and due to the specific position of the exit door, agents exiting from deck 1 have to travel upwards.

The situation regarding occupation of stairs is, instead, different. In fact, the maximum staircase capacity is reached both in the heel condition and in the case without ship motion. The maximum number of people inside the stairs is, thus, similar in all conditions, although there is a change in the time scales which is associated to the overall slowing down of the evacuation process. It is finally observed that results in the trim condition, again do not present marked differences with respect to the case without motions. The curves related to the trim condition, indeed, do not modify their general trend, and only a slight increase of the occupation time for each facility (deck or staircase) is observed, which is a consequence of the slowing down of the evacuation process. This effect is due to the reduction of the desired speed through the speed reduction coefficient (see Chapter 7), because in the trim condition the agents are able to apply a control force which fully balances the external actions.

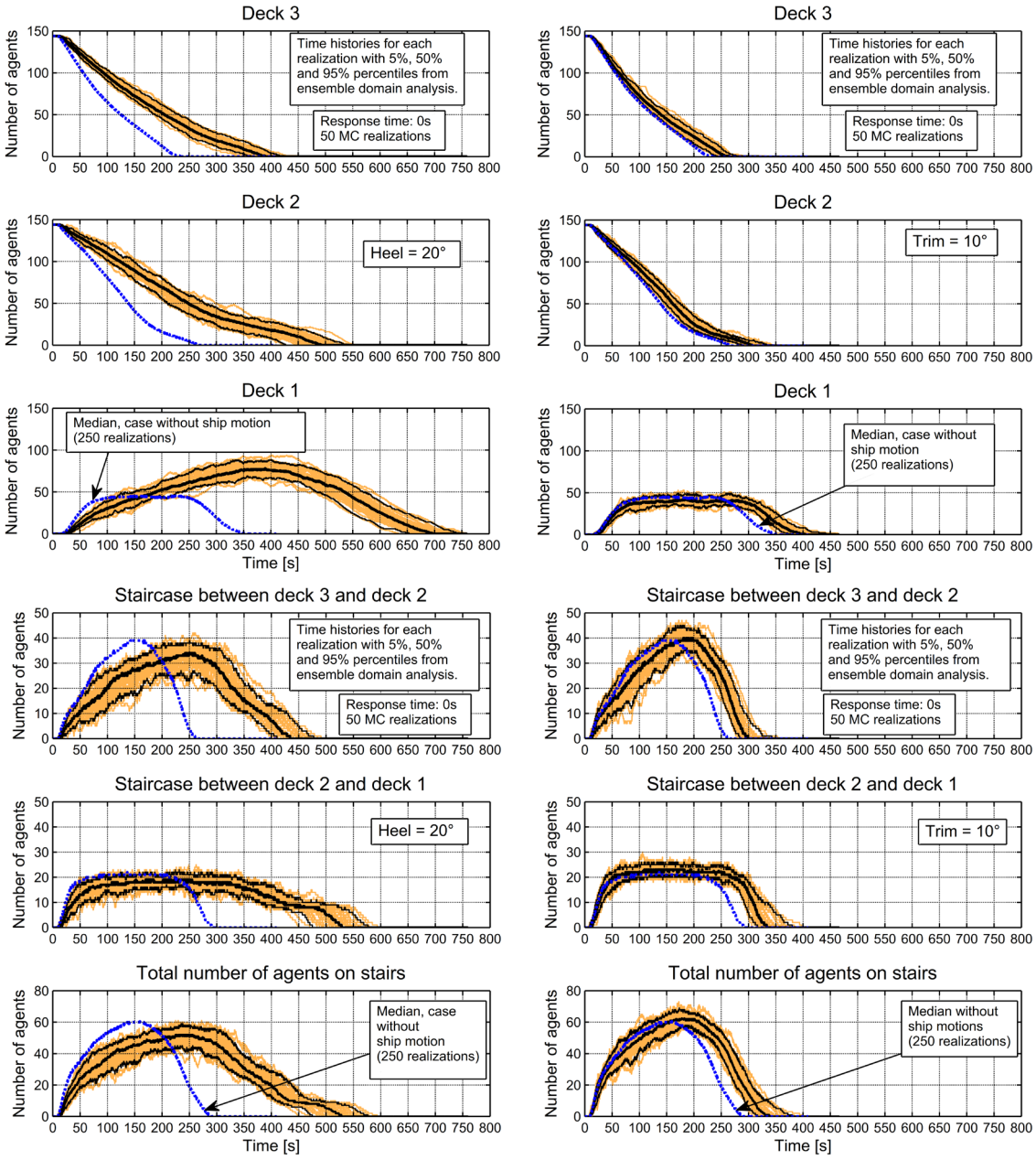

Figure 8.11: Two-cabin-deck test case. Heel condition (left) and trim condition (right). Number of agents on decks (top) and on stairs (bottom). Figures report time histories from each single realization, as well as 5%, 50% and 95% percentiles from ensemble domain analysis at each time instant. The median related to the case without ship motion is also reported, for comparison.

A similar analysis concerning the roll conditions 1 and 2 is reported in Figure 8.12.

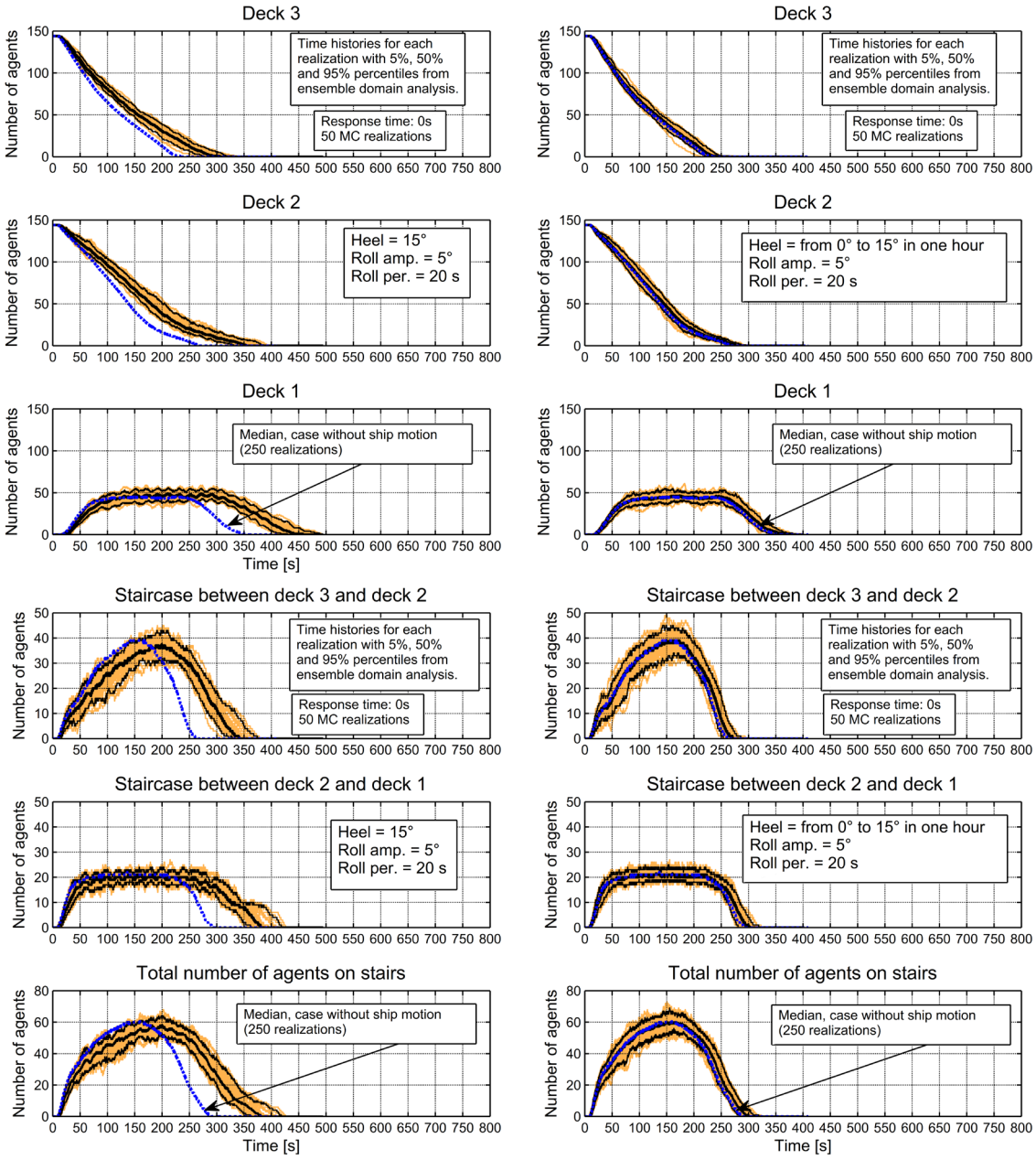

Figure 8.12: Two-cabin-deck test case. Roll condition 1 (left) and roll condition 2 (right). Number of agents on decks (top) and on stairs (bottom). Figures report time histories from each single realization, as well as 5%, 50% and 95% percentiles from ensemble domain analysis at each time instant. The median related to the case without ship motion is also reported, for comparison.

Although it was previously observed that the considered dynamic roll seems to have a slight effect on the total assembly duration, the analysis reported in Figure 8.12 allows to see some effects of the periodic motion. The phase of the periodic motions was the same for all the realizations (see (8.1)) and this leads to periodic oscillations on the instantaneous ensemble domain distributions. Such effects, in Figure 8.12, reflect as well visible oscillations in the median. In particular, it can be observed that in the roll condition 1 (particularly referring to deck 1, staircase 2-1 and total number of agents on stairs) the oscillations of the median are periodic with a period corresponding to the assumed roll period (20 s). Agents move faster when the roll angle is opposite with respect to the heel (i.e. instantaneous roll partially compensate heel), whereas they slow

down as the roll angle sums to the heel angle. Moreover, in roll condition 1, the agents control force cannot fully balance the external force when the roll motion sums to the heel angle, resulting in a modification of agents trajectories which further slows down the evacuation process. This behaviour is, instead, much less marked in the roll condition 2, as in this case the control force balances external forces, hence, agents trajectories are not significantly modified.

Finally the total number of exited agents at each time instant is reported, for each test condition, in Figure 8.13. Data in Figure 8.13 further confirm that the heel condition leads to a very marked effect, while the trim condition has a more limited impact. In the roll condition 1 the periodic behaviour due to dynamic roll motion is quite clearly visible, whereas this effect is not visible in the roll condition 2 where the perceived force balanced by the control forces thanks to limited heel within the simulation time period (heel takes one hour to linearly increase to 15°).

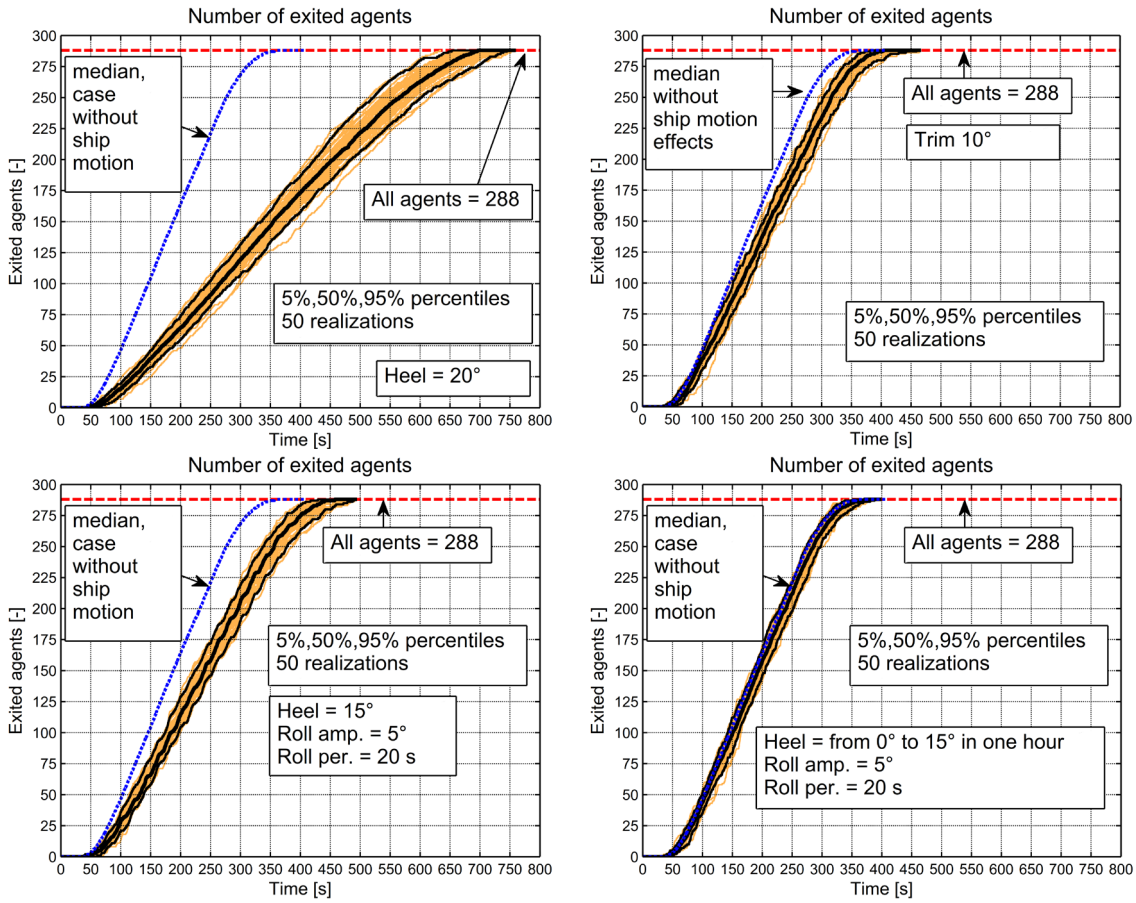

Figure 8.13: Two-cabin-deck test case. Heel condition (top-left), trim condition (top-right), roll condition 1 (bottom-left), roll condition 2 (bottom-right). Number of exited agents as function of time. Figures report time histories from each single realization, as well as 5%, 50% and 95% percentiles from ensemble domain analysis at each time instant. The median related to the case without ship motion is also reported, for comparison.

8.3.2.2 Combined heel and trim scenario

Motion scenarios suggested by Nicholl et al. [158] report a case of "heel or trim", but it appears that the combined effect of heel and trim was not considered. Therefore, for completeness, in the following, an additional condition with 20° of heel and 10° of trim is considered. The condition represents somehow a limit case for the present model. In fact, it was observed from the simulations that not always all agents were able to reach the exit in the maximum time used in the simulations, which was conventionally set to 1800 s (i.e. 30 min). In particular, on a total of 50 Monte Carlo simulations, only in 26 runs all agents were able to reach the exit in the specified simulation time limit of 30 min, corresponding to 50% of the cases.

Figure 8.14 shows the distribution of the total assembly duration (top) and the distribution of the time required to exit for the 99% of all agents (corresponding to 285 agents on a total population of 288 agents).

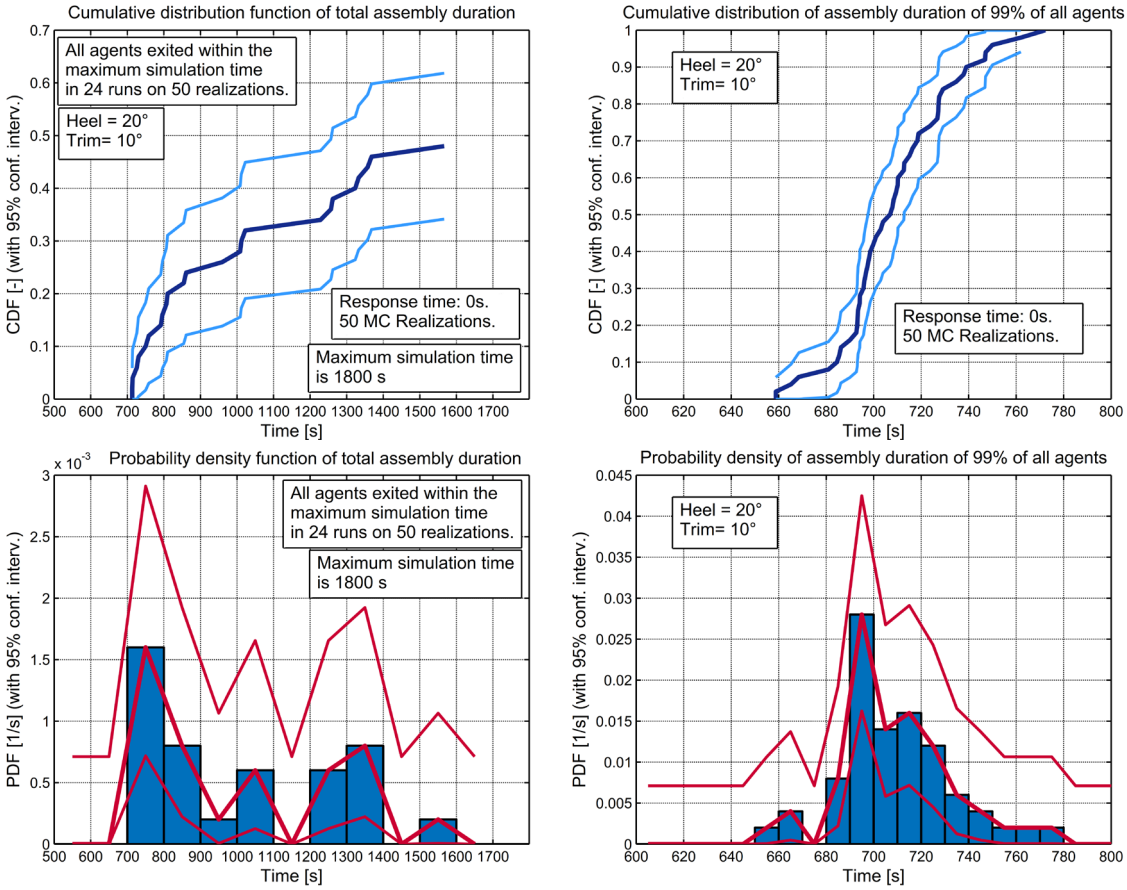

Figure 8.14: Two-cabin- deck test case. Combined heel and trim condition. Estimated cumulative distribution (left) and probability density function (right) of total assembly duration (top) and of assembly duration for 99% of all agents (bottom). Maximum simulation time: 1800 s.

It was observed from the simulations, that in this combined heel and trim condition, the total assembly duration is very significantly affected by the slowest agents. In fact, the slowest agents, in some simulations, were not able to reach the exit in the specified maximum simulation time of 1800 s, this leading to difficulties in the proper definition of PDF and CDF due, to, basically, the censoring effect. When, instead, only 99% of the agents (i.e. 285 agents) are conventionally considered for the determination of the

assembly duration, the slowest 1% of the agents (i.e. 3 agents) are not taken into account and they, therefore, do not affect the results. In all the 50 Monte Carlo realizations, the 99% of the agents was able to reach the exit within 30 min. Compared to the analysis based on all 285 agents, the distribution of assembly duration for the 99% of all agent is smoother, with much shorter tail, and the interquartile range is between 695 s and 725 s.

The analysis of the density at the stair entrance is reported in Figure 8.15. As expectable, the same asymmetry between port and starboard side areas which was observed in the heel condition (see Figure 8.10 and related commenting) is present also in this scenario, and it appears to be more marked. The densities measured in regions 3A and 3B for the present combined heel and trim condition, in particular, tend to be smaller than the corresponding ones measured in the heel condition in Figure 8.10. Moreover, a comparison between Figure 8.15 and results for the heel condition in Figure 8.10 clearly shows the slowing down of the evacuation process induced by the addition of trim to the ship heel.

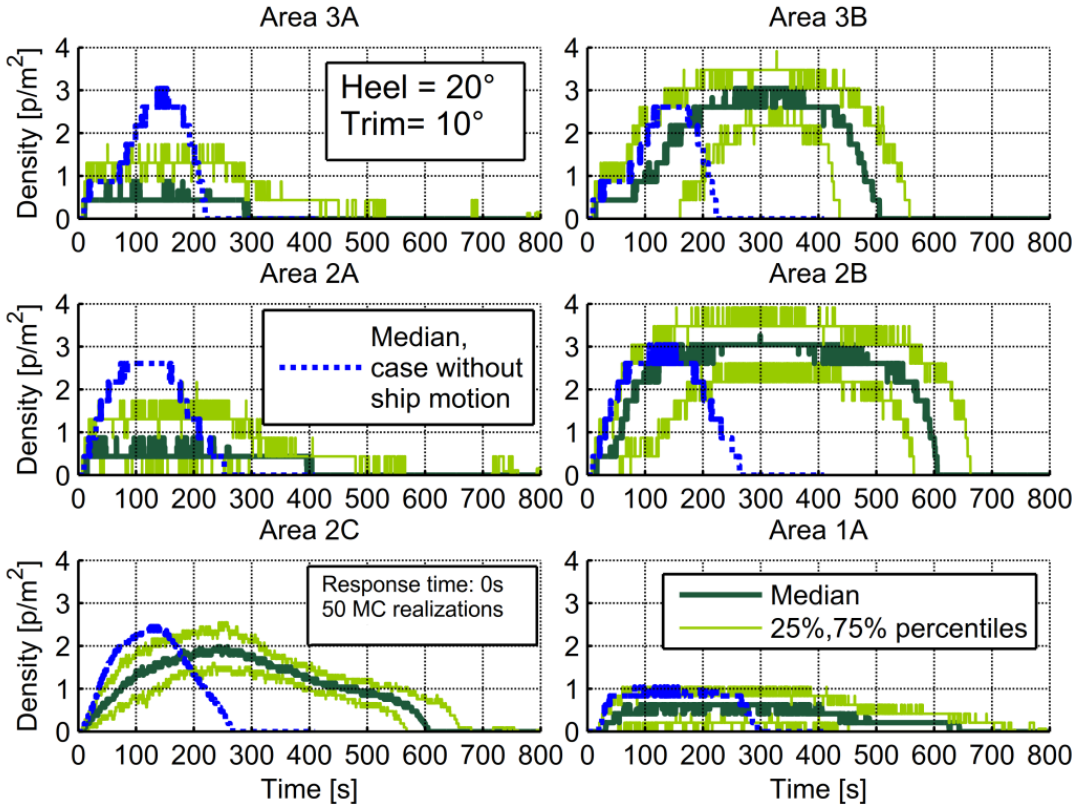

Figure 8.15: Two-cabin-deck test case. Combined heel and trim condition. Density inside each area in front of the stairs. The curves report the ensemble 25%, 50% and 75% percentiles for each time instant. Total number of Monte Carlo realizations: 50. The median of the case without ship motion is also reported, for comparison.

The number of agents on decks and stairs, for each time instant, is reported in Figure 8.16:

Considering the decks, the trend of curves is similar to the heel condition as reported in Figure 8.11, but some differences can be observed. First, in case of heel and trim condition, the time to completely evacuate deck 2 and deck 3 clearly increases compared to the condition without trim. The increase in the evacuation time appears to be associated with a marked reduction of the egress rate in the final part of the evacuation process from each deck. The increase of time for completely evacuating deck 1 (and, thus, to complete the evacuation) is, instead, more limited. At the same time, however, the peak of number of agents which are, at the same time, on deck 1, is smaller for the combined heel and trim condition compared to the condition where only heel is present. This may be a consequence of the overall slow down of the evacuation process from the decks 2 and 3.

Some clear differences are appreciable, between the heel and trim condition (Figure 1.16) and the heel condition (Figure 8.11), when considering the stairs. In the initial part of the evacuation process, the behaviour of number of agents in the various staircases is qualitatively similar for the two conditions, although larger values (and thus larger densities) together with a tendency towards a delaying of the process are observed in the heel and trim condition. However, in the final part of the evacuation the behaviour between the two conditions is markedly different. In fact, in the heel and trim condition, quite long time intervals are visible where the number of agents has a reduced decreasing rate (for staircase 3-2 approximately in the time interval [390 s,500 s]) or is almost constant (for staircase 2-1 approximately in the time interval [450 s,600 s]). This behaviour can be noticed also in the heel condition, but it is much less marked compared to the heel and trim case: it can be barely noticed in the staircase 3-2, while it is more visible when referring to the staircase 2-1. The snapshots provided in Figure 8.17 clarify the cause of this observed behaviour.

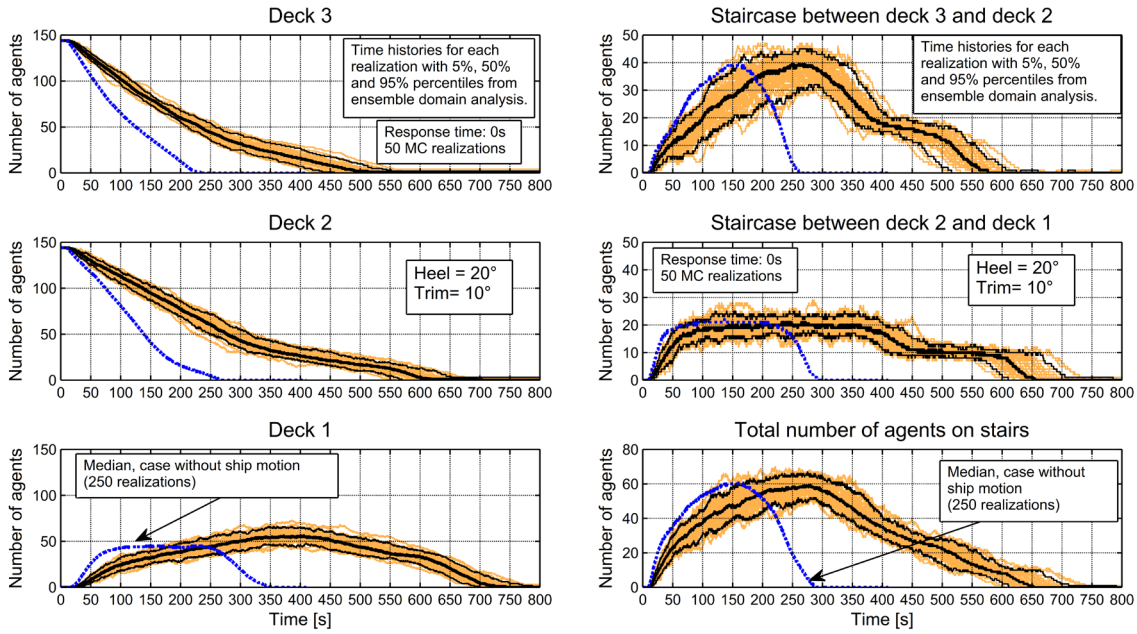

Figure 8.16: Two-cabin-deck test case. Combined heel and trim condition. Number of agents on decks (left) and on stairs (right). Figures report time histories from each single realization, as well as 5%, 50% and 95% percentiles from ensemble domain analysis at each time instant. The median related to the case without ship motion is also reported, for comparison.

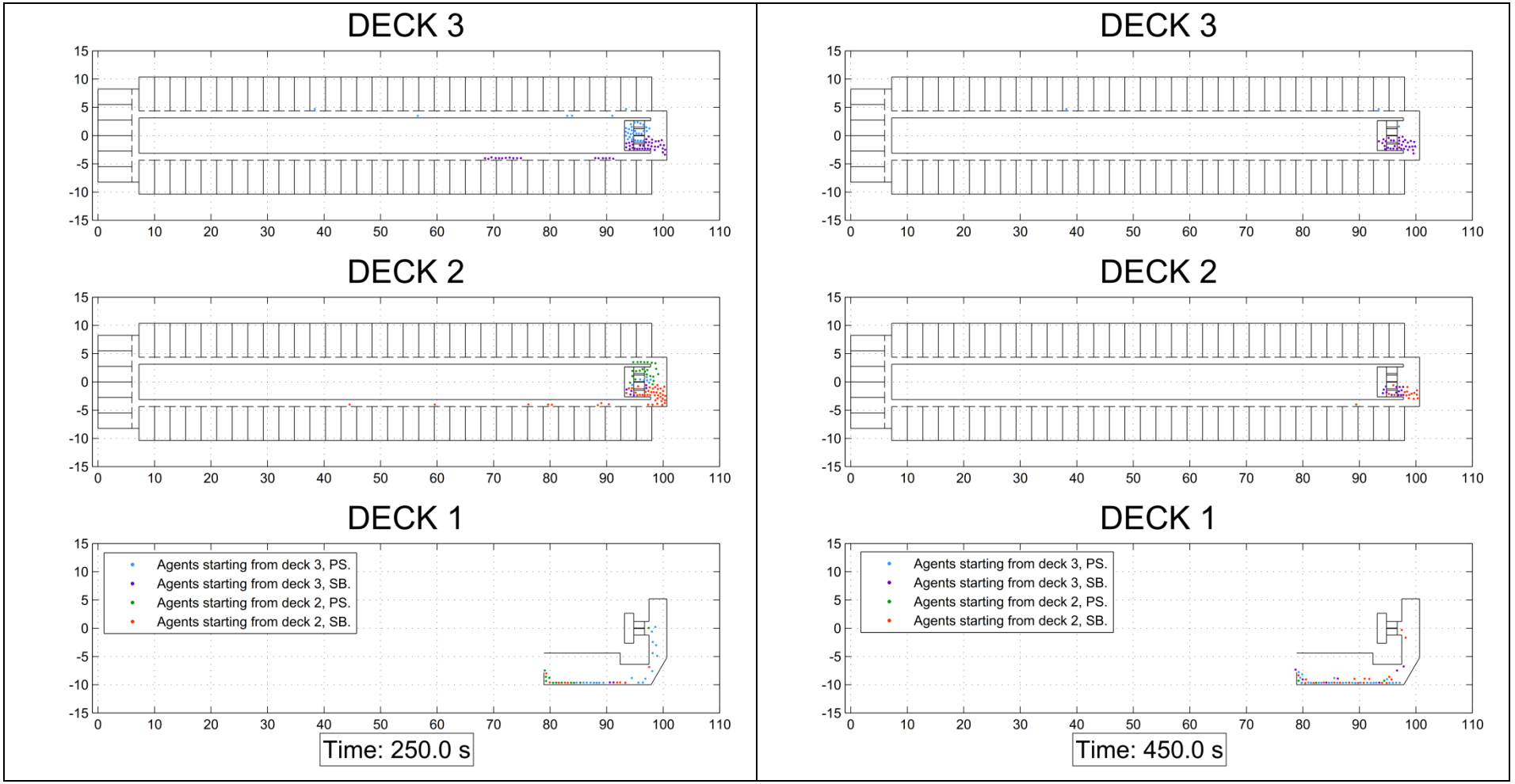

Figure 8.17: Two-cabin-deck test case. Combined heel and trim condition. Figures report snapshots of one of the realizations at 250 s (left) and at 450 s (right).

The observed phenomenon is due to the difficulty of agents coming from starboard to enter staircases due to the perceived force. The portside staircase is, hence, used more easily and rapidly with respect to the starboard one. As a result, the portside staircase is emptied after around 400 s, however the agents directed to the starboard staircase do not modify their target. The routing model, indeed does not implement a re-routing strategy capable of considering the density at the entrance of one facility in the choice of the route to follow. As a result the agents continue trying entering the more crowded starboard staircase although the portside staircase is empty. This, eventually, leads to the dropping of the number of agents to approximately half, as agents are basically using half of the staircase (see Figure 8.17).

The number of exited agents for the combined heel and trim condition is finally reported in Figure 8.18. It is observed that there is a significant reduction of the evacuation rate compared to the condition without ship motions. The exit rate in case for the combined heel and trim condition tend to be smaller with respect to the heel condition and to the trim condition, i.e. when heel and trim are considered separately (compare Figure 8.18 with Figure 8.13).

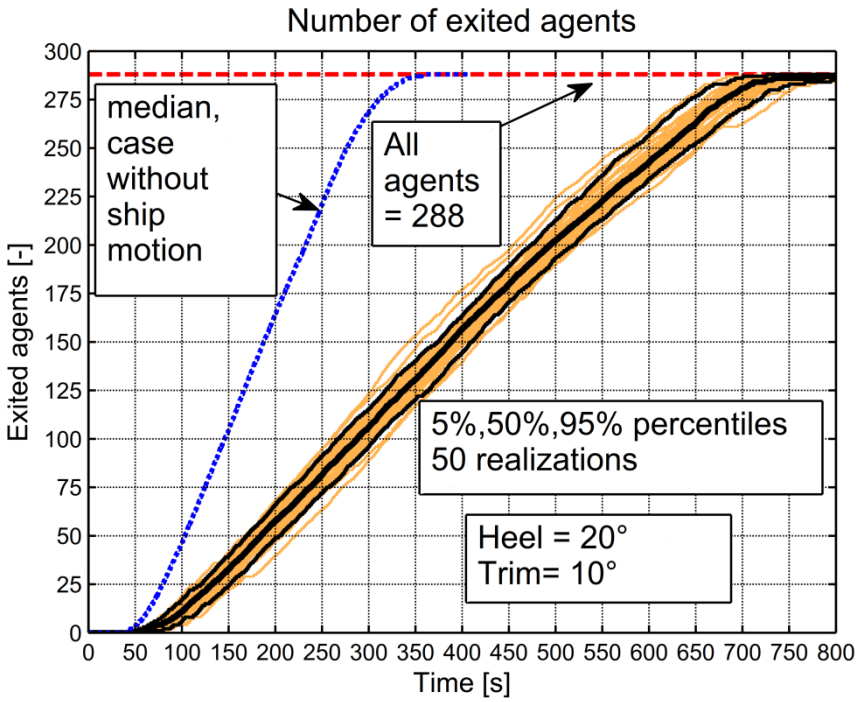

Figure 8.18: Two-cabin-deck test case. Combined heel and trim condition. Number of exited agents as function of time. The figure reports time histories from each single realization, as well as 5%, 50% and 95% percentiles from ensemble domain analysis at each time instant. The median related to the case without ship motion is also reported, for comparison.

8.4 Results using simulated motions for a cruise vessel

This section addresses the implementation, and the analysis of the corresponding evacuation results, of the two-cabin-deck test case considering more realistic conditions of motions.

Ship motions have been computed for a notational cruise vessel whose main dimensions have been chosen in order to be consistent with the cruise vessel considered in the SAFEGUARD Validation Data Set 2 SGVDS2 ([54]), from which the herein presented two-cabin-deck test case was derived.

The vessel considered for the calculations is carefully described in the present section. Moreover, the adopted modelling approach for the simulation of the dynamic motion of the ship, based on linear seakeeping, is presented. The environmental conditions considered for the test case, characterised by long-crested irregular beam waves, are described. The methodologies adopted to generate the ship motions from the linear seakeeping transfer functions and the assumptions used to apply such motions to the evacuation simulations are also clarified and discussed. Finally, the results obtained from evacuation simulations are presented and commented.

8.4.1 Description of the vessel

In order to obtain evacuation simulation results in more realistic motion conditions compared to those in notional, standard, motions as described in the previous sections, a sample vessel has been considered for which ship motions have been simulated and considered as input for the evacuation simulation tool.

The considered vessel is a notional cruise vessel, which will be herein referred to as CRV270. The main particulars of CRV270, in the considered loading condition, are reported in Table 8.2, while a representative set of transversal sections is shown in Figure 8.19. The vessel is assumed to be equipped with bilge keels, placed half forward and half aft of the anti-rolling fins, and the main characteristics of the bilge keels are reported in Table 8.3.

The CRV270 is a panamax cruise vessel which can be considered to be representative of cruise vessels having a gross tonnage up to about the order of 90000 GT. Although passengers and crew capacity vary significantly depending on the specific vessel business model, cruise vessels with hull form of dimensions similar to the CRV270 could accommodate indicatively up to about 2500 passengers, with a total number of people onboard (passengers and crew) of up to about 3350. Globally, the main dimensions of the sample vessel CRV270 have been chosen in order to be consistent with the SAFEGUARD information (Galea et al. [54], [186]) from which the considered simplified two-cabin-deck test case has been derived.

The draught and the metacentric height of the selected loading condition have been chosen taking into account typical operational values for cruise vessels. The yaw and pitch dry radii of inertia have been set to standard values (e.g. [91], [92]). Regarding the roll dry radius of inertia, cruise vessels are characterised by larger superstructures compared to standard vessels, which leads to large radii. Therefore, a relative large

value of k_{xx}/B has been used for CRV270, which is in line with the indications from Papanikolaou [166] and with the data from Matusiak and Hamberg [133]. The natural roll period reported in Table 8.2 was determined using data from linear hydrodynamic strip theory calculations, taking into account the coupling with yaw and sway.

The geometry of the two-cabin-deck test case is assumed to be positioned, on the vessel, in a way which is approximately in line with the SAFEGUARD Validation Data Set SGVDS2 ([54]). In particular, the geometry is assumed to be positioned as reported in Figure 8.1, with deck 1 placed at a height of 23 m from the ship baseline. Conventionally, herein, for sake of simplicity, the aft end of the test geometry has been assumed to coincide with the aft perpendicular. Although in a real vessel there would be a shift aft in order to have the balconies coinciding with the extreme end of the vessel, the effect of such a shift, for the calculations presented herein, is deemed to be minimal.

Table 8.2: CRV270. Main particulars in the considered loading condition.

Length between perpendiculars	L_{BP}	[m]	270
Breadth at waterline	B	[m]	32.2
Draught	T	[m]	8.0
Block coefficient (based on L_{BP})	C_B	[-]	0.716
Longitudinal prismatic coefficient (based on L_{BP})	C_P	[-]	0.731
Vertical position of centre of gravity above baseline	$\overline{KG}$	[m]	14.545
Transversal metacentric height	$\overline{GM}$	[m]	2.500
Dimensionless dry roll radius of inertia w.r.t. CoG	k_{xx}/B	[-]	0.45
Dimensionless dry pitch radius of inertia w.r.t. CoG	k_{yy}/L_{BP}	[-]	0.25
Dimensionless dry yaw radius of inertia w.r.t. CoG	k_{zz}/L_{BP}	[-]	0.25
Roll natural period	T_{roll}	[s]	20.2

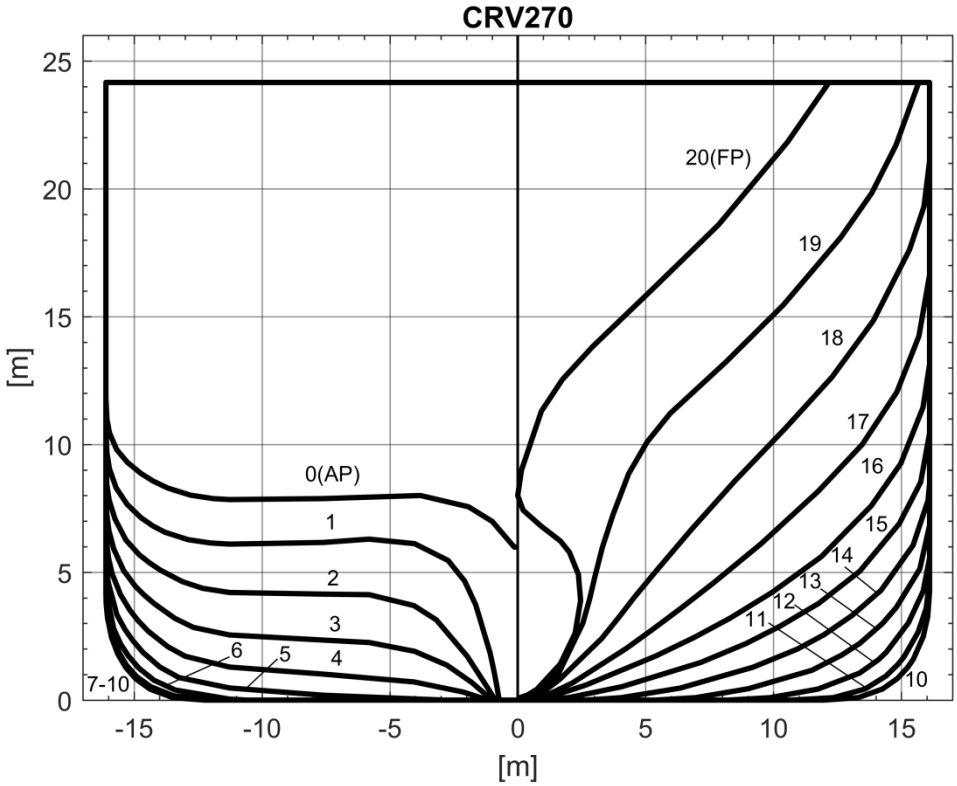

Figure 8.19: CRV270. Transversal sections.

Table 8.3: CRV270. Main data of bilge keels.

Total length	l_{bk}	[m]	86.4
Span	b_{bk}	[m]	0.800

8.4.2 Ship dynamical model

In order to provide ship motions for the use in the evacuation simulation reported hereinafter, some simplification assumptions have been used, bearing in mind that the scope of the present study is mostly to assess the effect of ship motions on the evacuation process rather than an accurate simulation of ship motions, which is, by itself, a subject of continuous research efforts, particularly when nonlinearities are important (e.g. [3]).

Motions of CRV270 have been simulated in intact condition. While it is known that evacuations occur also in damaged ship condition, herein it has been decided to concentrate on the intact case, which can be considered to be relevant to evacuation following, for instance, the spreading of a fire onboard. In particular, ship motion dynamics has been based on a linear approach, and the possible presence of asymmetric heeling, e.g. due to wind, has been taken into account in a simplified way by superimposing a mean roll angle to motions generated from response amplitude operators obtained from linear seakeeping calculations. Moreover, it is assumed that the

vessel is at zero speed and, for the simulations reported hereinafter in §8.4.7, only the beam sea condition will be considered. However, in the application of motions to the actual evacuation simulations, the linearly simulated state vector for the six ship degrees of freedom will be interpreted as appropriate corresponding nonlinear motions. Although this is a stretching of the application of linear theory, this is a step which allows a more direct coupling between the ship motion generator and the evacuation simulation tool. How this has been accomplished will be later explained §8.4.6.

The linear equations of motion, considering harmonic forcing, are therefore written as follows:

$$\left(\mathbf{M}+\mathbf{A}(\omega)\right)\cdot\ddot{\mathbf{x}}(\omega,\beta)+\left(\mathbf{B}(\omega)+\mathbf{B}_{\mathbf{add}}\right)\cdot\dot{\mathbf{x}}(\omega,\beta)+\mathbf{C}\cdot\mathbf{x}(\omega,\beta)=\mathbf{F}(\omega,\beta) \tag{8.2}$$

The above equations are written, in general, with respect to a generic point O, not necessarily coinciding with the ship centre of gravity. $\mathbf{M}$ is the 6x6 mass matrix, $\mathbf{A}(\omega)$ and $\mathbf{B}(\omega)$ are the 6x6 frequency (ω) dependent added mass matrix and damping matrix, respectively, $\mathbf{C}$ is the 6x6 restoring matrix. $\mathbf{F}(\omega,\beta)$ is the 6x1 vector of generalised forces, which depends on both the frequency and the wave angle of encounter β (0 deg: following waves, 90 deg: waves from starboard, 180 deg: head waves, 270 deg: waves from portside). The vector $\mathbf{x}(\omega,\beta)$ is the frequency and wave-angle-of-encounter dependent 6x1 response vector, and $\dot{\mathbf{x}}(\omega,\beta)$ and $\ddot{\mathbf{x}}(\omega,\beta)$ are its corresponding first (velocity) and second (acceleration) time derivatives. The matrix $\mathbf{B}_{\mathbf{add}}$ is an additional constant damping matrix which is primarily meant to take into account viscous effects on roll damping as described in the following §8.4.3. Since, as anticipated, calculations reported herein will be carried out at zero speed, the dependence on speed of the relevant terms in (8.2) has been omitted for the sake of simplicity of notation.

The solution of (8.2) is then carried out in frequency domain in the standard way as follows:

$$\begin{cases}\mathbf{x}(\omega,\beta)=\hat{\mathbf{H}}(\omega,\beta)\cdot e^{-j\omega t}\\ \mathbf{F}(\omega,\beta)=\hat{\mathbf{F}}(\omega,\beta)\cdot e^{-j\omega t}\end{cases}\Rightarrow$$
$$\hat{\mathbf{H}}(\omega,\beta)=\left(\mathbf{C}-\omega^2\cdot\left(\mathbf{M}+\mathbf{A}(\omega)\right)-j\omega\left(\mathbf{B}(\omega)+\mathbf{B}_{\mathbf{add}}\right)\right)^{-1}\cdot\hat{\mathbf{F}}(\omega,\beta) \tag{8.3}$$

where $\hat{\mathbf{H}}(\omega,\beta)$ is the 6x1 vector of complex amplitudes of the response at frequency ω when the wave encounter angle is β, and where it is implicitly considered that only the real part of $\mathbf{x}(\omega,\beta)$ is eventually retained.

Hydrodynamic coefficients and forces are herein calculated using an in-house code ([20]) based on the STF strip-theory approach (Salvesen et al. [187]). The solution of the hydrodynamic problem uses an extension of the Frank close-fit method (Frank [50])

in order to properly deal, if/when necessary, with sections characterised by multiple disconnected pieces below water, and irregular frequencies in the computational frequency range are removed by introducing lid panels. All calculations are carried out considering infinite water depth.

8.4.3 Tuning of additional roll damping

In order to take into account, in a simplified way, viscous effects on roll damping, an additional frequency independent damping term $B_{44,add}$ has been introduced in the roll degree of freedom in the matrix $\mathbf{B}(\omega)$ (element (4,4)). The determination of $B_{44,add}$ has been carried out through the following process.

At first, in absence of experimental data for the considered notional vessel, the equivalent dimensionless linear equivalent roll damping at a conventional reference rolling amplitude of 10 deg has been determined using the simplified Ikeda's method ([100], [101]), leading to figures as reported in Table 8.4. It is noted that, presently, the simplified Ikeda's method for the estimation of roll damping is basically the approach suggested for application in the framework of Second Generation Intact Stability Criteria (see SDC 4/5/1/Add.1 [194]).

Table 8.4: CRV270. Linear equivalent roll damping from Simplified Ikeda's Method.

Reference rolling amplitude	A	[deg]	10
Reference roll frequency	ω_{roll}	[rad/s]	0.311
Ship speed	V	[m/s]	0.0
Dimensionless linear equivalent roll damping	ν_{eq}	[-]	0.051

A tuning process has then been setup, where $B_{44,add}$ was systematically modified, until the equations of motion (8.2), in their homogeneous form without the forcing term $\mathbf{F}(\omega,\beta)$, were showing an eigenvalue associated to roll decay at ω_{roll} with a real part such to match the required target damping. Basically, the following eigenvalue/eigenvector problem was solved for different values of $B_{44,add}$:

$$\begin{cases} \left(\mathbf{M}+\mathbf{A}(\omega_{roll})\right)\cdot\ddot{\mathbf{x}}+\left(\mathbf{B}(\omega_{roll})+\mathbf{B}_{\mathbf{add}}\right)\cdot\dot{\mathbf{x}}+\mathbf{C}\cdot\mathbf{x}=\mathbf{0} \\ \mathbf{x}(\omega_{roll})=\mathbf{q}\cdot e^{\lambda t} \\ \text{with}\ \ \lambda=\lambda(\mathbf{B}_{\mathbf{add}})\in\mathbb{C} \\ (\mathbf{B}_{\mathbf{add}})_{i,j}=\begin{cases} B_{44,add} & \text{for}\ \ (i,j)=(4,4) \\ 0 & \text{otherwise} \end{cases} \end{cases} \tag{8.4}$$

The proper eigenvalue $\lambda(\mathbf{B}_{\mathbf{add}})$ associated to roll decay was identified among the eigenvalues of the system, and the corresponding dimensionless linear damping coefficient was estimated as

$$\nu_{44}\left(\mathbf{B}_{\mathbf{add}}\right)=-\frac{\mathrm{Re}\left\{\lambda\left(\mathbf{B}_{\mathbf{add}}\right)\right\}}{\left\|\lambda\left(\mathbf{B}_{\mathbf{add}}\right)\right\|} \tag{8.5}$$

where $\mathrm{Re}\left\{\lambda\left(\mathbf{B}_{\mathbf{add}}\right)\right\}$ and $\left\|\lambda\left(\mathbf{B}_{\mathbf{add}}\right)\right\|$ are, respectively, the real part and the modulus of the complex eigenvalue $\lambda\left(\mathbf{B}_{\mathbf{add}}\right)$.

From a numerical point of view, the actual eigenvalues problem (8.4) is not directly solved. Instead, first, the system is transformed from a second order 6x6 system to a first order 12x12 system as follows:

$$\begin{cases}\begin{bmatrix}\mathbf{1} & \mathbf{0}\\ \mathbf{0} & \mathbf{M}+\mathbf{A}\left(\omega_{roll}\right)\end{bmatrix}\cdot\dot{\mathbf{y}}+\begin{bmatrix}\mathbf{0} & -\mathbf{1}\\ \mathbf{C} & \mathbf{B}\left(\omega_{roll}\right)+\mathbf{B}_{\mathbf{add}}\end{bmatrix}\cdot\mathbf{y}=\mathbf{0}\\ \mathbf{y}=\begin{bmatrix}\mathbf{x}\\ \dot{\mathbf{x}}\end{bmatrix}\end{cases} \tag{8.6}$$

and then the corresponding following generalised eigenvalue problem is numerically solved:

$$\mathbf{y}=\begin{bmatrix}\mathbf{x}\\ \dot{\mathbf{x}}\end{bmatrix}=\mathbf{q}_y\cdot e^{\lambda t}\Rightarrow\begin{bmatrix}\mathbf{0} & -\mathbf{1}\\ \mathbf{C} & \mathbf{B}\left(\omega_{roll}\right)+\mathbf{B}_{\mathbf{add}}\end{bmatrix}\cdot\mathbf{q}_y=\lambda\cdot\begin{bmatrix}-\mathbf{1} & \mathbf{0}\\ \mathbf{0} & -\left(\mathbf{M}+\mathbf{A}\left(\omega_{roll}\right)\right)\end{bmatrix}\cdot\mathbf{q}_y \tag{8.7}$$

Strictly speaking, this procedure is not theoretically fully correct due to the frequency dependence of added mass and damping matrices. In fact, in a transient situation as it is a decay, the equations of motion to be considered should be those based on convolution integrals ([30]) with a corresponding time domain solution, and not those based on constant, although frequency dependent, added mass and damping matrices, with solution in frequency domain. As a result, the reported procedure is to be considered as an approximate one. However, for the case of roll motion, the described procedure, although approximate, is much more easily applicable than the corresponding one based on the transformation of motion equations to time domain ones, and it still leads to an accurate enough tuning of the additional roll damping coefficient $B_{44,add}$.

It also important to note that the value of the additional roll damping coefficient $B_{44,add}$ depends on the reference point which is used for the specification of the equations of motion (8.2). Herein, equations of motion are specified with respect to a point O which is on the waterplane, at a longitudinal coordinate corresponding to the mid perpendicular, and on the ship centreplane. This means that the coordinates of the reference point are $O=\left(135\,m,0\,m,8\,m\right)$ in the geometrical ship-fixed reference system with origin at the intersection between the aft perpendicular and the keel line of the vessel.

The dependence of the dimensionless linear roll damping coefficient ν_{44} on the additional linear damping coefficient $B_{44,add}$ is shown in Figure 8.20, while the final tuned value of $B_{44,add}$ is reported in Table 8.5.

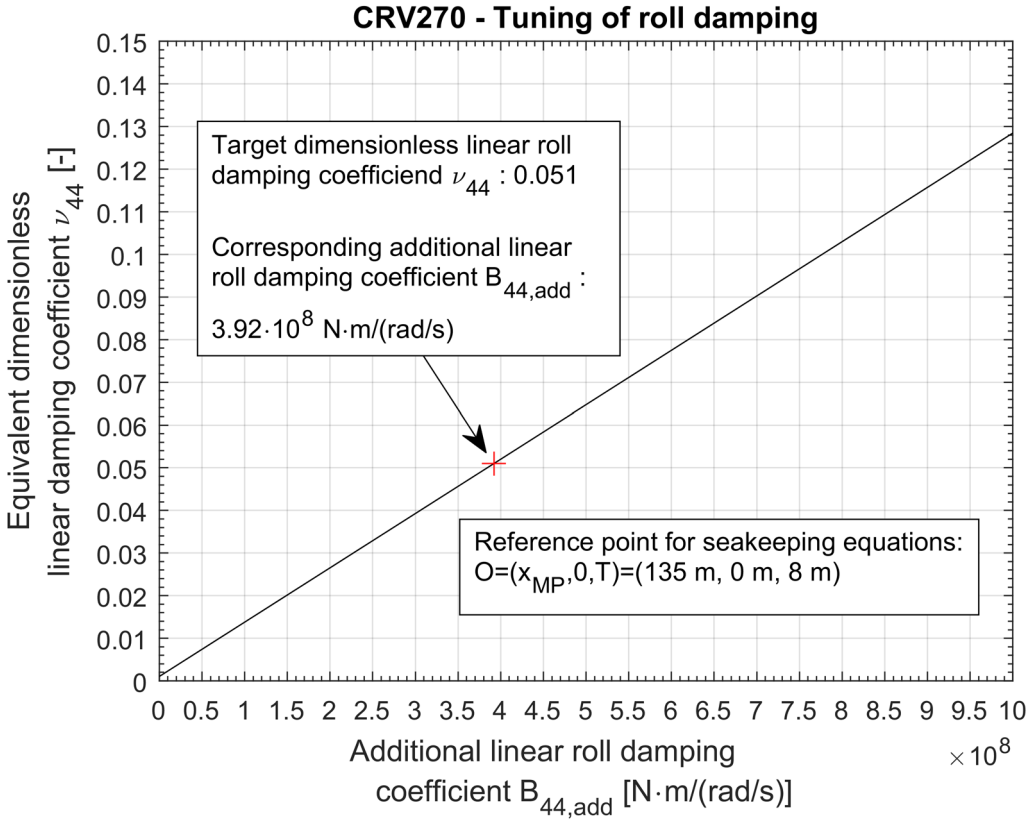

Figure 8.20: CRV270. Dependence of dimensionless linear roll damping coefficient ν_{44} on additional linear roll damping coefficient $B_{44,add}$.

Table 8.5: CRV270. Target dimensionless linear roll damping coefficient ν_{44} and corresponding additional linear roll damping coefficient $B_{44,add}$. Reference point for seakeeping equations: $O = (135\ m, 0\ m, 8\ m)$.

ν_{44}	[-]	0.051
$B_{44,add}$	$[N \cdot m / (rad / s)]$	$3.92 \cdot 10^8$

8.4.4 Response amplitude operators

Response amplitude operators (RAOs) have been calculated for CRV270 at zero speed in the considered loading conditions. Results of the calculations are herein reported for two points on the vessel:

- The point amidships, on the centreplane and on the waterplane, $O=(135\,m, 0\,m, 8\,m)$, which is the reference point used for hydrodynamic calculations;
- A point $P_E=(97\,m, 0\,m, 27.2\,m)$ which is placed close to the entrance/exit of stairs on the deck 2 of the test geometry (see Figure 8.1, Figure 8.2, Figure 8.3) and 0.9 m above the deck level, which corresponds to the vertical position which is used for the calculation of forces induced on agents due to ship motions (see section 7.2.1). RAOs at this point are intended to be representative of motions perceived by agents which are evacuating through the staircase of the considered test case.

Response amplitude operators for point O are shown in Figure 8.21 (surge, heave and pitch) and in Figure 8.22 (sway, roll and yaw). Translational motions are normalised by the wave amplitude, while angular motions are normalised by the wave slope. In order to give a global picture of the ship response to incoming waves, RAOs are reported as a function of both the wave heading β and the frequency. Regarding the heading, considering the port/starboard symmetry of the vessel, results are reported only for waves coming from starboard ($\beta \in [0°, 180°]$). However, as described later, evacuations simulations in presence of ship motions will be carried out considering long-crested irregular beam waves from starboard, i.e. $\beta = 90°$ (see §8.4.5, §8.4.7). Therefore, Figure 8.23 shows the RAOs of the dominant motions (heave, sway and roll) for this specific wave heading.

A similar set of information as that reported for the point O, is provided also for point P_E in Figure 8.24 (RAOs of surge, heave and pitch), Figure 8.25 (RAOs of sway, roll and yaw) and Figure 8.26 (RAOs of sway, heave and roll for $\beta = 90°$). Of course, RAOs of rotational motion do not depend on the analysis point, and therefore they are the same for point O and point P_E. Instead, translational motions are affected by the reference point and differences can be observed, which are most evident for the sway (lateral) motion. If we focus on the case of beam waves (compare Figure 8.23 and Figure 8.26), it can be noticed that the increase of vertical position above the baseline between O ($z = 8\,m$) and P_E ($z = 27.2\,m$) leads to a significant increase of peak sway motion. Such behaviour is induced by the effect of roll motion which leads to a peak of the sway RAO which increases from about 1.17 for O to about 1.50 for P_E. Moreover, a frequency shift can also be observed regarding the position of the peak of sway RAO, which is at a frequency slightly below the peak frequency for the roll RAO in case of point O, and at a frequency slightly above the peak frequency for the roll RAO in case of point P_E. It is also worth noting that, when the reference point is changed, not only the behaviour of the sway RAO magnitude changes close to the roll RAO peak frequency, but also the phase changes substantially, although in a relatively narrow frequency band.

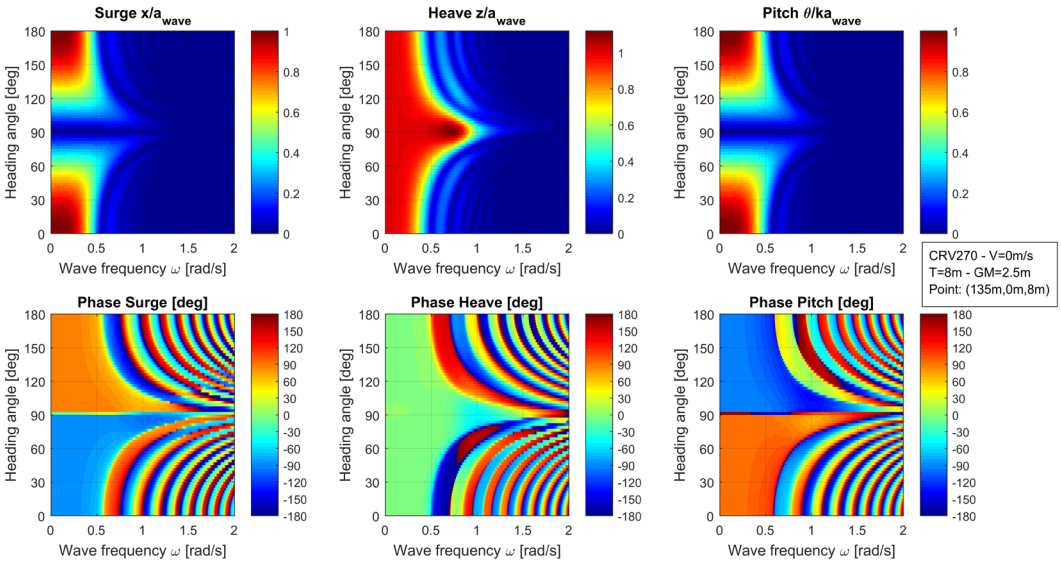

Figure 8.21: CRV270. RAOs (top row: amplitude, bottom row: phase) of surge, heave and pitch, as functions of wave heading and wave frequency. Point: $O = (135\ m, 0\ m, 8\ m)$.

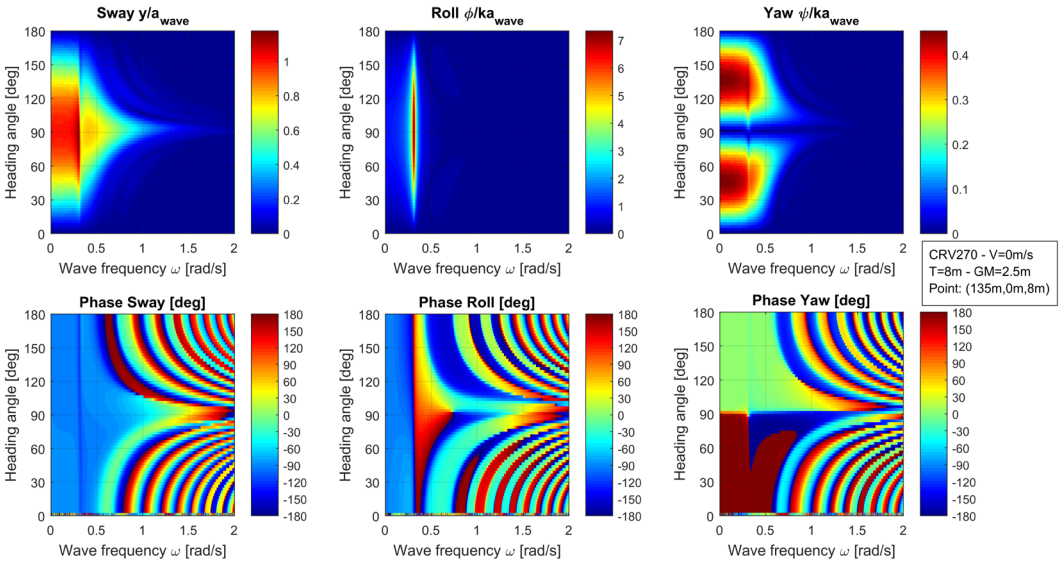

Figure 8.22: CRV270. RAOs (top row: amplitude, bottom row: phase) of sway, roll and yaw, as functions of wave heading and wave frequency. Point: $O = (135\ m, 0\ m, 8\ m)$.

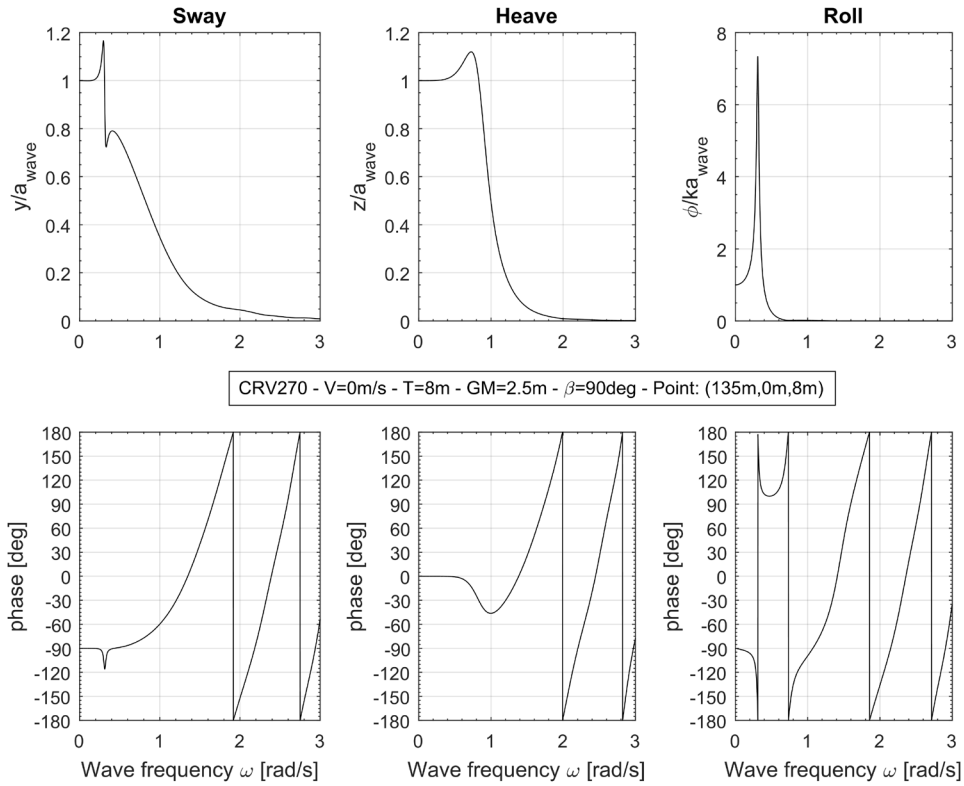

Figure 8.23: CRV270. RAOs (top row: amplitude, bottom row: phase) of sway, heave and roll as functions of wave frequency, for beam waves coming from starboard ($\beta = 90°$). Point: $O = (135\ m, 0\ m, 8\ m)$.

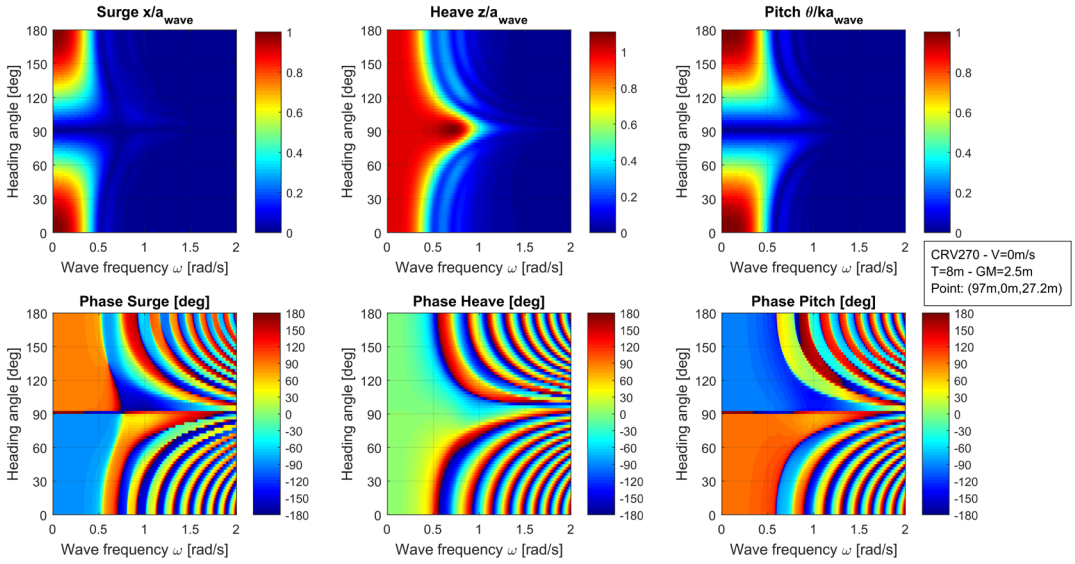

Figure 8.24: CRV270. RAOs (top row: amplitude, bottom row: phase) of surge, heave and pitch, as functions of wave heading and wave frequency. Point: $P_E = (97\ m, 0\ m, 27.2\ m)$.

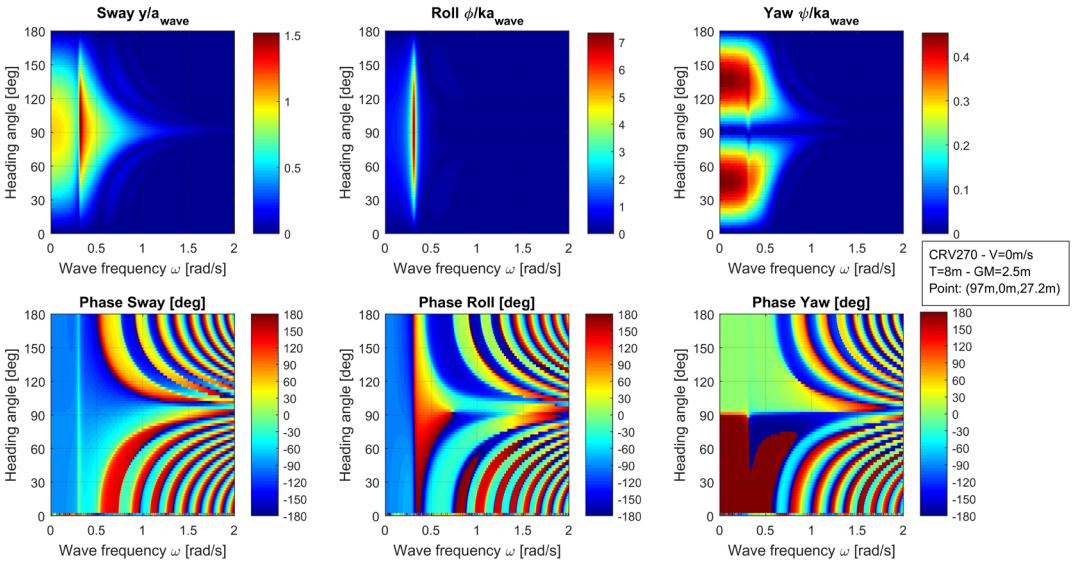

Figure 8.25: CRV270. RAOs (top row: amplitude, bottom row: phase) of sway, roll and yaw, as functions of wave heading and wave frequency. Point: $P_E = (97\ m, 0\ m, 27.2\ m)$.

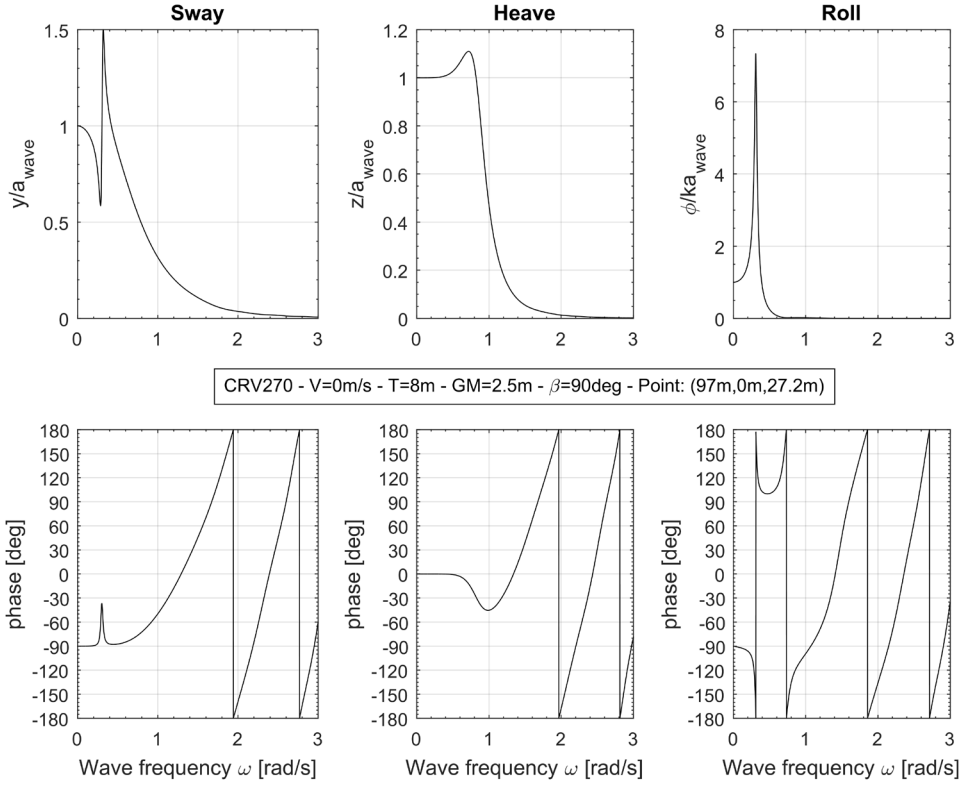

Figure 8.26: CRV270. RAOs (top row: amplitude, bottom row: phase) of sway, heave and roll, as functions of wave frequency, for beam waves coming from starboard ($\beta = 90°$). Point: $P_E = (97\ m, 0\ m, 27.2\ m)$.

8.4.5 Environmental conditions

The environmental conditions used for the study are characterised by long-crested irregular waves, having a JONSWAP spectrum $S_w(\omega)$ $[m^2/(rad/s)]$ as follows:

$$\begin{cases} S_w(\omega) = \dfrac{n_c}{\omega_p} \cdot \left(\dfrac{\omega_p}{\omega}\right)^5 \cdot \exp\left(-\dfrac{5}{4} \cdot \left(\dfrac{\omega_p}{\omega}\right)^4\right) \cdot \gamma^{\exp\left(-\frac{1}{2\cdot\sigma^2}\cdot\left(\frac{\omega-\omega_p}{\omega_p}\right)^2\right)} \\ \text{with} \\ \sigma = \begin{cases} 0.07 & \text{if } \omega \le \omega_p \\ 0.09 & \text{if } \omega > \omega_p \end{cases} \\ \text{and with constant } n_c \text{ such that:} \\ H_s = 4 \cdot \sqrt{\int_0^\infty S_w(\omega)\, d\omega} \end{cases} \tag{8.8}$$

The overshoot coefficient has been fixed to the standard value $\gamma = 3.3$ and the spectral peak frequency ω_p was taken to correspond to a period $T_p = 20.2\,s$, i.e. to the ship roll natural period (see Table 8.2). Starting from the calm water condition ($H_s = 0\,m$), the significant wave height considered in the study was progressively increased up to 12 m. An example sea spectrum for the case of unitary significant wave height $H_s = 1\,m$ is shown in Figure 8.27.

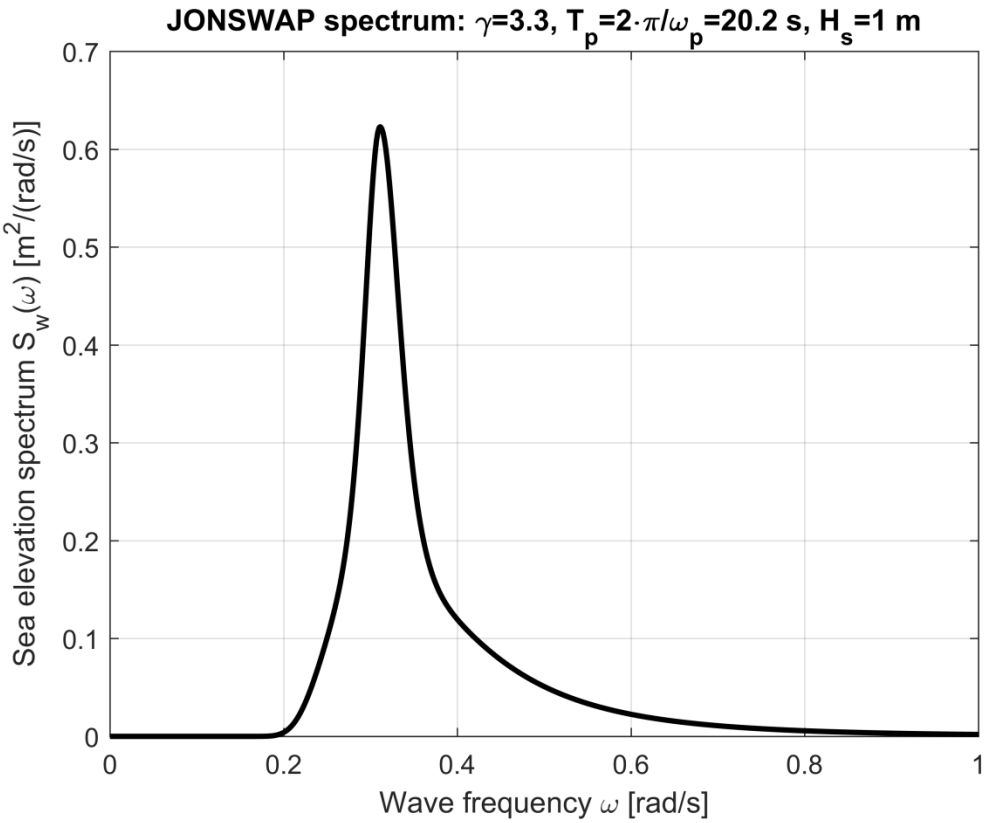

Figure 8.27: JONSWAP sea elevation spectrum considered in the present study, for unitary significant wave height.

A beam sea condition ($\beta = 90°$) was chosen for the simulations. This scenario was selected since it is the typical nominal scenario which is considered in case of dead-ship condition (e.g. SDC 4/5/1/Add.3 [195]), and it is expectable that a vessel which is to be evacuated could have lost her power, and she is therefore in dead-ship condition in accordance with the definition in SOLAS II-1/A/3/8 ([87]), or she is, in any case, at zero speed with limited manoeuvring capabilities. Although the purely beam sea condition is a convenient and representative reference scenario, which well suits the scope of the present study, it is nevertheless important to note that the behaviour of a vessel freely drifting in dead-ship condition under the action of wind and waves can be significantly more complex ([216]).

Example spectra of linear motions of sway, heave and roll for the two reference points, O and P_E, and for the unitary spectrum in Figure 8.27, as obtained by means of RAOs reported in Figure 8.23 and Figure 8.26, are shown in Figure 8.28. Together with motions, the sea spectrum is also reported, for the sake of reference and completeness. Together with the spectrum, each plot reports also the corresponding standard deviation of the process. From the obtained results it can noticed that motions per unit significant wave height are rather limited, as a consequence of the relatively large size of the considered sample cruise vessel, and this fact is to be borne in mind when assessing the results from evacuation simulations. In accordance with the RAOs shown in in Figure 8.23 and Figure 8.26, it can be noticed that the spectra of the vertical heave motion for both O and P_E, basically almost correspond to the sea spectrum itself, and this is due to

the fact that the heave response of the vessel to such long waves in beam sea is almost static. Differences among the spectra of sway motion at the two considered points can instead be seen, with a noticeable increase of the standard deviation for the case of sway calculated at the highest point P_E. The influence of roll on the sway motion, which was already noticed when discussing the RAOs in Figure 8.23 and Figure 8.26, is also visible in the sway spectra. In order to have a clearer view of the differences, spectra of sway motion at O and P_E are directly superimposed in Figure 8.29, where the sea spectrum is also reported as a reference: the change of sway spectral shape with a shift of the peak frequency, as well as the difference in the area under the spectrum (i.e. the process variance), are clearly noticeable when moving from one point to the other.

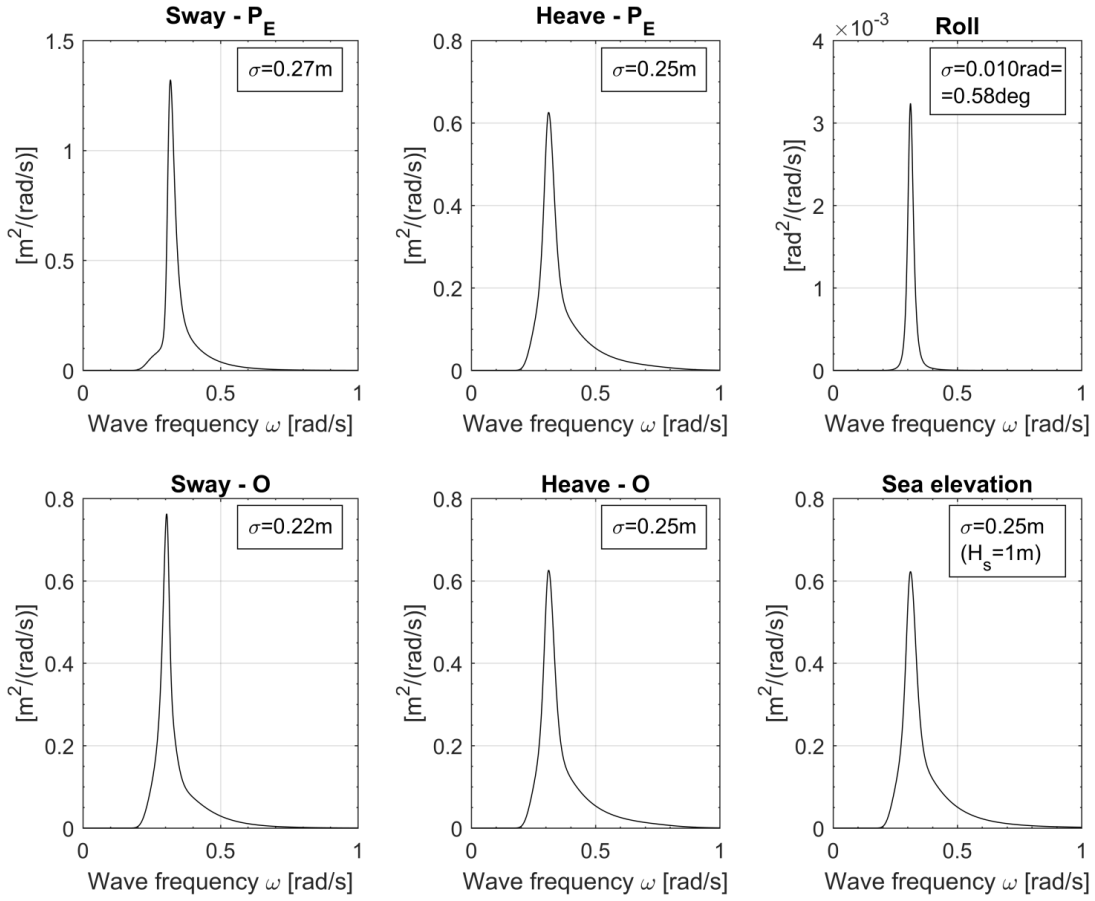

Figure 8.28: CRV270. Spectra of sway, heave and roll, as functions of wave frequency for points $O = (135\ m, 0\ m, 8\ m)$ (top row) and $P_E = (97\ m, 0\ m, 27.2\ m)$ (bottom row). Beam irregular waves coming from starboard ($\beta = 90°$) and characterised by a JONSWAP spectrum with $\gamma = 3.3$, $T_p = 2\pi / \omega_p = 20.2\ s$ and $H_s = 1\ m$.

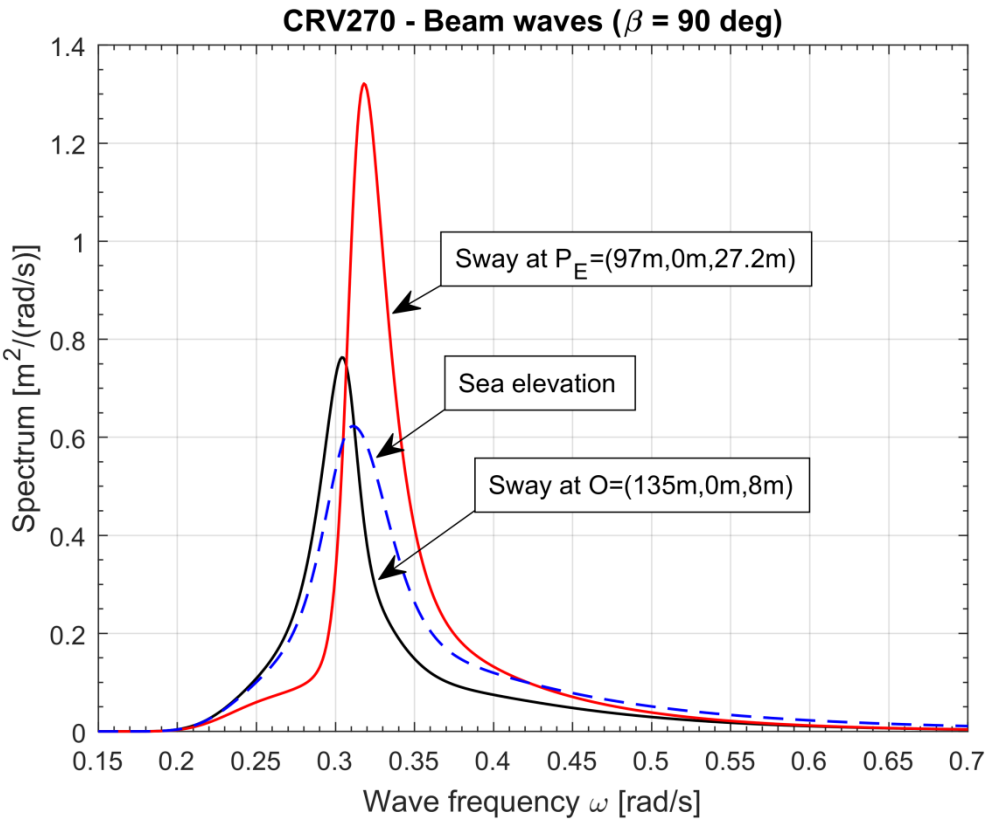

Figure 8.29: CRV270. Direct comparison of sea spectrum and spectra of sway for points $O=(135\ m, 0\ m, 8\ m)$ and $P_E=(97\ m, 0\ m, 27.2\ m)$. Beam irregular waves coming from starboard ($\beta=90°$) and characterised by a JONSWAP spectrum with $\gamma=3.3$, $T_p=2\pi/\omega_p=20.2\ s$ and $H_s=1\ m$.

8.4.6 Generation and use of ship motions for evacuation simulations

In order to provide input for evacuation simulations, ship motions have been generated starting from the linear seakeeping calculations. To this end, the sea spectrum has been discretised into a series of $N=5000$ frequency bins in the range $[0.0, 3.2]\ rad/s$ (to be precise the used range was $[0.001, 3.2]\ rad/s$ since linear seakeeping data were not available for exactly zero frequency). For each realization the amplitude and the phase of the wave component representative of each frequency bin have been both randomly generated in accordance with Tucker et al [215]. In addition, also the frequency of each wave component has been randomly generated for each realization using a uniform distribution within each bin. However, considering the large number of wave components, the effect of this additional variability is small. According to this generation procedure, the wave profile can be written as:

$$\begin{cases} \eta_w(t) = \sum_{i=1}^{N} a_{w,i} \cdot \cos(\omega_i \cdot t) + b_{w,i} \cdot \sin(\omega_i \cdot t) = \sum_{n=1}^{N} c_{w,i} \cdot \cos(\omega_i \cdot t + \delta_{w,i}) \\ c_i = \sqrt{a_i^2 + b_i^2} \\ c_{w,i} \cdot \cos(\delta_{w,i}) = a_{w,i} \\ c_{w,i} \cdot \sin(\delta_{w,i}) = -b_{w,i} \\ \text{with} \\ a_{w,i} \sim N(0, \sigma_{w,i}^2) \;\; ; \;\; b_{w,i} \sim N(0, \sigma_{w,i}^2) \;\; ; \\ \sigma_{w,i}^2 = \int_{\omega_{min,i}}^{\omega_{max,i}} S_w(\omega) d\omega \;\; ; \;\; COV\{a_{w,i}, b_{w,i}\} = 0 \\ \omega_i \sim U(\omega_{min,i}, \omega_{max,i}) \end{cases} \tag{8.9}$$

In (8.9), $N(\mu, \sigma^2)$ indicates a Gaussian distribution with mean μ and variance σ^2, $COV\{.,.\}$ indicates the covariance between two random variable, $U(x_{min}, x_{max})$ indicates a uniform distribution in an interval $[x_{min}, x_{max}]$, and $[\omega_{min,i}, \omega_{max,i}]$ is the frequency bin associated with the i-th wave component.

From the generated wave elevation, using linear seakeeping transfer functions, it is then possible to generate the corresponding vector of time dependent linear motions $\mathbf{x}(t) = (x_1(t), x_2(t), ..., x_6(t))^T$. In fact, the time history of the generic k-th ($k = 1,...,6$) linear degree of freedom, $x_k(t)$, takes the following form:

$$\begin{cases} \eta_w(t) = \sum_{i=1}^{N} a_{w,i} \cdot \cos(\omega_i \cdot t) + b_{w,i} \cdot \sin(\omega_i \cdot t) = \sum_{n=1}^{N} c_{w,i} \cdot \cos(\omega_i \cdot t + \delta_{w,i}) \Rightarrow \\ \Rightarrow x_k(t) = \sum_{i=1}^{N} T_k(\omega_i) \cdot \left[a_{w,i} \cdot \cos(\omega_i \cdot t + \gamma_k(\omega_i)) + b_{w,i} \cdot \sin(\omega_i \cdot t + \gamma_k(\omega_i)) \right] = \\ = \sum_{n=1}^{N} T_k(\omega_i) \cdot c_{w,i} \cdot \cos(\omega_i \cdot t + \delta_{w,i} + \gamma_k(\omega_i)) \\ \text{with } k = 1,...,6 \end{cases} \tag{8.10}$$

where $T_k(\omega_i)$ and $\gamma_k(\omega_i)$ are, respectively, the amplitude and the phase of the linear transfer function (motion per unit wave amplitude) for the k-th degree of freedom. From (8.10), the first and second derivative of the motions can also be readily determined, as follows:

$$\begin{cases} \dot{x}_k(t) = \sum_{n=1}^{N} -\omega_i \cdot T_k(\omega_i) \cdot c_{w,i} \cdot \sin\left(\omega_i \cdot t + \delta_{w,i} + \gamma_k(\omega_i)\right) \\ \ddot{x}_k(t) = \sum_{n=1}^{N} -\omega_i^2 \cdot T_k(\omega_i) \cdot c_{w,i} \cdot \cos\left(\omega_i \cdot t + \delta_{w,i} + \gamma_k(\omega_i)\right) \\ \\ \text{with } k = 1,...,6 \end{cases} \tag{8.11}$$

Finally, the possible presence of asymmetric heeling, e.g. due to wind, is herein taken into account in a simplified way by superimposing a mean roll angle $\bar{\phi}$ (a bias) to the motion $x_4(t)$, i.e.

$$x_4(t) \to \bar{\phi} + x_4(t) \tag{8.12}$$

Of course the condition of upright vessel is recovered for the case $\bar{\phi} = 0$. It is noted that the introduction of the bias term in (8.12) does not influence the first and second derivatives (8.11).

Therefore, summarising, generated linear motions for a generic realization, with corresponding derivatives, taking also into account the possible additional bias on roll, can be represented as follows:

$$\begin{cases} \eta_w(t) = \sum_{n=1}^{N} c_{w,i} \cdot \cos\left(\omega_i \cdot t + \delta_{w,i}\right) \\ x_k(t) = \bar{x}_k + \sum_{n=1}^{N} T_k(\omega_i) \cdot c_{w,i} \cdot \cos\left(\omega_i \cdot t + \delta_{w,i} + \gamma_k(\omega_i)\right) \\ \dot{x}_k(t) = \sum_{n=1}^{N} -\omega_i \cdot T_k(\omega_i) \cdot c_{w,i} \cdot \sin\left(\omega_i \cdot t + \delta_{w,i} + \gamma_k(\omega_i)\right) \\ \ddot{x}_k(t) = \sum_{n=1}^{N} -\omega_i^2 \cdot T_k(\omega_i) \cdot c_{w,i} \cdot \cos\left(\omega_i \cdot t + \delta_{w,i} + \gamma_k(\omega_i)\right) \\ \text{with } k = 1,...,6 \text{ and} \\ \bar{x}_k = \begin{cases} \bar{\phi} & \text{for } k = 4 \\ 0 & \text{otherwise} \end{cases} \end{cases} \tag{8.13}$$

The state vector $\mathbf{x}(t)$ according to (8.13) represents linearised motions, with possible superposition of a bias. In principle it is possible to determine linearised forces per unit mass acting on a generic agent moving in the ship-fixed reference frame. However, in the framework of this study, it has been decided to follow a different approach in order to allow a more direct coupling between the developed evacuation simulation model and ship motions generated from the linear seakeeping calculations. In particular, the state vector of generated linear motions for the six ship degrees of freedom in (8.13) has been interpreted as nonlinear motions.

More precisely, first, it is assumed, as a convention, that the state vector $\mathbf{x}(t)$ is calculated for the centre O of the seakeeping reference system, i.e. $\mathbf{x}(t)=\mathbf{x}_O(t)$. Then, $\left(x_{O,1}(t),x_{O,2}(t),x_{O,3}(t)\right)^T$ has been interpreted as the vector of translations of the centre of the ship fixed reference system O in components with respect to the earth-fixed reference system, $\left(\xi_O(t),\eta_O(t),\zeta_O(t)\right)^T$. This interpretation represents only a relatively small stretching of the linear theory. In fact, in general, in the linear seakeeping theory, $\left(x_{O,1}(t),x_{O,2}(t),x_{O,3}(t)\right)^T$ represent the vector of infinitesimal translations in the steadily translating seakeeping reference system, and this latter reference system is parallel to the earth fixed reference system. Since in the present case the analysis is carried out at zero speed, the two reference systems actually coincide. Therefore, the interpretation used herein basically corresponds to just consider translational motions to be of finite amplitude instead of being infinitesimal. Regarding rotational motions, i.e. $\left(x_{O,4}(t),x_{O,5}(t),x_{O,6}(t)\right)^T$ (note, however, that rotations do not depend on the reference point used for the calculation of motions), it has been decided to interpret this vector as the vector of Euler angles $\left(\phi(t),\vartheta(t),\psi(t)\right)^T$ according to the naval architecture convention (order of rotations: first yaw, then pitch, then roll). This interpretation is, instead, more arbitrary, due to the fact that nonlinear large amplitude rotations based on Euler angles are non-commutative and linear superposition does not hold, whereas, in the framework of the linear theory, rotations $x_{O,4}(t)$, $x_{O,5}(t)$ and $x_{O,6}(t)$ are assumed to be infinitesimal and can be superimposed. As a result, this interpretative stretching of the linear theory regarding rotations is slightly more substantial compared to that regarding translations, because it does not only involve moving from infinitesimal to non-infinitesimal rotations, but it also involves assuming that each given linear rotation corresponds to a, somewhat arbitrarily specified nonlinear rotation. From the point of view of the linear theory, the assumed stretching is valid because, in the limit of infinitesimal rotations, Euler angles tend to linear seakeeping rotations, i.e. $\left(\phi(t),\vartheta(t),\psi(t)\right)^T\to\left(x_{O,4}(t),x_{O,5}(t),x_{O,6}(t)\right)^T$. From the point of view of nonlinear motions, from a practical perspective, the implemented assumption can be considered to be sufficiently appropriate. This is a consequence of the fact that pitch ($x_{O,5}(t)$, $\vartheta(t)$) and yaw ($x_{O,6}(t)$, $\psi(t)$) motions are, typically, sufficiently small to allow a direct linearization, and roll ($x_{O,4}(t)$, $\phi(t)$) is, typically, the only motion which could achieve magnitudes such to require considering it as non-small . As a result, the stretching of the linear theory assumed herein regarding rotations becomes only partial, and mainly related to roll motion, while the other two rotations typically remain sufficiently small for the linear approach to be valid. Therefore, in summary, the state vector of linear motions is herein interpreted as follows:

$$\mathbf{x}_O(t) = \begin{pmatrix} x_{O,1}(t) \\ x_{O,2}(t) \\ x_{O,3}(t) \\ x_{O,4}(t) \\ x_{O,5}(t) \\ x_{O,6}(t) \end{pmatrix} \rightarrow \begin{pmatrix} \xi_O(t) \\ \eta_O(t) \\ \zeta_O(t) \\ \phi(t) \\ \vartheta(t) \\ \psi(t) \end{pmatrix} \tag{8.14}$$

Moreover, the same relation is assumed to hold also for the first and second derivative of motions, i.e:

$$\dot{\mathbf{x}}_O(t) = \begin{pmatrix} \dot{x}_{O,1}(t) \\ \dot{x}_{O,2}(t) \\ \dot{x}_{O,3}(t) \\ \dot{x}_{O,4}(t) \\ \dot{x}_{O,5}(t) \\ \dot{x}_{O,6}(t) \end{pmatrix} \rightarrow \begin{pmatrix} \dot{\xi}_O(t) \\ \dot{\eta}_O(t) \\ \dot{\zeta}_O(t) \\ \dot{\phi}(t) \\ \dot{\vartheta}(t) \\ \dot{\psi}(t) \end{pmatrix} \quad ; \quad \ddot{\mathbf{x}}_O(t) = \begin{pmatrix} \ddot{x}_{O,1}(t) \\ \ddot{x}_{O,2}(t) \\ \ddot{x}_{O,3}(t) \\ \ddot{x}_{O,4}(t) \\ \ddot{x}_{O,5}(t) \\ \ddot{x}_{O,6}(t) \end{pmatrix} \rightarrow \begin{pmatrix} \ddot{\xi}_O(t) \\ \ddot{\eta}_O(t) \\ \ddot{\zeta}_O(t) \\ \ddot{\phi}(t) \\ \ddot{\vartheta}(t) \\ \ddot{\psi}(t) \end{pmatrix} \tag{8.15}$$

It is to be noted that the assumed stretching has the drawback of being not consistent with respect to changes of the reference point which is used for the calculation of the reference linear motions. In fact, if linear motions are calculated, according to linear theory, for two different points of the vessel, and then the same transformation (8.14) is applied for the two different points, the resulting nonlinear motions at the two points are, in general, inconsistent from the point of view of nonlinear rigid body kinematics. This is due to the fact that linear kinematics is based on linearised rotation matrices, while nonlinear kinematics is based on nonlinear rotation matrices. The two approaches become, however, consistent and equivalent in the limit of small amplitude motions. For the purpose of the present study, however, the assumed approach has been considered sufficient for providing sufficiently realistic nonlinear ship motions to the evacuation simulation tool.

As already described in Chapter 7, forces per unit mass $\mathbf{f}$ which are perceived by an agent which is moving in the ship-fixed reference system, can be represented, from rigid body kinematics as follows:

$$(\mathbf{f})_S = -\begin{pmatrix} \mathbf{R}_{\Sigma \rightarrow S} \cdot (\ddot{\boldsymbol{\xi}}_O)_\Sigma + (\boldsymbol{\omega}')_S \times (\mathbf{x}_{a,O})_S + \\ + (\boldsymbol{\omega})_S \times ((\boldsymbol{\omega})_S \times (\mathbf{x}_{a,O})_S) + 2 \cdot (\boldsymbol{\omega})_S \times (\mathbf{x}_{a,O}')_S \end{pmatrix} + \mathbf{R}_{\Sigma \rightarrow S} \cdot (\mathbf{g})_\Sigma \tag{8.16}$$

In the previous equation $(.)_\Sigma$ and $(.)_S$ indicate vectors expressed, respectively, in components with respect to the earth-fixed and with respect to the ship-fixed reference system, dots indicates derivatives carried out in the earth-fixed reference system and primes indicate derivatives carried out in the ship-fixed reference frame. The quantities involved in the expression for $\mathbf{f}$ are the acceleration vector of the reference point $\ddot{\boldsymbol{\xi}}_O$,

the angular velocity of the ship $\boldsymbol{\omega}$, the position vector $\mathbf{x}_{a,O}$ of the agent with respect to the reference point O, and the gravitational acceleration $\mathbf{g}$. This latter, in the earth fixed reference system can be expressed as $(\mathbf{g})_{\Sigma} = (0,0,-g)^T$. The quantities which are necessary for the calculation of $\mathbf{f}$ at each time instant can be determined from the nonlinear state variables in (8.14) and (8.15). In fact, the rotation matrix $\underset{\Sigma \to S}{\mathbf{R}}$ takes the following form:

$$
\begin{aligned}
&\underset{\Sigma \to S}{\mathbf{R}} = \begin{bmatrix} r_{11} & r_{12} & r_{13} \\ r_{21} & r_{22} & r_{23} \\ r_{31} & r_{32} & r_{33} \end{bmatrix} \\
&r_{11} = \cos(\psi) \cdot \cos(\vartheta) \\
&r_{12} = \cos(\vartheta) \cdot \sin(\psi) \\
&r_{13} = -\sin(\vartheta) \\
&r_{21} = \cos(\psi) \cdot \sin(\phi) \cdot \sin(\vartheta) - \cos(\phi) \cdot \sin(\psi) \\
&r_{22} = \cos(\phi) \cdot \cos(\psi) + \sin(\phi) \cdot \sin(\psi) \cdot \sin(\vartheta) \\
&r_{23} = \cos(\vartheta) \cdot \sin(\phi) \\
&r_{31} = \sin(\phi) \cdot \sin(\psi) + \cos(\phi) \cdot \cos(\psi) \cdot \sin(\vartheta) \\
&r_{32} = \cos(\phi) \cdot \sin(\psi) \cdot \sin(\vartheta) - \cos(\psi) \cdot \sin(\phi) \\
&r_{33} = \cos(\phi) \cdot \cos(\vartheta)
\end{aligned}
\tag{8.17}
$$

The angular velocity expressed in components with respect to the ship fixed reference system can be determined, from the derivatives of Euler angles, as

$$
(\boldsymbol{\omega})_S = \begin{pmatrix} 1 & 0 & -\sin(\vartheta) \\ 0 & \cos(\phi) & \sin(\phi) \cdot \cos(\vartheta) \\ 0 & -\sin(\phi) & \cos(\phi) \cdot \cos(\vartheta) \end{pmatrix} \cdot \begin{pmatrix} \dot{\phi} \\ \dot{\vartheta} \\ \dot{\psi} \end{pmatrix} \tag{8.18}
$$

and its corresponding time derivative $(\boldsymbol{\omega}')_S$ can be obtained from the derivation chain rule as

$$\left(\boldsymbol{\omega}'\right)_S = \left(\begin{pmatrix} 0 & 0 & 0 \\ 0 & -\sin(\phi) & \cos(\phi)\cdot\cos(\vartheta) \\ 0 & -\cos(\phi) & -\sin(\phi)\cdot\cos(\vartheta) \end{pmatrix} \cdot \dot{\phi} + \begin{pmatrix} 0 & 0 & -\cos(\vartheta) \\ 0 & 0 & -\sin(\phi)\cdot\sin(\vartheta) \\ 0 & 0 & -\cos(\phi)\cdot\sin(\vartheta) \end{pmatrix} \cdot \dot{\vartheta} \right) \cdot \begin{pmatrix} \dot{\phi} \\ \dot{\vartheta} \\ \dot{\psi} \end{pmatrix} + \begin{pmatrix} 1 & 0 & -\sin(\vartheta) \\ 0 & \cos(\phi) & \sin(\phi)\cdot\cos(\vartheta) \\ 0 & -\sin(\phi) & \cos(\phi)\cdot\cos(\vartheta) \end{pmatrix} \cdot \begin{pmatrix} \ddot{\phi} \\ \ddot{\vartheta} \\ \ddot{\psi} \end{pmatrix} \tag{8.19}$$

Finally, the instantaneous relative position $\left(\mathbf{x}_{a,O}\right)_S$ and velocity $\left(\mathbf{x}_{a,O}'\right)_S$ of the generic agent in the ship-fixed reference frame are obtained directly from the evacuation simulation tool which solves the agents dynamics directly in the ship-fixed reference system.

Example time histories for the case $H_s = 10\,m$ with a superimposed heel angle of 5 deg to portside (i.e. $\bar{\phi} = -5$ deg) are shown in Figure 8.30 to Figure 8.34.

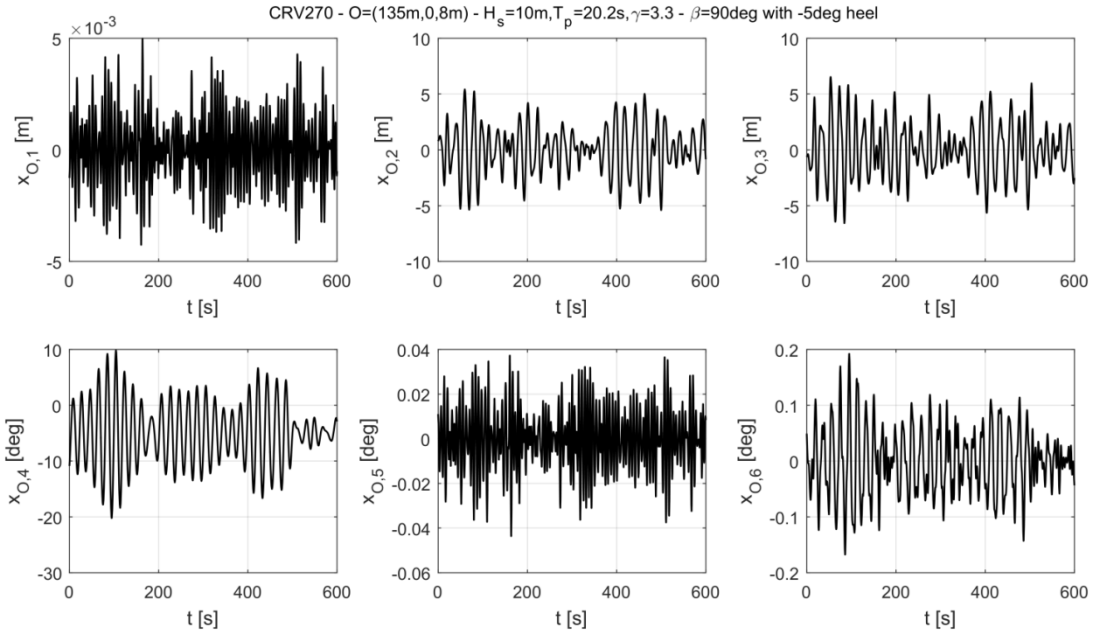

Figure 8.30: CRV270. Example of generated time histories of linear motions, $\mathbf{x}_O(t)$, for point $O = (135\,m, 0\,m, 8\,m)$. Beam irregular waves coming from starboard ($\beta = 90$ deg) and characterised by a JONSWAP spectrum with $\gamma = 3.3$, $T_p = 2\pi/\omega_p = 20.2\,s$ and $H_s = 10\,m$.

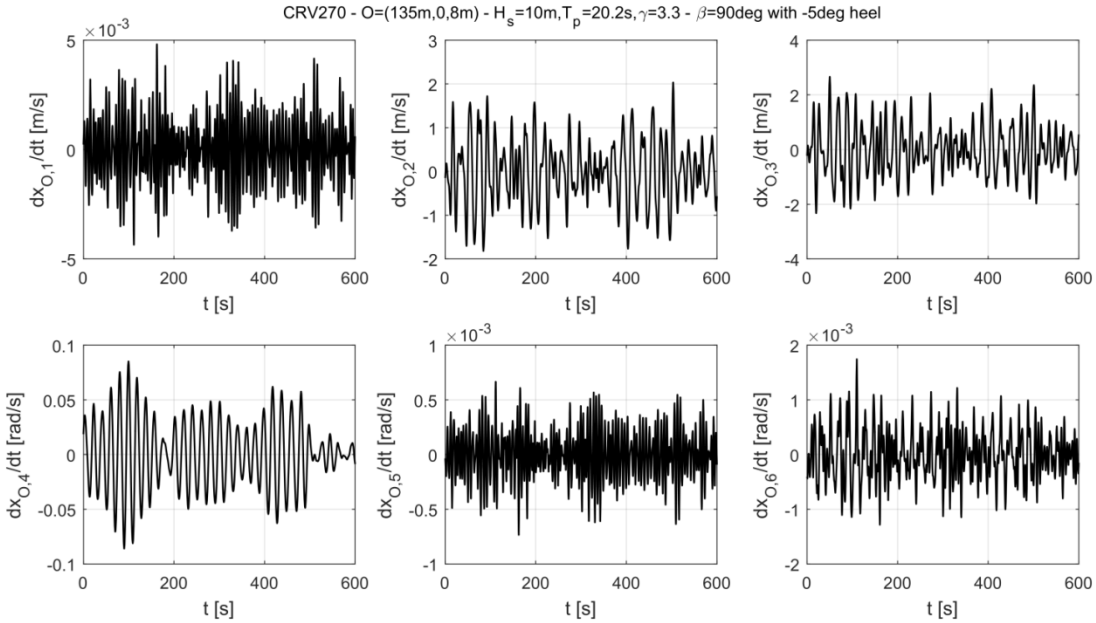

Figure 8.31: CRV270. Example of generated time histories of time derivatives of linear motions, $\dot{\mathbf{x}}_O(t)$, for point $O=(135\ m, 0\ m, 8\ m)$. Beam irregular waves coming from starboard ($\beta = 90$ deg) and characterised by a JONSWAP spectrum with $\gamma = 3.3$, $T_p = 2\pi/\omega_p = 20.2\ s$ and $H_s = 10\ m$.

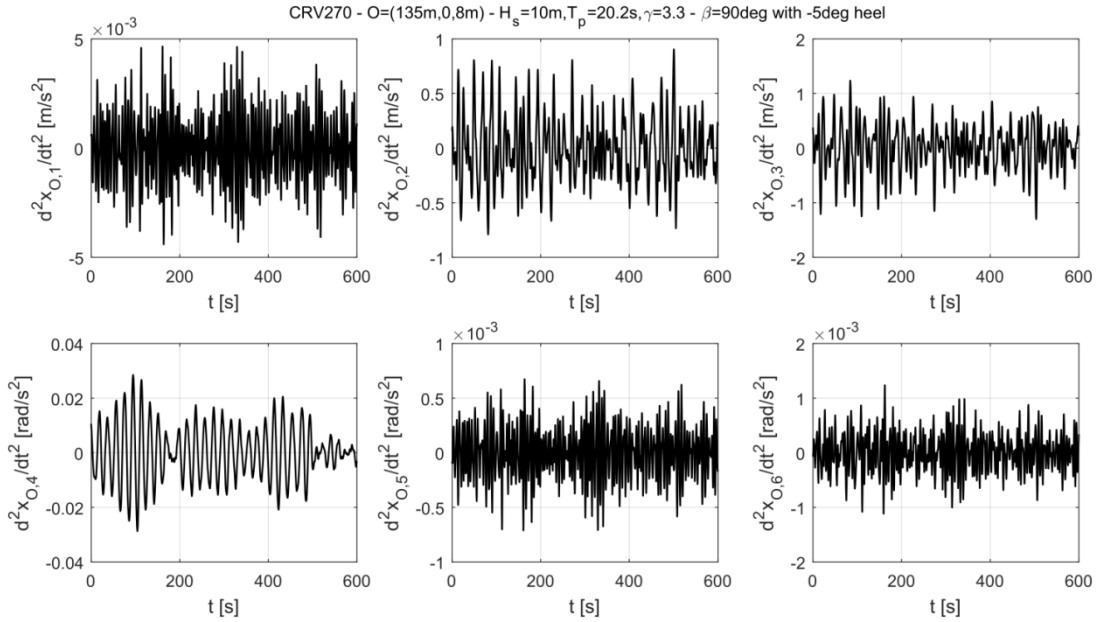

Figure 8.32: CRV270. Example of generated time histories of second time derivatives of linear motions, $\ddot{\mathbf{x}}_O(t)$, for point $O=(135\ m, 0\ m, 8\ m)$. Beam irregular waves coming from starboard ($\beta = 90$ deg) and characterised by a JONSWAP spectrum with $\gamma = 3.3$, $T_p = 2\pi/\omega_p = 20.2\ s$ and $H_s = 10\ m$.

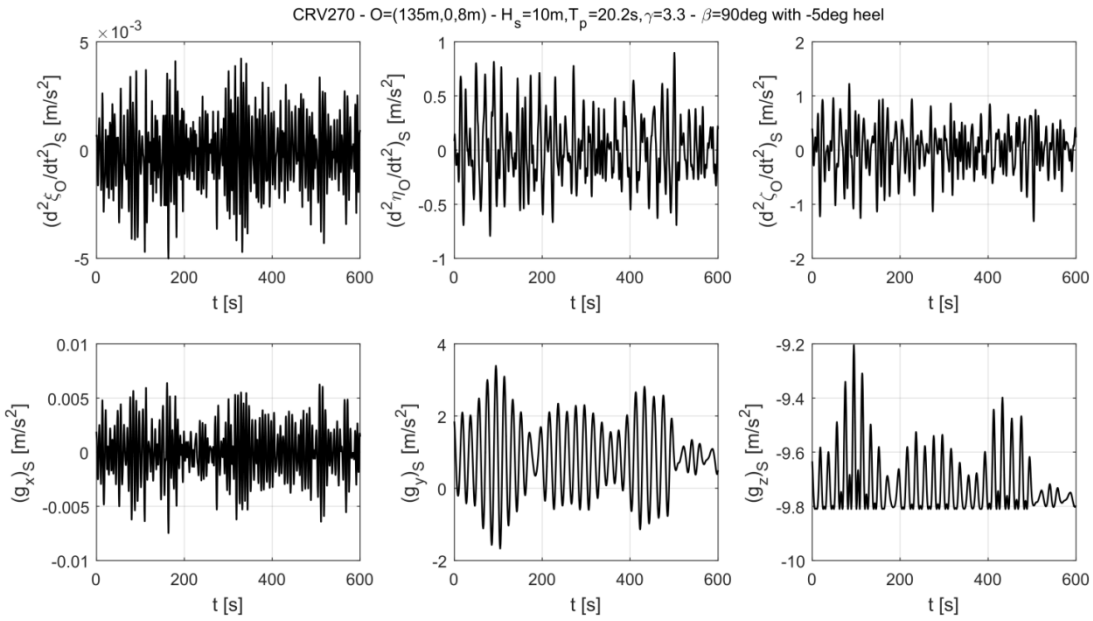

Figure 8.33: CRV270. Example of generated time histories for nonlinear translational accelerations $\left(\ddot{\boldsymbol{\xi}}_O(t)\right)_S$ for point $O=(135\ m, 0\ m, 8\ m)$ (top), and gravitational acceleration $(\mathbf{g})_S(t)$ (bottom), expressed in components with respect to the ship-fixed reference system. Beam irregular waves coming from starboard ($\beta = 90$ deg) and characterised by a JONSWAP spectrum with $\gamma = 3.3$, $T_p = 2\pi / \omega_p = 20.2\ s$ and $H_s = 10\ m$.

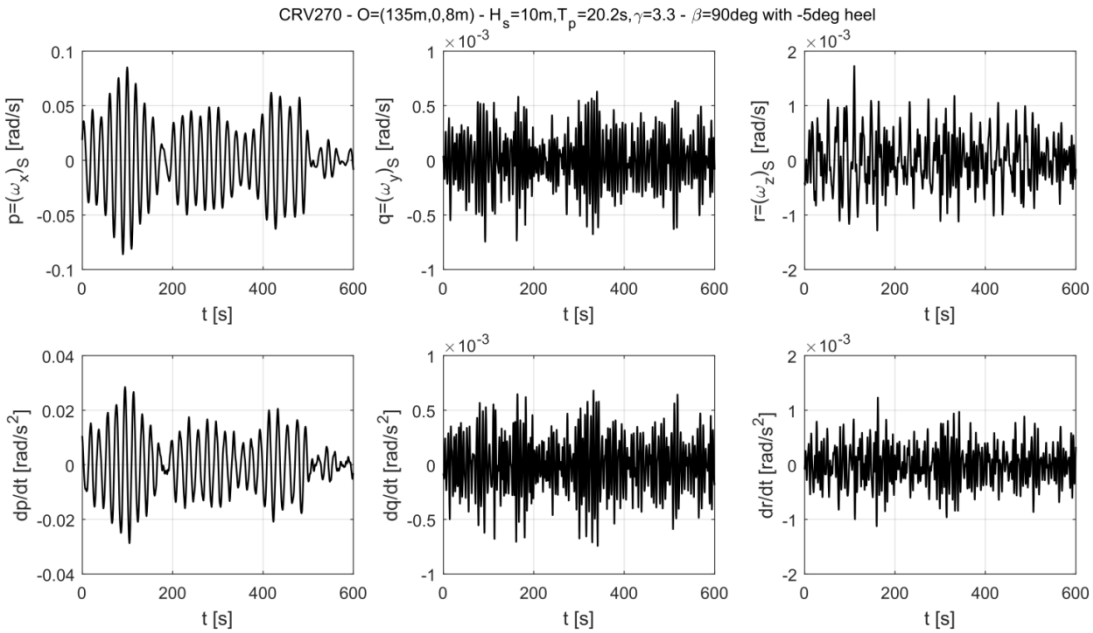

Figure 8.34: CRV270. Example of generated time histories for angular velocity $\left(\boldsymbol{\omega}(t)\right)_S$ (top) and corresponding derivative $\left(\boldsymbol{\omega}'(t)\right)_S$ (bottom), expressed in components with respect to the ship-fixed reference system. Reference point for linear seakeeping calculations: $O=(135\ m, 0\ m, 8\ m)$. Beam irregular waves coming from starboard ($\beta = 90$ deg) and characterised by a JONSWAP spectrum with $\gamma = 3.3$, $T_p = 2\pi / \omega_p = 20.2\ s$ and $H_s = 10\ m$.

8.4.7 Evacuation results

The developed two-cabin-deck test case was run by using ship motions derived from the calculations explained in the previous section, considering long-crested beam irregular waves coming from starboard ($\beta = 90°$) with significant wave heights $H_s = 0,\ 4,\ 8,\ 12\ m$. Superimposed heel angles of 0°, -10°, -20° were also considered, corresponding to upright vessel or vessel heeled to port side. The condition with zero significant wave height corresponds to the case of vessel without dynamic motions. The combination with zero significant wave height and zero heel angle corresponds to the standard scenario without motions. Instead, the case with zero significant wave height and 20° of heel corresponds to the heel condition in the previously discussed standard motion scenarios. However, herein the heel is to portside, while in the results reported for the standard motion scenarios, a starboard heel was considered. A total of 12 scenarios will eventually be considered in this section.

The total assembly duration of each of the tested combinations is reported in the form of box-plots in Figure 8.35. Each box-plot provides the minimum, the maximum, together with 25%, 50% (median) and 75% percentiles.

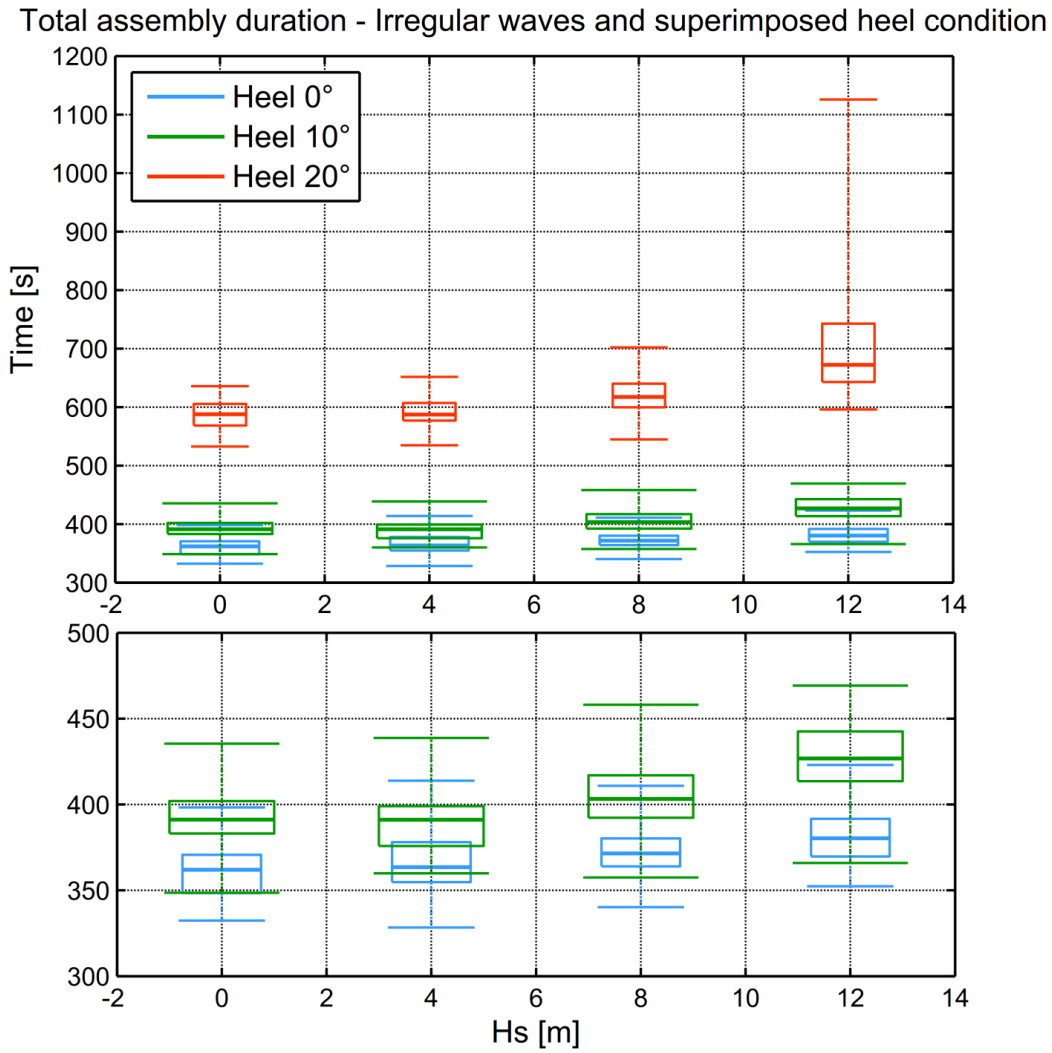

Figure 8.35: Two-cabin-deck test case. Irregular beam wave condition. Total assembly duration presented in the form of box plots for each performed combination of significant wave height and superimposed heel.

As expectable, results in Figure 8.35 indicate that the exit time increases with the heel angle and with the significant wave heights. However, the effect of dynamic motions appears to be small compared to the effect of heel, and it becomes evident only for large values of the significant wave heights, where dynamic motions sufficiently increase.

The impact of the significant wave height is reduced, in this case, because the dynamic motions of the ship are limited. This is due to the large dimensions and to the long natural roll period of the considered cruise vessel (see Table 8.2).

In the following, a more detailed analysis is therefore performed considering only the condition associated to the most severe significant wave height ($H_s = 12\,m$) without heel. The analysis is aimed to assess the effects of dynamics motions for the same quantities already analysed in the standard conditions.

The analysis of the density in the areas in front of the stairs (see Figure 8.2) is reported in Figure 8.36.

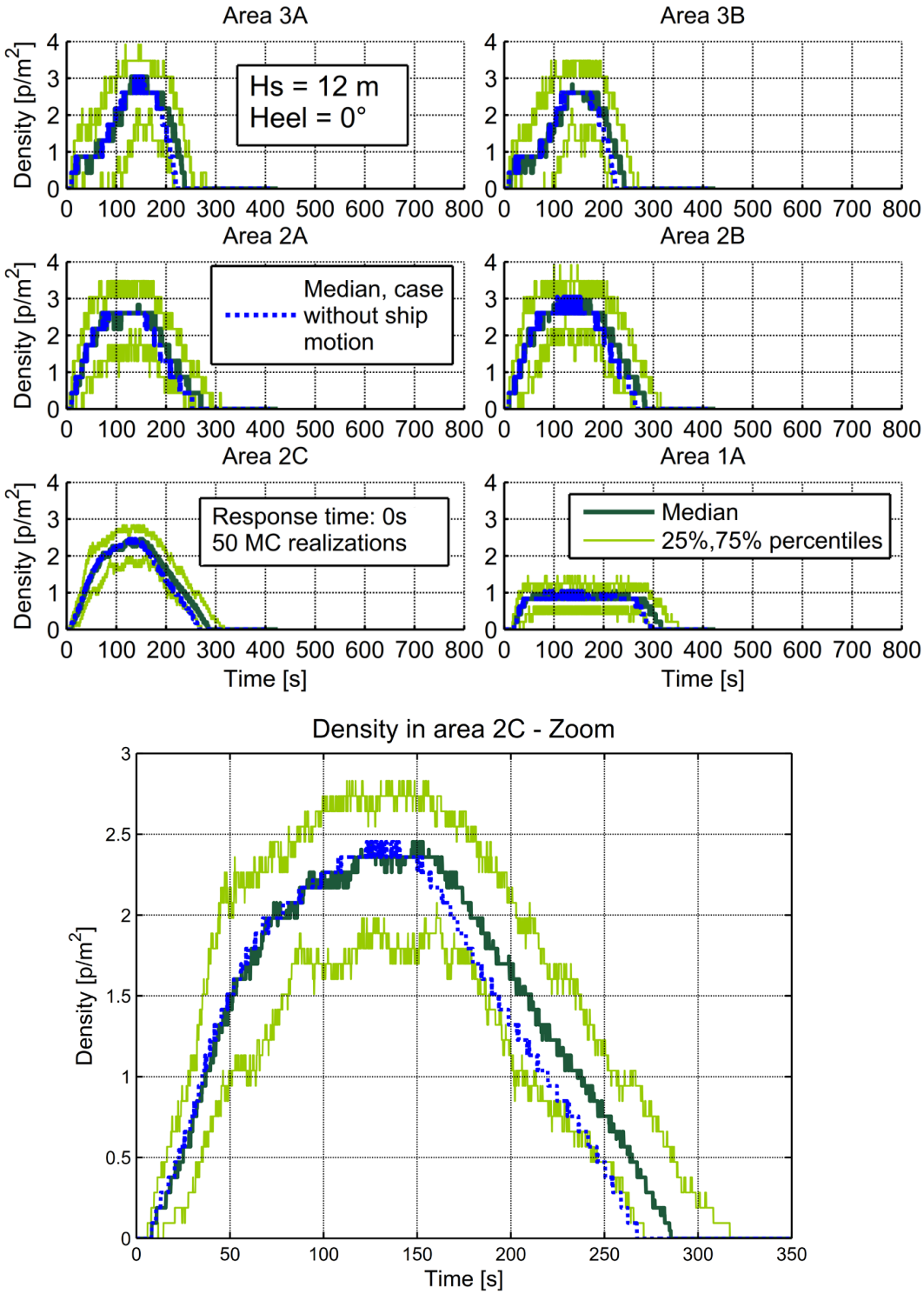

Figure 8.36: Two-cabin-deck test case. Irregular beam waves condition with $H_s = 12\ m$ and no heel. Top: density inside each area in front of the stairs. The curves report the ensemble 25%, 50% and 75% percentiles for each time instant. Total number of Monte Carlo realizations: 50. The median of the case without ship motion is also reported, for comparison. Bottom: zoom of the density in area 2C.

Figure 8.36 shows that there is no marked difference between the density measured in the areas in front of the staircase without ship motion and in the case with irregular waves and significant wave height 12 m.

Comparing, for each analysed area, the two median density curves related to the cases with and without ship motion, it can be observed that the curves are almost identical in the initial region of increasing density. However, after the density reaches its peak and the density decreases, some differences can be observed between the two cases. It appears that, in all analysed areas, thedecrease of density is slightly slower in the case with irregular wave compared to the case without ship motions. An explanation for the observed behaviour could be that that agents trajectories are not much affected by ship motions while agents are inside corridors or staircases, because those facilities are narrow and agents do not have the possibility to slide. However, when agents exit from corridors or staircases and enter the areas in front of the staircase, the motions of the ship start affecting their trajectories/positions delaying the emptying of these areas.

The observed delaying in the reduction of densities is confirmed by the observation of the results of analysis related to the occupation of each deck and staircase, as reported in Figure 8.37.

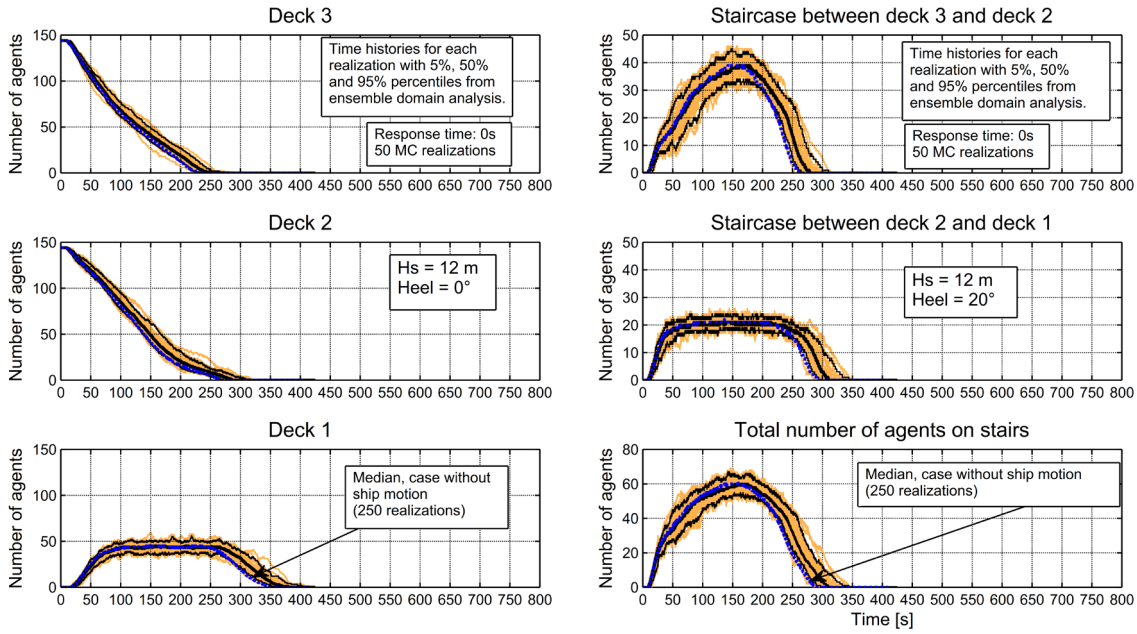

Figure 8.37: Two-cabin-deck test case. Irregular beam waves condition with $H_s = 12\ m$ and no heel. Number of agents on decks (left) and on stairs (right). Figures report time histories from each single realization, as well as 5%, 50% and 95% percentiles from ensemble domain analysis at each time instant. The median related to the case without ship motion is also reported, for comparison.

The results from the analysis related to the occupation of the staircases reported in Figure 8.37 (right) confirm the observations based on the analysis of the density in the areas in front of the staircases. It is observed, indeed, that the behaviour of the median in case with and without motions is almost the same in the initial part, where the number of agents increases. However, when the number of agents in the staircase starts

decreasing, the decrease is faster in the case without ship motion compared to the case with irregular waves.

As previously observed, the effect of the motion of the ship on agents is more marked in the areas in front of the stairs (see in particular areas 3B and 2B in Figure 8.36). Considering the case with irregular waves, the process of emptying the staircases is slowed down by the fact that the area in front of the staircase is occupied for a longer time with respect to the case without ship motion (see the delaying in the decreasing part of density curves in Figure 8.36 in presence of ship motion).

Data in Figure 8.37 also show that the case with irregular waves presents a slight delay in emptying the decks with respect to the case without ship motions. This behaviour was, however, expectable and it is mostly a consequence of the reduction of the unimpeded speed of the agents due to ship motions.

The total number of exited agents as function of time is reported in Figure 8.38. Results in the figure show that the exit rate of the agents is slightly reduced in the case with irregular waves with respect to the case without motions.

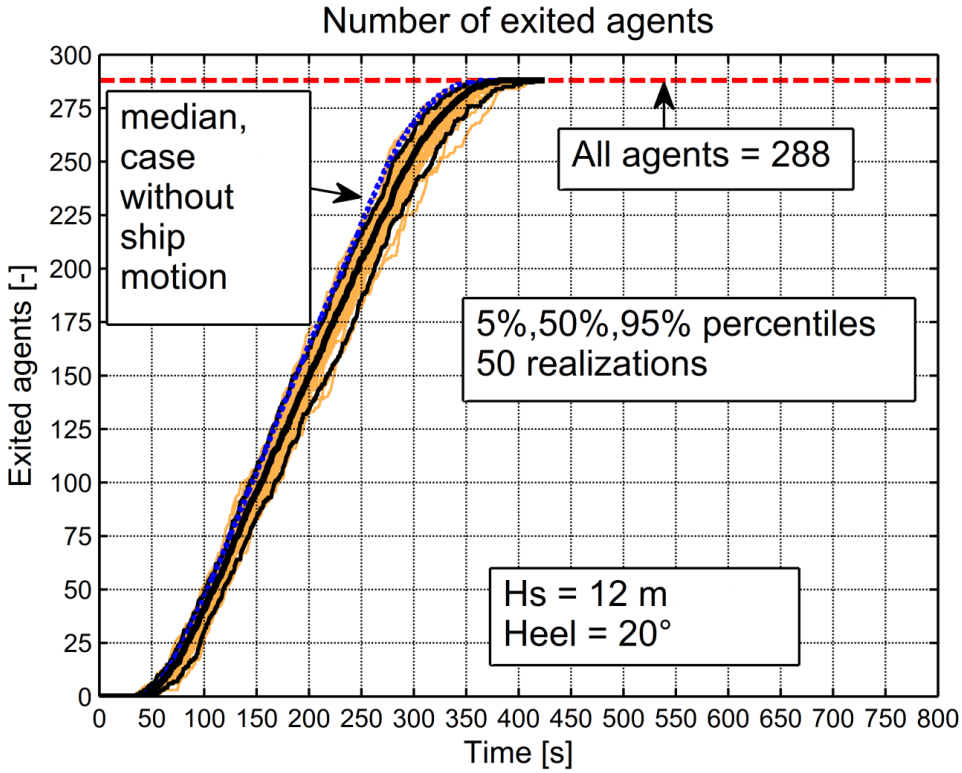

Figure 8.38: Two-cabin-deck test case. Irregular beam waves condition with $H_s = 12\ m$ and no heel. Number of exited agents as function of time. The figure reports time histories from each single realization, as well as 5%, 50% and 95% percentiles from ensemble domain analysis at each time instant. The median related to the case without ship motion is also reported, for comparison.

The section concludes with some qualitative observation concerning the behaviour of agents, as derived from the analysis of animations based on simulation data.

Figure 8.39 reports some representative snapshots of one realization related to the case with ship motions in irregular beam waves at a significant wave height $H_s = 12\,m$ and considering a superimposed heel angle of -10° (i.e. 10° to port side).

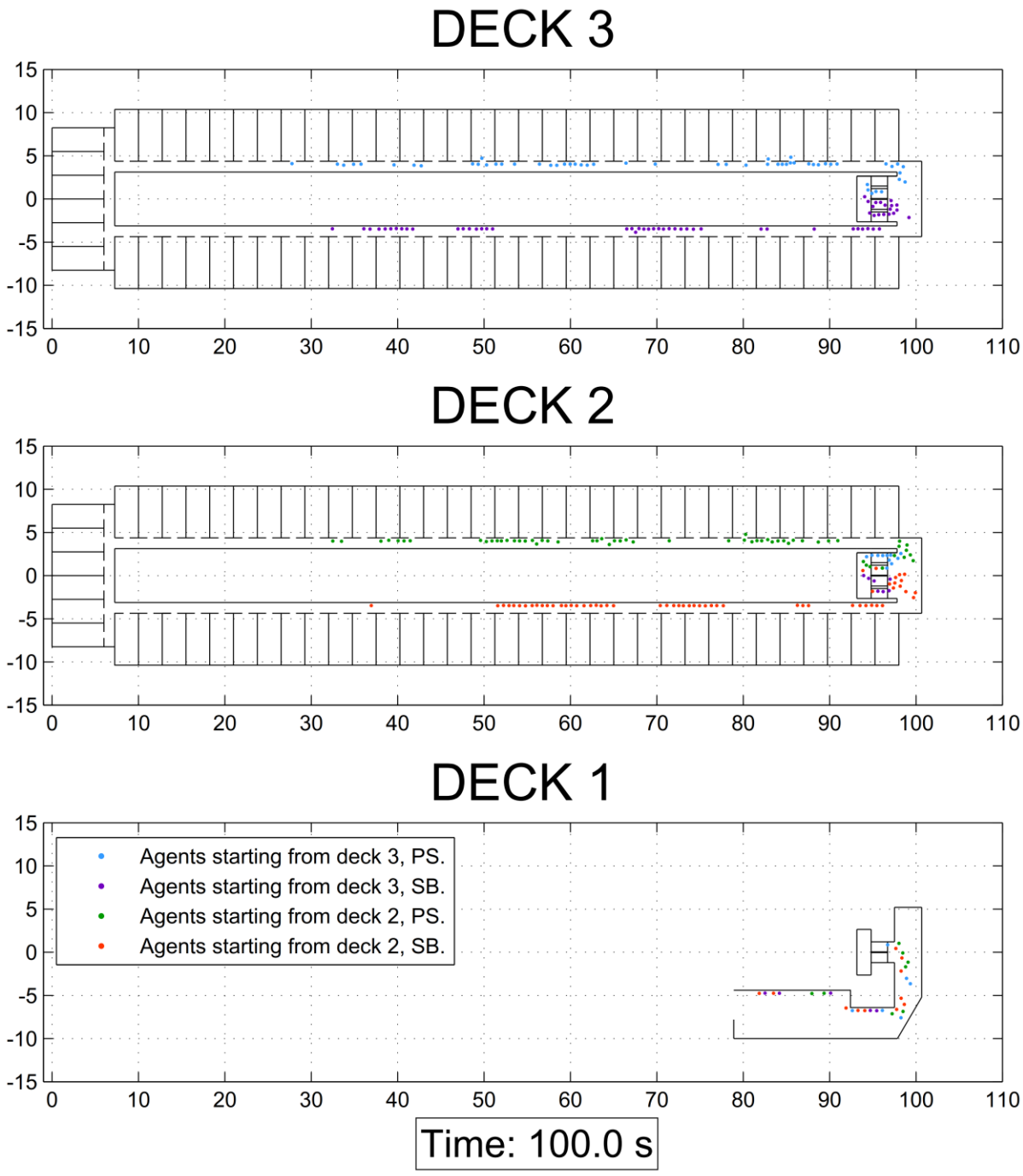

Figure 8.39: Two-cabin-deck test case. Irregular beam waves condition with $H_s = 12\,m$ and heel equal to -10° Snapshots from one of realizations at one time instant and on different decks.

The effect of heel is clearly visible in Figure 8.39 as agents mostly tend to move close to walls placed in the direction of the inclination of the ship (i.e. to port side). It is also noted that the effect of dynamic motions is visible in the animation obtained by

processing agents positions. In this condition the agents stop or speed up in accordance to the external force component generated by the motions, particularly roll.

Finally it was observed that, in case of large heel angles, agents travelling in a corridor on the inclined side of the ship have more difficulty than those travelling on the opposite side. This is due to the fact that agents tend to move alongside the wall when the external force cannot be entirely balanced (Figure 8.39 is an example). However, in the considered layout, the wall that agents tend to walk along to, is interrupted by the cabins entrances when the agents are on the inclination side. As a result, agents in such condition tend to be pushed inside each cabin. This does not occur, instead, for agents on the other side, at least for the considered configuration of cabins. Although, to the best of author's knowledge, there seems to be no experimental evidences in literature regarding this behaviour, it is nevertheless reasonable to think that people would travel faster if the handhold they are holding on is uninterrupted. It is quite unrealistic to think that people would consider closing the door of the cabin after exiting during an evacuation. However the use of self-closing doors to guarantee a continuous handhold in case of evacuation may actually improve the evacuation process.

8.5 Final remarks

This chapter presented and described a test geometry, which is specifically relevant to the maritime field. The test geometry is realistic, but it has a reduced complexity which facilitates its implementation and testing. The proposed geometry is the result of simplification of a portion of the geometry of an existing cruise vessel, as originally reported in the SAFEGUARD Validation Data Set 2 (SGVDS2, [186]). The test case was developed in order to provide a simplified and easily reproducible condition specifically targeting the maritime field. In fact, it appears that existing literature provides either archetypal geometries or geometries of high complexity, such as those of full vessels. The full vessels cases are often reported with a lack of details which then prevent reproduction. It looks, then that literature is somehow lacking a reference case of intermediate complexity for testing and comparing evacuation tools, and this motivated the development of the proposed geometry.

The developed geometry was used for evacuation simulation under different scenarios. The first set of scenarios comprised fixed geometry (calm water) and standard notional motions conditions (heel, trim, dynamic roll). These latter were based on the conditions suggested by Nicholl et al. [158] with the addition of a combined heel and trim scenario. Evacuation results in the considered standard scenarios indicate a marked effect of the 20° heel condition, with a corresponding almost doubling of the total assembly duration compared to case of upright vessel. This is the result of both the reduction of unimpeded speed as well as the direct action of external forces parallel to the deck. The reduction of the unimpeded speed leads, in general, to an increase of the time it takes to the agent to arrive at the designated assembly station. In addition, since, according to the model used for the agent control forces, agents are not able to fully balance forces parallel to deck at 20° of inclination, this eventually leads to a modification of the trajectories of the agents compared to the upright case. This modification leads to significantly asymmetric agents configurations, which eventually results in a further increase of the total assembly time. The dynamic roll considered in the standard scenarios was characterised by 5° of amplitude and 20 s of period. However, it effect was found to be, overall,

limited. The combined case of 20° of heel and 10° of trim significantly impacted the evacuation performance, with situation where not all the agents were able to evacuate in the time limit of 30 min, which was specified as maximum time for each single simulation.

The same geometry was then used for evacuation simulations using more realistic ship motions which have been computed considering that the test geometry is placed onboard of a notional cruise vessel, and considering long-crested irregular beam waves. The dimensions of the considered notional cruise vessel are approximately in line with the vessel from which the test geometry was originally derived. In order to provide input for evacuation simulations, ship motions have been generated starting from the linear seakeeping transfer functions. In addition, static heel was also considered, as a superimposed bias. The obtained results indicate that the effect of dynamic motions is limited, unless the significant wave height is very large. This appear to be a consequence of the overall large dimensions of the vessel, which leads to limited motions in absolute terms, and the long natural roll period, which leads to relatively small accelerations. However it should also be observed that the present model does not accounts the psychological effects of the vertical component of the perceived acceleration. The vertical acceleration might also have impact on the desired speed of the passengers increasing also the exit times.

The analysis of available data provided detailed information regarding the behaviour of agents with and without ship motions. The ensemble domain statistical analysis carried out of the Monte Carlo simulations allowed to clearly highlight peculiar characteristics of the evacuation process in presence of static inclinations and/or dynamic motions, particularly in front of the stairs entrance and along the cabins corridor.

The next chapter will propose an approach for introducing ship motion in the virtual reality experience of the user through a modification of the user control of the avatar and exploiting a haptic interface.

This page is intentionally left blank

9 REAL TIME USER INTERACTION WITH SHIP MOTIONS

The modelling of real time user interaction considering ship motions is extremely challenging. This is mainly due to the fact that it is very difficult to allow the user to perceive the accelerations generated by the motions of the ship. At the same time, however, the avatar (i.e. the agent controlled by the user) should be affected by the external forces in the same way as the agents.

The present chapter deals with this issue by proposing a modification to the avatar control force model previously described in Chapter 5 to account for ship motions.

Moreover, in order to mitigate the lack of perception of the acceleration, the same vibrotactile hardware described in Chapter 5 is herein adopted to provide the user with information concerning the direction and the magnitude of the external force.

9.1 Introduction

The use of virtual reality to enhance evacuation simulations from ships presents an additional problem due to the need of introducing the effect of ship motion in the simulation.

From a modelling perspective, in order to be physically consistent, the perceived force originated by ship motions should entirely be applied to the avatar. However the user should be able to oppose a sufficient control to balance the effects of the perceived force. Moreover the user should be informed about the intensity and the direction of the perceived forces in order to obtain a realistic behaviour. This last problem is perhaps the

most challenging. Although the progress with virtual reality allows reproducing reality with high fidelity through a high quality rendering and sound, the perception of accelerations is still impossible to be exactly and fully reproduced in the most general cases. This limit is not critical in applications where accelerations are applied for short time and/or have small magnitude. In case of a moving ship, however, the avatar is subjected to accelerations of potentially significant magnitude for the whole duration of the simulation. Thus, the lack of perception of accelerations represents a critical limitation to the application of virtual reality in this specific field.

The most straightforward way to simulate the effects of an external acceleration with virtual reality would be by actually applying an equal acceleration both to the user (in the reality) and to the avatar (in the virtual model). Motions could be (partially) reproduced by means of large and costly hardware installations such as those used for ship handling/bridge simulators (e.g. [14], [37], [110], [131]). However, such facilities are not suitable, due to costs, if the intention is to envision a broader use of virtual reality in the maritime evacuation field.

A different approach could instead be followed, where the transfer to the user of the information regarding the perceived acceleration direction and magnitude is carried out through a channel which is different from the natural one (represented by the proprioceptive apparatus).

Vibrotactile feedbacks have already been adopted to provide users with proprioceptive information ([6]). Moreover previous studies demonstrated the effectiveness of pulses of the vibrotactile interfaces to communicate absolute quantities such as distance ([218]) or force magnitude ([23]).The previously haptic interface developed in Chapter 5 has thus herein adopted to provide the user with haptic feedback informing on the direction and on the magnitude of the externally applied force per unit mass.

The present chapter presents a model to account ship motion effects in real time user participation through virtual reality. The first section will describe the modification made to the user control model in order to allow the user to effectively balance the perceived forces, which are directly applied to the avatar. The second section will describe the haptic interface developed with the purpose of communicating the perceived forces to the user.

9.2 The user control model

The effects of the ship motions on the user controlled avatar are modelled in a way quite similar to the previously described agent model.

In particular, the perceived forces are directly and fully applied to the avatar in order to be consistent with what is done for the agents, as described in Chapter 7, and with the physics of the system. The total force applied to the avatar is the sum of the control forces in case of ship motions $\mathbf{F}_a^{\text{cont,sm}}$ originated by the user, and regulated with the controller, and the perceived forces $\mathbf{F}_a^{\text{perc}}$, as reported in the equation below:

$$\mathbf{F}_a = \mathbf{F}_a^{\text{cont,sm}} + \mathbf{F}_a^{\text{perc}} \tag{9.1}$$

In the modelling of the behaviour of agents in presence of external forces, a control force was introduced in order to allow agents to control, to some extent, the effects of the external action. The user should be able to produce a comparable control force to balance the effects of perceived forces. It was however observed that the developed model for the user control force didn't allow the user to produce forces strong enough to oppose to the perceived force. Therefore a modified control force $\mathbf{F}_a^{\text{cont,sm}}$ for ship motion was defined.

It is recalled that the user control in case without ship motion is modelled in a way similar to the motive force, as follows:

$$\begin{aligned} &\mathbf{v}_a^0 = \mathbf{x}_a^0(t)\cdot v_a^{\max}, \\ &\mathbf{F}_a^{\text{contr}} = \frac{m_a}{\tau_a}\cdot\left(\mathbf{v}_a^0 - \mathbf{v}_a(t)\right) \end{aligned} \tag{9.2}$$

where τ_a $[\text{s}]$ is the relaxation parameter, m_a $[\text{kg}]$ is the mass of the avatar, $\mathbf{v}_a^0$ $[\text{m/s}]$ is the desired speed of the avatar which depends on the value of the axis $\mathbf{x}_a^0(t)$ set by the user through the controller ($\|\mathbf{x}_a(t)\| \le 1$) and has maximum magnitude $v_a^{0,\max}$ and $\mathbf{v}_a$ is the instantaneous speed of the avatar.

The control force $\mathbf{F}_A^{\text{contr}}$, however, does not allow the user to effectively oppose to high perceived acceleration as to this aim a stronger force is required.

For this reason, the parameter $v_{0,\max}$ is modified, referring to experimental values provided by Meyer-König et al. [135], to allow the user to oppose effectively to the external accelerations when they are detected. In particular, when in presence of ship motions, the maximum $v_{0,\max}$ is incremented by a value by $\delta v_{0,\max}$ which depends on the avatar perceived longitudinal angle γ_a^l. The control force in case of ship motion is hence defined as follows:

$$\begin{aligned} &v_a^{0,\max,\text{sm}}\left(\gamma_a^l, t\right) = v_{0,\max} + \delta v_{0,\max}\left(\gamma_a^l\right), \\ &\mathbf{v}_a^{0,\text{sm}} = \mathbf{x}_a(t)\cdot v_a^{\max,\text{sm}}, \\ &\mathbf{F}_a^{\text{contr,sm}} = \frac{m_a}{\tau_a}\cdot\left(\mathbf{v}_a^{0,\text{sm}} - \mathbf{v}_a(t)\right) \end{aligned} \tag{9.3}$$

where the avatar perceived longitudinal angle γ_a^l is defined considering $\mathbf{v}_a^{0,\text{sm}}$ in analogy with the definition of perceived longitudinal angle provided for agent in Chapter 7 (see Figure 7.2)):

In order to provide a meaningful relation between $\delta v_{0,\max}$ and the perceived longitudinal angle a limit situation is considered, namely the one of an upward inclination with

respect to the avatar motion. It is assumed that the avatar travels, with constant speed, exactly in the same direction of the inclination and has the desired speed set at its maximum value $\mathbf{v}_{0,\max}$. This situation is summarized by the following equilibrium condition between motive force and external force:

$$\frac{1}{\tau_A}\cdot\left(v_a^{0,\max}+\delta v_a^{0,\max}-v_s\right)+f_{\mathbf{v}_0}=0 \tag{9.4}$$

where v_s is the steady speed of the avatar, $\delta v_a^{0,\max}$ is the increment of the desired speed, $v_a^{0,\max}$ is the maximum possible speed of the avatar without ship motions and $f_{\mathbf{v}_0}$ is the component of the external force (per unit of mass) along $\mathbf{v}_a^0$. Assuming that the steady speed $\mathbf{v}_s$ is determined by the values provided by Meyer-König et al. [135] and reported in Figure 7.3, the new target speed value $v_{0,\max,\mathrm{sm}}(\gamma_l,t)$ is determined as follows:

$$v_{0,\max,\mathrm{sm}}(\gamma_l,t)=v_{0,\max}+\delta v_{0,\max}=-\tau\cdot f_{\mathbf{v}_0}+v_s(\gamma_l) \tag{9.5}$$

The definition of the parameter $\delta v_{0,\max}$ is obtained from equation (9.3):

$$\delta v_{0,\max}(\gamma_l)=-\tau\cdot f_{\mathbf{v}_0}+v_s(\gamma_l)+v_{0,\max} \tag{9.6}$$

where the value $\mathbf{v}_s(\gamma_l)$ is determined in accordance to agents model, by multiplying the maximum target speed $\mathbf{v}_{0,\max}$ with the reduction coefficients (see Figure 7.3).

Finally, the force exerted by the avatar (control force) is also clamped by the friction bound which is calculated in the same way as for the agent (see Chapter 7).

9.3 Haptic interface to perceive acceleration

The user is informed about the direction and magnitude of the forces perceived by the avatar f_a^{perc} through the use of the same haptic interface previously described in Chapter 5.

The vibrator which is opposite with respect to the force direction is activated in order to provide the user with a feedback of a pushing force oriented in the same direction as the perceived force. This is exemplified in Figure 2.8.

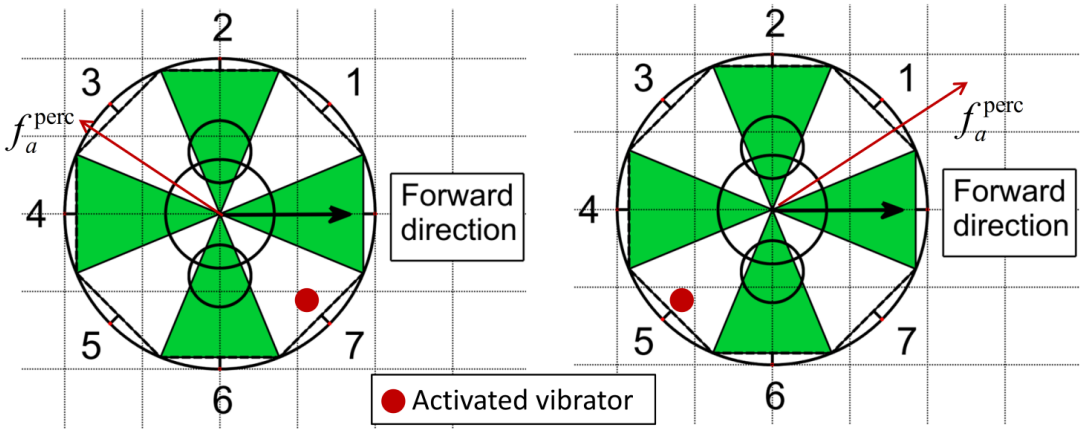

Figure 9.1: Examples of relation between perceived force by the avatar, and correspondingly activated vibrator.

The frequency of the vibration is constant and depends on the adopted vibrators. The vibrators should be active for a certain continuous amount of time δt_{imp} in order to be perceived. Some experiments were performed to calibrate this time amount and a value of 0.05 s was chosen, since it allows a sufficient perception of the vibrational impulse. The activation time is left constant. In the following one single activation of one actuator, lasting 0.05 s, will be called pulse.

The time elapsed between one pulse and another depends on the magnitude of the force. In particular at a time instant t a pulse is started or not in accordance to the following algorithm:

$$\begin{aligned} t - t_{last} &\geq I_a\left(F\left(t\right)\right) \Rightarrow \quad \text{start impulse} \\ t - t_{last} &< I_a\left(F\left(t\right)\right) \Rightarrow \quad \text{wait} \end{aligned} \tag{9.7}$$

where t_{last} [s] is the time instant where the last impulse was generated and $I_a\left(F\left(t\right)\right)$ [s] determines the relation between the force magnitude and the length of the time interval between the last generated impulse and the following.

Every time step one vibrator is actuated only if the time elapsed from the last activation is greater than the period associated with the provided force intensity.

A sketch of the generation of the impulses is provided by Figure 2.8. The figure is not in scale therefore should be considered only qualitatively. As an example, the time instant $t = t_{i+1}$ it is considered. At this time instant the last activation happened at $t_{last} = t_i$ and $t_{i+1} - t_i \leq I_a\left(f\left(t_{i+1}\right)\right)$ therefore another pulse is generated at $t = t_{i+1}$ .The interval $I_{i,i+1}$ is thus given by the value of the function I_a at the time instant $t = t_{i+1}$: $I_{i,i+1} = I_a\left(f\left(t_{i+1}\right)\right)$.

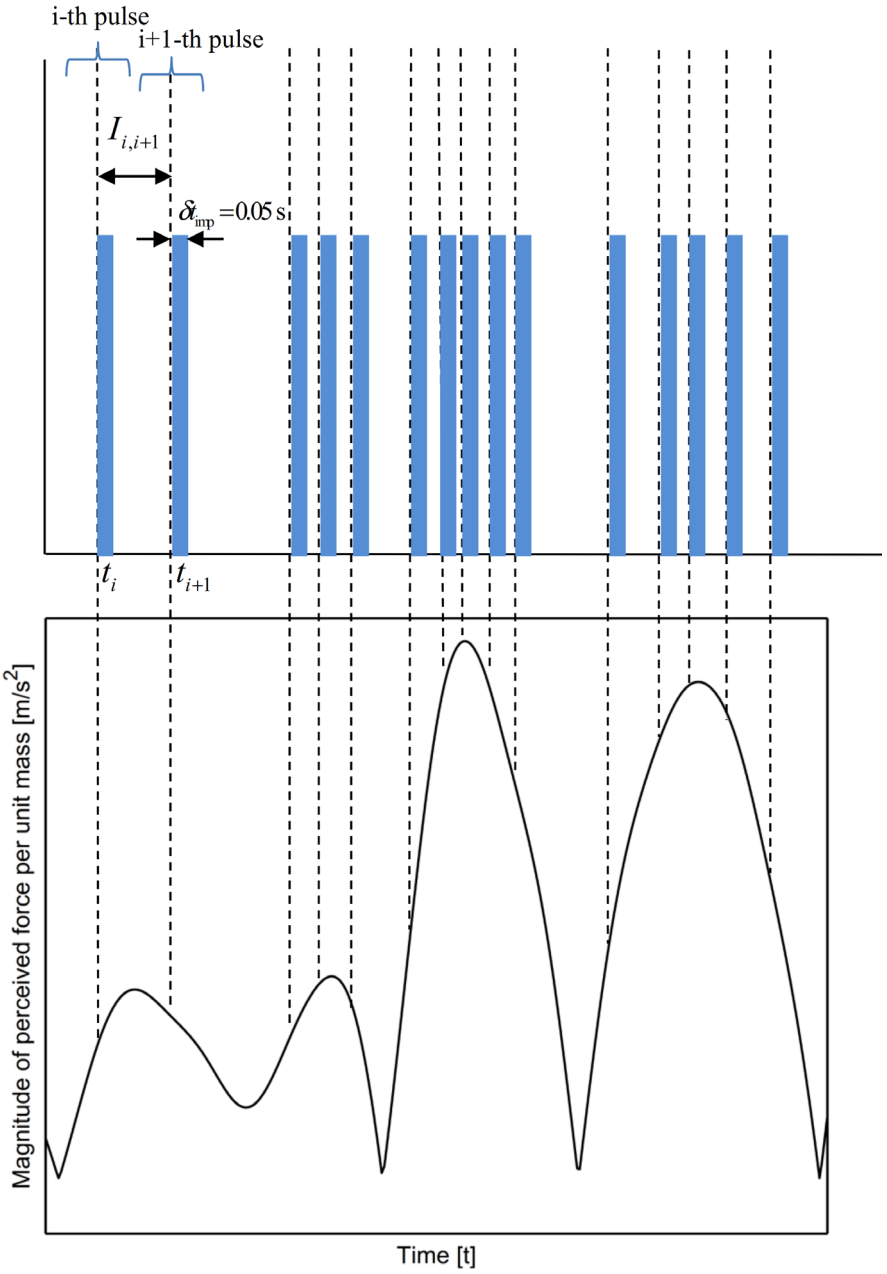

Figure 9.2: Dependence of the time interval between two vibration pulses used for the haptic interface and the perceived acceleration

The function $I_a(f)$, determining the relation between the force module and the length of the interval between two consecutive pulses, is described by the following parametric function which is also reported in figure 1:

$$\text{interv}(f)=\begin{cases} f\cdot\dfrac{\kappa_b-\kappa_a}{\phi_a}+\kappa_a & \text{if } f\in[0,\phi_a] \\ f\cdot\dfrac{\kappa_b}{\phi_b-\phi_a}-f_b\dfrac{\kappa_a}{\phi_b-\phi_a} & \text{if } f\in[\phi_a\ ,\phi_b] \\ 0 & \text{if } f>\phi_b \end{cases} \tag{9.8}$$

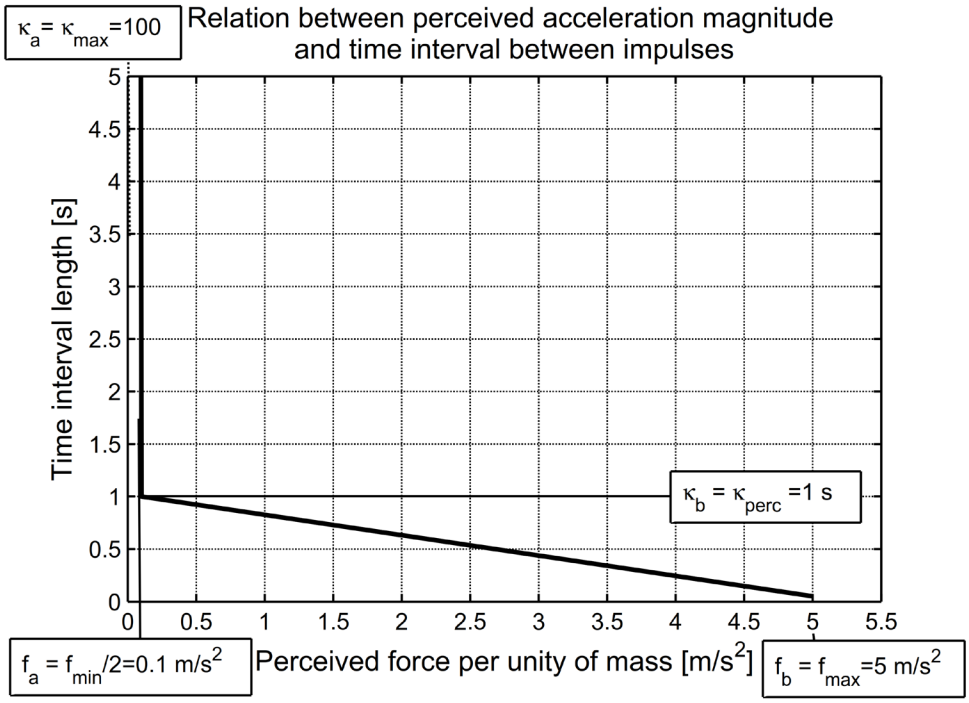

Figure 9.3: Dependence of the time interval between two vibration pulses used for the haptic interface and the perceived acceleration

The parameters of the function reported in (9.8), namely $\phi_a,\phi_b\ \left[m/s^2\right]$ and $\kappa_a,\kappa_b\ [s]$ are dependent on the following quantities:

- $f_{\min}\ \left[\text{m/s}^2\right]$ corresponds to the minimum force that can be communicated by the interface.
- $f_{\max}\ \left[\text{m/s}^2\right]$ is the force magnitude above which the vibrators activation interval is 0 seconds, i.e. activation intervals are continuous.
- $\tau_{\text{perc}}\ [\text{s}]$ represents the maximum possible time interval between two pulse so that the user perceives them as one consequential to another.
- $\tau_{\max}\ [\text{s}]$ is the maximum interval length value. The value is virtually infinite as the interval length should always grow as the force magnitude decreases. However, for robustness of the code, it was conventionally set to 100 s.

The determination of the parameters was carried out referring to simplified situations or empirically by performing some preliminary tests.

The value of $f_{\min}$ was chosen referring to a simplified situation. The considered condition is the one were the user is not moving the controller (i.e. the desired speed is zero). In this case

$$-\frac{1}{\tau_A}\cdot\dot{x}(t)+f=\ddot{x}(t) \tag{9.9}$$

where $\tau_A\,[\mathrm{s}]$ is the relaxation parameter and $\mathbf{x}(t)$ is the position of the avatar at time instant t. It is chosen not to consider forces leading to a steady velocity magnitude lower than 0.1 m/s. The steady velocity magnitude in the described condition is calculated as $f\cdot\tau_A$ thus the value of $f_{\min}$ is set equal to 0.2 m/s^2 ($\tau_A=0.5$ s).

The value for $f_{\max}$ was obtained from the bounds provided by Meyer-König et al. [135], in particular considering a maximum inclination of 30° and approximating the gravity acceleration to 10 m/s^2 we obtain that in this condition the force per unity of mass on the avatar is 5 m/s^2.

The parameters $t_{\mathrm{perc}}=t_b$ and f_a were more difficult to be determined with respect to the previous ones. This is due to the fact that they determine when the interface is able to communicate information to the user (through producing to pulses close enough to be interpreted as consecutive) and when the interface cannot communicate the information. It is thus required a formal definition of the concept of "communicating information".

Considering a series of impulses generated at intervals $I_1 \ldots I_n$ it is defined that one information is communicated by the interface to the user when the number of pulses n is equal or greater than 2 and the minimum interval is longer than $t_{\mathrm{perc}}=1\,[\mathrm{s}]$. The value $t_{\mathrm{perc}}=1\,[\mathrm{s}]$ and $f_a=f_{\min}/2$ were found reasonable, considering that communication, at least, should occur, for a period larger than 10°(it is observed that ships for which evacuation analysis is typically relevant have roll periods which are typically above 10 s) and amplitudes larger than $f_{\min}$.

A plot of the impulse in correspondence to the magnitude of the perceived acceleration is provided in Figure 9.4, where the impulses are generated starting from the motion generated in the irregular waves condition described in Chapter 8 with Hs=12 m and no superimposed heel.

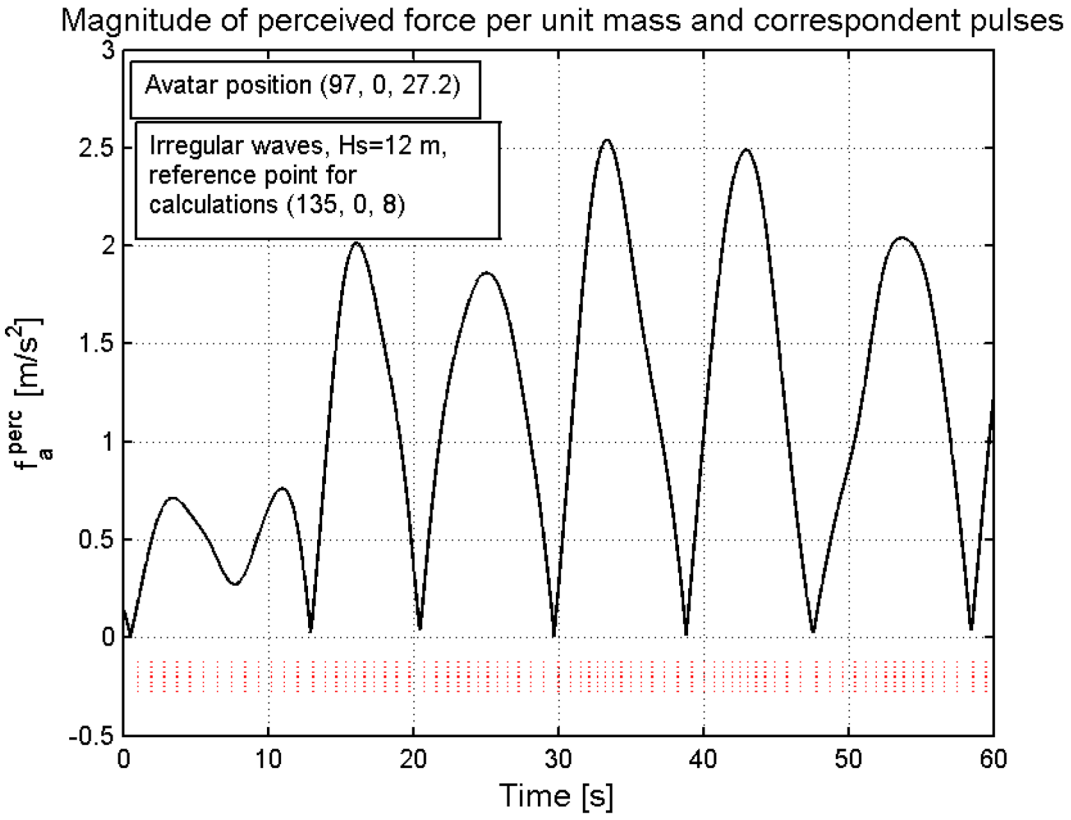

Figure 9.4: Example of magnitude of the external acceleration and correspondingly generated pulses.

Some preliminary tests have been performed with the described haptic interface to verify the correct implementation of the model. The performed tests showed that the interface effectively communicates the direction and the magnitude of the force to the users through impulses. However, experiments have not been performed, and are therefore needed, to acquire enough information on the effect of the interface on users' behaviour, and, more generally, on the behaviour of users when the avatar they control is affected by ship motions.

9.4 Final remarks

A model to account for the effects of ship motions on the avatar controlled by the user has been described.According to the developed model the perceived forces are applied entirely to the avatar. At the same time the maximum desired speed of the avatar is incremented in order to allow the user to balance, to some extent, the perceived forces through a potentially increased maximum motive force.

A vibrotactile interface was ideated and developed to communicate the magnitude and the direction of the perceived forces to the user through vibration impulses.

The model was implemented in the developed tool and verified. However, tests needs to be performed in order to obtain information related to the behaviour of user when the avatar is affected by ship motion. The effect of the developed haptic interface needs also to be assessed through experiments.

This page is intentionally left blank

10 CONCLUSIONS

The research described in this dissertation presented the development, implementation and application of a mathematical model for simulating the dynamics of evacuation processes, which also allows real time human interaction through the use of virtual reality. The research targeted, in particular, the maritime field.

The present research provided contributions to the following main topics:

- Modelling of evacuation dynamics specifically addressing the advanced evacuation analysis mentioned in IMO MSC.1/Circ.1533 [147].
- Application of virtual reality and haptic interfaces to the field of evacuation dynamics.
- Introduction of the effects of ship motions in the evacuation models.

10.1 Mathematical models for evacuation dynamics

The dissertation reported a detailed description of an evacuation model developed during the present research. The model is based on, and introduces a series of modifications to, the social-force approach by Helbing and Molnar [71] and the model embedded in the software FDS+Evac (Korhonen [112]). The mathematical model allows a natural integration with real time human interaction through the use of virtual reality. The implementation of the developed model was also discussed highlighting benefits and limitations of the chosen development environment.

Particular relevance was given to the process of calibration and sensitivity analysis of the parameters of the counterflow model which was developed in the present research, with particular focus on the parameters governing the counterflow force intensity and the level of interaction with agents not fully oriented towards the desired direction. Calibration and sensitivity analysis were carried out through comparison with experimental data and using IMO suggested tests 4 and 8 (MSC.1/Circ.1533 [147]).

The process of verification and validation of the developed evacuation model was carried out through comparisons with other models and with experimental outcomes and by referring to IMO test cases suggested in MSC.1/Circ.1533 [147]. The tool was able to fulfill the requirements of all test cases specified by MSC.1/Circ.1533 [147]. However, qualitative differences have been detected in the comparisons with the outcomes from other evacuation models, especially in IMO tests 4, 8 and 11.

The capability of the developed model of correctly reproducing the flow-density relation was assessed through comparisons with experimental data in two different test conditions: one considering unidirectional flow in a corridor, and the other one considering the flow in a T junction. The model proved to be able to qualitatively reproduce the experimental data in both conditions. Simulation results in unidirectional flow, however, showed a discontinuity in the flow-density graph which was not present in experimental data, and this might be due to the fact that humans can organize better than simulated agents when exiting from the bottleneck at the end of the corridor.

The capability of the tool of correctly simulating the exit from a bottleneck was proved by comparison with experimental data. Although, qualitatively, the density and the flow followed the trend observed from the experiments, the model, with default parameters, tends to underestimate the density and to overestimate the speed. A possible modification of some of the model parameters was tested, which allowed a better match with experimental results.

The capability of correctly reproducing a counterflow condition was assessed by comparison with experimental data. The model correctly reproduced the qualitative behaviour observed in the experiments, and, in addition, quantitative experimental outcomes were also correctly reproduced.

Finally a more realistic test case, more specific to the maritime field, was proposed. The geometry of the proposed test case was derived as a simplification of the SAFEGUARD Validation Data Set 2 (SGVDS2 - Galea et al. [54]): it comprises three decks connected by staircases, with the two uppermost being cabin decks. A simplified evacuation condition is simulated with the developed software, considering all cabins occupied. Detailed results have been reported in terms of total assembly duration, density in different areas close to the stairs, number of agents in different regions of the geometry. In all cases results from the Monte Carlo simulations have been reported by highlighting and quantifying the underlying aleatory uncertainty. All necessary information has been provided to allow a reproduction of the proposed two-cabin-deck test case, which could be used for comparisons among different mathematical models/tools.

In summary, the developed model was able to qualitatively reproduce most of the observed human behaviour and to obtain a satisfactory quantitative match with the available experimental data. Moreover the model proved to be suitable for the advanced evacuation analysis as mentioned in IMO MSC.1/Circ.1533 [147].

10.2 Use of virtual reality in evacuation models

Real time user interaction was made possible in the developed tool through the design and implementation of different input and output interfaces. Moreover, a vibrotactile interface was developed to enhance the users' perception of the surrounding environment.

Three different experiments using fully immersive virtual reality and the developed haptic interface were performed considering the counterflow condition proposed in MSC.1/Circ.1533 [147].

The first experiment, where subjects were asked to behave naturally, showed statistically significant differences between users and computer controlled agents. It was conjectured that the difference related to the short time distance interval could be due to the attitude of most of the users to overcome slow agents and not respect lanes. Moreover the analyses of travelled path and trajectories showed that the dispersion is the most relevant difference between experimental and simulation data. This difference may indicate that the modelled behaviour of agents underestimates the actual variability in the behaviour of real humans. In addition, the analysis of the trajectories showed that users seem to show a long range interaction behaviour which is not reflected by the short range interaction model developed herein.

The first experiment showed no statistically significant differences between the outcomes with and without the developed haptic interface. One of the possible causes of absence of evident effects of the haptic interface in the presented test case may be the fact that users were not explicitly instructed to avoid agents. To further investigate the reason of the lack of effects of the haptic interface two other experiments were performed. One experiment was carried out directly instructing the subjects to avoid agents while in the other experiment agents were not rendered. A difference in users' behaviour with and without haptic interface is clearly present when the visual and audio interfaces do not provide information about the simulated agents positions and presence. The developed haptic interface is thus effective in informing the user about the proximity of agents, but it may be conjectured that, in normal conditions, visual and audio information dominate over the vibrotactile one. Moreover, the analysis of the differences on the way users utilize the controller showed analogies between the situation where agents were not rendered but perceived by means of the haptic interface and the situation where agents were rendered. This suggests that users control the avatar in a similar way when perceiving the presence of agents only by vibration or only by vision. While the most marked difference between haptic and non-haptic outcomes in terms of use of controller was found in the test case with the highest density, the test case with the lowest density presented the sharpest difference in terms of travelled path. This can be explained by the fact that, in the situation of highest density, users are more constrained and thus unable to modify their path. However, only further research might clarify if this result is strictly related to the specific adopted haptic interface and to the considered test case, or it can be instead considered more generally applicable to evacuation experiments with virtual reality.

10.3 Ship motion effects in evacuation models

A new model capable of considering the effects of ship motions not only as a reduction of the desired speed of the agents, but also as a modification of their trajectory, has been developed and presented. The model has been described in detail with all the associated parameters. Finally, an implementation of the developed model was presented. In particular, results from IMO test 4 and test 8, performed with different periodic ship motions and different heel and trim angles have been reported.

The herein developed two-cabin decks test case was run also with ship motions scenarios: the first set of scenarios comprised fixed geometry (calm water) and standard notional inclinations/motions conditions (heel, trim, dynamic roll). The latter were based on the conditions suggested by Nicholl et al. [158] with the addition of a combined heel and trim scenario. Evacuation results in the considered standard scenarios indicate a marked effect of the 20° heel condition, with a corresponding almost doubling of the total assembly duration compared to the case of upright vessel. This is the result of both the reduction of unimpeded speed and of the direct action of external forces parallel to the deck induced by the inclination. The reduction of the unimpeded speed leads, in general, to an increase of the time it takes to the agent to arrive at the designated assembly station. In addition, since, according to the model used for the agent control forces, agents are not able to fully balance forces parallel to deck at 20° of inclination, this eventually leads to a modification of the trajectories of the agents compared to the upright case. This modification leads to significantly asymmetric agents configurations, which eventually results in a further increase of the total assembly time. The dynamic roll considered in the standard scenarios was characterised by 5° of amplitude and 20 s of period. However, its effect was found to be, overall, limited. The combined case of 20° of heel and 10° of trim significantly impacted the evacuation performance, with situations where not all the agents were able to evacuate in the time limit of 30 min, which was specified as maximum time for each single simulation.

The same geometry was then used for evacuation simulations using more realistic ship motions which have been computed considering that the test geometry is placed onboard of a notional cruise vessel, and considering long-crested irregular beam waves. The dimensions of the considered notional cruise vessel are approximately in line with the vessel from which the test geometry was originally derived. In order to provide input for evacuation simulations, ship motions have been generated starting from transfer functions determined from linear seakeeping calculations. In addition, static heel was also considered, as a superimposed bias. The obtained results indicate that the effect of dynamic motions is limited, unless the significant wave height is very large. This appears to be a consequence of the overall large dimensions of the vessel, which leads to limited motions in absolute terms, and of the long natural roll period, which leads to relatively small accelerations. However, it should be observed that, due to lacking of relevant reference data, the present model does not account for the possible psychological effects of the vertical component of the perceived acceleration. In fact, the variation of the vertical (normal to deck) acceleration might also have an impact on the desired speed of the passengers, which might eventually lead to an increase of the exit times. The analysis of available data provided detailed information regarding the behaviour of agents with and without ship motions. The ensemble domain statistical

analysis carried out of the Monte Carlo simulations allowed to clearly highlight peculiar characteristics of the evacuation process in presence of static inclinations and/or dynamic motions, particularly in front of the stairs entrance and along the cabins corridor.

10.4 Future developements

The described research opened different scenarios that still remain to be deeply explored.

From the modelling point of view additional validation tests and parameters sensitiveness analysis might be required for a reliable use of the developed model.

Considering the implementation of the virtual reality, this research has shown the possibility to apply virtual reality to the field of evacuation simulation. However, only one test condition was analysed through the use of virtual reality. The developed tool could be adopted to perform more experiments to gather additional data on human behaviour in different conditions (such as exit from a bottleneck, or ascending a stair) and compare the behaviour with real experiments.

Considering the modelling of the effects of ship motions, the presented model might be considered as a "quasi-static" one. In fact, the effects of ship motions on agents depend on the direction and magnitude of the instantaneous perceived force in a generic dynamic condition, but reference parameters are based on experiments carried out in static conditions. More advanced models, accounting for experiments carried out in dynamic conditions, would be necessary to describe human behaviour in presence of ship motions in a more accurate way. It is therefore advisable that, in the future, more detailed experimental data sets on the effect of dynamic motions could be made available to develop, validate and calibrate more advanced evacuation models.

The developed haptic interface has shown no evident effects on human behaviour in evacuation and this was proven to be mostly due to the major influence of visual perception with respect to the haptic perception. However it remains to be explored if the use of different haptic interfaces might induce different effects.

Further researches might investigate the possibility to convey other complex information through haptic stimuli (e.g. accelerations during impacts), also employing specific haptic devices to other body areas such as feet (avoiding stepping on other feet, as an example, is among people greatest concerns in mid-density conditions). The, avatar radius might also be matched with the one of the subjects allowing studying subjects with different body sizes.

The haptic interface proved to be effective when visual information is not available (i.e. not rendered agents). The developed haptic interface might, thus, be applied under different conditions from those tested in the performed experiment, such as evacuations with smoke and reduced visibility or evacuation in dark tunnels.

Morover the interface might be used to communicate information which is not possible to communicate through visual interfaces, such as the acceleration. This latest

possibility was partially explored, still in the field of interactive virtual reality simulation in the maritime field, with the development of a model proposed to embed the effects of the ship motions on user control and increase its perception of accelerations. The theorized model, however, still needs to be tested in an experiment in order to verify its effectiveness.

Other possibilities of increasing the feeling of presence of the user in the simulation with virtual reality, not explored in the present study, are represented by the development of more intuitive control interfaces, by the increase of the level of graphic and sound details and by the development of different haptic interfaces such as moving platforms to simulate ship motions.

The development of reliable evacuation simulation models for advanced evacuation analysis is still an on-going process. The use of virtual reality in the evacuation field is an emergent technique and thus still requires a great effort to become fully functional. It is hoped that the models, the results and the novelties presented in this dissertation could contribute to the development of more reliable evacuation models and to the spreading of the use of virtual reality in the ship evacuation field, for the design of safer ships and for a more thorough and accurate assessment of ship evacuation performance.

This page is intentionally left blank

REFERENCES

[1] Aguirre, B. E., El-Tawil, S., Best, E., Gill, K. B., and Fedorov, V., 2011. Contributions of social science to agent-based models of building evacuation. Contemporary Social Science, 6(3), pp. 415-432..

[2] Ashraf Tashrifullahi, S., and Hassanain, M. A. 2013. A simulation model for emergency evacuation time of a library facility using EVACNET4. Structural Survey, 31(2), pp. 75-92.

[3] Bačkalov, I., Bulian, G., Cichowicz, J., Eliopoulou, E., Konovessis, D., Leguen, J.-F., Rosén, A. and Themelis, N., 2016. Ship stability, dynamics and safety: Status and perspectives from a review of recent STAB conferences and ISSW events. Ocean Engineering, Vol. 116, 312-349, doi: 10.1016/j.oceaneng.2016.02.016.

[4] Balakhontceva, M., Karbovskii, V., Rybokonenko, D., and Boukhanovsky, A., 2015. Multi-agent simulation of passenger evacuation considering ship motions. Procedia Computer Science, 66, pp. 140-149.

[5] Baochen, Ni, Zehn Li, Xiang Li, 2017. Agent-based evacuation in passenger using a goal-driven decision making model. Polish Maritime research 24(2), pp. 56-67.

[6] Bark, K., Wheeler, J. W., Premakumar, S., and Cutkosky, M. R. 2008. Comparison of skin stretch and vibrotactile stimulation for feedback of proprioceptive information. In: Symposium on Haptic interfaces for virtual environment and teleoperator systems,IEEE, 13-14 March, Reno, NV, USA. pp. 71-78.

[7] Batty, M., Editorial of: Environment and Planning B: Planning and Design, 28, 2001, pp. 321 – 326.

[8] Bellomo, N., Piccoli, B., and Tosin, A. 2012. Modeling crowd dynamics from a complex system viewpoint. Mathematical models and methods in applied sciences, 22(supp02), 1230004.

[9] Berrou, J., Beecham, J., Quaglia, P., Kagarlis, M., and Gerodimos, A., 2007. Calibration and validation of the Legion simulation model using empirical data. Pedestrian and Evacuation Dynamics 2005, 167-181.

[10] Bles, W., Novy, S., and Boer, L.C., 2002. Influence of Ship Listing and Ship Motion on Walking Speed, In: Pedestrian and Evacuation Dynamics (PED), Berlin, Springer.

[11] Bloomfield, A., and Badler, N. I., 2003. Enhanced collision perception using tactile feedback. University of Pennsylvania Department of Computer and Information Science Technical Report No. MS-CIS-03-45.

[12] BMT.2007, S-CAPE. https://www.bmt.org/media/380169/S-CAPE.pdf.User manual. Last accessed 17/11/2017.

[13] Bode, N.W., Wagoum, A.U.K. and Codling, E.A., 2014. Human responses to multiple sources of directional information in virtual crowd evacuations. Journal of The Royal Society Interface 11(91): 20130904..

[14] Bos, J.E., Valk, P.J.L., Ledegang, W.D. and Nienhuis, B., 2013. Heavy Weather Ship Handling Simulation With and Without Motion. In: Proc. 13th International Ship Stability Workshop, 23-26 September, Brest, France..

[15] Bossman, S, Groenendaal, B. B., Findlater, J., Visser, T.and Markopoulos, P. P., 2003. Gentleguide: an exploration of haptic output for pedestrian guidance. In: Proceedings of International Conference on Mobile Human-Computer Interaction, Mobile HCI 2003, Human-Computer Interaction with Mobile Devices and Services. September 8-11, Udine, Italy. pp. 358-362.

[16] Bowman, D. A., Koller, D.and Hodges, L. F.,1998. A methodology for the evaluation of travel techniques for immersive virtual environments. Virtual reality, 3(2), pp. 120-131.

[17] Brown, R., Galea, E. R., Deere, S. and Filippidis, L., 2013. Passenger response time data-sets for large passenger ferries and cruise ships derived from sea trials. Transactions of the Royal Institution of Naval Architects, International Journal of Maritime Engineering, 155(A1), pp. 33-48.

[18] Brumley, A., and Koss, L., 1998. The Implication of Human Behaviour on the Evacuation of Ferries and Cruise Ships, Proceedings of AME`98, Australian Maritime Engineering, CRC Annual Post-Graduate Conference.

[19] Buckman, L. T., and Leather, J. A., 1994. Modelling station congestion the PEDROUTE way. Traffic engineering and control, 35(6), pp. 373-377.

[20] Bulian, G., Francescutto, A., 2009. Experimental results and numerical simulations on strongly nonlinear rolling of multihulls in moderate beam seas. Proceedings of the Institution of Mechanical Engineers - Part M Journal of Engineering for the Maritime Environment, Vol. 223, 189-210, DOI: 10.1243/14750902JEME126.

[21] Campanella, M., Hoogendoorn, S., and Daamen, W., 2009. Improving the Nomad microscopic walker model. IFAC Proceedings Volumes, 42(15), pp. 12-18.

[22] Chattaraj, U., Seyfried, A., Chakroborty, P., 2009. Comparison of pedestrian fundamental diagram across cultures. Advances in complex systems, 12(03), pp. 393-405.

[23] Chatterjee, A., Chaubey, P., Martin, J., and Thakor, N. V.,2008. Quantifying prosthesis control improvements using a vibrotactile representation of grip force. In: Region 5 Conference, 2008 IEEE pp. 1-5. IEEE.

[24] Chen, J., Ma, J., and Lo, S., 2016. Modelling Pedestrian Evacuation Movement on a Swaying Ship. In Traffic and Granular Flow'15, pp. 297-304.

[25] Chu, G., Sun, J., Wang, Q., and Chen, S., 2006. Simulation study on the effect of pre-evacuation time and exit width on evacuation. Chinese Science Bulletin, 51(11), pp. 1381-1388.

[26] Colombo, R. M., and Rosini M.,D., 2005. Pedestrian flows and non-classical shocks. Mathematical Methods in the Applied Sciences 28, 13, pp. 1553-1567.

[27] Colombo, R. M., Garavello, M. and Lécureux-Mercier,M.,2012. A class of nonlocal models for pedestrian traffic. Mathematical Models and Methods in Applied Sciences, 4, 1150023.

[28] Combustion Science & Engeneering Inc., 2015. International Survey of Computer Models for Fire and Smoke: egrees models. Avaliable online http://www.firemodelsurvey.com/EgressModels.html. Last accessed 20/11/2017 Combustion Science & Engeneering Inc.

[29] Crossland, P. 2003.The influence of ship motion induced lateral acceleration on walking speed, In: Pedestrian and Evacuation Dynamics 2003, London, UK, pp. 245-256.

[30] Cummins, W.E., 1962. The Impulse Response Function and Ship Motions. Schiffstechnik, Vol. 47, pp. 101-109.

[31] D'Orazio, M., Spalazzi, L., Quagliarini, E., and Bernardini, G., 2014. Agent-based model for earthquake pedestrians' evacuation in urban outdoor scenarios: Behavioural patterns definition and evacuation paths choice. Safety Science, 62, pp. 450-465.

[32] Daamen, W., 2002. SimPed: a pedestrian simulation tool for large pedestrian areas. In: Conference Proceedings EuroSIW. June 24-26. London. UK. pp. 24-26.

[33] Deere, S. J., Galea, E. R., Filippidis, L. and Brown, R., 2012. Data collection methodologies used in the SAFEGUARD project to collect human factors data. In: RINA SAFEGUARD Passenger Evacuation Seminar, 30 November. London, UK, pp. 13-23.

[34] Deere, S.J., 2012. Ship design with the human factor: evacuation and normal operations modelling in the ship design process. PhD Thesis, University of Greenwich.

[35] Degond, P., Appert-Rolland, C., Moussaid, M., Pettré, J.and Theraulaz, G., 2013. A hierarchy of heuristic-based models of crowd dynamics. Journal of Statistical Physics, 152(6), pp. 1033-1068.

[36] Der Kiureghian, A., and Ditlevsen, O., 2009. Aleatory or epistemic? Does it matter?. Structural Safety, 31(2), pp. 105-112.

[37] Desdemona, 2017. The next generation in motion simulation. http://www.desdemona.eu . Last accessed on 25 November 2017..

[38] Donegan,H.A. ,Pollock, A.J. and Taylor, I.R., 1994. Egress Complexity of a Building. Fire Safety Science, 4, pp. 601-612.

[39] Dressler, D., Groß, M., Kappmeier, J. P., Kelter, T., Kulbatzki, J., Plümpe, D., and Temme, S., 2010. On the use of network flow techniques for assigning evacuees to exits. Procedia Engineering, 3, pp. 205-215.

[40] Drury, J., Cocking, C., Reicher, S., Burton, A., Schofield, D., Hardwick, A., and Langston, P., 2009. Cooperation versus competition in a mass emergency evacuation: A new laboratory simulation and a new theoretical model. Behavior research methods, 41(3), pp. 957-970.

[41] Duives, D. C., Daamen, W. and Hoogendoorn, S. P., 2013. State-of-the-art crowd motion simulation models. Transportation research part C: emerging technologies, 37, pp. 193-209.

[42] Epic Games, Inc, 2017. Unreal Engine documentation. Avaliable online at https://docs.unrealengine.com/latest/INT/, last accessed on 20 Novemebr 2017.

[43] Fahy, R.F., 1994. Exit 89-an Evacuation Model For High-rise Buildings-model Description And Example Applications. Fire Safety Science 4, pp.657-668.

[44] Fang, Z., Song, W., Zhang, J., and Wu, H., 2010. Experiment and modeling of exit-selecting behaviors during a building evacuation. Physica A: Statistical Mechanics and its Applications, 389(4), pp. 815-824.

[45] Feinberg, W. E., and Johnson, N. R., 1995. Firescap: A computer simulation model of reaction to a fire alarm. Journal of Mathematical Sociology, 20(2-3), pp. 247-269.

[46] Feliciani, C., and Nishinari, K. 2016. An improved Cellular Automata model to simulate the behavior of high density crowd and validation by experimental data. Physica A: Statistical Mechanics and its Applications, 451, pp. 135-148.

[47] Feng, M., Dey, A., and Lindeman, R. W., 2016. An initial exploration of a multi-sensory design space: Tactile support for walking in immersive virtual environments. In: Proceedings. of IEEE Symposium on 3D User Interfaces (3DUI), pp. 95-104. 19-20 March, Los Angeles, California (USA).

[48] Filippoupolitis, A., Gelenbe, E., Gianni, D., Hey, L., Loukas, G., and Timotheou, S., 2012. Distributed agent-based building evacuation simulator. In: Summer Computer Simulation Conference 2008 (SCSC'08): Part of the 2008 Summer Simulation Multiconference. Curran Associates, Inc., Red Hook, NY, USA, pp. 46-53.

[49] Flores, G., Kurniawan, S., Manduchi, R., Martinson, E., Morales, L. M., and Sisbot, E. A., 2015. Vibrotactile guidance for wayfinding of blind walkers. IEEE transactions on haptics, 8(3), pp. 306-317.

[50] Frank, W., 1967. Oscillation of cylinders in or below the free surface of deep fluids. Report No. 2375, Naval Ship Research and Development Center, 1967.

[51] Fraser-Mitchell, J. N., 1999. Modelling human behaviour within the fire risk assessment tool CRISP. Fire and Materials, 23(6), pp. 349-355.

[52] FSS CODE, International Code For Fire Safety System, 2016. - Consolidated Edition as of 2016, International Maritime Organization (IMO), London, UK.

[53] Galea, E., Gwynne, S., Blackshields, D., Filippidis, L., and Lawrence, P., 2001.In: Predicting the evacuation performance of passenger ships using computer simulation, Vol. 2, pp. 853-864. Interscience Communications Ltd.

[54] Galea, E.R., Deere, S., and Filippidis, L., 2012. The SAFEGUARD validation data set. A guide to data and validation procedures – SVGDS2. Fire Safatey Engeneering Group, University of Greenwich, Downloadable from http://fseg.gre.ac.uk/validation/ship_evacuation last accessed on 8 December 2017.

[55] Galea, E.R., Deere, S., Brown, R. and Filippidis, L., 2013. An Experimental Validation of an Evacuation Model using Data Sets Generated from Two Large Passenger Ships. Journal of Ship Research, 57, pp. 155–170.

[56] Galea, E.R., Lawrence, P., Gwynne, S., Sharp, G., Hurst, N., Wang, Z. and Ewer, J., 2004. Integrated fire and evacuation in maritime environments. In: Proceedings of the 2nd International Maritime Conference on Design for Safety, pp. 183-192, October 27-30. Sakai, Japan.

[57] Ginnis, A. I., Kostas, K. V., Politis, C. G. and Kaklis, P. D., 2010. VELOS: A VR platform for ship-evacuation analysis. Computer-Aided Design, 42(11), pp. 1045-1058.

[58] Ginnis, A. I., Kostas, K. V., Politis, C. G. and Kaklis, P. D., 2015. VELOS-A VR environment for ship applications: current status and planned extensions. Virtual Realities, Volume 8844 of the series Lecture Notes in Computer Science, Springer International Publishing., pp. 33-55.

[59] Glen, I. 2004. BMT Fleet Technology: Conference Documentation. 1st International Conference on Escape, Evacuation and Recovery, Lloyd's List.

[60] Graham, R., 1990. Motion-Induced Interruptions as Ship Operability Criteria. Naval Engineers Journal, 102(2), pp. 65-71.

[61] Graham, R., Baitis, A. E., and Meyers, W. G., 1992. On the development of seakeeping criteria. Naval Engineers Journal, 104(3), pp. 259-275.

[62] Granberg, A., 2016. http://arongranberg.com/astar/. Last accessed 3 October 2016.

[63] Guarin, L., Hifi, Y. and Vassalos, D., 2014. Passenger Ship Evacuation–Design and Verification. In Virtual, Augmented and Mixed Reality. Applications of Virtual and Augmented Reality. Part of the Lecture Notes in Computer Science book series (LNCS, volume 8526), Springer International Publishing, pp. 354-365.

[64] Guo, R. Y., 2014. Simulation of spatial and temporal separation of pedestrian counter flow through a bottleneck. Physica A: Statistical Mechanics and its Applications, 415, pp. 428-439.

[65] Ha, S., Ku, N. K., Roh, M. I., Lee, K. Y., 2012. Cell-based evacuation simulation considering human behaviour in a passenger ship. Ocean Engineering, 53, pp. 138-152.

[66] Hanyok, L. W. 2013. Methods for Calculating Motion Induced Interruptions as Applied to a Space Capsule After Splashdown. Phd thesis, Virginia Tech.

[67] Harmon, M., and Joseph, J., 2011. Evacuation Planning Tool (EPT) for Emergency, Event and Space Planning. In: Pedestrian and Evacuation Dynamics, Springer, Boston, MA.pp. 785-788.

[68] Hart, P. E., Nilsson, N. J., and Raphael, B., 1968. A formal basis for the heuristic determination of minimum cost paths. IEEE transactions on Systems Science and Cybernetics, 4(2), pp. 100-107.

[69] Helbing, D. and Balietti, S., 2013. How to Do Agent-Based Simulations in the Future: From Modeling Social Mechanisms to Emergent Phenomena and Interactive Systems Design . Chapter "Agent-Based Modeling" of the book "Social Self-Organization" by Dirk Helbing (Springer, Berlin, 2012), 25-70. (Available at SSRN: https://ssrn.com/abstract=2339770)

[70] Helbing, D., and Johansson, A., 2011. Pedestrian, crowd and evacuation dynamics. Extreme Environmental Events. pp. 697-716.

[71] Helbing, D., and Molnar, P., 1995. Social force model for pedestrian dynamics. Physical Review E, 51(5), pp. 4282-4286.

[72] Helbing, D., Farkas, I. J., Molnar, P., and Vicsek, T., 2002. Simulation of pedestrian crowds in normal and evacuation situations. Pedestrian and evacuation dynamics, 21(2), pp. 21-58.

[73] Helbing, D., Farkas, I., and Vicsek, T., 2000. Simulating dynamical features of escape panic. Nature, 407(6803), pp. 487-490.

[74] Helbing, D., Johansson, A. and Al-Abideen, H.Z., 2007. Dynamics of crowd disasters: An empirical study. Physical Review E, 75, 046109.

[75] Heliövaara, S., Ehtamo, H., Helbing, D. and Korhonen, T., 2013. Patient and impatient pedestrians in a spatial game for egress congestion. Physical Review E, 87(1), 012802.

[76] Heliövaara, S., Korhonen, T., Hostikka, S. and Ehtamo, H., 2012. Counterflow model for agent-based simulation of crowd dynamics. Building and Environment, 48, pp. 89-100.

[77] Helton, J. C., and Burmaster, D. E., 1996. Guest editorial: treatment of aleatory and epistemic uncertainty in performance assessments for complex systems. Reliability Engineering and System Safety, 54(2), pp. 91-94.

[78] Henderson, L. F., 1974. On the fluid mechanics of human crowd motion. Transportation Research, 8(6), pp. 509-515.

[79] Henningsson, J. and Blomstrand Martén, J., 2014. Verification and Validation of Viswalk for Building Evacuation Modelling. Report 5481, Department of Fire Safety Engineering, Lund University. Downloadable at http://lup.lub.lu.se/student-papers/record/5337197, last accessed on 8 December 2017.

[80] Heskestad, A.W., Jensen, G. , Meland, O. and Torlen, E., 1995. ALLSAFE: An EngineeringTool for Evacuation Safety Design. In: Proceedings of the Fire Safety by DesignConference, 10-12 July, St Peter's Campus University of Sunderland, UK. Volume 3, pp. 71-80.

[81] Hoogendoorn, S., and Bovy, P., 2000. Gas-kinetic modeling and simulation of pedestrian flows. Transportation Research Record: Journal of the Transportation Research Board, (1710), pp. 28-36.

[82] Hughes, R. L. (2002). A continuum theory for the flow of pedestrians. Transportation Research Part B: Methodological, 36(6), pp. 507-535.

[83] Hughes, R. L., 2003. The flow of human crowds. Annual review of fluid mechanics, 35(1), pp. 169-182.

[84] Hupont, I., Gracia, J., Sanagustin, L., and Gracia, M. A., 2015. How do new visual immersive systems influence gaming QoE? A use case of serious gaming with Oculus Rift. In: 7th International Workshop on Quality of Multimedia Experience (QoMEX), IEEE, pp. 1-6. 26-28 May, Costa Navarino, Greece.

[85] Hystad, S.W., Olaniyan, O.S., Eid, J., 2016. Safe travel: passenger assessment of trust and safety during seafaring. Transp. Res. Part F Traffic Psychol. Behav. 38, pp. 29–36.

[86] IMO, 2000. International Code of Safety for High-Speed Craft, 2000 (2000 HSC Code). IMO, London, UK.

[87] IMO, 2016. International convention for the Safety of Life at Sea (SOLAS). Consolidated edition as of 2016.

[88] IMO, 2017. Introduction to IMO. www.imo.org/en/About/Pages/Default.aspx. Last accessed on 01/12/2017.

[89] Isobe, M., Adachi, T., Nagatani, T., 2004. Experiment and simulation of pedestrian counter flow. Physica A: Statistical Mechanics and its Applications, 336(3), pp. 638-650.

[90] Isobe, M., Helbing, D., and Nagatani, T., 2004. Experiment, theory, and simulation of the evacuation of a room without visibility. Physical Review E, 69(6), pp. 066132.

[91] ITTC, 2005. Recommended Procedure 7.5-02-07-04.2 - Model Tests on Damage Stability in Waves – Revision 02.

[92] ITTC, 2008. Recommended Procedure 7.5-02-07-04.1 - Model Tests on Intact Stability – Revision 02.

[93] Jennings, N. R., 2000. On agent-based software engineering. Artificial intelligence, 117(2), pp. 277-296.

[94] Jiang, Y. Q., Guo, R. Y., Tian, F. B. and Zhou, S. G., 2016. Macroscopic modeling of pedestrian flow based on a second-order predictive dynamic model. Applied Mathematical Modelling, 40(23), pp. 9806-9820.

[95] Jiang, Y. Q., Zhang, P., Wong, S. C. and Liu, R. X., 2010. A higher-order macroscopic model for pedestrian flows. Physica A: Statistical Mechanics and its Applications, 389(21), pp. 4623-4635.

[96] Johansson, A., Helbing, D., and Shukla, P. K., 2007. Specification of the social force pedestrian model by evolutionary adjustment to video tracking data. Advances in Complex Systems, 10(supp02), pp. 271-288.

[97] Johansson, F., Peterson, A., Tapani, A., 2015. Waiting pedestrians in the social force model. Physica A: Statistical Mechanics and its Applications, 419, pp. 95-107.

[98] Joyce, R. D., and Robinson, S., 2017. Passive Haptics to Enhance Virtual Reality Simulations. In: proc. of AIAA Modeling and Simulation Technologies Conference., pp. 1313 - 1323.10-13 August 2009, Chicago, llinois.

[99] Karkin, I., Grachev, V., Skochilov, A. and Zverev, V., 2010. "FlowTech" and "EvaTech": Two Computer-Simulation Methods for Evacuation Calculation. Pedestrian and Evacuation Dynamics 2008, pp. 537-54.

[100] Kawahara, Y., Maekawa, K. and Ikeda, Y., 2011. A Simple Prediction Formula of Roll Damping of Conventional Cargo Ships on the Basis of Ikeda's Method and Its Limitation. In: Neves, M.A.S., Belenky, V.L., Kat, J.O. de, Spyrou, K., Umeda, N. (Eds.), Contemporary Ideas on Ship Stability and Capsizing in Waves, Fluid Mechanics and Its Applications. Springer Netherlands, pp. 465–486.

[101] Kawahara, Y., Maekawa, K., Ikeda, Y., 2012. A Simple Prediction Formula of Roll Damping of Conventional Cargo Ships on the Basis of Ikeda's Method and Its Limitation. Journal of Shipping and Ocean Engineering, Vol.2, pp. 201–210.

[102] Kendik, E., 1986. Designing Escape Routes in Buildings. Fire Technology, 22(4), pp. 272-294.

[103] Kendik, E., 1986. Methods of design for means of egress: towards a quantitative comparison of national code requirements. Fire Safety Science, 1, pp. 497-511.

[104] Ketchell., N. 2006. A Technical Summary of the AEA EGRESS Code. Technical report,AEA Technology, https://www.esrtechnology.com/images/egresspage/Egress-Technical-Summary.pdf. Last accessed on 27/07/2017.

[105] Khalid, M. N. A., and Yusof, U. K. 2018. Dynamic crowd evacuation approach for the emergency route planning problem: Application to case studies. Safety Science, 102, 263-274.

[106] Kim, H., Park, J. H., Lee, D. and Yang, Y., 2004. Establishing the methodologies for human evacuation simulation in marine accidents. Computers & Industrial Engineering, 46(4), pp. 725–740.

[107] Kinateder, M., Pauli, P., Müller, M., Krieger, J., Heimbecher, F., Rönnau, I. and Mühlberger, A., 2013. Human behaviour in severe tunnel accidents: Effects of information and behavioural training. Transportation research part F: traffic psychology and behaviour, 17, pp. 20-32.

[108] Kinateder, M., Ronchi, E., Gromer, D., Müller, M., Jost, M., Nehfischer, M. and Pauli, P., 2014. Social influence on route choice in a virtual reality tunnel fire. Transportation research part F: traffic psychology and behaviour, 26, pp. 116-125.

[109] Klüpfel, H., and Meyer-König, T., 2005. Simulation of the Evacuation of a football stadium using the CA Model PedGo. Traffic and Granular Flow'03, pp. 423-428.

[110] Kongsberg Maritime AS, 2009. Kongsberg Maritime Simulation & Training - Ship's Bridge Simulator. https://www.kongsberg.com/~/media/Kongsberg%20Digital/Simulation/Ship%20Bridge%20Simulator/Downloads/KM_ShipsBridge-brosjyre.ashx. Last accessed on 27 November 2017.

[111] Korhonen T., Hostikka S., Heliövaara S. and Ehtamo H., 2008. FDS+Evac: An Agent Based Fire Evacuation Model. In: Klingsch W., Rogsch C., Schadschneider A.,

Schreckenberg M. (eds), Pedestrian and Evacuation Dynamics 2008. Springer, Berlin, Heidelberg.

[112] Korhonen, T., 2014. Fire Dynamics Simulator with Evacuation: FDS+Evac -Technical Reference and User's Guide (FDS 6.1.0, Evac 2.5.0, DRAFT). VTT Technical Research Centre of Finland.

[113] Kostas, K. V., Ginnis, A. A., Politis, C. G., and Kaklis, P. D., 2011. Motions Effect for Crowd Modeling Aboard Ships. In Pedestrian and Evacuation Dynamics 2012, pp. 825-833.

[114] Kretz, T. 2007. Pedestrian traffic-simulation and experiments. PhD dissertation. Universitat Duisburg-Essen, Germany.

[115] Kretz, T., and Schreckenberg, M., 2006. FAST-floor field-and agent-based simulation tool. arXiv preprint physics/0609097.

[116] Kretz, T., Grünebohm, A., Kaufman, M., Mazur, F., and Schreckenberg, M., 2006. Experimental study of pedestrian counterflow in a corridor. Journal of Statistical Mechanics: Theory and Experiment, 2006(10), P10001.

[117] Kretz, T., Hengst, S., Arias, A.P., Friedberger, S. and Hanebeck, U.D., 2012. Using extended range telepresence to collect data of pedestrian dynamics. In: proc. of Annual Meeting of the Transportation Research Board (Vol. 2012). 22-26 January. Washington D. C. (USA).

[118] Kukla, R., Kerridge, J., Willis, A. and Hine, J., 2001. PEDFLOW: Development of an autonomous agent model of pedestrian flow. Transportation research record: Journal of the transportation research board 1774. pp. 11-17.

[119] Kuligowski, E. D., Peacock, R. D., and Hoskins, B. L., 2005. A review of building evacuation models: US Department of Commerce, National Institute of Standards and Technology, Gaithersburg, MD.

[120] Kyriakou, M., Pan, X., and Chrysanthou, Y., 2016. Interaction with virtual crowd in Immersive and semi-Immersive Virtual Reality systems. Computer Animation and Virtual Worlds. Available online http://dx.doi.org/l0.1002/cav.I729.

[121] Lakoba, T. I., Kaup, D. J and Finkelstein, N. M., 2005. Modifications of the Helbing-Molnar-Farkas-Vicsek social force model for pedestrian evolution. Simulation, 81(5), pp. 339-352.

[122] Levin, B. M., 1989. EXITT-A simulation model of occupant decisions and actions in residential fires. Fire Safety Science, 2, pp. 561-570.

[123] Liao, W., Chraibi, M., Seyfried, A., Zhang, J., Zheng, X. and Zhao, Y., 2014, October. Validation of FDS+ Evac for pedestrian simulations in wide bottlenecks. In 17th International IEEE Conference on Intelligent Transportation Systems (ITSC) October 8-11, Qingdao, China, pp. 554-559.

[124] Liao, W., Seyfried, A., Zhang, J., Boltes, M., Zheng, X., Zhao, Y., 2014. Experimental study on pedestrian flow through wide bottleneck. Transportation Research Procedia, 2, pp. 26-33.

[125] Liao, W., Zhang, J., Zheng, X., and Zhao, Y., 2017. A generalized validation procedure for pedestrian models. Simulation Modelling Practice and Theory, 77, pp. 20-31.

[126] Lindeman, R. W., Sibert, J. L., Mendez-Mendez, E., Patil, S. and Phifer, D., 2005. Effectiveness of directional vibrotactile cuing on a building clearing task. In: Proceedings of the SIGCHI conference on Human factors in computing systems, 22 – 27 April, Montreal, Canada. , pp. 271-280.

[127] Löhner, R., 2010. On the modeling of pedestrian motion. Applied Mathematical Modelling, 34(2), pp. 366-382.

[128] Mabrouk, T. F., 2015. MASCM: Multi Agent System for Cloud Management. In: Software Engineering in Intelligent Systems, pp. 371-377. Springer International Publishing.

[129] Majumder, J., Vassalos, D., Guarin, L., Vassalos, G. C., and Safety at Sea Ltd., 2005. Modelling and simulation of shipboard environment and operations. Ship Technology Research, 52(4), pp. 159-171.

[130] Manley, M., Kim, Y., Christensen, K., and Chen, A., 2011. Modeling emergency evacuation of individuals with disabilities in a densely populated airport. Transportation Research Record: Journal of the Transportation Research Board, (2206), pp. 32-38.

[131] MARIN, 2017. FSSS/Fast Small Ship Simulator. http://www.marin.nl/web/Facilities-Tools/Simulators/Simulator-Facilities/FSSS-Fast-Small-Ship-Simulator.htm. Last accessed on 25 November 2017.

[132] Massive Software, 2017. Massive, http://www.massivesoftware.com , last accessed on 27/06/2017.

[133] Matusiak, J. and Hamberg, K., 2006. Considerations on the Weather Criterion Applicability for the Stability Assessment of Large Vessels. Proc. 9th International Conference on Stability of Ships and Ocean Vehicles (STAB2006), Rio de Janeiro, 25-29 September 2006, pp. 447-454.

[134] McDaniel, T., Krishna, S., Balasubramanian, V., Colbry, D., and Panchanathan, S., 2008. Using a haptic belt to convey non-verbal communication cues during social interactions to individuals who are blind. In: Proceedings of IEEE International Workshop on Haptic Audio visual Environments and Games (HAVE), 18-19 October, University of Ottawa, Canada. pp. 13-18..

[135] Meyer-König, T., Valanto, P., and Povel, D., 2005. Implementing ship motion in AENEAS - model development and first results. In: Pedestrian and evacuation dynamics, Springer Berlin Heidelberg, pp. 429-441.

[136] Min, Y., and Yu, Y., 2013. Calculation of mixed evacuation of stair and elevator using EVACNET4. Procedia Engineering, 62, pp. 478-482.

[137] Mohamed, A. I., Kabir, M. N., Alginahi, Y. M., and Haron, F., 2012. Software evaluation for crowd evacuation: Case study Masjid An-Nabawi. Phd dissertation. Universiti Sains Malaysia, Malaysia.

[138] Montecchiari, G., Bulian, P., Gallina, P., 2016. Development of a new evacuation simulation tool targeting real-time human participation. Proceedings of 26th European Safety and Reliability Conference (ESREL2016), 25-29 September 2016, Glasgow, Scotland, UK. In: Risk, Reliability and Safety: Innovating Theory and Practice, pp. 571-578.

[139] Montecchiari, G., Bulian, G., Gallina, P., 2017. Ship evacuation simulation using a game engine: modelling and testing. Under review.

[140] Montecchiari, G., Bulian, G., Gallina, P., 2017. Towards real-time human participation in virtual evacuation through a validated simulation tool. Proceedings of the Institution of Mechanical Engineers, Part O: Journal of Risk and Reliability, First Published May 4, doi: 10.1177/1748006X17705046.

[141] Montecchiari, G., Gallina, P., Bulian, G., 2017. An experiment using immersive virtual reality and a haptic interface to study human behaviour in evacuation. Proc. of 27th European Safety and Reliability Conference ESREL2017, in “Safety and Reliability: Theory and Application”,, 18-22 September, Portoroz, Slovenia. pp. 1893-1901.

[142] Montecchiari, G., Gallina, P., Bulian, G., Scalera, L., 2017. The effects of a vibrotactile interface on evacuation simulation with virtual reality. Under review.

[143] Moussaïd, M., Kapadia, M., Thrash, T., Sumner, R. W., Gross, M., Helbing, D. and Hölscher, C., 2016. Crowd behaviour during high-stress evacuations in an immersive virtual environment. Journal of The Royal Society Interface, 13(122), 20160414.

[144] Moussaid, M., Perozo, N., Garnier, S., Helbing, D., Theraulaz, G., 2010. The walking behavior of pedestrian social groups and its impact on crowd dynamics.PLoS ONE 5(4), e10047.

[145] MSC 78/INF.8, 2004. An experimental study in the walking speed prediction in evacuation analysis. Submitted by Korea, 6 February 2004, International Maritime Organization (IMO), London, UK.

[146] MSC.1/Circ.1238, 2007 - Guidelines for evacuation analysis for new and existing passenger ships. International Maritime Organization (IMO), 30 October, London, UK.

[147] MSC.1/Circ.1533, 2016. - Revised guidelines for evacuation analysis for new and existing passenger ships. 6 June, International Maritime Organization (IMO), London, UK.

[148] MSC.404(96), 2016. Amendments to the International Convention for the Safety Of Life at Sea, 1974, as Amended. Adopted on 19 May, International Maritime Organization (IMO), London, UK.

[149] MSC/Circ.1001, 2001. Interim guidelines for a simplified evacuation analysis of high-speed passenger craft, 26 June. IMO, London, UK.

[150] MSC/Circ.1033, 2002. Interim guidelines for evacuation analyses for new and existsing passenger ships, 6 June 2002. IMO, London, UK.

[151] MSC/Circ.1166, 2005. Guidelines for a simplified evacuation analysis for high-speed passenger craft, 27 June 2005. IMO, London, UK.

[152] MSC/Circ.909, 1999. Interim Guidelines for a Simplified Evacuation Analysis on Ro-Ro-Passenger Ships.4 June, International Maritime Organization (IMO), London, UK.

[153] Muramatsu, M., Irie, T., and Nagatani, T., 1999. Jamming transition in pedestrian counter flow. Physica A: Statistical Mechanics and its Applications, 267(3), pp. 487-498.

[154] Murphy, S. Ó., Brown, K. N., and Sreenan, C., 2013. The EvacSim pedestrian evacuation agent model: development and validation. In: Proceedings of the 2013 Summer Computer Simulation Conference. Society for Modeling and Simulation International, July 07 – 10, Toronto, Canada, pp. 38 - 46.

[155] Musse, S. R., and Thalmann, D., 2001. Hierarchical model for real time simulation of virtual human crowds. IEEE Transactions on Visualization and Computer Graphics, 7(2), pp. 152-164.

[156] Nelson, H. E., 1990. FPETOOL: Fire protection engineering tools for hazard estimation. Center for Fire Research.

[157] Niazi, M., and Hussain, A. 2011. Agent-based computing from multi-agent systems to agent-based models: a visual survey. Scientometrics, 89(2), pp. 479-499.

[158] Nicholls, I., Hifil, Y., Lee, B. S., Galea, E. R., Deerez, S., Blackshields, D., and Sharp, G., 2012.The SAFEGUARD hell scenario evaluation banchmark and recommandation to IMO to update MSC Circ 1238. Safeguard Passenger Evacuation Seminar, 30 November, London,UK.

[159] Nilsson, D., Johansson, M., and Frantzich, H., 2009. Evacuation experiment in a road tunnel: A study of human behaviour and technical installations. Fire Safety Journal, 44(4), pp. 458-468.

[160] NVDIA 2017. PhysX user manual. http://docs.nvidia.com/gameworks/content/gameworkslibrary/physx/guide/Index.html. Last accessed on 17 January 2017.

[161] Oculus VR, 2017. Documentation on Oculus Rift avaliable online at https://developer.oculus.com/documentation/https://www.oculus.com/, last accessed on 20 Novemebr 2017.

[162] Okazaki, S., and Matsushita, S., 1993. A study of simulation model for pedestrian movement with evacuation and queuing. In: International Conference on Engineering for Crowd Safety, 17-18 March, London, UK. pp. 271-280.

[163] Olivier, A. H., Bruneau, J., Cirio, G. and Pettré, J. 2014. A virtual reality platform to study crowd behaviors. Transportation Research Procedia, 2, pp. 114-122.

[164] Olivier, A. H., Bruneau, J., Kulpa, R., and Pettré, J., 2017. Walking with virtual people: Evaluation of locomotion interfaces in dynamic environments. IEEE Transactions on Visualization and Computer Graphics.DOI 10.1109/TVCG.2017.2714665.

[165] Pamungkas, D.S. and Ward, K., 2016. Electro-tactile feedback system to enhance virtual reality experience. International Journal of Computer Theory and Engineering 8(6), pp. 465-470.

[166] Papanikolaou, A., 2014. Ship Design - Methodologies of Preliminary Design. Springer Netherlands, ISBN: 978-94-017-8750-5, DOI: 10.1007/978-94-017-8751-2.

[167] Park, K. P., Ham, S. H. and Ha, S., 2015. Validation of advanced evacuation analysis on passenger ships using experimental scenario and data of full-scale evacuation. Computers in Industry, 71, pp. 103-115.

[168] Pelechano, N., Allbeck, J. M., Badler and N. I., 2007. Controlling individual agents in high-density crowd simulation. In Proceedings of the 2007 ACM SIGGRAPH/Eurographics symposium on Computer animation. August 03-04. San Diego, California, pp. 99-108.

[169] Pennycott, A. and Hifi, Y., 2010. Evacuability of a Flooded Passenger Ship. In: Proc. 3rd Workshop on Risk-Based Approaches in the Marine Industries, 18-20 October 2010, Trieste, Italy.

[170] Pérez Arias, A., Hanebeck, U. D., Ehrhardt, P., Hengst, S., Kretz, T. and Vortisch, P., 2011. Extended range telepresence for evacuation training in pedestrian simulations. In: Pedestrian and Evacuation Dynamics, pp. 199-208.

[171] Pérez Arias, A., Hanebeck, U.D., Ehrhardt, P., Hengst, S., Kretz, T., Vortisch, P. and Vortisch, P. 2009. A framework for evaluating the VISSIM traffic simulation with extended range telepresence. In: Proceedings of the 22nd Annual Conference on Computer Animation and Social Agents (CASA 2009), pp. 13-16. June 17-19. Amsterdam, Netherlands.

[172] Poon, L. S. 1994. EvacSim: A simulation model of occupants with behavioural attributes in emergency evacuation of high-rise building fires. Fire Safety Science, 4, pp. 681-692.

[173] PTV 2011. VISSIM 5.30-05 User Manual. PTV Planung Transport Verkehr AG, Karlsruhe, Germany, April.

[174] Qu, Y., Gao, Z., Xiao, Y., and Li, X., 2014. Modeling the pedestrian's movement and simulating evacuation dynamics on stairs. Safety Science, 70, pp. 189-201.

[175] Reisser-Weston, E. Simulating Human Behaviour in Emergency Situations. In RINA, International Conference of Escape, Fire, and Rescue, 1996.

[176] Rivers, E., Jaynes, C., Kimball, A., Morrow, E., and Zarnke, M., 2011. Using Case Study Data to Validate 3D Agent-Based Simulation Tool for Egress Modeling. In Fire and Evacuation Modeling Technical Conference, Baltimore, Md.

[177] Robin, T., Antonini, G., Bierlaire, M. and Cruz, J., 2009. Specification, estimation and validation of a pedestrian walking behaviour model. Transportation Research Part B: Methodological, 43(1), pp. 36-56.

[178] Roggen, D., Wirz, M., Tröster, G. and Helbing, D., 2011. Recognition of crowd behaviour from mobile sensors with pattern analysis and graph clustering methods. arXiv:1109.1664 [physics.soc-ph].

[179] Ronchi, E. 2014. The need for a verification and validation protocol for evacuation models. In: Fire and Evacuation Modeling Technical Conference, Courtyard Gaithersburg Washingtonian Center in Gaithersburg, MD, USA. pp. 8-10, 2014.

[180] Ronchi, E., Fahy, R., Colonna, P., and Berloco, N., 2014. Validation and calibration of the EXIT89 evacuation model for road tunnel evacuation applications. In: Pedestrian and Evacuation Dynamics 2012.pp. 543-550.

[181] Ronchi, E., Kinateder, M., Müller, M., Jost, M., Nehfischer, M., Pauli, P., and Mühlberger, A. 2015. Evacuation travel paths in virtual reality experiments for tunnel safety analysis. Fire Safety Journal, 71, pp. 257-267.

[182] Rosenthal, J., Edwards, N., Villanueva, D., Krishna, S., McDaniel, T., and Panchanathan, S., 2011. Design, implementation, and case study of a pragmatic vibrotactile belt. IEEE Transactions on Instrumentation and Measurement, 60(1), pp. 114-125.

[183] Ross, D. A., Blasch, B. B., 2000. Wearable interfaces for orientation and wayfinding. In: Proceedings of the fourth international ACM conference on Assistive technologies, November 13–15, Arlington, VA, USA. pp. 193–200.

[184] Rybokonenko, D., Balakhontceva, M., Voloshin, D., and Karbovskii, V., 2015. Agent-based modeling of crowd dynamics on a moving platform. Procedia Computer Science, 66, pp. 317-327.

[185] SAFEGUARD project, 2011. SAFEGUARD, the News Letter, 1 June 2011 .

[186] SAFEGUARD, 2012. The SAFEGUARD Validation Data Set (SGVDS1, SGVDS2), available at www.safeguardproject.info, 3 December (Last Accessed May 1, 2017).

[187] Salvesen, N., Tuck, E.O., Faltinsen, O., 1970. Ship Motions and Sea Loads. Trans. SNAME, Vol.78, pp. 250-287.

[188] Santos, A., Queiròs, M., Montecchiari, G., 2017. Evacuation exercises and simulations toward improving safety at public buildings. Proc. 31st Environmental Informatics Conference EnvirInfo 2017, 13-15 September 2017, Luxembourg, in “From Science to Society – New Trends in Environmental Informatics”, pp. 25-35.

[189] Scalera, L., Seriani, S., Gallina, P., Di Luca, M., Gasparetto, A., 2017. An experimental setup to test dual-joystick directional responses to vibrotactile stimuli, In: Proceedings of IEEE World Haptics 2017, June 6-9.Fürstenfeldbruck (Munich), Germany. , pp. 72-77.

[190] Schadschneider, A., Klüpfel, H., Kretz, T., Rogsch, C. and Seyfried, A., 2009. Fundamentals of pedestrian and evacuation dynamics. In: Multi-Agent Systems for Traffic and Transportation Engineering, Ana Bazzan and Franziska Klügl (eds), pp. 124-154.

[191] Schaeffer, S. E., 2007. Graph clustering. Computer science review, 1(1), pp. 27-64.

[192] SDC 2/INF.9, 2014. Outline of research on simulation of evacuation and progress of casualty. Submitted by Japan, 12 December, International Maritime Organization (IMO), London, UK.

[193] SDC 3/WP.6, 2016. - Report of the Working Group on Fire Protection. International Maritime Organization (IMO), 21 January, London, UK.

[194] SDC 4/5/1/Add.1, 2016. Report of the correspondence group (part 2). Submitted by Japan, 11 November, London, UK.

[195] SDC 4/5/1/Add.3, 2016. Report of the correspondence group (part 4). Submitted by Japan, 11 November, London, UK.

[196] Seyfried, B. Steffen, W. Klingsch, and M. Boltes, 2005. The Fundamental Diagram of Pedestrian Movement Revisited", Journal of Statistical Mechanics: Theory and Experiment 10 (2005) P10002, arXiv:physics/0506170 [physics.soc-ph].

[197] Sharma, S. B., and Tabak, V., 2008. Rapid Agent Based Simulation of People Flow for Design of Spaces. available online at :Cumulative Index of Computer Aided Architectural Design (CumInCAD), https://cumincad.architexturez.net/system/files/pdf/ddss2008-46.content.pdf.

[198] Shen, T., and Chien, S., 2005. An Evacuation Simulation Model (ESM) for Building Evaluation. Graduate School of Fire Science and Administration, Central Police University, Taiwan International Journal on Architectural Science, 6(1), pp. 15-30.

[199] Shendarkar, A., Vasudevan, K., Lee, S., and Son, Y. J. 2008. Crowd simulation for emergency response using BDI agents based on immersive virtual reality. Simulation Modelling Practice and Theory, 16(9), pp. 1415-1429.

[200] Shestopal, V. O. and Grubits, S. J., 1994. Evacuation Model for Merging Traffic Flows in Multi-Room and Multi-Story Buildings. In: Fire Safety Science -Proceedings of the 4th International Symposium, pp. 625-632.

[201] Sin, H. G., and Joo, Y. J., 2013. A study on prototype model for mesoscopic evacuation using Cube Avenue simulation model. Journal of Korea Spatial Information Society, 21(5), pp. 33-41.

[202] Sin, H. G., and Joo, Y. J., 2017. Development of urban disaster evacuation model using Cube Avenue. Spatial Information Research,5, pp. 1-9.

[203] SLF 49/INF.5, 2006. Time dependent survival probability of a dameged passenger ship. Submitted by Germany, 21 April, International Maritime Organization (IMO), London, UK.

[204] Smith, A., James, C., Jones, R., Langston, P., Lester, E., and Drury, J., 2009. Modelling contra-flow in crowd dynamics DEM simulation. Safety Science, 47(3), pp. 395-404.

[205] Sørensen, J. G and Dederichs, A. S., 2014. Evacuation from a complex structure–The effect of neglecting heterogeneous populations. Transportation Research Procedia, 2, pp. 792-800.

[206] Stahl, F. I., 1982. BFIRES-II: a behavior based computer simulation of emergency egress during fires. Fire technology, 18(1), pp. 49-65.

[207] Sun, J., Guo,Y., Li, C., Lo,S., Lu, S., 2017. An experimental study on individual walking speed during ship evacuation with the combined effect of heeling and trim. Ocean Engineering, in press. Available online https://doi.org/10.1016/j.oceaneng.2017.10.008, last accessed on 20 November 2017.

[208] Tajima, Y., Takimoto, K.and Nagatani, T., 2002. Pattern formation and jamming transition in pedestrian counter flow. Physica A: Statistical Mechanics and its Applications, 313(3), pp. 709-723.

[209] Takahashi, K., Tanaka, T. and Kose, S., 1989. An Evacuation Model For Use In Fire Safety Design Of Buildings. Fire Safety Science 2, pp. 551-560.

[210] Teknomo, K.,2016. Microscopic Pedestrian Flow Characteristics: Development of an Image Processing Data Collection and Simulation Model. PhD dissertation. Tohoku University, Tohoku, Japan.

[211] Thompson, P. A., and Marchant., E. W., 1994. Simulex; developing new computer modelling techniques for evaluation. Fire Safety Science 4, pp. 613-624.

[212] Thornton, C., O'Konski, R., Hardeman, B., and Swenson, D., 2011. Pathfinder: An agent-based egress simulator. In: Pedestrian and Evacuation Dynamics, Springer, Boston, MA. pp. 889-892.

[213] Tirosh, O. and Sparrow, W. A., 2004. Gait termination in young and older adults: effects of stopping stimulus probability and stimulus delay. Gait and posture, 19(3), pp. 243-251.

[214] TraffGo-HT, 2013. PedEd PedGo PedView AENEASEd AENEASSim AENEASView User Manual. available at http://www.traffgo-ht.com/downloads/pedestrians/downloads/documents/manual.pdf , last accessed on 1 May 2017

[215] Tucker, M. J., Challenor, P. I. and Carter, D. J. T., 1984. Numerical simulation of a random sea: a common error and its effect upon wave group statistics. Applied Ocean Research 6(2), pp. 118-122.

[216] Umeda, N., Koga, S., Ueda, J., Maeda, E., Tsukamoto, I., Paroka, D., 2007. Methodology for Calculating Capsizing Probability for a Ship under Dead Ship Condition. In: Proc. 9th International Ship Stability Workshop, 30-31 August, Hamburg, Germany, pp. 30 – 31.

[217] Unity Technologies 2017. https://unity3d.com/. Last accessed on 17 November 2017

[218] Van Erp, J. B., Van Veen, H. A., Jansen, C., and Dobbins, T., 2005. Waypoint navigation with a vibrotactile waist belt. ACM Transactions on Applied Perception (TAP), 2(2), pp. 106–117.

[219] Vassalos, D., Kim, H. S., Christiansen, G. and Majumder, J., 2002. A mesoscopic model for passenger evacuation in a virtual ship-sea environment and performance-based evaluation. In: Pedestrian and Evacuation Dynamics. Springer Netherlands,pp. 369-391.

[220] Vermuyten, H., Beliën, J., De Boeck, L., Reniers, G. and Wauters, T., 2016. A review of optimisation models for pedestrian evacuation and design problems. Safety Science, 87, pp. 167-178.

[221] Wang, P., Fang, Z. and Yuan, J.P., 2005. A new model and its validation for prediction of safety evacuation in high-rise building (in Chinese), Fire Saf. Sci. 15 (2), pp. 75–79.

[222] Waterson, N. P. and Pellissier, E. 2010. The step pedestrian microsimulation tool – A technical summary. Mott MacDonald Limited, Croydon, UK, 6 July. Available at http://www.steps.mottmac.com/files/page/398343/STEPS___Technical_Summary.pdf (Last accessed on 17 May 2017) .

[223] Weidmann, U., 1993. Transporttechnik der Fussgänger.Schriftenreihe des IVT. 90 (Zweite ergänzte Auflage), März, ETH Zürich, Zürich.

[224] Weifeng, F., Lizhong, Y., and Weicheng, F., 2003. Simulation of bi-direction pedestrian movement using a cellular automata model. Physica A: Statistical Mechanics and its Applications, 321(3), pp. 633-640.

[225] Weng, W. G., Chen, T., Yuan, H. Y., and Fan, W. C., 2006. Cellular automaton simulation of pedestrian counter flow with different walk velocities. Physical Review E, 74(3), 036102.

[226] Witmer, B. G., and Singer, M. J. 1998. Measuring presence in virtual environments: A presence questionnaire. Presence: Teleoperators and virtual environments, 7(3), pp. 225-240.

[227] Wooldridge, M., and Jennings, N. R., 1995. Intelligent agents: Theory and practice. Knowledge engineering review, 10(2), 115-152.

[228] Xi, H., Lee, S., and Son, Y. J., 2011. An integrated pedestrian behaviour model based on extended decision field theory and social force model. In: Human-in-the-Loop Simulations, pp. 69-95. Springe, London.

[229] Xu, M., Wu, Y., Lv, P., Jiang, H., Luo, M., and Ye, Y., 2015. miSFM: On combination of Mutual Information and Social Force Model towards simulating crowd evacuation. Neurocomputing, 168, pp. 529-537.

[230] Yang, L., Li, J., and Liu, S., 2008. Simulation of pedestrian counter-flow with right-moving preference. Physica A: Statistical Mechanics and its Applications, 387(13), pp. 3281-3289.

[231] Yuen, J. K. K., and Lee, E. W. M., 2012. The effect of overtaking behavior on unidirectional pedestrian flow. Safety science, 50(8), pp. 1704-1714.

[232] Zainuddin, Z., Thinakaran, K., and Abu-Sulyman, I. M., 2009. Simulating the Circumambulation of the Ka'aba using SimWalk. European Journal of Scientific Research, 38(3), pp. 454-464.

[233] Zhang, D., Shao, N., and Tang, Y., 2017. An evacuation model considering human behavior. In: 14th International Conference on Networking, Sensing and Control (ICNSC), 2017, IEEE, pp. 54-59. May 16-18 Calabria, Italy.

[234] Zhang, J., 2012. Pedestrian fundamental diagrams: comparative analysis of experiments in different geometries. PhD Thesis, Schriften des Forschungszentrums Jülich, IAS Series, Vol. 14, Universität Wuppertal, Germany.

[235] Zhang, J., Britto, D., Chraibi, M., Löhner, R., Haug, E., and Gawenat, B., 2014. Quantitative validation of PEDFLOW for description of unidirectional pedestrian dynamics. Transportation Research Procedia, 2, pp. 733-738.

[236] Zhang, J., Klingsch, W., Schadschneider, A. and Seyfried, A., 2012. Ordering in bidirectional pedestrian flows and its influence on the fundamental diagram. Journal of Statistical Mechanics: Theory and Experiment, 2012(02), P02002.

[237] Zhang, J., Klingsch, W., Schadschneider, A., and Seyfried, A., 2013. Experimental study of pedestrian flow through a T-junction. In: Kozlov V., Buslaev A., Bugaev A., Yashina M., Schadschneider A., Schreckenberg M. (eds) Traffic and Granular Flow '11, pp. 241-249.

[238] Zhang, J., Song, W., and Xu, X., 2008. Experiment and multi-grid modeling of evacuation from a classroom. Physica A: Statistical Mechanics and its Applications, 387(23), pp. 5901-5909.

[239] Zheng, X., Zhong, T. and Liu, M., 2009. Modeling crowd evacuation of a building based on seven methodological approaches. Building and Environment, 44(3), pp. 437-445.